

Anti-inflammatory Drug-loaded Electrospun Scaffolds Aimed at Modulating Inflammation in Chronic Skin Wounds

Usanee Detamornrat

Thesis submitted to the University of Nottingham

for the degree of Doctor of Philosophy

September 2019

Abstract

The prolonged inflammation in chronic wounds is one of the key factors that delays the healing of wounds. During the inflammation phase, neutrophils and macrophages release TNF-α and IL-1β to induce the production or expression of pro-inflammatory mediators: prostaglandin E_2 (PGE_2), matrix metalloproteinases (MMPs) and nitric oxide (NO). Herein the medicated electrospun scaffolds were developed and aimed to provide a fibrous structure that mimics the architecture of natural extracellular matrix (ECM) to support cell proliferation. In addition, the scaffolds were also designed to deliver anti-inflammatory drugs to inhibit the production/expression of the pro-inflammatory mediators.

The anti-inflammatory effect of ibuprofen sodium (IBU Na) was related to the inhibition of cyclooxygenase (COX) enzymes and PGE_2 production. IBU Na was incorporated into PLGA electrospun scaffolds (at 1, 2, and 5 % w/w). SEM images have confirmed that all scaffolds consisted of smooth rounded microfibres. IBU Na was found to have a great impact on the properties of PLGA scaffolds—higher contents of IBU Na led to the decreases in ultimate tensile strength and Young's modulus of the scaffolds. Moreover, IBU Na was found to accelerate the scaffold degradation. ToF-SIMS revealed that most IBU Na was located on the surfaces of the fibres, which can explain the rapid burst release profile of IBU Na in PBS. Higher metabolic activity of cells was observed, implying that PLGA-IBU Na scaffolds could support the proliferation of mouse fibroblasts.

Doxycycline hydrochloride (DOX HCl) is an analogue in tetracycline family. It exhibits anti-inflammatory effect *via* the inhibition of MMPs. In this case, PCL was selected as the polymer for fabricating DOX HCl-loaded scaffolds (at 1, 2 and 5% w/w). PCL-DOX HCl scaffolds consisted of nano-sized fibres with smooth surface and rounded morphology. DOX HCl enhanced the ultimate tensile strength and Young's modulus of the scaffolds. The scaffolds remained their fibrous integrity over 90-day incubation in PBS. The scaffolds supported the adhesion and proliferation of primary human dermal fibroblasts.

Apart from conventional scaffold fabrication, this work shows that coaxial electrospun scaffold can also be fabricated. The structure of the scaffold's fibres constituted of PCL shell and PLGA core. DOX HCl and IBU Na were loaded into PCL shell at 1% w/w and PLGA core at 5% w/w, respectively. Even though the incorporated drugs in the scaffolds increased the ultimate tensile strength of the scaffolds, they unfortunately speeded up the process of scaffold degradation. The release of DOX HCl and IBU Na from the scaffolds were rapid in PBS. This is due to the deposition of these two drugs at the surfaces of fibres. The coaxial scaffolds could also support the proliferation of primary human dermal fibroblasts.

The efficacy testing was carried out to assess the ability of the scaffolds to inhibit the production/expression of pro-inflammatory mediators stimulated by TNF-α and IL-1β. Unfortunately, the significant increase in the productions of PGE_2 and nitrite in primary human dermal fibroblasts induced by the cytokines were

not achieved. This was due to the presence of basic fibroblast growth factor (bFGF) in cell culture media. On the other hand, the expression of MMP-1 enzyme was successfully induced by TNF-α and IL-1β. The results demonstrated that PCL-DOX HCl scaffolds could inhibit the cytokine-induced MMP-1 expression in a dose dependent manner. The coaxial PCL-DOX HCl 1%/PLGA-IBU Na 5% scaffolds also showed an inhibiting effect on the cytokine-induced MMP-1 expression, which corresponded to the presence of IBU Na in the scaffolds not DOX HCl.

Acknowledgements

First of all, I would like to express my gratitude to my supervisors, Dr. Lee Buttery and Prof. Felicity Rose, for their guidance, advice and all supports throughout my study whenever I needed. Many thanks for giving me the opportunities to develop both scientific and non-scientific related skills and to learn to work professionally and independently.

I am very grateful to the University of Nottingham for providing me the Vice-Chancellor's Scholarship for Research Excellence (International) to pursue this unforgettable journey. I would like to extend thankfulness to Dr. Lee Buttery and Prof. Kevin Shakesheff for supporting me during the scholarship application.

I would like to thanks Christine Grainger-Boultby and Dr. Elisabeth Steer for SEM trainings and excellent assistances, Paul Cooling and Thomas Booth for all trainings in Boots building, Dr. Long Jiang and Dr. Nichola Starr for guiding me for ToF-SIMS analysis, and Denise McLean for TEM trainings and kind words.

Thanks to all colleagues and friends in Division of Regenerative Medicine and Cellular Therapies past and present. In particular, Mahi, Annesi, Marta, Afnan and Aruna for all supports and advice, Mat for his help and suggestions, Elisa,

Francesco, Jopeth and Inchirah for their supports and social event organisation, and Teresa and Ann for great technical supports.

I also would like to thank Zubair, Steve, Lok, Jen, Brian, Minh and Glen for encouraging me to get through a hard time during the writing period.

My PhD journey would not be this joyful without Lara, Pritesh, Elisabetta, Lalitha, Aishwarya, Sandhya and Jazz. Thanks for making this journey full with happiness and wonderful time. It means a lot to me.

I would not have come this far without the endless and unconditional supports from Yao. Thank you so much for believing in me and always being by my side to share both happiness and sadness together. I would like to extend my thanks to Ouan, Hed, Mee and Taohuay for their incredible supports and magical times we spent together.

Finally, I would like to thanks my parents and my sisters for their love, never ending supports and encouragement. Thanks for letting me independently explore this journey. Without you all, I would not have become myself as today.

Table of Contents

Abstract i

Acknowledgements iv

List of Figures xiv

List of Tables xxv

Abbreviations xxviii

Chapter 1 Introduction 1

1.1 Skin 1

1.2 Wounds 5

1.3 Wound healing 5

1.3.1 Haemostasis 6

1.3.2 Inflammation 6

1.3.3 Proliferation 7

1.3.4 Remodeling 7

1.4 Types of wounds 9

1.4.1 Factors that retard wound healing in chronic wounds 10

1.4.2 Persistent inflammation in chronic wounds 10

1.4.2.1 Matrix metalloproteinases 11

1.4.2.2 Cyclooxygenases 12

1.4.2.3 Nitric oxide 12

1.5 Incidence of chronic wounds 14

1.6 Wound care and dressings 15

1.7 Skin tissue engineering 19

1.7.1 Skin substitutes 20

1.7.1.1 Cells 20

1.7.1.2 Growth factors 21

1.7.1.3 Scaffolds 22

1.8 Electrospinning 24

1.8.1 General set-up and principle 24

1.8.2 Parameters in electrospinning process 25

1.8.2.1 Polymer solution parameters 26

1.8.2.2 Process parameters 28

1.8.2.3 Environment parameters 29

1.9 Drug-loaded electrospun scaffolds 31

1.9.1 Surface immobilisation 31

1.9.2 Blend electrospinning 32

1.9.3 Coaxial electrospinning 32

1.9.4 Emulsion electrospinning 33

1.9.5 Secondary carrier electrospinning 33

1.10 Aims and objectives 34

Chapter 2 Materials and General Methods 37

2.1 Materials 37

2.2 General Methods 40

2.2.1 Characterisation of polymer and polymer-drug solutions 40

2.2.1.1 Viscosity measurement 40

2.2.1.2 Conductivity measurement 40

2.2.2 Characterisation of electrospun scaffolds 41

2.2.2.1 Morphology and fibre diameter 41

2.2.2.2 Porosity by gravimetric method 41

2.2.2.3 Mechanical properties 43

2.2.2.4 Water contact angle 44

2.2.2.5 Drug encapsulation efficiency 46

2.2.2.6 Superficial drug distribution by Time of Flight Secondary Ion Mass Spectrometry 47

2.2.2.7 Drug release 48

2.2.2.8 Drug-polymer interaction by NMR 48

2.2.2.9 *In vitro* degradation study 49

2.2.3 Cell culture 50

2.2.3.1 Mouse embryonic fibroblasts 50

2.2.3.2 Primary human dermal fibroblasts 50

2.2.4 Cryopreservation 51

2.2.5 Drug cytotoxicity 51

2.2.6 Cell proliferation on the scaffolds 52

2.2.6.1 Cell seeding 52

2.2.6.2 PrestoBlue® assay 53

2.2.6.3 LIVE/DEAD® assay 54

2.2.6.4 Cell morphology by SEM imaging 54

2.2.6.5 Cell infiltration by confocal microscopy 55

2.2.7. Statistical analysis 56

Chapter 3 Fabrication and Characterisation of Ibuprofen Sodium-loaded PLGA Electrospun Scaffolds 57

3.1 Introduction 57

3.2 Aims and Objectives 64

3.3 Experimental overview 66

3.4 Materials and Methods 67

3.4.1 Preparation of polymer solutions for electrospinning 67

3.4.2 Fabrication of PLGA and IBU Na-loaded PLGA scaffolds using electrospinning technique 67

3.4.3 Characterisation of the scaffolds 68

3.4.4 Cell studies 68

3.5 Results and Discussion 68

3.5.1 The studies of polymer solution's properties (viscosity and conductivity) 69

3.5.2 Characterisation of PLGA and IBU Na-loaded PLGA electrospun scaffolds 73
3.5.2.1 Scaffold morphology and fibre diameter 73
3.5.2.2 Porosity 76
3.5.2.3 Mechanical properties 78
3.5.2.4 Water contact angle 82
3.5.2.5 Drug encapsulation efficiency 85
3.5.2.6 Superficial drug distribution determined by ToF-SIMS 86
3.5.2.7 Drug release profiles of IBU Na from the PLGA scaffolds 92
3.5.2.8 PLGA-IBU Na interactions 98
3.5.2.9 Degradation profile of the scaffolds 102
3.5.3 Cytotoxic concentration of IBU Na 105
3.5.4 Cell proliferation study 106
3.5.4.1 Cellular metabolic activity by PrestoBlue® assay 106
3.5.4.2 LIVE/DEAD® assay 108
3.5.4.3 Cell morphology 112
3.5.4.4 Cell infiltration into the structure of electrospun scaffolds 114
3.6 Conclusion 118
Chapter 4 Fabrication and Characterisation of Doxycycline Hydrochloride-loaded PCL Electrospun Scaffolds 120
4.1 Introduction 120
4.2 Aims and Objectives 127
4.3 Experimental overview 128
4.4 Materials and Methods 129
4.4.1 Preparation of polymer and polymer-drug solutions for electrospinning 129
4.4.2 Fabrication of PCL and DOX HCl-loaded PCL scaffolds using electrospinning technique 129
4.4.3 Characterisation of the scaffolds 130

4.4.4 Cell studies 130

4.5 Results and Discussion 130

4.5.1 Characterisation of polymer solution properties (viscosity and conductivity) 132

4.5.2 Characterisation of the electrospun scaffolds 134

4.5.2.1 Scaffold morphology and fibre diameter 134

4.5.2.2 Total porosity 138

4.5.2.3 Mechanical properties 138

4.5.2.4 Water contact angle 141

4.5.2.5 Drug encapsulation efficiency 143

4.5.2.6 Superficial drug distribution determined by ToF-SIMS 144

4.5.2.7 Drug release profiles of DOX HCl from PCL scaffolds 151

4.5.2.8 Doxycycline hydrochloride-PCL interaction by NMR 154

4.5.2.9 Degradation profiles of the scaffolds 158

4.5.3 Drug cytotoxicity 161

4.5.4 Cell proliferation 162

4.5.4.1 Cellular metabolic activity by PrestoBlue® assay 162

4.5.4.2 LIVE/DEAD® assay 164

4.5.4.3 Cell morphology by SEM 166

4.6 Conclusion 169

Chapter 5 Fabrication and Characterisation of Dual Drug-loaded Coaxial PCL/PLGA Electrospun Scaffolds 171

5.1 Introduction 171

5.2 Aims and Objectives 175

5.3 Experimental overview 176

5.4 Materials and Methods 177

5.4.1 Preparation of polymer and polymer-drug solutions 177

5.4.2 Coaxial electrospinning set-up 178

5.4.3 Transmission electron microscopy (TEM) 179
5.4.4 Characterisation of the scaffolds 179
5.4.5 Cell studies 179
5.5 Results and Discussion 180
5.5.1 The studies of polymer solution's properties 182
5.5.1.1 Viscosity 182
5.5.1.2 Conductivity 182
5.5.2 The characterisation of scaffold properties 184
5.5.2.1 Fibre morphology and fibre diameter 184
5.5.2.2 Determination of core-shell structure 187
5.5.2.3 Total porosity 190
5.5.2.4 Mechanical properties 191
5.5.2.5 Water contact angle 193
5.5.2.6 Drug encapsulation efficiency 195
5.5.2.7 Drug-drug interaction by NMR spectroscopic analysis 196
5.5.2.8 Superficial drug distribution determined by ToF-SIMS 198
5.5.2.9 Drug release profiles 207
5.5.2.10 Degradation profile of the scaffolds 210
5.5.3 Drug cytotoxicity 213
5.5.4 Cell proliferation on the coaxial electrospun scaffolds 217
5.5.4.1 Cellular metabolic activity by PrestoBlue® assay 217
5.5.4.2 LIVE/DEAD® assay 220
5.5.4.3 Cell morphology by SEM 220
5.5.4.4 Cytoskeletal architecture of primary human dermal fibroblasts 223
5.6 Conclusion 226
Chapter 6 Investigation of Doxycycline Hydrochloride- and Ibuprofen Sodium-doped Scaffolds in Simulated Cytokine-induction Inflammation Environments 228

6.1 Introduction 228

6.2 Aims and Objectives 230

6.3 Experimental overview 232

6.4 Methods 233

6.4.1 Cell seeding 233

6.4.2 Conditions 233

6.4.3 Assays 234

6.4.3.1 Cell viability by PrestoBlue® assay 234

6.4.3.2 Detection of nitrite by Griess assay 235

6.4.3.3 MMP-1 ELISA assay 236

6.4.3.4 PGE_2 ELISA assay 237

6.5 Results and Discussion 239

6.5.1 Evaluation of the PCL-DOX HCl scaffolds 240

6.5.1.1 DOX HCl solutions 240

6.5.1.2 PCL-DOX HCl scaffolds 250

6.5.2 Evaluation of the coaxial electrospun scaffolds 258

6.5.2.1 DOX HCl solution, IBU Na solution and the mixture of drugs 258

6.5.2.2 Coaxial electrospun scaffolds 267

6.6 Conclusion 273

Chapter 7 Concluding Remarks and Future work 276

7.1 Conclusions 276

7.2 Future work 281

References 283

Chapter 8 Appendix 333

8.1 Supplementary data for Chapter 3 333

8.1.1 Effect of PLGA8515 concentrations on the morphology of the scaffolds 333

8.1.2 Standard curve for determining drug encapsulation efficiency 334

8.1.3 Standard curve for drug release study 334

8.1.4 Determination of cellular metabolic activity using PrestoBlue® assay 335
8.2 Supplementary data for Chapter 4 336
8.2.1 The morphology of doxycycline hydrochloride (DOX HCl)-loaded electrospun scaffolds 336
8.2.2 Drug release profiles 337
8.2.2.1 PLGA8515-DOX HCl scaffolds 337
8.2.2.2 PLGA5050-DOX HCl and PLA-DOX HCl scaffolds 337
8.2.3. Drug degradation in the scaffolds 338
8.2.4 Standard curve for determining drug encapsulation efficiency 338
8.2.5 Standard curve for drug release study 339
8.2.6 Determination of cellular metabolic activity using PrestoBlue® assay 340
8.2.7 The release of doxycycline hydrochloride (DOX HCl) from PCL scaffolds in cell culture media 341
8.3 Supplementary data for Chapter 5 342
8.3.1 The morphology of the scaffold and core-shell structure of fibres 342
8.3.2 Standard curve for drug release study 343
8.3.3 Drug release profile of coaxial PLGA-IBU Na 1% (shell)/ PCL-DOX HCl 5% (core) electrospun scaffolds 344
8.3.4 Determination of cellular metabolic activity using PrestoBlue® assay 345
8.4 Supplementary data for Chapter 6 346
8.4.1 PCL-DOX HCl scaffolds 346
8.4.1.1 Determination of cellular metabolic activity using PrestoBlue® assay 346
8.4.1.2 Determination of nitrite concentration using Griess assay 346
8.4.2 Coaxial electrospun scaffolds 347
8.4.2.1 Determination of cellular metabolic activity using PrestoBlue® assay 347
8.4.2.2 Determination of nitrite concentration using Griess assay 347

List of Figures

Figure 1.1.	Functions of the skin	1
Figure 1.2.	The structure of skin	2
Figure 1.3.	The structure of epidermis layer	3
Figure 1.4.	Important events in acute wounds and chronic wounds	9
Figure 1.5.	The relative amount of nitric oxide produced by cells during phases in wound healing process	13
Figure 1.6.	Representative images showing the morphology of Alvetex™ scaffold and Mimetix® scaffold	23
Figure 1.7.	General set-up of the electrospinning process	25
Figure 1.8.	Schematic illustrations of different drug incorporation techniques into electrospun fibres	31
Figure 2.1.	Uniaxial tensile test of the electrospun scaffolds	43
Figure 2.2.	Static water contact angle on different types of material	44
Figure 2.3.	Modes of water contact angle measurements	46
Figure 2.4.	CellCrown™ insert body, cap and the electrospun scaffold immobilised with the insert	53
Figure 2.5.	Schematic showing experimental design for the cell proliferation study on electrospun scaffolds with mouse fibroblasts and primary human dermal fibroblasts	56
Figure 3.1.	Chemical structure of PLGA	58
Figure 3.2.	Production of pro-inflammatory mediator, prostaglandin E_2 and the mechanism of action of ibuprofen	60
Figure 3.3.	Chemical structure of ibuprofen sodium	61
Figure 3.4.	Diagram illustrating the application of electrospun scaffolds in diabetic foot ulcer	62
Figure 3.5.	Diagram showing the application of electrospun scaffolds to provide IBU Na and support cell proliferation	64
Figure 3.6.	Regeneration of ibuprofen acid form from ibuprofen sodium facilitated by HFIP	71
Figure 3.7.	Means and standard deviations of viscosity and conductivity of the PLGA solutions and PLGA-IBU Na solutions	72
Figure 3.8.	Diagram summarises the concentrations of the PLGA solutions used for fabricating the blank PLGA scaffolds and IBU Na-loaded PLGA scaffolds	73

Figure 3.9.	Representative SEM images of PLGA, PLGA-IBU Na 1%, PLGA-IBU Na 2% and PLGA-IBU Na 5% electrospun scaffolds	75
Figure 3.10.	Fibre diameter and total porosity of PLGA, PLGA-IBU Na 1%, PLGA-IBU Na 2% and PLGA-IBU Na 5% electrospun scaffolds	77
Figure 3.11.	Mechanical properties of electrospun scaffolds evaluated by a uniaxial tensile test	78
Figure 3.12.	Water contact angles of the electrospun scaffolds determined by static and dynamic modes of sessile drop method	83
Figure 3.13.	Representative positive ToF-SIMS spectra of the surface of electrospun scaffolds	87
Figure 3.14.	Representative negative ToF-SIMS spectra of the surface of electrospun scaffolds	87
Figure 3.15.	Representative negative ToF-SIMS spectra of the surface of electrospun scaffolds	88
Figure 3.16.	Normalised total ion intensity	88
Figure 3.17.	The 2D images show the distribution of positive ions	90
Figure 3.18.	The 2D images show the distribution of negative ions	91
Figure 3.19.	Cumulative drug release of IBU Na from PLGA scaffolds in PBS over 60 days and within the first 24 hours	93
Figure 3.20.	Dissociation and migration of ibuprofen sodium to the surface of polymer-drug jet during electrospinning.	95
Figure 3.21.	Triphasic drug release profile	97
Figure 3.22.	^{1}H NMR spectrum of IBU Na in d_6-DMSO	99
Figure 3.23.	^{1}H NMR spectrum of PLGA 8515 in d_6-DMSO	99
Figure 3.24.	^{1}H NMR spectrum of PLGA8515-IBU Na 5% scaffolds	101
Figure 3.25.	Degradation profile of the scaffolds in PBS solution (pH 7.4) shown as % weight loss	102
Figure 3.26.	Representative SEM images showing morphological changes of the scaffolds over time	103
Figure 3.27.	Cytotoxic effect of IBU Na was evaluated by PrestoBlue® assay	105
Figure 3.28.	Cell proliferation on TCP, PLGA, PLGA-IBU Na 1%, PLGA-IBU Na 2% and PLGA-IBU Na 5% electrospun scaffolds determined by cellular metabolic activity	107

	of mouse fibroblasts (3T3 cells) over 14 days using PrestoBlue® assay	
Figure 3.29.	Fold change in cell proliferation on TCP, PLGA, PLGA-IBU Na 1%, PLGA-IBU Na 2% and PLGA-IBU Na 5% electrospun scaffolds determined by cellular metabolic activity of mouse fibroblasts	107
Figure 3.30.	Representative fluorescent images obtained from the LIVE/DEAD® assay on day 1 of cell culture	109
Figure 3.31.	Representative fluorescent images obtained from the LIVE/DEAD® assay on day 3 and day 5 of cell culture	110
Figure 3.32.	Representative fluorescent images obtained from the LIVE/DEAD® assay on day 7 and day 14 of cell culture	111
Figure 3.33.	Representative SEM images showing cell morphology of mouse fibroblasts on the electrospun scaffolds	112
Figure 3.34.	Confocal micrographs of mouse fibroblasts on various electrospun scaffolds at day 14 of cell culture	115
Figure 3.35.	Representative SEM images of mouse fibroblasts on the PLGA scaffolds after being cultured for 14 days at various magnifications	116
Figure 4.1.	Chemical structure of doxycycline hydrochloride	125
Figure 4.2.	Chemical structure of poly(ε-caprolactone)	126
Figure 4.3.	Diagram illustrating the application of electrospun scaffolds to deliver DOX HCl and support cell proliferation	127
Figure 4.4.	Means and standard deviations of viscosity and conductivity of polymer solutions	133
Figure 4.5.	Representative SEM images and histograms for fibre diameter distribution of PCL, PCL-DOX HCl 1%, PCL-DOX HCl 2% and PCL-DOX HCl 5% scaffolds	136
Figure 4.6.	Fibre diameter and total porosity of PCL, PCL-DOX HCl 1%, PCL-DOX HCl 2% and PCL-DOX HCl 5% electrospun scaffolds	137
Figure 4.7.	Mechanical properties of electrospun scaffolds evaluated by a uniaxial tensile test	140
Figure 4.8.	Water contact angles of electrospun scaffolds were determined by static and dynamic modes of a sessile drop method	141
Figure 4.9.	Representative negative ToF-SIMS spectra of the	144

surface of electrospun scaffolds for PCL
Figure 4.10. Representative negative ToF-SIMS spectra of the surface of electrospun scaffolds for DOX HCl 145
Figure 4.11. Representative negative ToF-SIMS spectra of the surface of electrospun scaffolds for DOX HCl. 145
Figure 4.12. Representative positive ToF-SIMS spectra of the surface of electrospun scaffolds for PCL 146
Figure 4.13. Representative positive ToF-SIMS spectra of the surface of electrospun scaffolds for DOX HCl 146
Figure 4.14. Normalised total ion intensity of positive and negative charges 147
Figure 4.15. The 2D images show the distribution of PCL, DOX HCl, and total negative ions on the top surface of scaffolds. 149
Figure 4.16. The 2D images show the distribution of PCL, DOX HCl, and total positive ions on the top surface of scaffolds. 150
Figure 4.17. Cumulative drug release of DOX HCl from PCL scaffolds in PBS over 30 days and within the first 5 hours 151
Figure 4.18. ^{1}H NMR spectrum of doxycycline hydrochloride in d_6-DMSO 154
Figure 4.19. ^{1}H NMR spectrum of polycarbolactone in d_6-DMSO 156
Figure 4.20. ^{1}H NMR spectrum of PCL-DOX HCl 5% in d_6-DMSO 157
Figure 4.21. Degradation profiles of the scaffolds in PBS solution (pH 7.4) shown as % weight loss 159
Figure 4.22. Representative SEM images showing morphological changes of the scaffolds over time 160
Figure 4.23. Cytotoxic effect of DOX HCl was evaluated by PrestoBlue® assay 161
Figure 4.24. Cell proliferation on TCP, PCL, PCL-DOX HCl 1%, PCL-DOX HCl 2% and PCL-DOX HCl 5% electrospun scaffolds determined by cellular metabolic activity of mouse fibroblasts (3T3 cells) over 14 days using PrestoBlue® assay. 162
Figure 4.25. Cell proliferation on TCP, PCL, PCL-DOX HCl 1%, PCL-DOX HCl 2% and PCL-DOX HCl 5% electrospun scaffolds determined by cellular metabolic activity of primary human dermal fibroblasts over 7 days using PrestoBlue® assay. 163

Figure 4.26.	Fluorescent images obtained from LIVE/DEAD® assay illustrating the presence of viable (green) and dead (red) cells of primary human dermal fibroblasts on the surface of the electrospun scaffolds after 1 and 7 days of cell culture.	165
Figure 4.27.	Representative SEM images showing cell morphology of mouse fibroblasts on the electrospun scaffolds	166
Figure 4.28.	Representative SEM images showing cell morphology of primary human dermal fibroblasts on the electrospun scaffolds	167
Figure 5.1.	The activities of ibuprofen and doxycycline	172
Figure 5.2.	Schematic of coaxial electrospinning set-up	174
Figure 5.3.	Disassembled coaxial nozzle, the formation of Taylor cone at the exit of the coaxial nozzle, and the formation of scaffold using coaxial electrospinning technique	179
Figure 5.4.	The structure of the coaxial fibre, polymers and drugs.	181
Figure 5.5.	Means and standard deviations of viscosity and conductivity of polymer and polymer-drug solutions.	183
Figure 5.6.	Representative SEM images and histograms for fibre diameter distribution of PCL/PLGA, PCL-DOX HCl 1%/PLGA, and PCL-DOX HCl 1%/PLGA-IBU Na 5% scaffolds.	185
Figure 5.7.	Means and standard deviations of fibre diameter of the scaffolds	186
Figure 5.8.	Representative TEM images illustrate the structure of coaxial electrospun fibres	188
Figure 5.9.	Total porosity of the scaffolds determined by gravimetric method	190
Figure 5.10.	Mechanical properties of electrospun scaffolds evaluated by a uniaxial tensile test.	192
Figure 5.11.	Water contact angles of electrospun scaffolds determined by static and dynamic modes of a sessile drop method.	193
Figure 5.12.	^{1}H NMR spectra of IBU Na, DOX HCl, and a mixture of IBU Na and DOX HCl in d_6-DMSO.	197
Figure 5.13.	Representative positive ToF-SIMS spectra of the surface of electrospun scaffolds	199
Figure 5.14.	Representative negative ToF-SIMS spectra of the surface of electrospun scaffolds	199

Figure 5.15.	Representative negative ToF-SIMS spectra of the surface of electrospun scaffolds for DOX HCl	200
Figure 5.16.	Representative negative ToF-SIMS spectra of the surface of electrospun scaffolds for DOX HCl	200
Figure 5.17.	Representative positive ToF-SIMS spectra of the surface of electrospun scaffolds for PCL	201
Figure 5.18.	Representative negative ToF-SIMS spectra of the surface of electrospun scaffolds for PLGA	201
Figure 5.19.	Normalised total ion intensity	203
Figure 5.20.	The 2D images show the distribution of IBU Na, DOX HCl, PCL, PLGA and total positive ions on the top surface of scaffolds	205
Figure 5.21.	The 2D images show the distribution of IBU Na, DOX HCl, PCL, PLGA and total negative ions on the top surface of scaffolds	206
Figure 5.22.	Cumulative drug release of DOX HCl and IBU Na from the scaffolds in PBS solutions over 30 days and within the first 5 hours	208
Figure 5.23.	Degradation profiles of the scaffolds in PBS (pH 7.4) shown as % weight loss	210
Figure 5.24.	Representative SEM images showing morphological changes of the scaffolds over time	212
Figure 5.25.	Cytotoxic effect of DOX HCl and IBU Na mixtures in mouse fibroblasts (3T3 cells) evaluated by PrestoBlue® assay	213
Figure 5.26.	Cytotoxic effect of DOX HCl and IBU Na mixtures in primary human dermal fibroblasts evaluated by PrestoBlue® assay	215
Figure 5.27.	Cell proliferation on TCP, PCL/PLGA, PCL-DOX HCl 1%/ PLGA, and PCL-DOX HCl 1%/PLGA-IBU Na 5% electrospun scaffolds determined by cellular metabolic activity of mouse fibroblasts (3T3 cells) over 14 days using PrestoBlue® assay.	218
Figure 5.28.	Cell proliferation on TCP, PCL/PLGA, PCL-DOX HCl 1%/ PLGA, and PCL-DOX HCl 1%/PLGA-IBU Na 5% electrospun scaffolds determined by cellular metabolic activity of primary human dermal fibroblasts over 14 days	219

	using PrestoBlue® assay	
Figure 5.29.	Fluorescent images obtained from LIVE/DEAD® assay Illustrating the presence of viable (green) and dead (red) cells of primary human dermal fibroblasts on the surface of the electrospun scaffolds after 1 and 7 days of cell culture	220
Figure 5.30.	Representative SEM images showing cell morphology of mouse fibroblasts on the electrospun scaffolds	221
Figure 5.31.	Representative SEM images showing cell morphology of primary human dermal fibroblasts on the electrospun scaffolds	222
Figure 5.32.	Representative confocal images of primary human dermal fibroblasts grown on tissue culture plastic and the scaffolds for 14 days	224
Figure 6.1.	A schematic outlining the experimental procedure to perform the efficacy testing	238
Figure 6.2.	% Cell viability of primary human dermal fibroblasts when treated with the mixture of 10 ng/mL TNF-α and 10 ng/mL IL-1β, DOX HCl solutions (50, 100 and 250 µM), or pre-treated with DOX HCl solutions (50, 100 and 250 µM) for 2 hours before the exposure to the cytokines.	241
Figure 6.3.	Normalised concentration of nitrite produced by primary human dermal fibroblasts when treated with the mixture of 10 ng/mL TNF-α and 10 ng/mL IL-1β, DOX HCl solutions (50, 100 and 250 µM), or pre-treated with DOX HCl solutions (50, 100 and 250 µM) for 2 hours before the exposure to the cytokines	243
Figure 6.4.	Normalised concentration of MMP-1 enzyme expressed by primary human dermal fibroblasts when treated with the mixture of 10 ng/mL TNF-α and 10 ng/mL IL-1β, DOX HCl solutions (50, 100 and 250 µM), or pre-treated with DOX HCl solutions (50, 100 and 250 µM) for 2 hours before the exposure to the cytokines	245
Figure 6.5.	Normalised concentration of PGE_2 produced by primary human dermal fibroblasts when treated with the mixture of 10 ng/mL TNF-α and 10 ng/mL IL-1β, DOX HCl solutions (50, 100 and 250 µM), or pre-treated with	247

DOX HCl solutions (50, 100 and 250 μM) for 2 hours before the exposure to the cytokines.

Figure 6.6. % Cell viability of primary human dermal fibroblasts when treated with the mixture of 10 ng/mL TNF-α and 10 ng/mL IL-1β, the scaffolds in cell culture media, or pre-treated with the scaffolds in cell culture media for 2 hours before the exposure to the cytokines. 251

Figure 6.7. Normalised concentration of nitrite produced by primary Human dermal fibroblasts when treated with the mixture of 10 ng/mL TNF-α and 10 ng/mL IL-1β, the scaffolds in cell culture media, or pre-treated with the scaffolds in cell culture media for 2 hoursbefore the exposure to the cytokines. 253

Figure 6.8. Normalised concentration of MMP-1 enzyme expressed by primary human dermal fibroblasts when treated with the mixture of 10 ng/mL TNF-α and 10 ng/mL IL-1β, the scaffolds in cell culture media, or pre-treated with the scaffolds in cell culture media for 2 hours before treated with the cytokines. 254

Figure 6.9. Normalised concentration of PGE_2 produced by primary human dermal fibroblasts when treated with the mixture of 10 ng/mL TNF-α and 10 ng/mL IL-1β, the scaffolds in cell culture media, or pre-treated with the scaffolds in cell culture media for 2 hours before treated with the cytokines. 256

Figure 6.10. % Cell viability of primary human dermal fibroblasts when treated with the mixture of 10 ng/mL TNF-α and 10 ng/mL IL-1β, DOX HCl solution (50 μM), IBU Na solution (400 μM), the mixture of DOX HCl solution (50 μM) and IBU Na solution (400 μM) or pre-treated with the drug solutions for 2 hours before the exposure to the cytokines. 259

Figure 6.11. Normalised concentration of nitrite produced by primary human dermal fibroblasts when treated with the mixture of 10 ng/mL TNF-α and 10 ng/mL IL-1β, DOX HCl solution (50 μM), IBU Na solution (400 μM), the mixture of DOX HCl solution (50 μM) and IBU Na solution 261

(400 μM) or pre-treated with the drug solutions for 2 hours before the exposure to the cytokines.

Figure 6.12. Normalised concentration of MMP-1 enzyme expressed by primary human dermal fibroblasts when treated with the mixture of 10 ng/mL TNF-α and 10 ng/mL IL-1β, DOX HCl solution (50 μM), IBU Na solution (400 μM), the mixture of DOX HCl solution (50 μM) and IBU Na solution (400 μM) or pre-treated with the drug solutions for 2 hours before the exposure to the cytokines. 262

Figure 6.13. Normalised concentration of PGE_2 produced by primary human dermal fibroblasts when treated with the mixture of 10 ng/mL TNF-α and 10 ng/mL IL-1β, DOX HCl solution (50 μM), IBU Na solution (400 μM), the mixture of DOX HCl solution (50 μM) and IBU Na solution (400 μM) or pre-treated with the drug solutions for 2 hours before the exposure to the cytokines. 264

Figure 6.14. % Cell viability of primary human dermal fibroblasts when treated with the mixture of 10 ng/mL TNF-α and 10 ng/mL IL-1β, the coaxial scaffolds in cell culture media, or pre-treated with the coaxial scaffolds in cell culture media for 2 hours before the exposure to the cytokines. 267

Figure 6.15. Normalised concentration of nitrite produced by primary human dermal fibroblasts when treated with the mixture of 10 ng/mL TNF-α and 10 ng/mL IL-1β, the coaxial scaffolds in cell culture media, or pre-treated with the coaxial scaffolds in cell culture media for 2 hours before the exposure to the cytokines. 268

Figure 6.16. Normalised concentration of MMP-1 enzymes expressed by primary human dermal fibroblasts when treated with the mixture of 10 ng/mL TNF-α and 10 ng/mL IL-1β, the coaxial scaffolds in cell culture media, or pre-treated with the coaxial scaffolds in cell culture media for 2 hours before the exposure to the cytokines. 269

Figure 6.17. Normalised concentration of PGE_2 produced by primary human dermal fibroblasts when treated with the mixture of 10 ng/mL TNF-α and 10 ng/mL IL-1β, the coaxial scaffolds in cell culture media, or pre-treated with the 271

	coaxial scaffolds in cell culture media for 2 hours before treated with the cytokines.	
Figure 8.1.	Representative SEM images of the scaffolds that were fabricated with different concentrations of PLGA8515 polymer in HFIP solutions.	333
Figure 8.2.	Standard curve for ibuprofen sodium (IBU Na) determined by HPLC	334
Figure 8.3.	Standard curve for ibuprofen sodium (IBU Na) obtained from UV-Vis spectrophotometry	334
Figure 8.4.	The colour changes of PrestoBlue® reagent from resazurin (blue) to resorufin (red) by different numbers of cells	335
Figure 8.5.	Reduction of PrestoBlue® reagent from resazurin (non-fluorescent) to resorufin (highly fluorescent) by different numbers of living mouse fibroblasts (3T3 cells)	335
Figure 8.6.	Representative SEM images of DOX HCl-loaded electrospun scaffolds fabricated with PLGA8515, PLGA5050, PLA and PCL polymers	336
Figure 8.7.	Cumulative drug release of DOX HCl from PLGA8515-DOX HCl 1% and PLGA8515-DOX HCl 5% scaffolds in PBS over 90 days (2,160 h)	337
Figure 8.8.	Cumulative drug release of DOX HCl from PLGA5050-DOX HCl 5% and PLA-DOX HCl 5% scaffolds in PBS over 30 days (720 h)	337
Figure 8.9.	The degradation of DOX HCl encapsulated in the scaffolds	338
Figure 8.10.	Standard curve for doxycycline hydrochloride (DOX HCl) determined by HPLC	338
Figure 8.11.	Standard curve for doxycycline hydrochloride (DOX HCl) obtained from UV-Vis spectrophotometry	339
Figure 8.12.	Reduction of PrestoBlue® reagent from resazurin (non-fluorescent) to resorufin (highly fluorescent) by different numbers of living mouse fibroblasts (3T3 cells)	340
Figure 8.13.	Reduction of PrestoBlue® reagent from resazurin (non-fluorescent) to resorufin (highly fluorescent) by different numbers of living primary human dermal fibroblasts.	340

Figure 8.14.	The release of doxycycline hydrochloride (DOX HCl) from PCL scaffolds in cell culture media.	341
Figure 8.15.	Representative images of the scaffolds after incubating in cell culture media for 24 hours.	341
Figure 8.16.	Representative SEM and TEM images of coaxial PLGA-IBU Na 1% (shell)/PCL-DOX HCl 5% (core) scaffolds	342
Figure 8.17.	Standard curve for ibuprofen sodium (IBU Na) in the mixture of ibuprofen sodium and doxycycline hydrochloride determined by UV-Vis spectrometry at the wavelength of 222 nm.	343
Figure 8.18.	Standard curve for doxycycline hydrochloride (DOX HCl) in the mixture of ibuprofen sodium and doxycycline hydrochloride determined by UV-Vis spectrometry at the wavelength of 350 nm	343
Figure 8.19.	Cumulative drug release of IBU Na and DOX HCl from coaxial PLGA-IBU Na 1% (shell)/PCL-DOX HCl 5% (core) electrospun scaffolds in PBS over 30 days (720 h)	344
Figure 8.20.	Reduction of PrestoBlue® reagent from resazurin (non-fluorescent) to resorufin (highly fluorescent) by different numbers of living mouse fibroblasts (3T3 cells)	345
Figure 8.21.	Reduction of PrestoBlue® reagent from resazurin (non-fluorescent) to resorufin (highly fluorescent) by different numbers of living primary human dermal fibroblasts	345
Figure 8.22.	Reduction of PrestoBlue® reagent from resazurin (non-fluorescent) to resorufin (highly fluorescent) by living primary human dermal fibroblasts.	346
Figure 8.23.	Standard curve for nitrite quantification	346
Figure 8.24.	Reduction of PrestoBlue® reagent from resazurin (non-fluorescent) to resorufin (highly fluorescent) by living primary human dermal fibroblasts	347
Figure 8.25.	Standard curve for nitrite quantification	347

List of Tables

Table 1.1.	Phases of wound healing	8
Table 1.2.	Types of dressings, examples of commercial products, and key properties of them	17
Table 1.3.	Effect of parameters on the fibre diameter of electrospun scaffolds	30
Table 2.1.	List of materials and lab consumables	37
Table 2.2.	The complete formulation of cell culture media for primary human dermal fibroblasts	50
Table 3.1.	Viscosity and conductivity values of the solvent, PLGA solutions, and PLGA-IBU Na solutions	72
Table 3.2.	Means and standard deviations of fibre diameter and total porosity of PLGA, PLGA-IBU Na 1%, PLGA-IBU Na 2% and PLGA-IBU Na 5% electrospun scaffolds	77
Table 3.3.	Means and standard deviations of ultimate tensile strength, % strain at break and Young's modulus of PLGA, PLGA-IBU Na 1%, PLGA-IBU Na 2% and PLGA-IBU Na 5% scaffolds	79
Table 3.4.	Mechanical properties of the skin from different parts of human body	81
Table 3.5.	Means and standard deviations of static water contact angle, advancing water contact angle, receding water contact angle, and contact angle hysteresis of the scaffolds	83
Table 3.6.	Encapsulation efficiency of IBU Na in the PLGA scaffolds.	85
Table 3.7.	% cumulative drug release of IBU Na from the PLGA scaffolds over 60 days in PBS solutions	93
Table 3.8.	% Weight loss of the scaffolds over time determined in the *in vitro* degradation study	102
Table 3.9.	Summary of scaffolds' properties	117
Table 4.1.	Classification of matrix metalloproteinases (MMPs), their biological effects and substrates	121
Table 4.2.	Viscosity and conductivity values of polymer and polymer-drug solutions	133
Table 4.3.	Means and standard deviations of fibre diameter and total porosity of PCL, PCL-DOX HCl 1%, PCL-DOX HCl 2%	137

	and PCL-DOX HCl 5% electrospun scaffolds	
Table 4.4.	Means and standard deviations of ultimate tensile strength, % strain at break and Young's modulus of PCL, PCL-DOX HCl 1%, PCL-DOX HCl 2%, and PCL-DOX HCl 5% scaffolds	140
Table 4.5.	Means and standard deviations of static water contact angle, advancing water contact angle, receding water contact angle, and contact angle hysteresis of the scaffolds	142
Table 4.6.	% encapsulation efficiency of DOX HCl in PCL scaffolds	143
Table 4.7.	% Cumulative drug release of DOX HCl from the PCL scaffolds over 30 days in PBS solutions.	152
Table 4.8.	% Weight loss of the scaffolds over time determined in the *in vitro* degradation study	159
Table 4.9.	Summary of scaffold properties	168
Table 5.1.	Viscosity and conductivity values of polymer and polymer-drug solutions	183
Table 5.2.	Means and standard deviations of fibre diameter of the scaffolds	186
Table 5.3.	Means and standard deviations of total porosity of the scaffolds	190
Table 5.4.	Means and standard deviations of ultimate tensile strength, % strain at break and Young's modulus of the scaffolds	192
Table 5.5.	Means and standard deviations of static water contact angle, advancing water contact angle, receding water contact angle, and contact angle hysteresis of the scaffolds	194
Table 5.6.	% Encapsulation efficiency of DOX HCl and IBU Na in the scaffolds.	195
Table 5.7.	Positive and negative ions used to identify polymers and drugs	198
Table 5.8.	Cumulative drug release of DOX HCl and IBU Na from the scaffolds over 30 days in PBS solutions	208
Table 5.9.	% Cumulative weight loss of the scaffolds after being immerged in PBS at different time points	211
Table 5.10.	The effect of different concentrations of IBU Na on cell viability when the concentration of DOX HCl was fixed, and vice versa	216
Table 5.11.	Summary of scaffolds' properties	225

Table 6.1.	The formulation of cell culture media for primary human dermal fibroblasts used in the efficacy testing	233
Table 6.2.	Summary of cell viability, the expression of MMP-1 enzyme and the production of nitrite and PGE_2 by primary human dermal fibroblasts after being treated under the specific conditions (DOX HCl solutions)	249
Table 6.3.	Summary of cell viability, the expression of MMP-1 enzyme and the production of nitrite and PGE_2 by primary human dermal fibroblasts after being treated under the specific conditions (PCL-DOX HCl scaffolds)	257
Table 6.4.	Summary of cell viability, the expression of MMP-1 enzyme and the production of nitrite and PGE_2 by primary human dermal fibroblasts after being treated under the specific conditions (DOX HCl and IBU Na solutions)	266
Table 6.5.	Summary of cell viability, the expression of MMP-1 enzyme and the production of nitrite and PGE_2 by primary human dermal fibroblasts after being treated under the specific conditions (coaxial electrospun scaffolds)	272

Abbreviations

°	degree
Ø	diameter
%	percentage
τ_R	retention time
µ	micro
µL	microlitre
µm	micrometre
µM	micromolar
°C	degree Celsius
^{1}H NMR	proton nuclear magnetic resonance
2D	two-dimensional
3D	three-dimensional
AB/AM	antibiotic/antimycotic solution
ANOVA	analysis of variance
bFGF	basic fibroblast growth factor
BSA	bovine serum albumin
ca.	circa
cm	centimetre
cm^3	cubic centimetre
CO_2	carbon dioxide
COX	cyclooxygenase
d_6-DMSO	deuterated dimethyl sulfoxide
DOX HCl	doxycycline hydrochloride
DMEM	Dulbecco's Modified Eagle Medium

DMSO	dimethyl sulfoxide
D-PBS	Dulbecco's Phosphate Buffered Saline
DSC	differential scanning calorimetry
ECM	extracellular matrix
EDTA	ethylenediaminetetraacetate
EGF	epidermal growth factor
Em	emission
eNOS	endothelial nitric oxide synthase
Eq	equation
Ex	excitation
FBS	foetal bovine serum
g	gram
GPC	gel permeation chromatography
h	hour
HFIP	hexafluoroisopropanol
HPLC	high performance liquid chromatography
IBU Na	ibuprofen sodium
IFN-γ	Interferon gamma
IL-1β	interleukin-1 beta
iNOS	inducible nitric oxide synthase
KCl	potassium chloride
kDa	kilodalton
KGF	keratinocyte growth factor
kV	kilovoltage
L	litre

LPS	lipopolysaccharide
M	molar
mΩ	milliohm
mg	milligram
MHz	megahertz
min	minute
mL	millilitre
mm	millimetre
mM	millimolar
MMPs	matrix metalloproteinases
M_n	number average molecular weight
MPa	megapascal
MW	weight average molecular weight
m/z	mass-to-charge ratio
nm	nanometre
nM	nanomolar
NF-kB	nuclear factor kappa light chain enhancer of activated B cells
NHS	National Health Service
nNOS	neuronal nitric oxide synthase
NO	nitric oxide
NO_2^-	nitrite
NO_3^-	nitrate
NOS	nitric oxide synthase
NSAIDs	non-steroidal anti-inflammatory drugs

p	pico
Pa	Pascal
PBS	phosphate buffered saline
PCL	polycaprolactone
PDGF	platelet-derived growth factor
PEG	polyethylene glycol
PFA	paraformaldehyde
pg	picogram
PGA	poly(glycolic acid)
PGE_2	prostaglandin E_2
PGH_2	prostaglandin H_2
PLA	poly(lactic acid)
PLA_2	phospholipase A_2
PLGA	poly(lactic-co-glycolic acid)
pM	picomolar
ppm	parts-per-million
rh	recombinant human
RH	relative humidity
ROS	reactive oxygen species
rpm	revolution per minute
s	second
S	siemens
SD	standard deviation
SEM	scanning electron microscopy
TACE	tumor necrosis factor alpha converting enzyme

TCP	tissue culture plastic
TEM	transmission electron microscopy
TGF-β	transforming growth factor beta
TIMPs	tissue inhibitors of metalloproteases
TNF-α	tumor necrosis factor alpha
ToF-SIMS	time of flight secondary ion mass spectrometry
U	unit
U.S. FDA	United States Food and Drug Administration
UV	ultraviolet
VEGF	vascular endothelial growth factor
Vis	visible
v/v	volume by volume
WHO	World Health Organization
w/w	weight by weight
w/v	weight by volume
XRD	X-ray diffraction

Chapter 1

Introduction

1.1 Skin

The skin is the largest, self-renewing, highly matrix structured organ, covering the human body.[1] The skin has numerous functions (Figure 1.1). For example, maintaining homeostasis through thermoregulation and protecting the body against microorganism invasion, ultraviolet radiation, and physical and chemical stimuli. Whilst, it also provides a sensation for pain, pressure and tactile perception.[2–5]

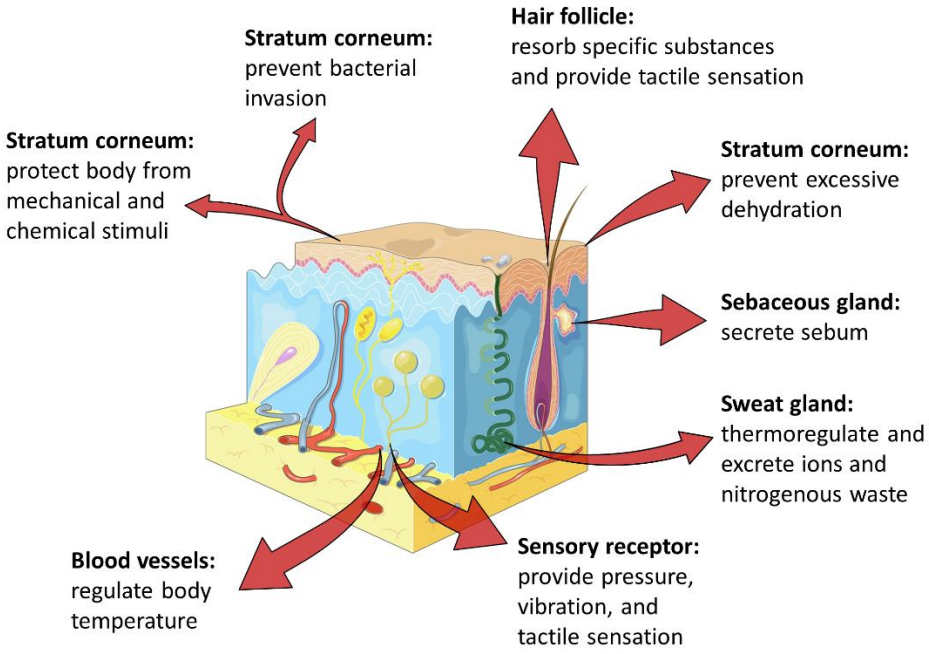


Figure 1.1. Functions of the skin[5]

The structure of this highly complex organ is divided into three anatomical layers: epidermis, dermis and hypodermis (Figure 1.2).[6]

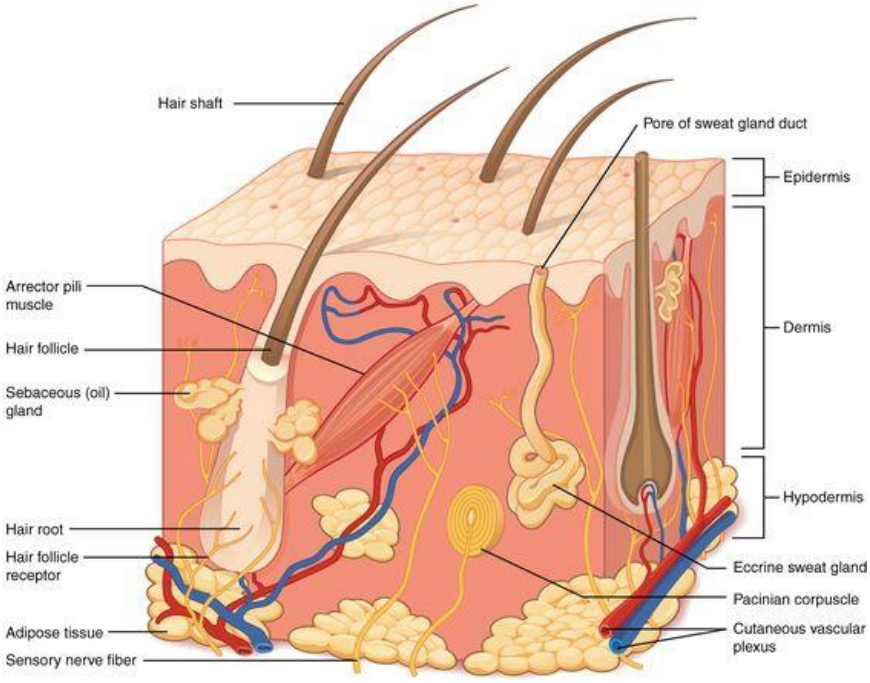


Figure 1.2. The structure of skin.[7]

Epidermis is the outermost layer of the skin where keratinocytes, Langerhans cells, Merkel cells, and melanocytes can be found (Figure 1.3). The predominant keratinocytes are constantly produced in the stratum basale. Later, they proliferate and move upward to the granular layer (stratum granulosum) where they undergo differentiation and keratinization. During keratinization, keratinocytes move upwards to the skin surface, become stratified, lose their nuclei, and eventually form a barrier keratin layer called the stratum corneum (a network of anucleated corneocytes and extracellular lipid matrix).[6–9] The complete renewal cycle takes approximately every 28 days in the healthy epidermis.

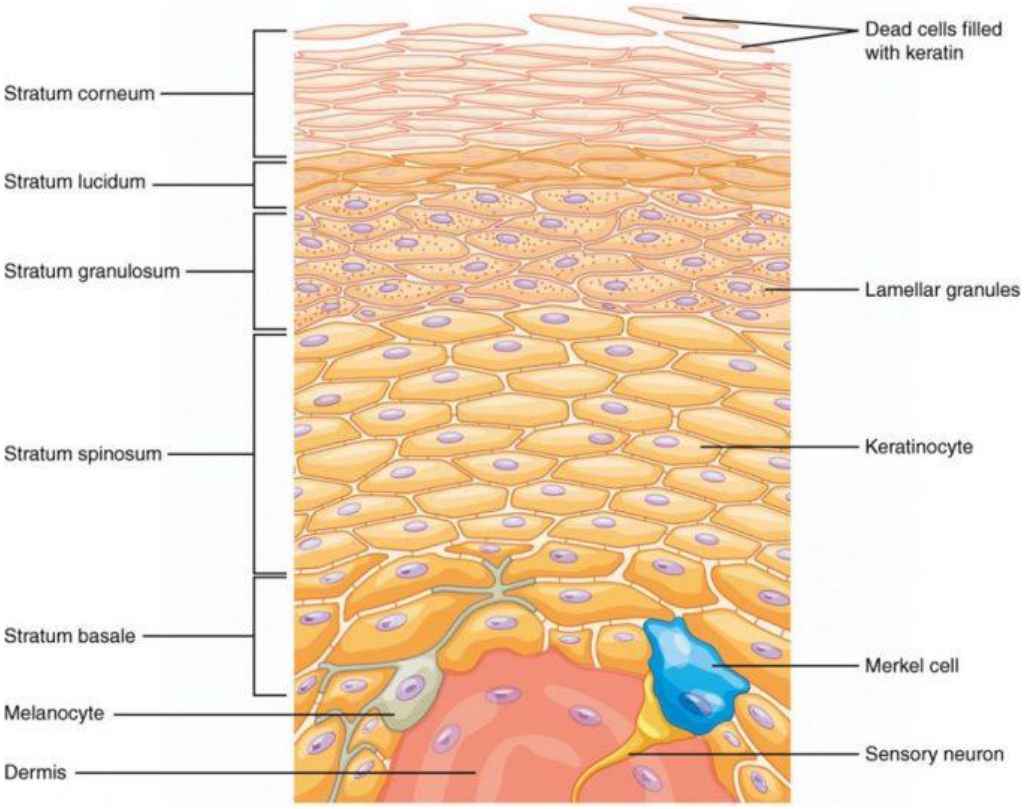


Figure 1.3. The structure of epidermis layer.[7]

The second layer of the skin is dermis. Dermis is the thickest layer of the skin, approximately 1-2 mm in depth.[6] The roles of the dermis are regulating body temperature, supplying nutrients to the epidermis, and supporting the sensation. This layer accommodates various cell types, including fibroblasts, adipocytes and phagocytes. In addition, small blood vessels, hair follicles, sweat glands, lymphatic capillaries, nerve fibres, and Meissner corpuscles (touch receptors) are also located in this layer.[7]

Dermal fibroblasts are primary cells in the dermis. They secrete collagen, specifically type I and type III collagen, to support mechanical strength of the skin. Moreover, they produce elastic fibres, which are composed of elastin and

fibrillin microfibrils. Elastin allows the stretching and recoiling of fibres, providing skin elasticity.[9]

Mast cells are inflammatory cells found in the perivascular areas of the dermis. They secrete vasoactive and pro-inflammatory mediators that play an important roles in inflammatory reactions, collagen remodeling, and wound healing.[10] For instance, mast cells secrete histamine that induces pore formation in blood vessels, hence facilitating protein leakage and extravasation of leukocytes into the wound site.[11]

The dermis itself consists of two sublayers: papillary and reticular layers.[7] The papillary layer is underlaying the epidermis. This layer is composed of loose, areolar connective tissue with highly vascular network. The reticular layer, located underneath the papillary layer, covers approximately 80% of dermis. The structure of this layer is well-vascularized and consists of dense irregular connective tissue. Due to the tight meshwork of fibres in this layer, skin possesses the properties of resistance against tearing and flexibility.

The innermost layer of the skin is the hypodermis also known as the subcutaneous layer.[7] It is where loose connective tissues and insulating adipose tissues hold the skin and the underlying organs together, and provides blood vessels for supplying nutrients to the skin.[9]

1.2 Wounds

Wounds result in the normal anatomical structures and functions of the skin being damaged or disrupted.[12] There are various causes for wound to occur. For instance, exposure to mechanical stimuli (*e.g.* sharp and abrasion), toxic chemicals/irritants, thermal sources, or underlying diseases (*e.g.* diabetes, malignancies, and infection).[13,14] The spectrum of wound severity is broad, ranging from a merely superficial defect of epithelial tissues to serious injuries of the subcutaneous tissue with damages of other key systems like nerves, muscles, or parenchymal organs.[13]

1.3 Wound healing

Wound healing is a spontaneous dynamic process to restore skin integrity and function and usually occurs in defined, orderly and timely manner. Such complicated biological processes synchronize with other multiple pathways and cascades. Associated with these mechanisms are various types of cells (*e.g.* immune cells, endothelial cells, keratinocytes and fibroblasts), growth factors, cytokines and extracellular matrix (ECM).[13,15,16]

The wound healing process occurs in four overlapping, distinct time-dependent phases: haemostasis, inflammation, proliferation and remodeling.[13,16,17]

1.3.1 Phase 1: Haemostasis

Soon after a wound, bleeding and vasoconstriction take place to minimise fluid loss and prevent bacterial infection.[9,18] As a result of bleeding, platelet aggregation leads to the formation of a blood clot, which provides a provisional matrix for infiltrating cells such as neutrophils. Whilst, platelets later recruit fibroblasts, endothelial cells and immune cells to initiate the next healing phase by secreting growth factors and cytokines.[16,19,20]

1.3.2 Phase 2: Inflammation

The subsequent inflammation phase occurs shortly after the haemostasis phase and typically lasts up to 7 days.[13,14] In the early inflammation phase (24-36 h after the injury), neutrophils infiltrate into the wound site and release reactive oxygen species and protease enzymes to suppress bacterial infection as well as to remove cellular debris using phagocytosis process. Once neutrophils complete their task, neutrophil apoptosis takes place, followed by phagocytosis of cell remnants and apoptotic bodies by macrophages. In the late inflammation phase (48-72 h after injury), macrophages undergo phagocytosis to eradicate bacteria and necrotic tissues. In addition, these immune cells also release cytokines (*e.g.* tumor necrosis factor (TNF)), growth factors (*e.g.* fibroblast growth factor (FGF)) and proteases (*e.g.* collagenase) to recruit fibroblasts, endothelial cells and keratinocytes to the wound site.[16] Lymphocytes are the last cells attracted to the site of injury after 72 h in response to interleukin-1 (IL-1), complement components and immunoglobulin G breakdown product.

1.3.3 Phase 3: Proliferation

The proliferation phase starts within several days after injury.[13] This phase is mainly responsible for granulation tissue formation.[9,13] The healthy tissue plus the endothelial progenitors surrounding the wound act as sources of vascular endothelial cells and capillaries to promote angiogenesis in the wound. Macrophages and endothelial cells secrete vascular endothelial growth factor (VEGF) to promote the formation of new blood vessels. Meanwhile, FGF, VEGF and platelet-derived growth factor (PDGF) promote angiogenesis by inducing fibroblast production. Fibroblasts proliferate and secrete type I and III collagen, major components of ECM, to gradually replace the fibrin matrix. The mechanical strength of wound increases as the deposition of collagen and the level of cross-linking increases. In addition, fibroblasts differentiate into myofibroblasts. These differentiated fibroblasts express α-smooth muscle actin, which can diminish the wound size. This granulation tissue can be observed within 5-20 days after the initial wound. The granulation tissue then provides the surfaces for keratinocyte proliferation from wound edges. In the case of deep wounds, hair follicles will be the source of keratinocytes.

1.3.4 Phase 4: Remodeling

Remodeling is the healing state where wound sites regain most of their tensile strength.[9] However, the elasticity is not fully restored. The scar formation can occur in this phase, which can be present for months to years. After the wound is fully covered with new granulation tissue and the dermis regeneration is successful, the angiogenesis will stop and start apoptosis.

Table 1.1 summaries the onset of each phase in wound healing, key cells, and important events undergoing during the phase

Table 1.1. Phases of wound healing[13,14,20]

Phase	Time post-injury	Cells involved	Important events
Haemostasis	Immediate	• Platelets	• Blood clotting • Release of growth factors
Inflammation	Day 1-4	• Neutrophils • Macrophages • Monocytes	• Phagocytosis • Secretion of MMPs to remove debris • Secretion of growth factors and cytokines to stimulate fibroblast proliferation
Proliferation (granulation and contraction)	Day 4-21	• Macrophages • Fibroblasts • Keratinocytes • Epithelial cells • Angiocytes • Pericytes • Lymphocytes • Neurocytes	• Angiogenesis • Collagen production • Restoration of skin functions • Granulation tissue formation • Wound closure
Remodeling (maturation)	Day 21-2 years	• Fibroblasts • Fibrocytes	• Restoration of skin tensile strength

1.4 Types of wounds

Wounds can be classified into 2 types based on the healing time: acute and chronic wounds (Figure 1.4). Acute wounds can recover from damage within 30 days with complete restoration of the functions and anatomy.[13] On the other hand, chronic wounds require much longer time, typically up to 3 months, to heal; and the skin conditions after normal phase of healing process are usually not the same as its original stage.[19,21]

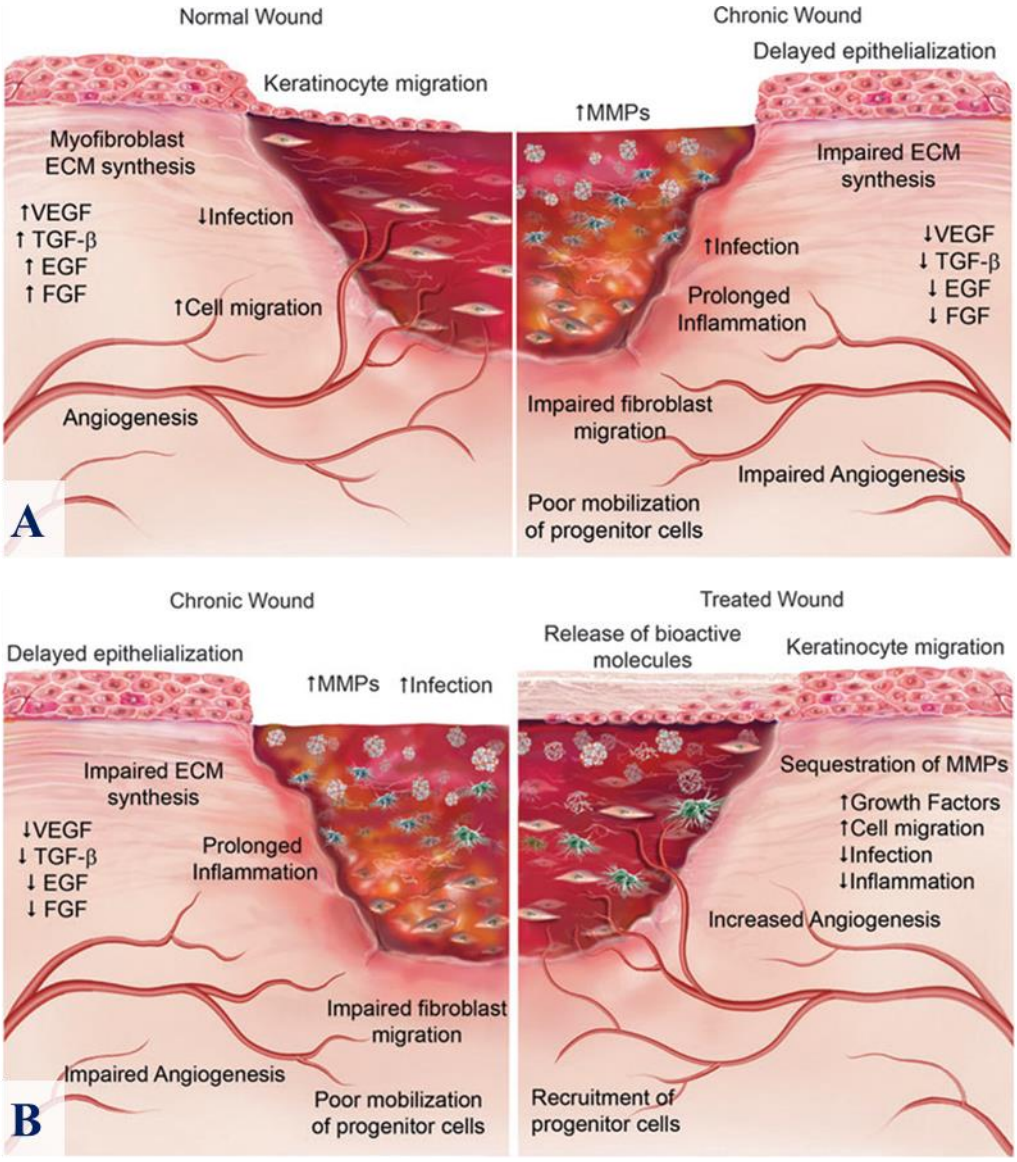


Figure 1.4. (A) Important events in acute wounds and chronic wounds. (B) The events involved in the delayed healing of chronic wounds and the wounds after successful healing.[19]

1.4.1 Factors that retard wound healing in chronic wounds

The delayed wound healing in chronic wounds results from many factors. These factors arise from either the wound itself and the status and condition of the subject, including underlying diseases.[20] The example factors from wounds are oxygenation, infection and venous sufficiency. Whilst, the common underlying diseases that retard healing are diabetes, ischemia, keloids, cancers, AIDs and fibrosis. Lastly, the factors such as age, gender, hormones, stress, obesity, alcoholism, smoking, and medications being used can all affect wound healing.

Diabetic foot ulcers, venous leg ulcers and pressure ulcers are well known examples of chronic wounds. Although the pathology at the molecular level is different, these chronic wounds share common characters, which are the disproportionate production of pro-inflammatory cytokines (*e.g.* TNF-α and IL-1β), proteases (*e.g.* matrix metalloproteinases (MMPs)), and reactive oxygen species.[14,22–25] Moreover, the proliferation of dermal and epidermal cells are impaired and infection is often persistent.[14]

1.4.2 Persistent inflammation in chronic wounds

Inflammation is crucial to the wound healing process as it enhances the restoration of homeostasis following the injury or infection by removing pathogens and triggering the proliferative process. However, the inflammation phase often cannot be resolved in chronic wounds because of several factors, which are the impaired cellular and systemic responses against the stress, tissue hypoxia, repetitive trauma, and bacterial infection.[20] This leads to the

amplification of the inflammation, causing the imbalance between pro-inflammatory cytokines, chemokines, proteases, and their inhibitors. Therefore, the proliferative phase cannot occur in the appropriate timely manner.

1.4.2.1 Matrix metalloproteinases (MMPs)

Neutrophils and activated macrophages elevate the production of pro-inflammatory cytokines (TNF-α and IL-1β), leading to the higher expression of MMPs and reduced level of tissue inhibitors of metalloproteases (TIMPs). MMPs are a family of zinc-dependent endopeptidases that are produced by various cells, for example, keratinocytes, fibroblasts, endothelial cells, neutrophils, macrophages, mast cells and eosinophils.[22]

The imbalance between MMPs and endogenous TIMPs leads to the destruction and degradation of ECM, growth factors and their receptors.[18,26] The breakdown products of ECM promote inflammation further by repeating the cycle. As a result, more neutrophils and macrophages are attracted to the wound site, amplifying the inflammation cycle.[22] Moreover, cell migration and fibroblast proliferation are impaired. Altogether, the chronic wounds stall in the inflammation phase of healing and the proliferative phase of wound healing cannot occur.[20]

1.4.2.2 Cyclooxygenase (COX) enzymes

In response to the excessive level of IL-1β and TNF-α, the expression of cyclooxygenase (COX) enzymes is upregulated.[27,28] COX enzymes can be categorised into 2 isoforms: COX-1 and COX-2.[29,30] A constitutive COX-1 isoform acts as a house-keeping enzyme that regulates renal and vascular homeostasis. In addition, it protects gastrointestinal tract by stimulating the secretion of mucus. Whereas, COX-2 is an inducible isoform, transiently upregulated in response to wound formation. COX enzymes convert arachidonic acid to prostaglandin H_2 (PGH_2) which is further converted to prostaglandin E_2 (PGE_2), a predominant inflammatory mediator and fibroblast modulator produced in the skin.[31] PGE_2 has both pro-inflammatory and anti-inflammatory effects, which depends on timing of production and concentration. PGE_2 has been found to decrease fibroblast proliferation, inhibit collagen synthesis and enhance the expression of MMPs.[32]

1.4.2.3 Nitric oxide (NO)

The excessive neutrophil infiltration in the inflammation phase leads to over-production of reactive oxygen species (ROS), causing damage to ECM and cell membranes. In addition, premature cell senescence also occurs. In early phase of wound healing, the production and secretion of nitric oxide (NO) is greatly induced by a variety of cytokines, growth factors and inflammatory cells, mainly macrophages. Subsequently, fibroblasts, keratinocytes and endothelial cells contribute to ongoing NO synthesis but to a lesser degree (Figure 1.5).[33]

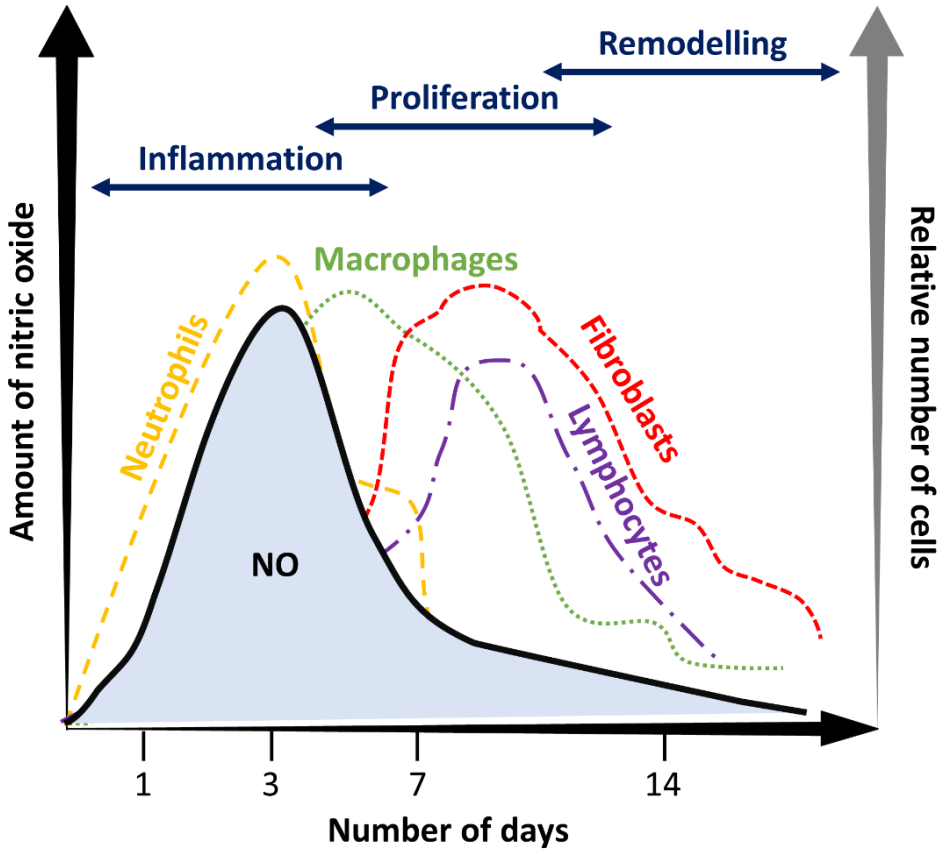


Figure 1.5. The relative amount of nitric oxide produced by cells during phases in wound healing process.[33]

NO is a small gaseous radical generated from the conversion of L-arginine to L-citrulline by three distinct isoforms of nitric oxide synthase (NOS).[33,34] Two constitutive isoforms (endothelial (eNOS) and neuronal (nNOS)) generate low concentration of NO in nmol/L range. Whilst, the inducible isoform (iNOS) leads to the release of NO in µmol/L range when triggered by stimulating factors as mentioned above.

All isoforms are found to express in the skin tissue.[34] Constitutive nNOS isoform is predominantly expressed by keratinocytes and melanocytes while eNOS isoform can be generated in keratinocytes of the basal epidermal layer, dermal fibroblasts, endothelial capillaries, and eccrine glands. The expression of iNOS isoform is mostly induced in keratinocytes, fibroblasts, Langerhans cells, and endothelial cells.

The role of NO in wounds is to modulate chemoattractant cytokines (IL-8 and transforming growth factor beta 1 (TGF-β1)) and inflammatory cells (monocytes and neutrophils) that involve in the initiation of post-wound inflammation.[34] At the wound site, monocytes and neutrophils are activated to produce pro-inflammatory cytokines, TNF-α and IL-1, which are implicated in wound healing and also the induction of iNOS.

As NO is a short half-life free radical, the level of NO is typically estimated by its stable metabolites, nitrite (NO_2^-) and nitrate (NO_3^-) level. These two metabolites are elevated early in subcutaneous wound fluids and found to be related to collagen deposition.[33,34]

1.5 Incidence of chronic wounds

In the healthcare systems worldwide, chronic wounds are a challenging persistent complication that causes the individual, society and the healthcare system burden as a whole. In the UK, there are up to reported 575,600 chronic wound related cases annually.[35] The treatment of wounds costs approximately 3.4-4.6 billion US dollars every year to the National Health Service (NHS).

Similar trend is revealed in the USA, where chronic wounds affect 6.5 million people and more than 25 billion US dollars spent on treating wound-related complications each year.[36] Aging as well as underlying diseases, in particular, increase the prevalence of chronic wounds and make wounds more difficult to heal. As a result, function loss, amputation and eventually morbidity occur.[14]

1.6 Wound care and dressings

Wound care has been proved to be very important to chronic wounds. Wound care predominantly refers to debridement or removal of necrotic debris, a nutrient source of infection.[37,38] Debridement can be achieved by a surgery or an enzymatic digestion in which the former is the major execution. The purpose of debridement is to get rid of dead tissues and to expose healthy and well-vascularised tissues that are able to proliferate and form new granulation tissue.

In adjunct with debridement, wound dressings are introduced to promote wound healing.[18,37] The dressings enhance the healing by stimulating re-epithelialization, inducing collagen synthesis, promoting angiogenesis by creating hypoxia environment, and reducing infection by decreasing pH in the wound bed.

The ideal wound dressings are expected to prevent infection, to retain moisture in the wound bed, to promote cell migration and proliferation, to promote angiogenesis, and to be sterile, non-toxic and non-allergic.[39]

However, poor adhesion of wound dressings and the need of frequent changing can cause pain and impede wound healing.[40–42] More recent examples of wound dressings are produced with various types of materials to improve their properties. For example, films, hydrogels, foams and tissue engineered substitutes. As there are many options, the suitable dressing should be selected based on the wound type.

Table 1.2 provides the information about types of wound dressings, the suppliers and properties of those dressings.

Table 1.2. Types of dressings, examples of commercial products, and key properties of them.[43]

Type of dressing	Commercially available products	Properties
Gauze	• Curity • Vaseline Gauze • Xeroform	• Inexpensive • Drying • Require frequent changing • May cause further injury on changing
Hydrocolloids	• Aquacel • Comfeel • DuoDERM • Granuflex • Tegasorb	• Long times between changes • Do not cause pain on removal • Fluid-trapping occlusive • Not for infected wounds, neuropathic ulcers and highly exudating wounds • Permeable to water vapour but impermeable to bacteria • Absorb wound exudates
Films	• Bioclusive • Blisterfilm • Cutifilm • Flexigrid • Opsite • Tegaderm	• Occlusive • Retains moisture • Highly elastic and flexible • Do not require additional tapping • Only for non- or low-exudative wounds
Hydrogels	• Carrasyn • Curagel • Nu-Gel • Purilon • Restore • SAF-gel • XCell • Intrasite • Aquaform	• Rehydrates dry wounds • Easy removal/changes • May cause over-hydration • Suitable for dry wounds, necrotic wounds, pressure wounds and burn wounds • Non irritant • Low mechanical strength to handle • Accumulate exudate which leads to maceration and bacterial proliferation

Type of dressing	Commercially available products	Properties
Foams	• 3M Adhesive Foam • Allevyn • Lyofoam • Tielle	• Moderately absorbent • Insulating • Allow gaseous exchange and water vapour • Suitable for lower leg ulcers, highly exudating wounds and granulating wounds • Require frequent dressing
Alginates	• Algisite • Kaltostat • Sorbsan • Tegagen	• Highly absorbent • Suitable for moderate to heavy drainage wounds • Not suitable for dry wounds, third degree burn wounds and severe wounds with exposed bone
Hydrofibres	• Aquacel Hydrofibre	• Highly absorbent
Medicated dressing	• Cutisorb • Debridace	• Commonly incorporated antibacterial agents, growth factors and enzymes • Prevent infection • Promote tissue regeneration • Directly or indirectly remove necrotic tissues
Tissue engineered skin substitutes	• Alloderm • Apligraf • Biobrane • Bioseed • Dermagraft • Epicel • EZ Derm • Hyalograft • Integra • Omnigraft • Laserskin • Myskin • TransCyte	• Addresses deficient growth factors and cytokines • Secrete and stimulate wound growth factors • Suitable for diabetic foot ulcers and venous leg ulcers • Expensive • Risk of infection • Antigenicity

In recent years, the development of wound dressing from biodegradable and biocompatible materials has been extensively studied. As their structures are degraded once placed onto the wound, biodegradable wound dressings do not need to be changed and this can reduce pain associated with changing dressings. The rate of degradation can also be adjusted by selecting suitable polymers to fabricate the dressings. In addition, wound dressings are also able to carry drugs or bioactive molecules that can enhance wound healing.

The fabrication of wound dressings can be done by several methods. One of the well-known techniques to produce non-woven fibres is electrospinning technique.

1.7 Skin tissue engineering

Skin tissue engineering is an interdisciplinary field that combines the principles and technologies of life sciences, engineering and material sciences to develop skin substitutes for promoting the healing of wounds.[44,45] The basic principle of tissue engineering is that cells are isolated from the tissue and then grown on three-dimensional (3D) synthetic ECM (also called as a scaffold) to form new tissue which has similar biochemical and phenotypic characteristics to the original tissue.[46,47] The resulting engineered tissue will be transferred to the wound area to replace the damaged tissue.

1.7.1 Skin substitutes

Skin substitutes are a group of materials designed to provide wound coverage to aid wound closure and replace both structural and functional integrities of the skin after the injury.[48] Skin substitutes can be categorised according to their material composition (biological, synthetic and the combination)[48,49], time of permanence (permanent, semi-permanent and temporary)[48–50], replaced region (epidermis, dermis and the combination)[48–52], layering (single and double layered substitutes)[48,49,52] and the presence or absence of cellular components (cellular and acellular scaffolds)[49,51].

There are three main components involved in the manufacture of skin substitutes, which are cells, growth factors, and scaffolds.[53]

1.7.1.1 Cells

Skin cells produce and secrete ECM and growth factors to support and promote cell proliferation and differentiation. It is worth noting that skin substitutes may not need to contain cells. For instance, Alloderm® is an acellular skin substitute mimicking a dermal layer that facilitates the migration and the attachment of patient's own cells.[54] However, the healing of wounds that are treated with cellular skin substitutes may be faster than acellular substitutes as there is no waiting time for cell migration from the host tissue.[54]

A variety of cells have been incorporated into skin substitutes such as keratinocytes, fibroblasts, macrophages and endothelial cells. It was reported

that the skin substitutes containing both fibroblasts and keratinocytes are better resemble to the native skin than those constituting with single cell type.[54,55] In addition, the crosstalk between these cells by secreting growth factors (*e.g.* keratinocyte growth factor (KGF), VEGF, PDGF) and cytokines (IL-1) benefits cell proliferation and angiogenesis.[54]

The examples of skin substitutes that consist of both keratinocytes and fibroblasts are Apligraf® and Orcel®. Apligraf® is a US FDA approved skin substitute for treating diabetic foot ulcers and venous leg ulcers.[55] Apligraf® is prepared by growing dermal fibroblasts on a bovine type I collagen layer for 6 days in cell culture media.[54] Human keratinocytes are subsequently seeded and incubated for 4 more days.[54] On day 10, cell culture media is removed to create an air-liquid interface allowing the differentiation of keratinocytes and the formation of stratum corneum layer to occur.[54] It was found that air-liquid interface culture created a micro-environment of the skin, resulting in more complete differentiation of keratinocytes when compared to conventional cell culture that submerged cells in cell culture media.[56]

1.7.1.2 Growth factors

In order to accelerate the healing process, growth factors are incorporated into skin substitutes. The growth factors not only expedite the migration and proliferation of cells but also promote angiogenesis.[53,54] The common growth factors used in skin substitutes are FGF, VEGF, PDGF, TGF-β, and epidermal growth factor (EGF).[51,54]

1.7.1.3 Scaffolds

Three-dimensional scaffolds are an important part of skin substitutes. The scaffolds provide ECM-like structures that temporarily support the attachment, proliferation, infiltration and differentiation of cells, leading to the formation of dermal and epidermal layers.[54,57,58] Moreover, the scaffolds can promote neovascularisation in the wound sites.[54] The scaffolds used in skin substitutes should be biocompatible, biodegradable, permeable to oxygen, nutrients and metabolic wastes, and protective against infection and mechanical damage.[57]

Various types of scaffolds are used in skin tissue engineering including porous (*e.g.* foam and sponge) and fibrous scaffolds (*e.g.* nano- and microfibres), hydrogels, microspheres, and acellular scaffolds (*e.g.* collagen, gelatin, fibrin and elastin).[52,57,58] These scaffolds can be manufactured from natural and/or synthetic materials.[49] Some of the common natural materials are collagen, glycosaminoglycans, fibronectin, elastin and gelatin.[49,54] Decellularised native ECM is also classified in this group and called as acellular scaffolds. Synthetic materials are biocompatible and biodegradable polymers such as poly(lactic acid) (PLA), poly(glycolic acid) (PGA), poly(lactide-co-glycolide) (PLGA), polycaprolactone (PCL) and polyethylene glycol (PEG).[49,54]

The scaffolds can be prepared by several methods such as solvent casting, particulate leaching, freeze-drying, gas foaming, electrospinning, micro-patterning, micro-molding and 3D printing.[55,58,59]

The examples of available commercial products used for dermal fibroblasts and keratinocytes co-culture are Alvetex™ and Mimetix® scaffolds (Figure 1.6). Alvetex™ scaffold is a highly porous cross-linked polystyrene scaffold developed by the Przyborski research group. Cells cultured on Alvetex™ scaffolds possess their natural 3D structure and interact with adjacent cells to create the equivalent of a thin tissue layer *in vitro*.[60]

Mimetix® scaffolds are PLLA microfibres produced by electrospinning. The scaffolds are available in two different configurations; aligned or randomly-oriented fibres. The aligned fibrous structure can be used for cells that need physical guidance.

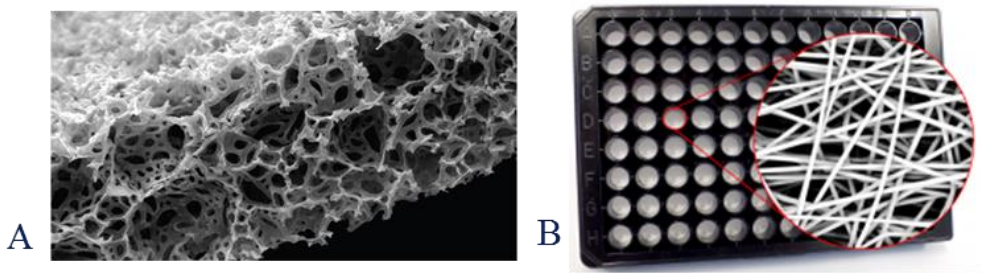


Figure 1.6. Representative images showing the morphology of (A) Alvetex™ scaffold (*image soruce*: https://www.reprocell.com/what-is-alvetex-i70); and (B) Mimetix® scaffold (*image soruce*: http://www.amsbio.com/mimetix.aspx).

1.8 Electrospinning

Electrospinning is a technique for producing nanometer to micrometer fibres.[61–64] Such fibres can be used to fabricate scaffolds to support cell proliferation in skin tissue engineering.[65–67] The scaffolds made of these fine fibres possess high surface area to volume ratio, which resembles the natural ECM.[62–64,68] As a consequence, they can induce the adhesion and growth of cells, fibroblasts in particular.[64] Fibroblasts will then produce new ECM such as collagen, growth factors, and cytokines to repair the damaged tissues. In addition, the highly porous structures of the scaffolds enable the nutrient and gas exchanges between cells and environment, as well as cell migration.[69,70] With these 2 keys properties: mimicking natural ECM and being highly porous, the scaffolds produced by electrospinning can facilitate the formation of granulation tissue and re-epithelialisation during wound healing.[71]

1.8.1 General set-up and principle

In a standard setup of electrospinning, the equipment consists of three main parts: a polymer solution-filled syringe connected to a metal needle, a high voltage supply and a collector (shown in Figure 1.7).[72]

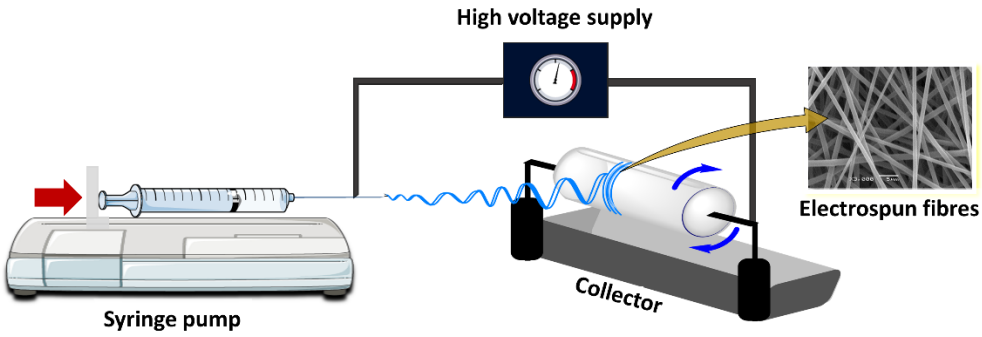


Figure 1.7. General set-up of the electrospinning process

Polymer solution is pumped at a pre-set constant flow rate through a needle.[61,72,73] A high voltage electric field is then applied across the injected polymer solution beam to induce charges. This leads to a Taylor cone formation observed as a conical pattern of the polymer solution at the needle tip. Above a critical voltage, the repulsive electrostatic force overcomes the surface tension of the polymer solution, causing the stretching of the charged polymer solution from the Taylor cone towards the grounded collector as a thin jet. While the jet is continuously lengthened and whipped, excess solvent is simultaneously evaporated to obtain solidified polymer as a nano- or microfibrous structure on the collector.

1.8.2 Parameters in electrospinning process

Properties of resulting scaffolds can be greatly affected by various parameters in which are divided into three categories: polymer solution, process and environment parameters.

1.8.2.1 Polymer solution parameters

1.8.2.1.1 Concentration

The concentration of polymer solution plays an important role in fibre production. Typically, increases in the polymer concentration result in higher viscosities, which provide enough chain entanglement across polymer chains.[72] This entanglement overcomes the surface tension of the polymer solution and allows the formation of uniform bead-less electrospun fibres. A critical solution viscosity is required to maintain molecular chain entanglement to form fibres during the electrospinning process. Otherwise, bead or bead-on-string morphologies will be obtained. Furthermore, increase in solution concentration/viscosity results in increased fibre diameter.

1.8.2.1.2 Molecular weight

The molecular weight of polymer reflects the number of chain entanglements in a solution and therefore solution viscosity.[73] Hence, polymers with high molecular weights are preferable for electrospinning in order to enable a sufficient number of intermolecular entanglements. At the same concentration, higher molecular weight polymers tend to provide fibrous scaffolds while lower molecular weight polymers give bead morphology. Increasing the molecular weight of the polymer can reduce the number of beads in the scaffolds.[74]

1.8.2.1.3 Conductivity

The conductivity of polymer solution is also a critical parameter in the electrospinning process as the high values of conductivity facilitate the production of fibres.[72] A Taylor cone will only form if the polymer solution has high enough conductivity because there is no charge at the surface of polymer solution droplet at low conductivities. As a result, the electrospun fibres cannot be produced.[72,74] In addition, the conductivity of solution influences the morphology of electrospun fibres. Son *et al.* observed that higher the dielectric constant of solvent, lower the fibre diameter.[75]

1.8.2.1.4 Surface tension

Surface tension represents the cohesive forces between liquid molecules to hold the smallest surface area at the interface. High surface tension solutions then require higher forces to break the droplets of solutions, thus increased difficulties in the electrospinning. The surface tension of polymer solution can define the morphology of fabricated electrospun scaffolds. The high surface tension leads to the instability of polymer jets and, as a consequence, electrospraying takes place to produce beads. To achieve the electrospinning, low surface tension of polymer solution is preferable to promote the formation of bead-less fibres.[73,76]

1.8.2.2 Process parameters

Apart from polymer solution properties, the process parameters also need to be taken into account. The process parameters cover applied voltage, flow rate, and gap distance.

1.8.2.2.1 Applied voltage

A high voltage is the main parameter needed for the successful electrospinning. The voltage can influence the morphology of scaffolds *via* the change in the original shape of polymer jet at the needle tip.[72] Optimum voltage enhances the formation of a Taylor cone while too high or too low voltage hinders it, resulting in limited formation of bead-free fibres.[76] The magnitude of voltage required for ejecting the charged jet is dependent on the solution viscosity, conductivity, and surface tension.[77] Polymer solutions with high viscosity, low conductivity and/or high surface tension require higher voltages and vice versa.[74] A high voltage causes increased repulsive electrostatic forces, which lead to more extensive stretching of the electrospun jet, resulting in thinner fibres.[74,78,79]

1.8.2.2.2 Flow rate

The rate of pumping polymer solution should complement the applied voltage to ensure that the speed of pulling and injecting solutions are suitable. For example, when a high voltage is applied to the polymer solution, a high flow rate should be applied to ensure the electrically-induced extraction of the polymer solution from the needle tip. Higher flow rates increase the fibre diameter because more polymer solution is injected.[74]

1.8.2.2.3 Gap distance

The gap distance, which is the distance between the needle tip and the collector, can also influence electrospinning. A minimum distance is required to provide the fibres sufficient time to dry before being collected at the collector. As the distance is extended, the solvent has more time to evaporate and the fibre jet travels further, resulting in a smaller fibre size. Beading is observed when the distance is too wide or too narrow.[72,73]

1.8.2.3 Environment parameters

The environment parameters, such as temperature and humidity, also have a great impact on the rate of solvent evaporation, affecting the electrospinning results. Therefore, these two factors should be carefully adjusted.

1.8.2.3.1 Temperature

Temperature not only influences the rate of solvent evaporation but also the viscosity of the solution.[80] By raising the temperature in the electrospinning process, the solvent evaporates faster.[74] Faster evaporation rate cause the fibre to dry before being collected, whereas, lower evaporation rates cause the polymer to be too wet to be collected. The suitable temperature depends on the boiling point of the solvent. Higher temperatures would be recommended for solvents with a high boiling point to ensure that the evaporation rate is appropriate. Moreover, viscosity decreases at higher temperatures, hence the fibre diameter decreases.

1.8.2.3.2 Humidity

The humidity of the environment during electrospinning also affects the rate of solvent evaporation. Hu *et al.* suggested that low humidity (less than 35%) is ideal for electrospinning and humidity higher than 35% hinders the continuous formation of fibres.[81] Pelipenko *et al.* explained that at low relative humidity, the polymer solution dries and solidifies very quickly due to rapid solvent evaporation.[74] Meanwhile, it is treated with voltage-induced stretching for a shorter time, resulting in bigger sizes of fibres. The higher relative humidity allows the polymer solution jet to have more time to travel and be stretched by electrical forces as well as the solvent evaporation rate is slower. As a result, the thinner fibres are formed. However, too humid conditions can lead to the formation of bead-on-string morphology and the fusion of fibres eventually.

Table 1.3 summarises the effect of key parameters when increased on fibre diameter of electrospun scaffolds.

Table 1.3. Effect of parameters on the fibre diameter of electrospun scaffolds

Category	Parameter	Effect on fibre diameter
Polymer solution	↑ Viscosity	↑
	↑ Conductivity	↓
Process	↑ Voltage	↓
	↑ Flow rate	↑
	↑ Gap distance	↓
Environment	↑ Humidity	↑
	↑ Temperature	↓

1.9 Drug-loaded electrospun scaffolds

Drug-loaded electrospun scaffolds can be prepared by several techniques (*see* Figure 1.8): immobilisation, blend electrospinning, coaxial electrospinning, emulsion electrospinning and secondary carrier electrospinning.[82]

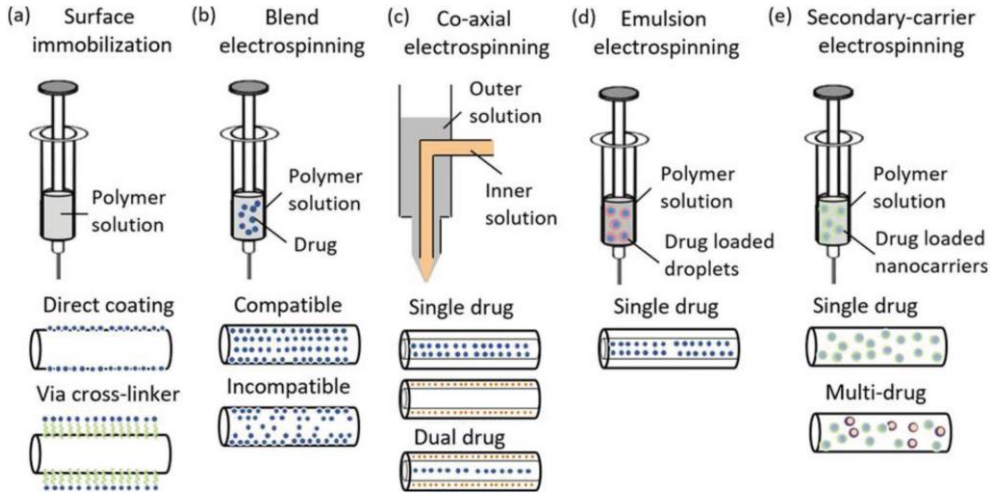


Figure 1.8. Schematic illustrations of different drug incorporation techniques into electrospun fibres[82]

1.9.1 Surface immobilisation

Surface immobilisation is an approach to functionalise the surface of fibres *via* chemical (covalent bonding) or physical interactions (electrostatic interaction, van der Waals interaction or hydrogen bonding).[83] Wettability and the ability to enhance cellular adhesion of the scaffolds can also be modified by this approach. To immobilise drug on the surface of fibres, the scaffolds are simply immersed in the drug solution, and allow passive adsorption of the drug on the surface of fibres to occur.[84]

1.9.2 Blend Electrospinning

Drug incorporation into fibres by blend electrospinning is based on the mixture of drug and polymer in the same solution. The miscibility and compatibility between drug and polymer play an important role on drug distribution in the fibres as well as the release kinetic of drug from the fibres. To achieve a sustained drug release profile, hydrophilic drugs should be blended with hydrophilic polymers.[82] Similarly, polymers blended with hydrophobic drugs should be hydrophobic to prevent phase separation.[82] The advantage of this method is the simplicity of setup. However, the sustained drug release profile may not be achieved if drug and polymer have too different hydrophilicity/lipophilicity.

1.9.3 Coaxial electrospinning

As mentioned earlier, an initial burst release of drug from the fibres prepared by blend electrospinning is observed if the compatibility between drug and polymer is poor. To modify the release profile of drug, coaxial electrospinning was introduced. The spinneret used in blend electrospinning is replaced by two concentrically aligned capillaries in coaxial electrospinning.[82] Two polymer solutions are pumped simultaneously through the capillaries, generating core-shell fibres. In this setting, drug in the core will be covered by the sheath of polymer. Therefore, the release of drug is more sustained when compared to blend electrospinning, as drug must travel through the sheath before reaching dissolution media.[82] The release profile can be modified by varying polymer compositions, drug loadings and process parameters in electrospinning. Owing

to the design of spinneret, coaxial fibres can incorporate two drugs simultaneously. The limitations of coaxial electrospinning are the complex setup and the working parameters must be well-adjusted to achieve the formation of core-shell structure.

1.9.4 Emulsion electrospinning

Another approach to produce core-shell fibres is emulsion electrospinning. The emulsion is prepared by mixing an aqueous phase with an oil phase. A surfactant is added to increase the stability of the emulsion.[82] The emulsion is then injected through a single nozzle, like the one that is used in blend electrospinning. Under electrostatic field, the solvent near the surface evaporates more rapidly than the solvent in the centre of the polymer jet.[85] As a result, the viscosity of the outer layer is higher than the inner layer. This subsequently facilitates the movement of emulsion droplets from the surface to the centre. These droplets later are condensed and stretched to form the core of the coaxial fibres. Emulsion electrospinning is a one-step approach to form core-shell in which the setup is simpler than coaxial electrospinning.

1.9.5 Secondary Carrier Electrospinning

Secondary carriers like micelles, liposomes, nanogels, nanoparticles and nanotubes are used to prepare multiple drug-loaded fibres.[82] By physically entrapping the secondary carriers in the fibres, multiple drugs can be delivered simultaneously. The benefits of this approach are that the degradation of fragile

biomolecules in organic solvent is avoidable and the release of drugs can be designed to be sequential and prolonged.

1.10 Aims and objectives

Since electrospun scaffolds are useful to accelerate wound healing as reported in many studies. In addition, modulating inflammation that causes delay in wound healing shows an improvement in the healing rate of such wounds. The overarching aim of this thesis is to fabricate medicated electrospun scaffolds to support cell proliferation and also modulate the inflammation.

This thesis presents work towards three main aims.

1. To produce an anti-inflammatory drug-loaded electrospun scaffolds using monoaxial electrospinning.

   With the objective to develop biodegradable electrospun scaffolds that support cell proliferation and carry anti-inflammatory drug, it was important to show that monoaxial electrospinning was capable of producing such scaffolds constituting of suitable biodegradable polymers for each drug.

   Specific objectives included:

   - Fabrication of biocompatible and biodegradable electrospun scaffolds loaded with either ibuprofen sodium or doxycycline hydrochloride with different drug loadings
   - Characterisation of the scaffold properties

- Evaluation of attachment and proliferation of mouse fibroblasts (3T3 cells) and primary human dermal fibroblasts on the anti-inflammatory drug-loaded electrospun scaffolds

2. To develop dual drug-loaded electrospun fibres with coaxial electrospinning.

   As the formation of core-shell structure in the fibres using coaxial electrospinning was based on the use of two different polymer solutions, the capability of the coaxial electrospun scaffolds to carry two drugs was investigated.

   Specific objectives included:

   - Production of coaxial electrospun scaffolds containing both ibuprofen sodium (IBU Na) and doxycycline hydrochloride (DOX HCl) based on the developed electrospun scaffolds in the first aim.
   - Characterisation of the scaffold properties
   - Evaluation of attachment and proliferation of mouse fibroblasts (3T3 cells) and primary human dermal fibroblasts on the dual drug-loaded coaxial electrospun scaffolds

3. To test efficacy of fabricated drug-loaded scaffolds against inflammation using an *in vitro* cytokine based inflammation skin cell model.

   To prove that the scaffolds are capable of delivering anti-inflammatory drug(s) to modulate the production/expression of inflammatory mediators, the *in vitro* cytokine induced inflammation model was set up.

Specific objectives included:

- Stimulation of the production/expression of inflammatory mediators (PGE_2, nitric oxide and MMP-1) in primary human dermal fibroblasts using pro-inflammatory cytokines (TNF-α and IL1-β)
- Assessment of cytotoxicity towards primary human dermal fibroblasts after the exposure to the scaffolds
- Evaluation of the efficacy of doxycycline hydrochloride (DOX HCl) at different concentrations to inhibit the production/expression of the inflammatory mediators
- Evaluation of the efficacy of the mixture of doxycycline hydrochloride (DOX HCl) and ibuprofen sodium (IBU Na) to inhibit the production/expression of the inflammatory mediators
- Investigation of the efficacy of drug-loaded electrospun scaffolds to inhibit the production/expression of the inflammatory mediators

Chapter 2

Materials and General Methods

2.1 Materials

General materials and lab consumables used throughout in this thesis are listed in Table 2.1.

Table 2.1. List of materials and lab consumables

Materials	Source/Supplier
Plastic and glass wares	
T25, T75 and T175 cell culture flasks	Nunc™, Thermo Fisher Scientific, Denmark
Tissue culture treated plastic well plates (12, 24 and 48 wells)	Falcon BD, Biosciences, UK
Non tissue culture treated plastic well plates (12, 24 and 48 wells)	Falcon BD, Biosciences, UK
Non treated 96 well flat bottom assay plates	Costar®, UK
Filters (0.2 µm)	Sartorius™ Stedim Ltd., UK
Syringes (1, 2, 5 and 10 mL)	B. Bruan, UK
Bijou bottles (7 mL)	Scientific Laboratory Supplies Ltd., UK
CellCrown™ 24 well plate inserts	Scaffdex Ltd., Finland
NMR tubes (5 mm diameter)	Sigma-Aldrich, USA
Polymers	
PLGA8515, MW 63 kDa, acid end group, Lot no. LP831	Evonik, USA
PLGA5050, Resomer® Select 5050 DLG 4A, Lot no. LP1175	Evonik, USA
P(DL)LA, M_n 50 kDa, Lot no. LP1074	Evonik, USA
PCL, M_n 80,000, Lot no. MKBR4731V	Sigma-Aldrich, UK

Materials	Source/Supplier
Solvents	
d_6-Dimethylsulfoxide (d_6-DMSO) for NMR	Sigma-Aldrich, USA
Dimethylsulfoxide (DMSO)	Sigma-Aldrich, USA
Dichloromethane (DCM)	Sigma-Aldrich, USA
Hexafluoroisopropanol (HFIP)	Fluorochem, UK
Drugs	
Ibuprofen sodium salt, analytical standard, ≥ 98%, Lot no. BCBR4459	Sigma-Aldrich, UK
Doxycycline hydrochloride, ≥ 98%, Lot no. 167648	Sigma-Aldrich, UK
Cells	
Mouse fibroblast cell line (3T3 cells) p.30–40	University of Nottingham, UK
Primary dermal fibroblast; normal, human, adult (ATCC® PCS-201-012™) p.4–7	LGC Standards, Middlesex, UK
Cell media and supplements	
Dulbecco's modified Eagle's medium (DMEM, 1X)	Gibco®, Life technologies™, UK
Fibroblast basal media (ATCC® PCS-201-030™)	LGC Standards, Middlesex, UK
Fibroblast growth kit-low serum (ATCC® PCS-201-041™)	LGC Standards, Middlesex, UK
Fetal bovine serum, heat inactivated	Sigma-Aldrich, UK
L-Glutamine solution 200 mM	Sigma-Aldrich, UK
Consumables for cell cultures	
Antibiotic antimycotic solution (100x) (AB/AM)	Sigma-Aldrich, UK
Trypsin solution from porcine pancreas (10X) 25 g porcine trypsin per liter in 0.9% sodium chloride	Sigma-Aldrich, UK
0.05% Trypsin-EDTA (1X) for primary human dermal fibroblasts	Gibco®, Thermo Fisher Scientific, UK
Trypsin neutralising solution (ATCC® PCS-999-004™)	LGC Standards, Middlesex, UK

Materials	Source/Supplier
Dulbecco's Phosphate Buffered Saline (D-PBS, 1X) without calcium chloride and magnesium chloride	Gibco®, Life technologies™, UK
Dimethyl Sulfoxide Hybri-Max™, ≥ 99.7%, Lot no. RNBF2510	Sigma-Aldrich, UK
Reagents/Kits/Dyes	
PrestoBlue® cell viability reagent	Invitrogen by Thermo Fisher Scientific, UK
Viability/Cytotoxicity assay kit for animal live & dead cells	Biotium, Inc., California, USA
Hoechst 33258	Sigma-Aldrich, UK
Anti-Rabbit IgG Polyclonal, Alexa Fluor® 488 Phalloidin (Ex/Em:495/518 nm)	Cell Signaling Technology®, UK
Reagents for cell fixation	
Hexamethyldisilazane, 99.9%	Sigma-Aldrich, UK
Glutaraldehyde solution, Grade I 25% in H_2O specially purified for use as an electron microscopy fixative	Sigma-Aldrich, UK
Paraformaldehyde (P6148)	Sigma-Aldrich, UK
Ethanol	Fisher Scientific, UK

2.2 General Methods

2.2.1 Characterisation of polymer and polymer-drug solutions

2.2.1.1 Viscosity measurement

The rheological test was performed using a Physica MCR 301 rheometer (Anton Paar, Austria) with a cone-plate measuring system CP25-1/s (cone radius 24.970 mm, cone angle 1.022°, sample volume 0.3 mL) at a constant temperature of 20 °C. The shear rate ranged from 2 to 100 s^{-1}. The measurements were done in sextuplicate. The presented values of viscosity were taken at the shear rate of 10.9 s^{-1}, which relates to the flow rate used in the electrospinning process.

2.2.1.2 Conductivity measurement

The conductivity measurement was performed at room temperature with the conductivity meter (Seven Compact^{TM} S230, Mettler Toledo) equipped with Inlab 720 conductivity probe (CH-8606 Schwerzenbach, Mettler Toledo AG). The reference temperature was set at 25 °C and potassium chloride standard solution (KCl, conductivity: 1,413 $\mu S \cdot cm^{-1}$) was used for calibration. The measurements were repeated ten times for each sample and shown as average ± standard deviation.

2.2.2 Characterisation of electrospun scaffolds

2.2.2.1 Morphology and fibre diameter

Dry electrospun scaffolds were mounted on aluminium stubs with a pre-fixed, double-sided carbon tape and were then coated with gold using a Leica EM SCD005 gold sputter coater for 4 minutes at 25 mA. The coated scaffolds were visualized with a JEOL 6060 LV scanning electron microscope (SEM). The voltage and working distance were set between 13–20 kV and 12–15 mm, respectively to capture images of scaffolds at various magnifications. Samples for SEM imaging were sampling from the top, middle and bottom areas of each scaffold. A selected SEM image from each part of the scaffold was used for fibre diameter measurement with an Image J software. Hundred measurements per scaffold were performed to achieve the average fibre diameter. The distribution of fibre diameter was also presented as a histogram.

2.2.2.2 Porosity by gravimetric method

The scaffolds were cut into squares (1 × 1 cm). Width and length of scaffolds were measured with a ruler. The thickness of scaffolds was measured with a digital caliper (precision 0.001 mm, Mitutoyo, Coventry, UK) under a microscope to make sure that the samples were not squeezed during the measurement. Dimensions of scaffolds were then used for calculating scaffolds' volume (Eq 1).

$$Scaffold's\ volume = W \times L \times H \qquad \text{Eq 1}$$

Where W: the width of the scaffold (cm)

L: the length of the scaffold (cm)

and H: the thickness of the scaffold (cm)

The mass of scaffolds was measured using a balance (Mettler Toledo XS105 Dual Range), and used to calculate the apparent density of the scaffolds (Eq 2).

$$Apparent\ density\ (g\ cm^{-3}) = \frac{Mass\ (g)}{Volume\ (\mathrm{cm^3})} \quad \text{Eq 2}$$

Total porosity was calculated using the following equation (Eq 3):

$$\%\ Total\ porosity = \left(1 - \frac{apparent\ density}{bulk\ density}\right) \times 100 \quad \text{Eq 3}$$

Where the bulk density of PLGA and PCL are 1.26 and 1.145 g cm^{-3}, respectively.[86,87]

For coaxial electrospun scaffolds, the bulk densities of the scaffolds were calculated from the bulk densities of PLGA and PCL using Eq 4.

$$Total\ bulk\ density = \frac{Mass_{total}\ (g)}{Volume_{PCL}\ (cm^3) + Volume_{PLGA}(cm^3)} \quad \text{Eq 4}$$

2.2.2.3 Mechanical properties

The mechanical properties of all scaffolds were obtained from stress-strain curves measured using a uniaxial tensile test (Figure 2.1). Rectangular samples (1 × 2 cm) were cut and subjected to stress-strain measurement using a texture analyser (TA-HD Plus texture Analyser, stable Micro System Instron 3345, UK) equipped with a 50 N load cell at across-head speed of 10 mm min^{-1}. The thickness of scaffolds was measured with a digital caliper under a microscope. All measurements were performed at room temperature and all samples are dry. Three to six specimens from each scaffold were tested to study Young's modulus, ultimate tensile strength, and strain at breaking point.

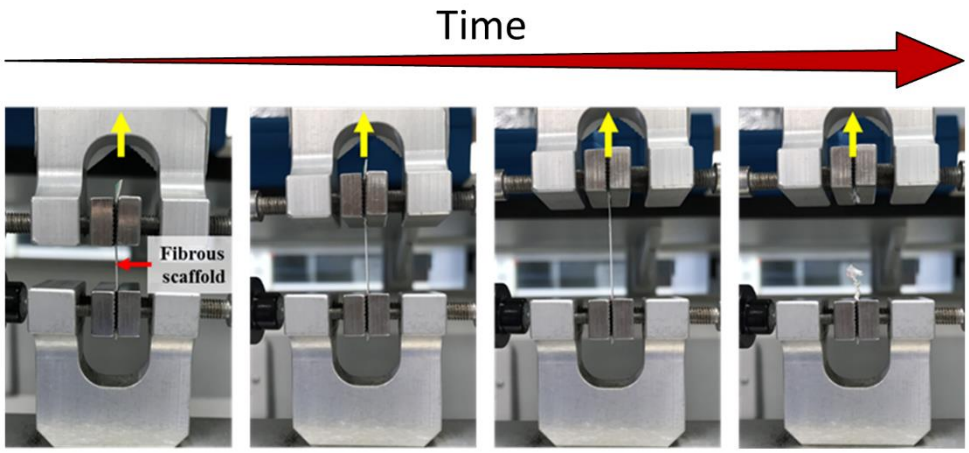


Figure 2.1. Uniaxial tensile test of the electrospun scaffolds. The fibrous scaffold was fixed between the tensile grips. The force was applied by pulling the upper tensile grip upward at a constant speed. The experiment was terminated when the scaffold broke.

2.2.2.4 Water contact angle

Contact angle is defined as the angle formed by liquid at the three-phase boundary where liquid, solid and gas meet. The information of contact angle could be used as an indication of wettability of material in interest by a liquid, usually water (Figure 2.2).

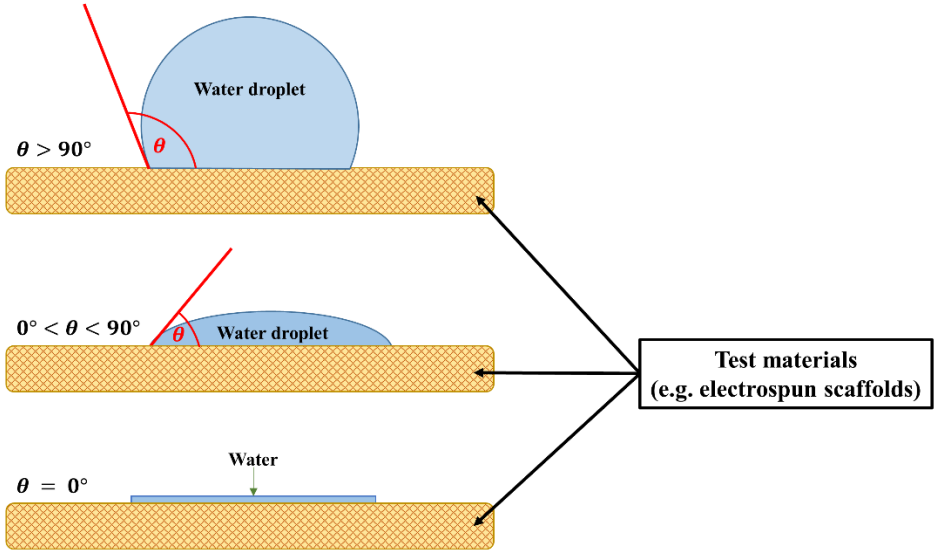


Figure 2.2. Static water contact angle on different types of material measured by a sessile drop method: not wettable (upper), wettable (middle) and completely wettable (lower).

2.2.2.4.1 Static sessile drop method

The water contact angle measurement was performed using a sessile drop method (Figure 2.3). The electrospun scaffolds (1 × 2 cm rectangles) were fixed on the glass slide with tape. One drop of ultra-pure water (18.2 mΩ·cm^{-1} at room temperature, approximately 5 µL) was dropped on the surface of the scaffolds (Figure 2.3). Images of a water drop on the surface of scaffolds were recorded (1-second interval for 10 frames) and analysed for contact angle using a modular CAM 200 optical contact angle metre (KSV Instruments, Finland) equipped

with a camera (JAI®, Denmark). The measurements were performed in triplicate for each sample.

2.2.2.4.2 Dynamic sessile drop method

Advancing and receding water contact angles were measured using a dynamic sessile drop method (Figure 2.3). The electrospun scaffolds were fixed on the glass slide with tape. Initially, one drop of ultra-pure water (18.2 mΩ·cm^{-1} at room temperature, approximately 5 µL) was dropped on the surface of the scaffolds and the tip of water dispensing needle was moved into the centre of the water droplet. The volume of droplet was gradually increased while recording water contact angle. The maximum water contact angle was defined as an advancing contact angle (θ_{adv}). The receding contact angle (θ_{rec}) was measured when the volume of the water droplet was gradually decreased to the point that the droplet almost detached from the needle tip (minimum water contact angle). The measurements were repeated in triplicate for each sample.

To evaluate the topographical heterogeneity of the scaffold surface, contact angle hysteresis was calculated from advancing and receding contact angles using Eq 5.

$$Contact\ angle\ hysteresis\ =\ \theta_{adv}\ -\ \theta_{rec} \qquad \text{Eq 5}$$

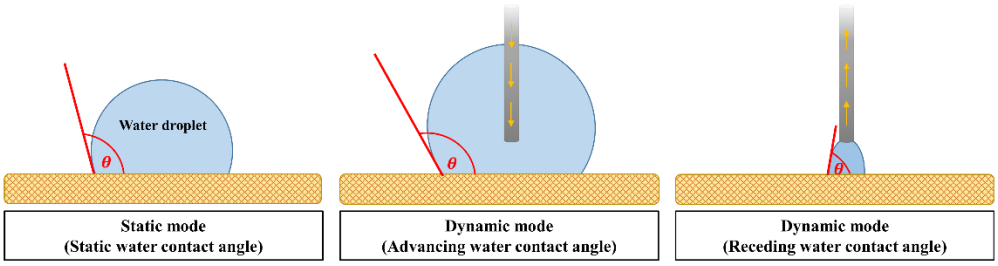


Figure 2.3. Modes of water contact angle measurements and the data obtained from each mode.

2.2.2.5 Drug encapsulation efficiency

Drug-loaded electrospun scaffolds (approximately 50 mg) were cut and dissolved in a mixture of dichloromethane and dimethylsulfoxide (4:1, 5 mL). The solvent mixture was agitated and then allowed to form a biphasic layer liquid. One mL from the layer of dichloromethane (total volume: 4 mL) was sampled and subsequently filtered through a PTFE syringe filter (0.2 µm) to get rid of the precipitated polymer. The filtered solution was injected to high performance liquid chromatography (HPLC) for drug concentration analysis. The amount of the drug in the solution was calculated by comparing with the standard curve of known concentration drug solutions.

HPLC was performed on a Dionex UltiMate 3000 system compromising a Dionex LPG-3400A pump, WPS-30000SL autosampler, TCC-3000SD column compartment, DAD-3000 diode-array detector, fitted with the appropriate Phenomenex column (0.46 cm Ø × 25 cm for analytical HPLC) equipped with the corresponding guard column (0.4 cm Ø × 1 cm). Wavelengths are reported in nm, retention times (τ_R) are reported in minutes and solvent flow rates are reported in $mL \cdot min^{-1}$.

2.2.2.6 Superficial drug distribution by Time of Flight Secondary Ion Mass Spectrometry (ToF-SIMS)

ToF-SIMS is a highly surface-sensitive analytical method that uses incident ion sources to impact on solid at the very outermost surface. The generated secondary ions are analysed by a time of flight mass spectrometer to determine the surface chemistry of a substrate.

All experiments were kindly advised and performed by Dr. Long Jiang. The electrospun scaffolds were cut into small squares and attached to cover glasses using double tape. Powders of ibuprofen sodium (IBU Na) and doxycycline hydrochloride (DOX HCl) were separately dispersed as a thin layer on a double tape which was already attached on a cover glass. Samples were loaded into a ToF-SIMS IV instrument (Münster, Germany) equipped with a bismuth liquid metal ion gun (LMIG) and argon gas cluster ion beam (GCIB).

The images are acquired with a 2D surface imaging mode. The analysis beam was generated by a 25 kV bismuth source liquid metal ion gun utilising a Bi^{3+} rastered over three different areas of the scaffolds with a surface area of 500×500 μm with 256×256 pixels for a total of 15 scans. Data were collected both positive and negative secondary ion polarities. Data processing was acquired with SurfaceLab6 software (ION-TOF GmbH, Germany) to obtain spectra and relevant peaks.

2.2.2.7 Drug release

The electrospun scaffolds were cut into circular discs using a 15 mm diameter punch (n = 3). The discs were placed in a tube containing 15 mL of pre-warmed phosphate buffer saline (PBS, pH 7.4, 37 °C). The samples were incubated at 37 °C with agitation at 100 rpm (thermostatted shaker). At each predetermined time point, 5 mL of solutions were collected and replaced with an equal volume of fresh PBS. Absorbance was recorded on a UV-Vis spectrophotometer (Varian Cary® 50) at the wavelength of 222 nm and 350 nm for IBU Na and DOX HCl, respectively. The amount of drug released at each time point was quantified using the equation obtained from standard curves.

2.2.2.8 Drug-polymer interaction by NMR

The scaffolds were cut into pieces (approximately 30 mg) and dissolve in 2 mL of d_6-DMSO. The solution (ca. 0.5 mL) was then transferred into a glass NMR sample tube (5 mm diameter, Wilmad® NMR tubes, Sigma-Aldrich, USA). ^{1}H and ^{13}C NMR spectra were recorded on Bruker AVII500 (500/125 MHz) or Bruker AV400 (400/100 MHz) spectrometers. The spectra were analysed and the peaks were annotated using MestReNova software. Proton and carbon chemical shifts (δ_H, δ_C) are quoted in ppm, and referenced to residual protonated solvent. Resonances are described using the following abbreviations; s (singlet), d (doublet), t (triplet), q (quartet), quin. (quintet), m (multiplet), br (broad), app (apparent), dd (doublet of doublets) *etc*. Coupling constants (*J*) are given in Hz and are rounded to the nearest 0.1 Hz. H' and H'' refer to diastereotopic protons attached to the same carbon atom, and imply no particular stereochemistry.

Assignment of spectra was assisted by the results of DEPT, COSY, HSQC, and HMBC experiments.

2.2.2.9 *In vitro* degradation study

The dried scaffolds were cut as 1 × 1 cm square (n = 5). Each scaffold was measured for initial weight (W_i) using a balance (Mettler Toledo XS105 Dual Range). The scaffolds were then placed in a vial containing 2 mL of PBS (pH 7.4) and incubated at 37 °C and 5% CO_2. At each time point, the solution was totally removed and the scaffolds were washed with 5 mL of distilled water. The scaffolds were dried in a vacuum oven at 30 °C for 72 h before the remaining weight (W_f) was measured by the same balance (Mettler Toledo XS105 Dual Range). Percentage of weight loss was calculated from the following equation (Eq 6):

$$\%Weight\ loss\ = \left(\frac{W_i - W_f}{W_i}\right) \times 100\% \qquad \text{Eq 6}$$

The scaffolds were returned to the vials and incubated in 2 mL of fresh PBS at 37 °C and 5% CO_2 for the next time point analysis. Representative scaffolds was visualised by SEM imaging to observe physical changes.

2.2.3 Cell culture

2.2.3.1 Mouse embryonic fibroblasts (NIH 3T3 cell line)

Mouse fibroblasts were cultured in Dulbecco's modified Eagle's medium (DMEM) supplemented with 10% v/v fetal bovine serum, 1% v/v L-glutamine (final concentration: 2 mM), and 1% v/v antibiotic antimycotic solution (100x) (final concentration: 250 ng/mL amphotericin B, 100 units/mL penicillin and 100 µg/mL streptomycin). The media was replaced every other day and culture was maintained in a tissue culture incubator at 37 °C and 5% carbon dioxide. Cell passaging was performed when cell confluency was reached 80%.

2.2.3.2 Primary human dermal fibroblasts

Primary dermal fibroblasts; normal, human, adult (ATCC® PCS-201-012™) were maintained in fibroblast basal media (ATCC® PCS-201-030™) supplemented with fibroblast growth kit-low serum (ATCC® PCS-201-041™) and antibiotic antimycotic solution (100x) (Sigma-Aldrich, UK). The complete compositions in cell culture media are shown in Table 2.2.

Table 2.2. The complete formulation of cell culture media for primary human dermal fibroblasts

Component	Final concentration
rh bFGF	5 ng/mL
L-glutamine	7.5 mM
Ascorbic acid	50 mg/mL
Hydrocortisone Hemisuccinate	1 mg/mL
rh Insulin	5 mg/mL
Fetal Bovine Serum	2%
Penicillin	10 units/mL
Streptomycin	10 µg/mL
Amphotericin B	25 ng/mL

2.2.4 Cryopreservation

Cells were re-suspended in cryopreservation media comprising of complete cell culture media, 10% v/v FBS and 10% v/v DMSO (D5879, Sigma-Aldrich, UK). An aliquot of cell suspension containing one million cells was transferred to each cryovial. Cryovials were placed in CoolCell® container and stored at -80 °C for 24 hours. For long-term storage, cryovials were then transferred to store in liquid nitrogen (-196 °C to -210 °C).

2.2.5 Drug cytotoxicity

The effect of IBU Na, DOX HCl, and a mixture of IBU Na and DOX HCl at various concentrations on cellular metabolic activity was studied using PrestoBlue® assay. Briefly, non-fluorescent dye resazurin was taken up by live cells and metabolised into fluorescent product resorufin. Fibroblasts (20,000 cells) were cultured in 24-well tissue culture plates at 37 °C and 5% CO_2 for 24 hours to allow cell attachment. Drug solutions (in complete cell culture media for IBU Na, in complete cell culture media and DI water for DOX HCl) with different concentrations were added to cells (n = 6/concentration for mouse fibroblasts and n = 3/concentration for primary human dermal fibroblasts) and the plates were returned to the incubator for another 24 hours. All solutions were removed from the wells and replaced with 500 µL of 10% v/v PrestoBlue® solution in complete cell culture media. After 30-minute incubation, 150 µL from each well was transferred to a transparent, flat-bottomed 96-well plate. The fluorescence intensity of each sample was recorded by a plate reader (Tecan Infinite M2000) at excitation/emission wavelength of 560/590 nm. Complete

cell culture media was used as a no cell control for IBU Na (complete cell culture media and DI water for DOX HCl) and its fluorescence was deducted from each sample's fluorescence to account for background fluorescence. The vehicle control (non-treated cells in the same vehicle used to prepare drug solutions) was included to ensure that the outcome was only the effect of drug added. Metabolic activity of cells treated with drug(s) was compared to the vehicle control.

2.2.6 Cell proliferation on the scaffolds

2.2.6.1 Cell seeding

Discs of scaffolds (1.5 cm diameter) were fixed with CellCrown^{TM} inserts and fitted into non-tissue culture 24-well plates (Figure 2.4). The scaffolds were rinsed with 2 mL of PBS (D-PBS in case of primary human dermal fibroblasts) to remove any contaminants. Complete cell culture media (2 mL) was added to the scaffolds and the plates were returned to the incubator for 1 h. The centre of scaffolds was seeded with 20,000 cells and cultured in the incubator (37 °C, 5% CO_2). Figure 2.5 summarises the timeline and procedures used in cell proliferation study.

In each experiment, the standard curve of cell number-cellular metabolic activity was generated on the same day as cell seeding on the scaffolds. The range of cell numbers was designed to cover expected cell numbers at the end of assay. Different numbers of cells were seeded to tissue culture 24-well plates in triplicate and allowed to have firm cell attachment in the incubator for 6 h. At 6

h post cell seeding, PrestoBlue® assay was performed to determine cellular metabolic activity of each cell number and the linear range of standard curve was generated for analysis.

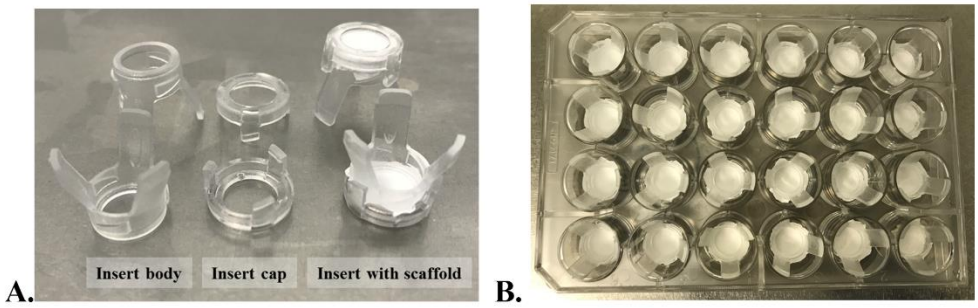


Figure 2.4. (A) CellCrown™ insert body, cap and the electrospun scaffold immobilised with the insert. (B) The scaffolds immobilised with CellCrown™ inserts were fitted into a non-tissue culture 24-well plates.

2.2.6.2 PrestoBlue® assay

The PrestoBlue® assay was performed to measure the metabolic activity of cells on the scaffolds. At each time point, the scaffolds were moved to new non-tissue culture 24-well plates, followed by incubated with 10% v/v PrestoBlue® reagent in complete cell culture media (1.5 mL per well). The reagent was incubated with the scaffolds for 60 minutes at 37 °C and 5% carbon dioxide before 150 µL from each well was transferred to a flat-bottomed 96-well plate. The fluorescence intensity emitted by resorufin was detected by a plate reader (Tecan Infinite M2000) at excitation/emission wavelength of 560/590 nm. Complete cell culture media was used as a no cell control and its fluorescence was deducted from each sample's fluorescence to account for background fluorescence. After the assay, PrestoBlue® reagent was discarded and the scaffolds were gently washed with 2 mL of PBS (D-PBS for primary human

dermal fibroblasts). Finally, the scaffolds were moved to new non-tissue culture 24-well plates and the wells were filled with 2 mL of fresh complete cell culture media. The plates were returned to the incubator for the next time point.

2.2.6.3 LIVE/DEAD® assay

To visualise live and dead cells on the scaffolds, at each time point, the scaffolds were incubated with a mixture of 2 dyes (0.25 µL calcein-AM and 1 µL ethidium homodimer-1) from LIVE/DEAD® assay kit in complete cell culture media (2 mL per well) for 40 minutes in the incubator (37 °C, 5% CO_2). Cell culture media was removed and replaced by PBS (D-PBS for primary human dermal fibroblast) before taking images of cells on the scaffolds with a Nikon SMZ1500 fluorescence microscope. Viable cells took and metabolised calcein-AM which emitted green fluorescence. Whereas, ethidium homodimer-1 bound to nucleic acids of dead cells and was visualised as red fluorescence.

2.2.6.4 Cell morphology by SEM imaging

To observe the morphology of cells on the scaffolds, the scaffolds were washed with 2 mL of PBS (D-PBS for primary human dermal fibroblasts) and fixed with 10% v/v glutaraldehyde in water at 4 °C overnight. After removing glutaraldehyde, the scaffolds were washed with 2 mL of sterile water three times and were dehydrated with increasing concentrations of aqueous ethanol (30, 50, 70, 90 and 100%). Subsequently, the scaffolds were treated with hexamethyldisilazane and kept in a fume hood until completely dry. The

morphology of cells was then visualised using the same procedures as SEM imaging for observing fibre morphology.

2.2.6.5 Cell infiltration by confocal microscopy

At the end of cell proliferation study, CellCrown™ inserts were removed and the scaffolds were fixed with 3.7% w/v paraformaldehyde solution at 4 °C overnight. The scaffolds were washed three times with 2 mL of sterile water to remove paraformaldehyde and incubated in the solution of fluorescence dyes (Hoescht 33258 and/or Alexa Fluor® 488 conjugated antibody (1:20 Alexa Fluor® 488 in PBS)) for 15 minutes at room temperature. Followed by washing three times with 2 mL PBS after staining, the scaffolds were visualised by an inverted laser scanning confocal microscope (Zeiss LSM700) at the wavelength of 405 nm for Hoeschst 33258 and 488 nm for Alexa Fluor® 488. Continuous z-stacks were taken from bottom to top of the scaffolds at the magnification of 10X. The data analysis was processed with Zen software (Zeiss).

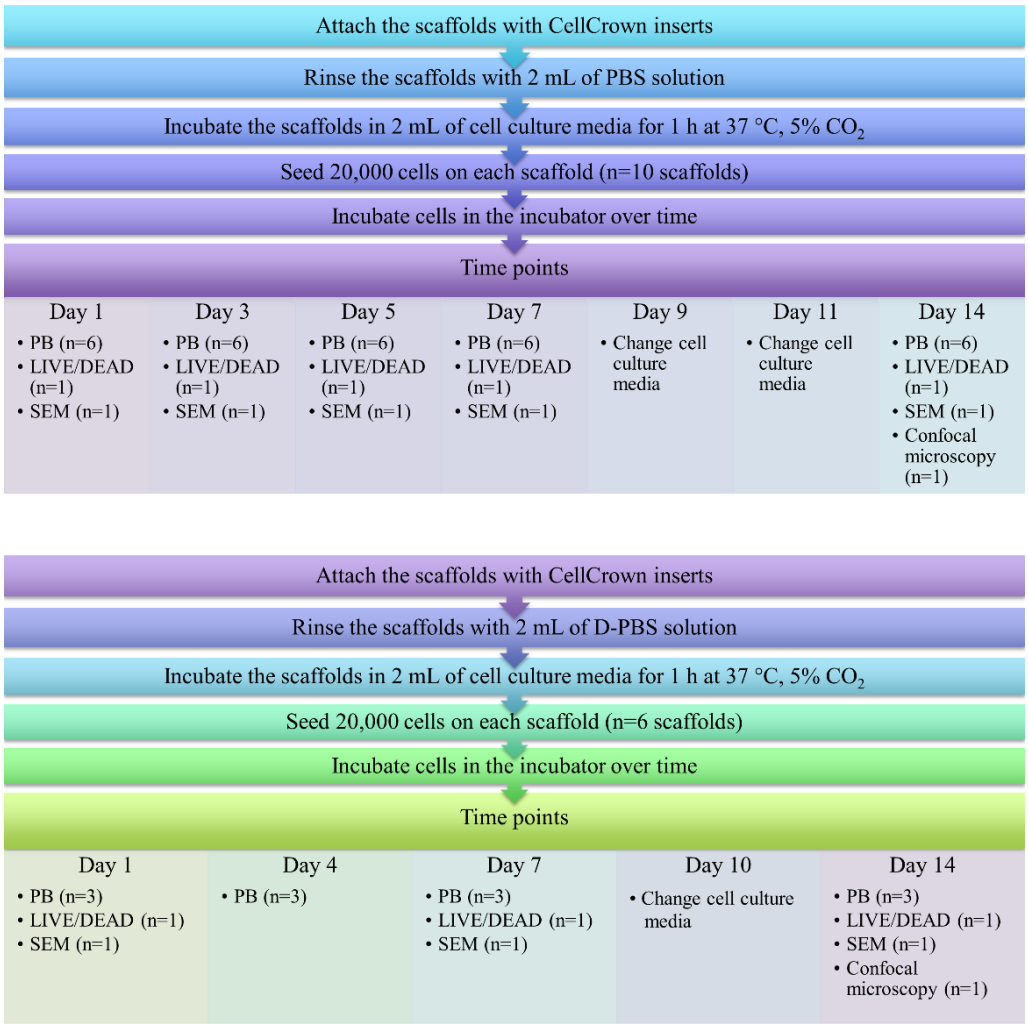


Figure 2.5. Schematic showing experimental design for the cell proliferation study on electrospun scaffolds with mouse fibroblasts (upper) and primary human dermal fibroblasts (lower).

2.2.7. Statistical analysis

Graphpad Prism 7 software (San Diego, CA, USA) was used for all analyses. Where appropriate, mean ± standard deviation was calculated. The statistical analysis was performed using the Student's t-test for two samples, and one-way ANOVA with Tukey's multiple comparisons for more than two samples. The following format is used throughout to define a level of statistical significance otherwise stated; ns for p-value ≥ 0.05, * for p-value < 0.05, ** p-value < 0.01, *** p-value < 0.001, and **** p-value < 0.0001.

Chapter 3

Fabrication and Characterisation of Ibuprofen Sodium-loaded PLGA Electrospun Scaffolds

3.1 Introduction

Chronic inflammation of wounds not only retards wound healing but also causes pain to individuals both physiologically and psychologically.[42] This results in poor quality of life and failure in wound treatment. In addition, wound management such as cleansing, debridement, and changing dressings all impact on pain and can exacerbate the inflammation.[88–90] Therefore, the development of wound dressings that do not require frequent changes is needed.

The electrospinning technique enables production of materials with fibrous structure in nano- to micrometre ranges, mimicking natural ECM such as collagen fibres and fibrils. Versatile feasibility of electrospinning allows the production of such structures with various types of materials, including natural and synthetic polymers.

Natural polymers have been widely used for electrospinning. Examples of natural polymers include cellulose, chitosan, alginate, collagen, gelatin, silk and DNA. They exhibit good biocompatibility and low immunogenicity.[81] Some of which also provide an anti-bacterial property.[81] Moreover, naturally-derived polymers facilitate cell affinity through surface cell recognition sites and their hydrophilic nature.[91,92] However, natural polymers have poor mechanical

strength and batch variation issues.[92] Synthetic polymers are of interest as they offer better mechanical strength and tuneable properties. Nevertheless, synthetic polymers also have some disadvantages. For example, the lack of surface cell recognition sites and high hydrophobicity that lead to low cell affinity.[92,93]

Poly(lactide-co-glycolide) or PLGA is a biocompatible and biodegradable synthetic copolymer that has been approved by the US FDA for use in medical devices and drug products.[94,95] The applications of PLGA are observed in various fields including resorbable sutures, controlled-release drug delivery systems, and regenerative medicine.

Figure 3.1 shows a chemical structure of PLGA which consists of poly(lactic acid) (PLA, either D-, L- or D,L-lactides) and poly(glycolic acid) (PGA) in various ratios.

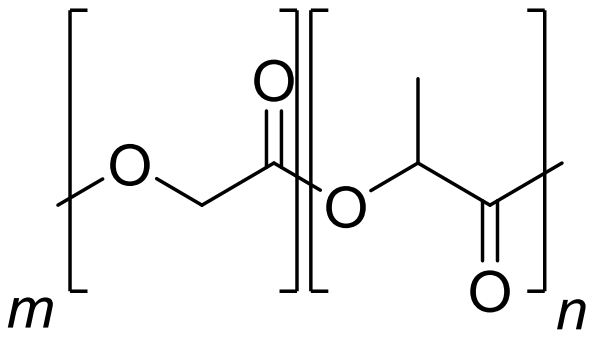


Figure 3.1. Chemical structure of PLGA. The structure of PLGA consists of poly(glycolic acid) and poly(lactic acid) in m and n units, respectively.

Properties of PLGA depend on the ratio of lactic acid to glycolic acid. Due to a pendant methyl group on the alpha carbon, lactic acid is more likely to be hydrophobic, while glycolic acid is hydrophilic.[95] Therefore, a high ratio of lactic acid to glycolic acid leads to higher hydrophobicity in comparison with the copolymers with lower ratios. Furthermore, better mechanical strength and longer degradation time were also observed in previous studies.[96] The degradation of 50:50, 75:25 and 85:15 ratios of PLA to PGA have been found to be between 1–2 months, 4–5 months and 5–6 months, respectively.[97]

The degradation of PLGA occurs *via* hydrolysis of the ester linkages of the polymer in acidic or basic aqueous environments, yielding water-soluble lactic acid and glycolic acid monomers.[98–100] These monomers will be metabolised further by the Krebs cycle.[96,101] In addition, the enzymatic degradation of PLGA undergoes in the presence of trypsin[102], proteases[101], glycosidases[101] or phosphatases[101], causing surface erosion.[101] Taking all into account, PLGA is considered safe for use in humans. In addition, PLGA degradation produces lactate that accelerates angiogenesis, activates pro-collagen factors and recruits endothelial progenitor cells to the wound site.[103] However, the accumulation of the acidic degradation products may cause local inflammation.[104] This concern can be resolved if the structure of dressings are highly porous to allow the diffusion of degradation products of PLGA to the local environment.[105]

While frequency of need to change wound dressings can be improved by the use of biodegradable wound dressings, the biodegradability of the scaffolds alone may not be effective enough to manage wound pain and inflammation. The

World Health Organization (WHO) recommends the use of non-steroidal anti-inflammatory drugs (NSAIDs) to modulate mild/moderate pain in wounds.[106,107] NSAIDs exhibits anti-inflammatory effects that can promote the healing in both acute and chronic injuries.[108]

As illustrated in Figure 3.2, the mechanism of action of NSAIDs relates to the inhibition of cyclooxygenase (COX) enzymes. NSAIDs compete with arachidonic acid released from cell membrane phospholipids to bind the active site of COX enzymes, resulting in the reduced production of prostaglandins and thromboxanes.[109,110] Additionally, the most commonly used NSAIDs, like ibuprofen, can scavenge free radical species as well as inhibit activity of nitric oxide synthase (NOS).[111]

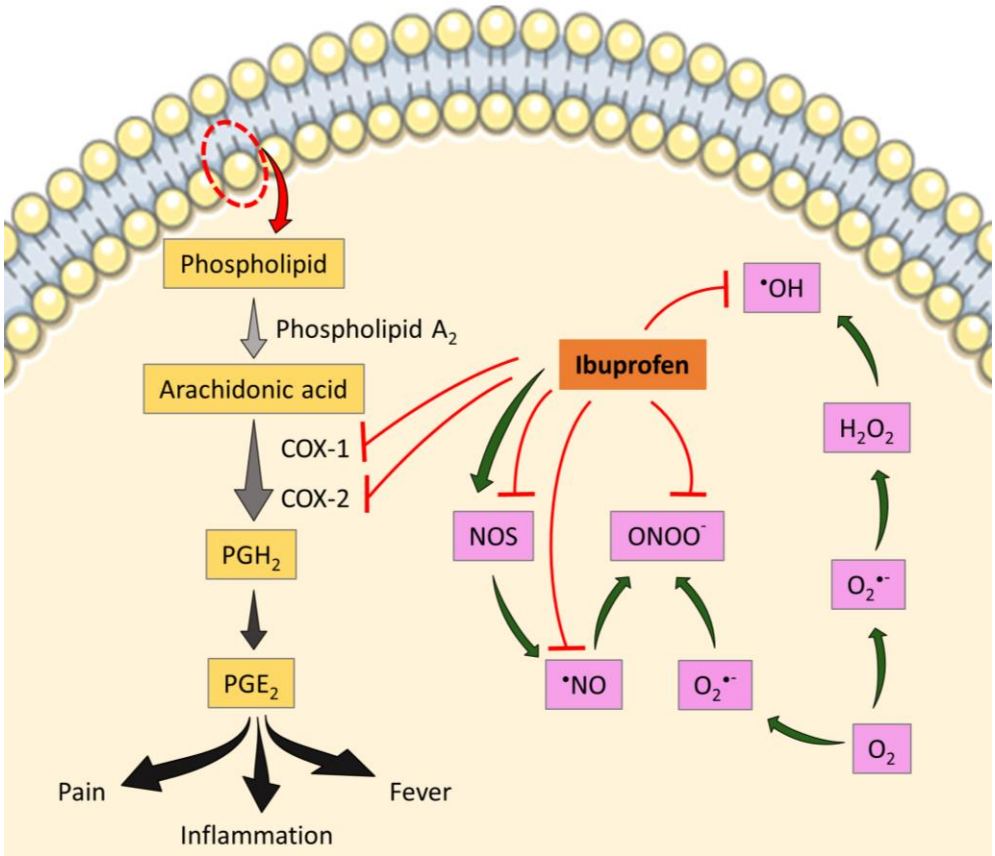


Figure 3.2. Production of pro-inflammatory mediator, prostaglandin E_2 (PGE_2) from phospholipids in cell membrane and its effects, and the mechanism of action of ibuprofen.[111]

Ibuprofen (Figure 3.3) has been used for decades to treat pain, fever and inflammation-related diseases. It is considered safe and can be purchased over-the-counter, however, long-term usage *via* oral administration may lead to severe adverse effects such as gastrointestinal tract ulcers and bleeding, dyspepsia, renal failure, and cardiovascular damage.[107,111]

Topical administration of NSAIDs has become an alternative for users due to its benefits over oral intake as it not only provides high drug concentration at the target site, but also simultaneously avoids systematic absorption and distribution that lead to systematic adverse effects.[112]

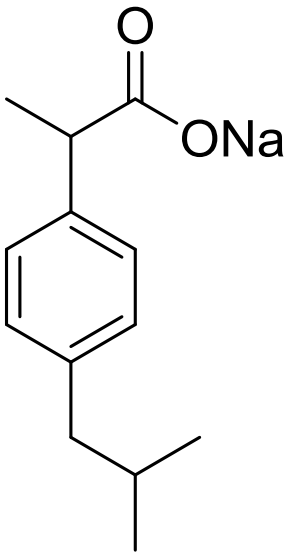


Figure 3.3. Chemical structure of ibuprofen sodium

According to the characteristics of chronic wounds that have a poor blood supply, the therapeutic drug level required for tackling an inflammation may not be achieved at the wound site by oral drug administration. Consequently, local drug delivery should be considered to solve the issue.

Taking into consideration the need of biodegradable dressings and the benefits of topical drug administration, the fabrication of medicated wound dressings by electrospinning is selected potentially useful approach as the drug can be simply blended into polymer solution before electrospinning. This allows drug to be encapsulated within the fibres, and subsequently to be released at the wound area. The electrospun scaffold also provides a temporary structure for cells to attach and proliferate. Figure 3.4 illustrates the use and functions of electrospun fibres in the treatment of chronic wounds such as diabetic foot ulcers.

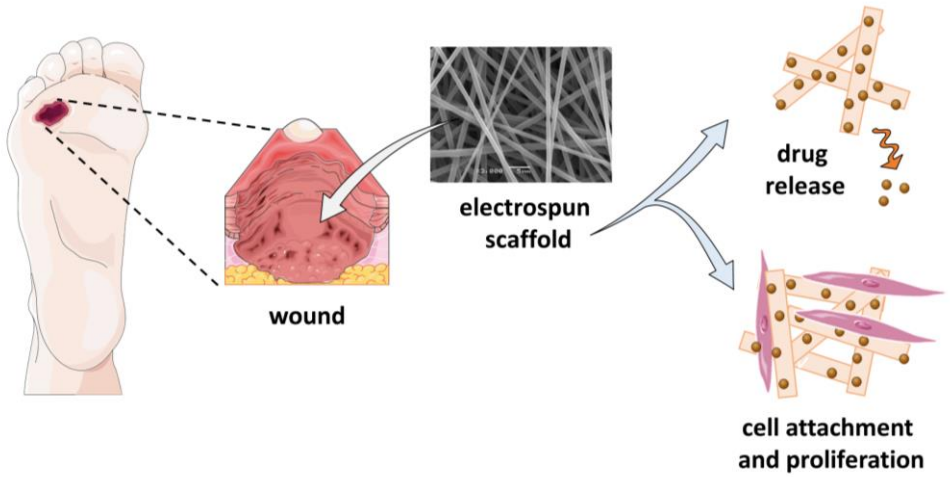


Figure 3.4. Diagram illustrating the application of electrospun scaffolds in diabetic foot ulcer to promote wound healing by providing drug and temporary structure for cell proliferation.

Studies both *in vitro* and *in vivo* have showed an efficacy of ibuprofen released from electrospun scaffolds in pain relief as well as anti-inflammation. By decreasing lipopolysaccharide stimulated NF-kB translocation[90] and gene expression of TNF-α by ibuprofen[113], the inflammation is significantly reduced. The clinical trial also reported that the patients with exuding, painful venous ulcers felt less pain when treated with ibuprofen-loaded wound dressings.[114]

Moreover, the inflammation that arose post-operation in periodontal regeneration could be improved with ibuprofen-loaded PCL fibres.[115]

Although several electrospun scaffolds containing ibuprofen have been developed, this work is the first to report the production of electrospun scaffolds fabricated with PLGA8515 loaded with a water-soluble form of ibuprofen (ibuprofen sodium, IBU Na) for chronic wounds.

As most wounds have limited wound fluid, the concentration of poor water soluble ibuprofen in the wound area may not achieve therapeutic concentrations. Therefore, IBU Na was chosen to replace the acid form of ibuprofen and expected to relieve pain more rapidly.

In this study, the fibre diameter of the electrospun scaffolds was aimed to be produced in the range of collagen fibre diameter (1–20 μm).[116–118] This is to mimic the size of collagen, a main component of natural ECM that provides tensile strength, regulates cell adhesion, supports chemotaxis and migration, and directs tissue development.[119]

3.2 Aims and Objectives

It was hypothesised that electrospun scaffolds made from a biocompatible and biodegradable polymer with appropriate drug loading can support cell proliferation as well as deliver drug molecules to modulate inflammation in the skin wounds (Figure 3.5).

The aim of this chapter was to investigate fabrication of IBU Na-loaded fibrous PLGA scaffolds using electrospinning. Moreover, electrospun scaffolds were characterised with various techniques to examine their physical properties, and used to explore cell-scaffold interaction with mouse fibroblasts.

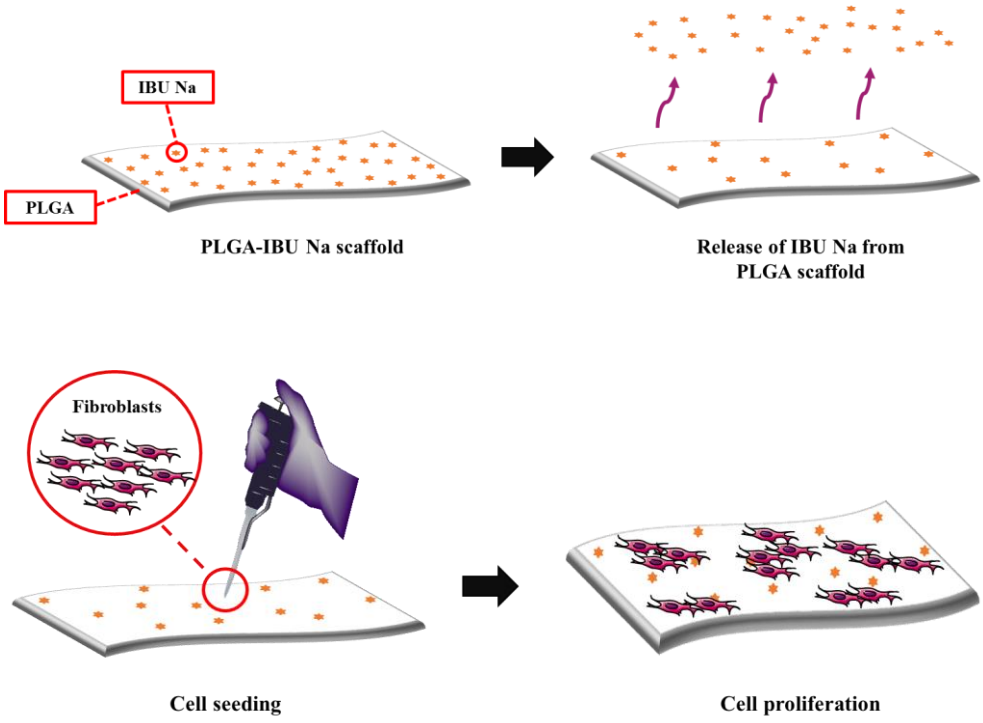
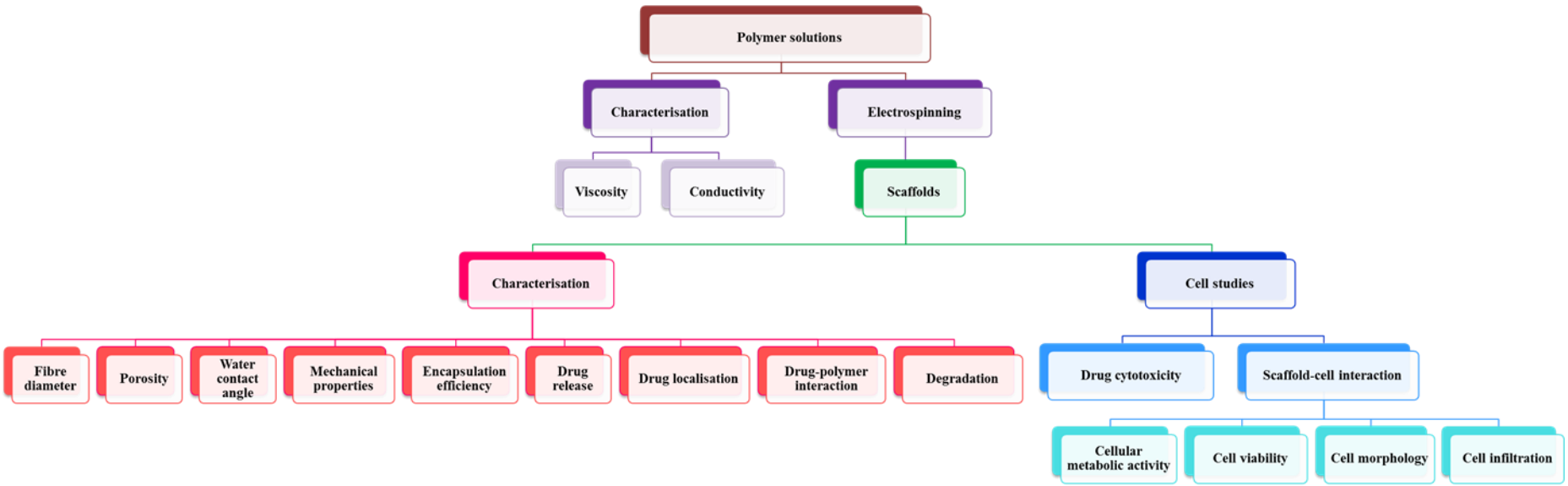


Figure 3.5. Diagram showing the application of electrospun scaffolds to provide IBU Na and support cell proliferation.

The aims were achieved with the following objectives:

1. Manufacture IBU Na-loaded electrospun scaffolds with different drug loadings from biocompatible and biodegradable PLGA8515.
2. Characterise the electrospun fibres in terms of fibre diameter, porosity, water contact angle, mechanical strength, drug encapsulation efficiency, drug release, drug localisation, drug-polymer interaction and degradation.
3. Investigate fibroblast cell proliferation, morphology and infiltration when cultured on the electrospun scaffolds.

3.3 Experimental overview



3.4 Materials and Methods

3.4.1 Preparation of polymer solutions for electrospinning

PLGA with the ratio of 85% D,L-lactide to 15% glycolide (PLGA8515, MW 63 kDa, acid end group, Evonik, UK) was selected for fabricating scaffolds. The polymer was dissolved in hexafluoroisopropanol (HFIP, analytical grade, Fluorochem, UK) by magnetic stirring overnight to form a 25% w/v polymer solution for electrospinning.

For drug-loaded electrospun scaffolds, IBU Na (98% GC grade, Sigma-Aldrich, UK) was added to the 40% w/v PLGA solution in HFIP with the concentration of 1, 2 and 5% w/w relative to the weight of the polymer. The concentration of PLGA used for fabricating PLGA-IBU Na scaffolds was increased from 25% w/v to 40% w/v to compensate the effects of increasing conductivity and decreasing viscosity of PLGA solutions by IBU Na on fibre diameter. This is to ensure that fibre diameters of PLGA and all PLGA-IBU Na electrospun scaffolds are comparable. Hence, the effects of different fibre diameters on scaffold properties and cell behaviour are avoidable. The PLGA-IBU Na solutions were stirred overnight prior to the electrospinning fabrication. All PLGA-IBU Na solutions were clear and no drug precipitation was observed.

3.4.2 Fabrication of PLGA and IBU Na-loaded PLGA scaffolds using electrospinning technique

Electrospun scaffolds were fabricated using a climate-controlled electrospinning apparatus (IME Technologies, Netherlands). A polymer solution was loaded

into a 5 mL syringe connected to one end of a tubing. The other end of the tubing was fitted with a blunt tipped stainless-steel needle (internal diameter of 0.8 mm). The polymer solution was pumped at a constant flow rate of 2 mL h^{-1} using a programmable syringe pump (Harvard Apparatus, USA) and was electrospun horizontally with 14 kV accelerating voltage (18 kV for PLGA scaffolds) supplied by a high voltage power supply. Electrospun scaffolds were collected on an aluminium foil sheet wrapped around a grounded aluminium-rotating collector (rotating at 150 rpm). The gap distance was set at 10 cm. The electrospinning processes were all performed at 20 °C and 30% relative humidity. All scaffolds were placed in a vacuum oven at 25 °C for 24 h to remove residual solvent.

3.4.3 Characterisation of the scaffolds

See Chapter 2 General Methods.

3.4.4 Cell studies

See Chapter 2 General Methods.

3.5 Results and Discussion

In this chapter, monoaxial electrospinning was implemented to manufacture IBU Na-loaded scaffolds. The electrospun scaffolds were made of PLGA due to its biocompatibility and biodegradability. Since the application was aimed to be used for chronic skin wounds, which typically heal slowly (typically 3–13

months).[14,120–122] Therefore, PLGA with the ratio of 85% PLA to 15% PGA (85:15) was selected for fabricating the scaffolds because its degradation time (5–6 months) is the longest when compared to the ratios of 50:50 (1–2 months) and 75:25 (4–5 months).[123] It is expected that the scaffolds will provide a temporary structure for cell attachment, promote cell proliferation, and gradually degrade while chronic wounds heal themselves.

To obtain uniform PLGA fibres, the conditions used in the electrospinning process were optimised. It was found that the minimum concentration of PLGA in HFIP solution required to produce fibres without beads was at 25% w/v (*see* Appendix). IBU Na was blended with PLGA at 1, 2 and 5% w/w relative to the dry weight of PLGA prior to being dissolved in the solvent. The maximum drug loading was set at 5% w/w, because when IBU Na was loaded at 10% w/w, scaffolds became brittle 3 days after. Even though a production of PLGA scaffolds loaded with 10% w/w ibuprofen (acid form) has been reported, the *in vitro* degradation study revealed that such scaffolds degraded and lost all of integrity within 6 days.[90] Such a rapid degradation profile of the scaffolds is, therefore, not suitable for supporting chronic wound healing, which generally takes more than 30 days.

3.5.1 The studies of polymer solution's properties: viscosity and conductivity

Key properties of polymer solutions for electrospinning, viscosity and conductivity, were examined in order to understand the properties of the resulting fibrous scaffolds.

The viscosity of polymer solutions can dictate the morphology of produced scaffolds.[72] At the optimum viscosity, the chain entanglement overcomes the surface tension of polymer solutions, resulting in a continuous jet towards the grounded collector to generate uniform fibres. If the viscosity of polymer solutions is too low, beads or bead-on-string morphologies will be obtained. In contrast, too viscous polymer solutions hinder the electrospinning process and perhaps lead to needle blockage.

The viscosity is directly governed by the concentration of the polymer solution.[72] The concentration that provides a minimum viscosity to produce uniform fibres is called a critical concentration.

In this work, the critical concentration of the PLGA solution was found at 25% w/v, which had a viscosity value of 0.60 ± 0.01 Pa·s. Figure 3.7A shows that increasing PLGA concentration to 40% w/v led to approximately a 5-fold increase in viscosity (2.43 ± 0.05 Pa·s).

Incorporation of IBU Na at 1%, 2% and 5% w/w significantly decreased the viscosity of 40% w/v PLGA solutions to 2.22 ± 0.09, 2.19 ± 0.04 and 1.73 ± 0.12 Pa·s for 1%, 2%, and 5% drug loading, respectively. As the PLGA backbone is connected by ester linkages, which are susceptible to hydrolysis, the presence of weak acid species, like ibuprofen (pKa of 4.40)[124], can facilitate the hydrolysis of PLGA, hence the decrease in viscosities of the solutions.[90,125]

Even though IBU Na does not clearly exhibit acid/base properties, the solvent in which IBU Na is dissolved–HFIP–does show itself as an organic weak acid (with pKa of 9.3[126]). As a consequence, HFIP can potentially protonate IBU^- to generate acid form of ibuprofen that will undergo acid catalysis of ester linkages in PLGA chains (*see* Figure 3.6).

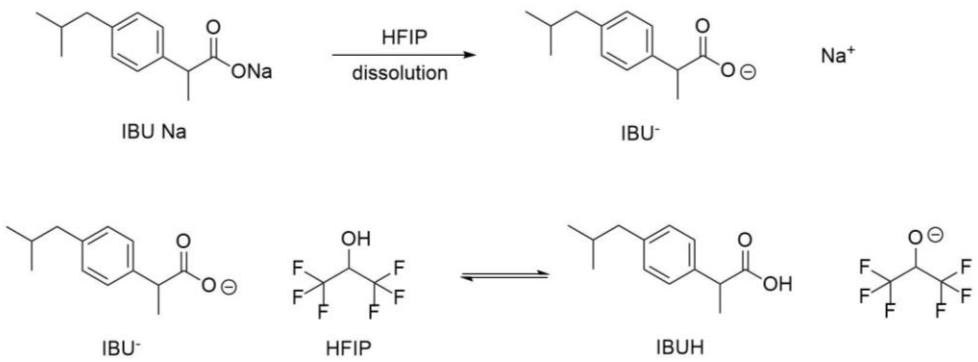


Figure 3.6. Regeneration of ibuprofen acid form from ibuprofen sodium facilitated by HFIP.

Since conductivity also has an impact on the appearance and fibre diameter of the scaffolds[72], a high conductive solvent, such as HFIP, was selected to enhance the electrospinning process. The results in Figure 3.7B shows that increasing concentration of PLGA from 25% w/v to 40% w/v did not significantly increase the conductivity. On the other hand, the sodium salt form of ibuprofen greatly increased conductivity by making the PLGA solutions become electrolytes. There was not a linear relationship between conductivity and drug loading although a higher conductivity of the solutions was observed when a greater amount of IBU Na was added.

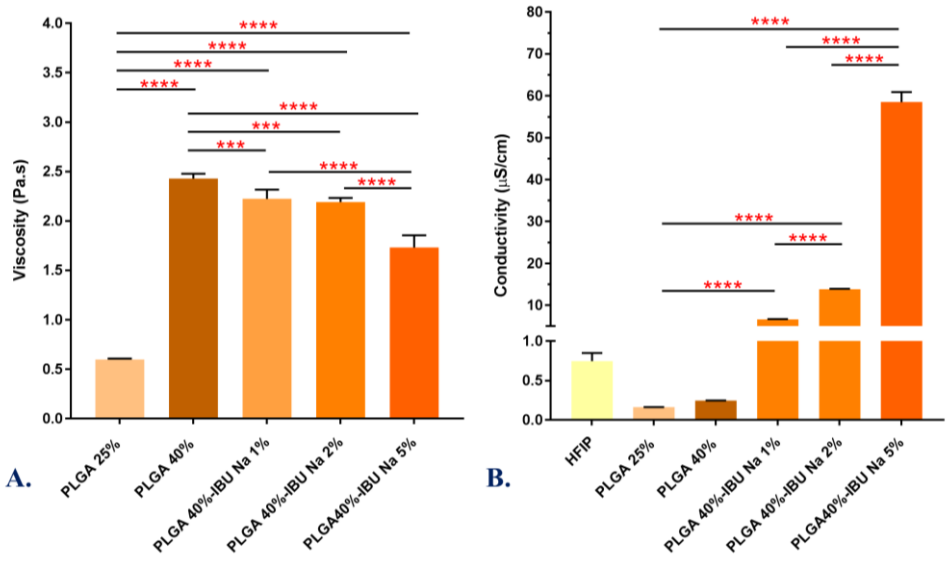


Figure 3.7. Means and standard deviations of (A) viscosity and (B) conductivity of the PLGA solutions and PLGA-IBU Na solutions. The values presented were averaged from six and ten measurements for viscosity and conductivity, respectively. *** defines statistical significance at *p*-value < 0.001 and **** defines statistical significance at *p*-value < 0.0001.

Table 3.1. Viscosity and conductivity values of the solvent, PLGA solutions, and PLGA-IBU Na solutions. The viscosity and conductivity values reported were the means and standard deviations obtained from six and ten measurements, respectively.

Solution	Viscosity (Pa·s)	Conductivity (µS·cm^{-1})
HFIP*	N/A	0.75 ± 0.10
PLGA 25%	0.60 ± 0.01	0.16 ± 0.001
PLGA 40%	2.43 ± 0.05	0.24 ± 0.003
PLGA 40%-IBU Na 1%	2.22 ± 0.09	6.66 ± 0.05
PLGA 40%-IBU Na 2%	2.19 ± 0.04	13.83 ± 0.12
PLGA 40%-IBU Na 5%	1.73 ± 0.12	58.48 ± 2.42

* Solvent of all the polymer solutions

The preliminary results indicated that the average fibre diameter of the scaffolds fabricated from PLGA 40% w/v was 2.07 ± 0.60 µm. While the average fibre diameter of all IBU Na-loaded scaffolds made from PLGA 40% w/v solutions were approximately 1 µm. To avoid the consequence of fibre diameter variation in further studies, non-drug-loaded PLGA scaffolds were fabricated from PLGA 25% w/v solutions, called '*blank PLGA scaffolds*' henceforth. Figure 3.8

summarises all the concentrations of the PLGA solutions that were used in the fabrication process of the blank PLGA and IBU Na-loaded PLGA scaffolds.

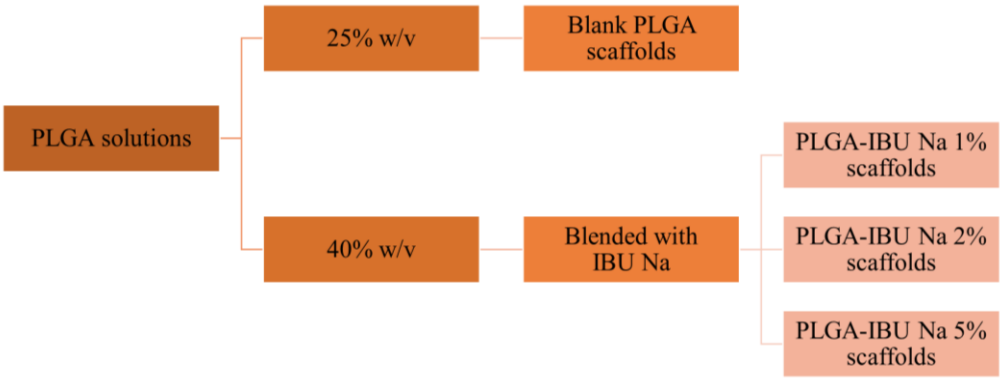


Figure 3.8. Diagram summarises the concentrations of the PLGA solutions used for fabricating the blank PLGA scaffolds and IBU Na-loaded PLGA scaffolds

3.5.2 Characterisation of PLGA and IBU Na-loaded PLGA electrospun scaffolds

3.5.2.1 Fibre morphology and fibre diameter

Representative SEM images in Figure 3.9 revealed uniform fibrous structures of all scaffolds with random fibre orientations. The surfaces of the fibres were smooth, and no drug crystals were observed. The average fibre diameter of the scaffolds ranged between 980 nm and 1.20 µm with comparable patterns of size distribution, as presented in the histograms. PLGA-IBU Na 5% scaffolds possessed the finest diameter when compared to the other scaffolds (Figure 3.10A).

As shown in Figure 3.9, the orientation of fibres in PLGA scaffolds is more random when compared to fibres in PLGA-IBU Na scaffolds. Furthermore, higher loadings of IBU Na leads to higher degrees of fibre orientation. This is a result of the increasing conductivity from the addition of IBU Na. Literatures suggest that salt increases the charge density on the surface of polymer jet under the electrical field while electrospinning.[72,127–133] This causes the greater repulsive force between charges, which facilitates the stretching of polymer jet by electrical force. Consequently, the straighter shape, smaller fibre diameter and higher degree of fibre orientation are obtained.

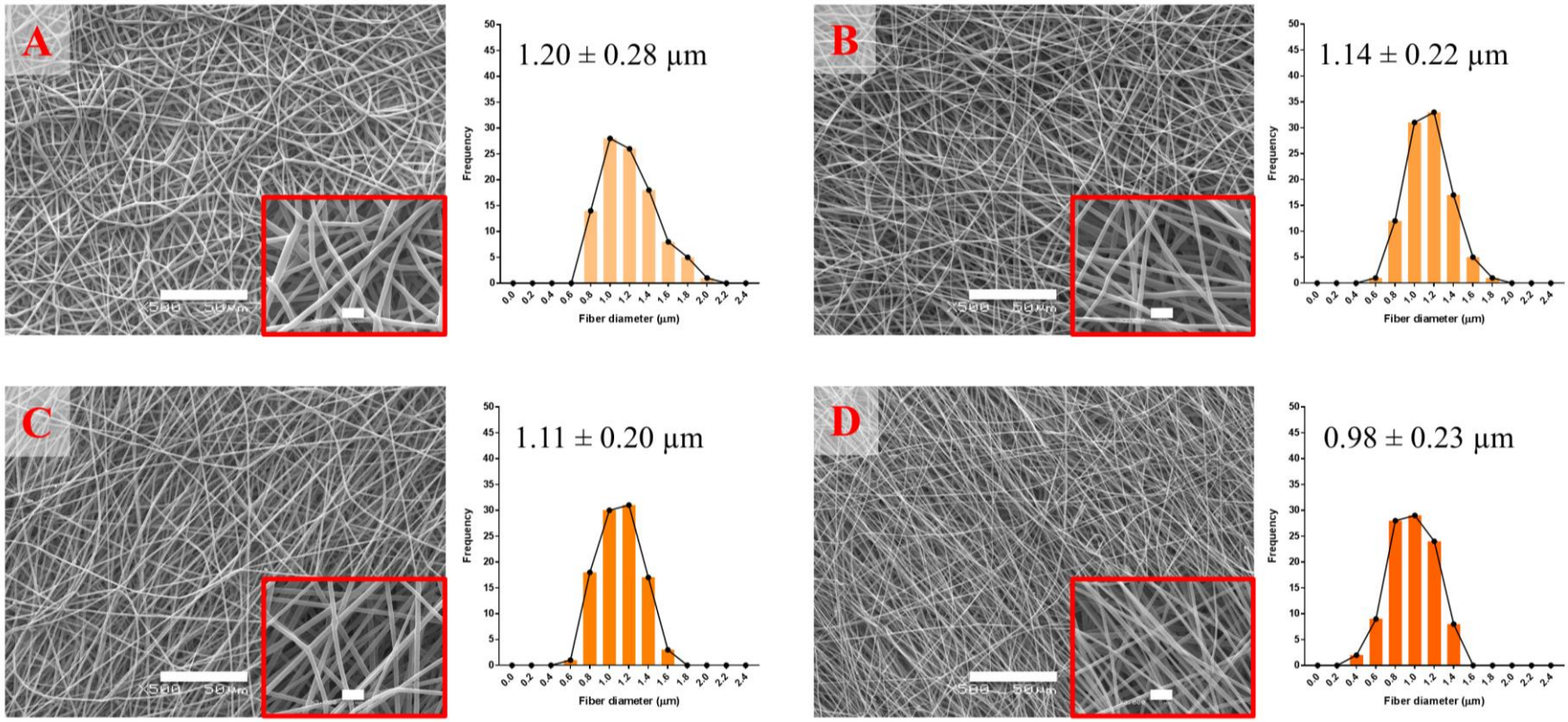


Figure 3.9. Representative SEM images of (A) PLGA, (B) PLGA-IBU Na 1%, (C) PLGA-IBU Na 2% and (D) PLGA-IBU Na 5% electrospun scaffolds at the magnification of 500X (scale bar 50 µm) and 3,000X (scale bar 5 µm, small images in red windows). The histograms show the size distribution of the fibre diameters, and the values shown above the histograms are mean ± standard deviation of the fibre diameter measured by ImageJ software from the representative SEM images of the scaffolds (n=100 fibres).

As discussed above, IBU Na promotes the hydrolysis process of the PLGA backbone, and simultaneously introduces more charged species to the solutions prior to electrospinning. These two consequences lead to a significant drop in the viscosity as well as an increase in conductivity of the polymer solutions. As the surface charge density of the jet of the injected polymer solution increases during electrospinning, the polymer jet is more stretched before reaching the grounded collector, as a result, the smaller diameter fibres are formed.

Whilst there are no significant differences in fibre diameters between PLGA-IBU Na 1% and PLGA-IBU Na 2% scaffolds. In stark contrast, with 5% w/w IBU Na loading, the fibre diameter is significantly smaller than those of 1% and 2% w/w IBU Na loaded PLGA scaffolds. This perhaps is a result from a magnitude of the increasing conductivity; the degree of rising in conductivity is larger when comparing between the loadings of 2% w/w and 5% w/w IBU Na (44.65 $\mu S \cdot cm^{-1}$) with the loadings of 1% w/w and 2% w/w IBU Na (7.17 $\mu S \cdot cm^{-1}$), *see* Table 3.1 (above).

3.5.2.2 Porosity

Highly porous scaffolds are ideal for enhancing cell infiltration and facilitating the exchange of nutrients and cell waste products. In this study, the total porosity of the scaffolds was determined by a gravimetric method and presented in Figure 3.10B and Table 3.2. The results show that PLGA scaffolds had the lowest porosity at 55.83 ± 0.27%. Whilst all IBU Na-loaded PLGA scaffolds possessed porosity greater than 77%. This could be the effect of IBU Na loaded into PLGA scaffolds as the sodium salt increased surface charge density, creating a

repulsive Coulombic force between fibres.[134] As a result, the packing volume decreased and the loose structure of the scaffolds was obtained.[76,135]

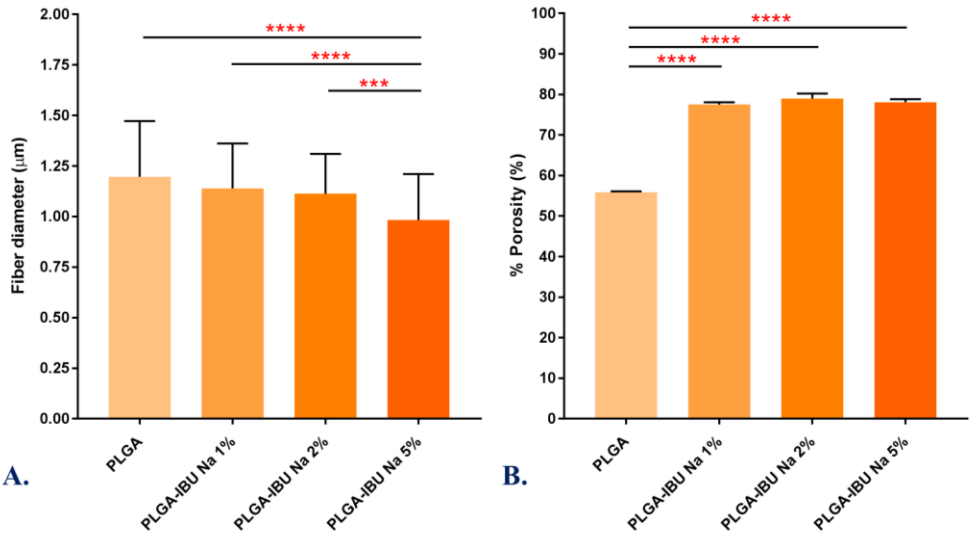


Figure 3.10. (A) Fibre diameter and (B) total porosity of PLGA, PLGA-IBU Na 1%, PLGA-IBU Na 2% and PLGA-IBU Na 5% electrospun scaffolds. Fibre diameter was measured from representative SEM images of the scaffolds using ImageJ software (n = 100 fibres). Total porosity of the scaffolds was determined by gravimetric method in triplicate. The values shown as means and standard deviations. *** defines statistical significance at *p*-value < 0.001 and **** defines statistical significance at *p*-value < 0.0001.

Table 3.2. Means and standard deviations of fibre diameter (n = 100) and total porosity (n = 3) of PLGA, PLGA-IBU Na 1%, PLGA-IBU Na 2% and PLGA-IBU Na 5% electrospun scaffolds.

Scaffold	Fibre diameter (µm)	Porosity (%)
PLGA	1.20 ± 0.28	55.83 ± 0.27
PLGA-IBU Na 1%	1.14 ± 0.22	77.53 ± 0.53
PLGA-IBU Na 2%	1.11 ± 0.20	79.00 ± 1.22
PLGA-IBU Na 5%	0.98 ± 0.23	78.05 ± 0.77

3.5.2.3 Mechanical properties

To assess the mechanical properties of the scaffolds, a uniaxial tensile test was performed. The stress-strain curves (Figure 3.11A) indicate that the scaffolds started to deform at about 7–10% strain; except for PLGA-IBU Na 5%, it deformed at approximately 4% strain. The stress-strain curves of the scaffolds also imply that PLGA-IBU Na 5% scaffolds were brittle due to the low plastic deformation prior to the break point. On the other hand, the other scaffolds were considered ductile, and significantly deforming before breaking.

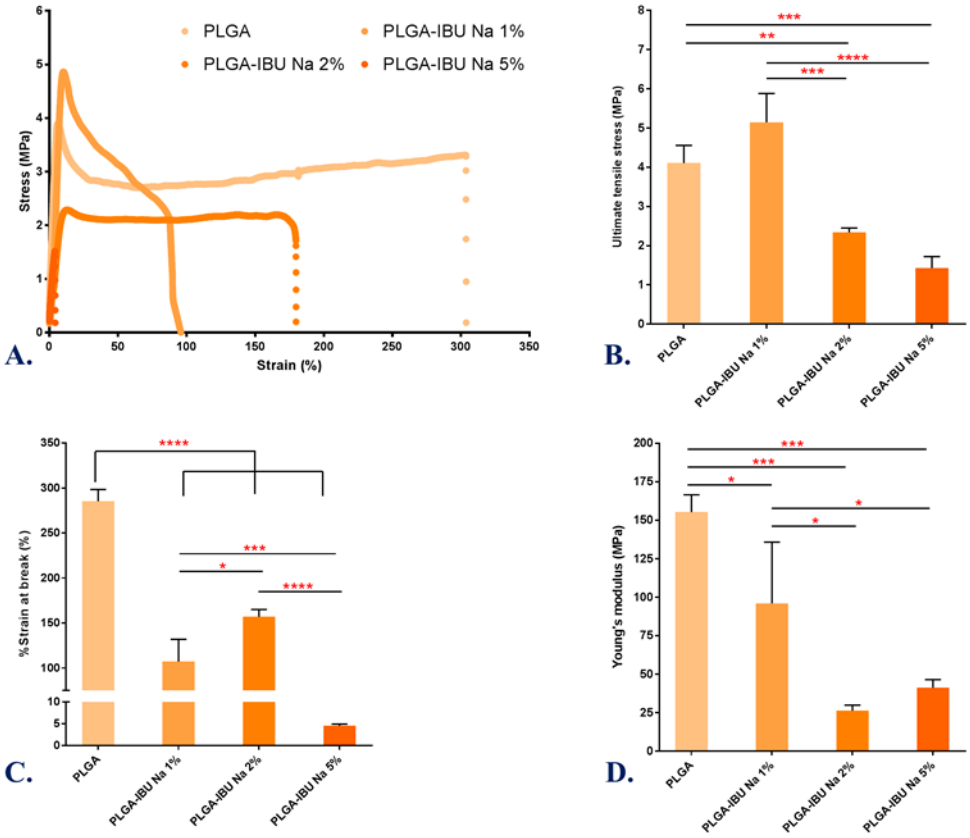


Figure 3.11. Mechanical properties of electrospun scaffolds evaluated by a uniaxial tensile test. Each scaffold was tested in triplicate. (A) representative stress-strain curves, (B) ultimate tensile strength, (C) % strain at break and (D) Young's modulus. The values are shown as means and standard deviations. *, **, *** and **** define a significant difference between the scaffolds at *p*-value < 0.05, < 0.01, < 0.001 and < 0.0001, respectively.

Table 3.3. Means and standard deviations of ultimate tensile strength, % strain at break and Young's modulus of PLGA, PLGA-IBU Na 1%, PLGA-IBU Na 2% and PLGA-IBU Na 5% scaffolds (n=3).

Scaffold	Ultimate tensile strength (MPa)	% Strain at break (%)	Young's modulus (MPa)
PLGA	4.11 ± 0.45	285.31 ± 13.10	155.29 ± 11.34
PLGA-IBU Na 1%	5.15 ± 0.74	107.09 ± 24.74	96.09 ± 39.73
PLGA-IBU Na 2%	2.34 ± 0.11	156.87 ± 8.19	26.37 ± 3.58
PLGA-IBU Na 5%	1.43 ± 0.29	4.50 ± 0.42	41.35 ± 5.16

Figure 3.11B presents the ultimate tensile strength of the scaffolds. It was found that the ultimate tensile strengths of PLGA scaffolds (4.11 ± 0.45 MPa) and PLGA-IBU Na 1% scaffolds (5.15 ± 0.74 MPa) were not significantly different. However, higher contents of IBU Na resulted in a dramatic drop in ultimate tensile strength: 2.34 ± 0.11 MPa for PLGA-IBU Na 2% scaffolds, and 1.43 ± 0.29 MPa for PLGA-IBU Na 5% scaffolds.

The ability of scaffolds to deform before breakage were indicated by % strain at break. It was observed that PLGA scaffolds could most withstand the stretching force, as shown in Figure 3.11C. Their % strain at break was 285.31 ± 13.10%. Meanwhile, PLGA-IBU Na 1% and PLGA-IBU Na 2% scaffolds lost approximately half or more of the ability to deform before break. The greatest decrease in % strain at break was observed from PLGA-IBU Na 5% scaffolds. The scaffolds could deform themselves only 4.50 ± 0.42% from their original shape before break.

The Young's moduli of the scaffolds were obtained from the gradient of the linear range of the stress-strain curves and presented in Figure 3.11D. PLGA and PLGA-IBU Na 1% scaffolds had Young's moduli above 100 MPa while PLGA-IBU Na 2% and PLGA-IBU NA 5% scaffolds had Young's moduli lower than 50 MPa.

Taking all into consideration, the addition of IBU Na to PLGA scaffolds reduced the mechanical strength as well as elasticity of the scaffolds. Particularly, loading IBU Na at 5% w/w resulted in brittle scaffolds, as manifested in the susceptibility to the stress (pulling force). However, the changes in mechanical properties did not impact the scaffold handling.

The findings from this study agreed with previous studies that the acid form of ibuprofen at 5% w/w drug loading significantly reduced the modulus of PLGA7525 electrospun scaffolds.[136] The breakdown of PLGA leads to a lower molecular weight, resulting in loose bonding between polymer chains by Van der Waals forces.[137] As a consequence, the strength and Young's modulus of the scaffolds reduce. In addition, the decrease in Young's moduli was found to be related with high porosity of the scaffolds.[69,138,139]

The mechanical strength of the skin depends on the location, thickness as well as age of individual. Literatures reported that ultimate tensile strength, Young's modulus and ultimate tensile strain of the skin are in the range of 1–30 MPa[140], 0.1–113 MPa[140] and 35–115%[62], respectively. This suggests that IBU Na-loaded PLGA scaffolds possess mechanical properties within the same range as the

skin. Table 3.4 shows ultimate tensile strength and Young's modulus of the skin from different body parts. According to the results, PLGA-IBU Na 1% scaffolds have the ultimate tensile strength (5.15 ± 0.74 MPa) in the range of the skin from the arm. Whilst, the ultimate tensile strength of PLGA-IBU Na 2% (2.34 ± 0.11 MPa) and PLGA-IBU Na 5% scaffolds (1.43 ± 0.29 MPa) are in the range of the skin from the abdomen area. This suggests that different loadings of IBU Na into PLGA scaffolds result in different mechanical properties of the PLGA scaffolds, which will be used to dictate the area that the scaffolds should be applied. However, there are still limited reports regarding the mechanical properties of the skin from specific body parts. The target site of application of such scaffolds should be investigated further.

Table 3.4 Mechanical properties of the skin from different parts of human body[140,141]

Body part	Ultimate tensile strength (MPa)	Young's modulus (MPa)
Abdomen	1.0 – 24.0	N/A
Arm	5.7 – 12.6	19.5 – 87.1
Back	10.0 – 28.8	83.3 ± 34.9
Leg	N/A	6 – 22
Forehead	N/A	0.33 ± 0.04
Forearm	N/A	1.03 ± 0.06
Submandibular skin	N/A	1.28 ± 0.06
Postauricular mastoid	N/A	0.86 ± 0.05
Temporoparietal skin	N/A	0.65 ± 0.05

*N/A: not applicable

3.5.2.4 Water contact angle

To determine hydrophilicity-hydrophobicity properties or wettability of the scaffolds, a sessile drop method with static and dynamic modes were carried out. As shown in Figure 3.12, the static mode of measurement showed insignificant difference between water contact angles of PLGA, PLGA-IBU Na 1% and PLGA-IBU Na 2% scaffolds. These scaffolds were classified as hydrophobic materials as their values of water contact angle were more than 90°,[142] ranging between 93° and 100°. Whereas, PLGA-IBU Na 5% scaffolds could not hold the water droplet. Therefore, PLGA-IBU Na 5% scaffolds were classified as a completely wettable material. Loboa *et al*. (2017) also observed the reduction of water contact angle from 135.8° to 87.9° when 20% w/w of ibuprofen (acid form) was incorporated into PLA electrospun scaffolds.[143]

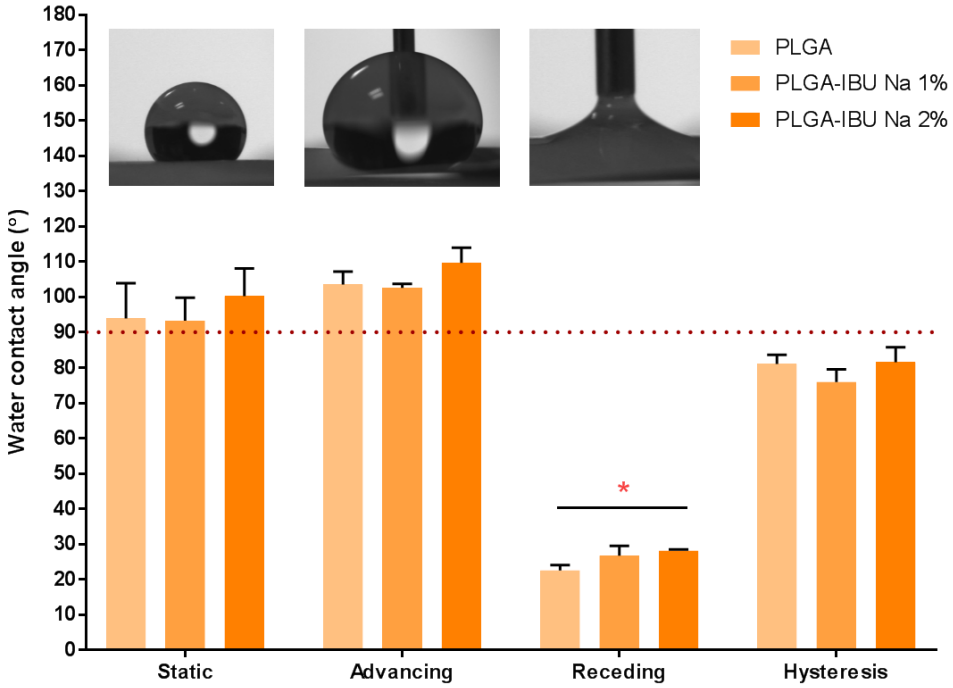


Figure 3.12. Water contact angles of the electrospun scaffolds were determined by static and dynamic modes of sessile drop method. The values are presented in forms of means and standard deviations of static water contact angle, advancing water contact angle, receding water contact angle, and contact angle hysteresis (the difference between advancing and receding water contact angle) (n = 3). The small figures above the bar charts are the representative images of the water droplet on electrospun scaffolds when tested by static mode (left), advancing in dynamic mode (middle), and receding in dynamic mode (right). * defines a significant difference between the scaffolds at *p*-value < 0.05.

Table 3.5. Water contact angles of the electrospun scaffolds were determined by static and dynamic modes of the sessile drop method. The values are represented as means and standard deviations of static water contact angle, advancing water contact angle, receding water contact angle, and contact angle hysteresis (the difference between advancing and receding water contact angle) (n = 3).

Scaffold	Static contact angle (°)	Advancing contact angle (°)	Receding contact angle (°)	Contact angle hysteresis (°)
PLGA	93.93 ± 10.01	103.57 ± 3.68	22.52 ± 1.57	81.04 ± 2.61
PLGA-IBU Na 1%	93.33 ± 6.50	102.63 ± 1.12	26.73 ± 2.78	75.90 ± 3.65
PLGA-IBU Na 2%	100.29 ± 7.81	109.68 ± 4.31	28.10 ± 0.38	81.58 ± 4.23
PLGA-IBU Na 5%	N/A	N/A	N/A	N/A

*N/A: not applicable

Considering that the scaffold is formed by the overlaying of randomly-oriented fibres, pores or gaps are created between fibres. The surface of the electrospun scaffolds therefore becomes inhomogeneous. The surface roughness of the scaffolds can cause a deviation from actual water contact angle value due to gas entrapped in the gaps between fibres, which disrupts the liquid-solid interface.[144,145] That is, the gas-liquid interface has formed instead. As a result, water contact angle of materials is increased.

In order to circumvent the interference of the gas present in the system, the maximum and minimum water contact angles were measured. Such values are obtained by increasing/decreasing the volume of the water droplet until the water contact angle has reached its maximum (advancing contact angle)/minimum (receding contact angle), respectively. The difference between advancing and receding contact angles is called the contact angle hysteresis. This value is indicative of the surface roughness.[142,146]

Advancing water contact angle is a measure of the dry-wetting behaviour of a surface of material. Whilst, the receding contact angle is a measure of the remaining interaction forces between the water droplet and the scaffold. The difference between the advancing and receding contact angles is contact angle hysteresis which can be used to assess roughness of the material.[147] According to the Cassie and Baxter model, the contact area between the surface of scaffold and water is minimised due to pores between fibres, while the contact area between the air and water is maximised. Water droplet is spherical on the surface of the scaffold, resulting in high water contact angle and contact angle hysteresis

values.[142] Additionally, if the surface of material is chemically homogeneous, advancing and receding contact angles are constant and do not depend on the size of the water droplet.[147]

The advancing water contact angle of the scaffolds (excluding PLGA-IBU Na 5% scaffolds) ranged between 102° and 110°. No significant difference was observed between the scaffolds. However, the receding mode revealed smaller water contact angle of PLGA scaffolds when compared to PLGA-IBU Na 2% scaffolds. Large contact angle hysteresis of PLGA, PLGA-IBU Na 1% and PLGA-IBU Na 2% scaffolds was greater than 75°, indicating that these scaffolds had rough surface topography.[142,146]

3.5.2.5 Drug encapsulation efficiency

The amount of IBU Na in the scaffolds was quantified in order to determine % encapsulation efficiency. As shown in Table 3.6, the encapsulation of IBU Na was in the range of 46–64% of its initial loading amount. The significantly higher encapsulation efficiency was observed when PLGA scaffolds were loaded with 5% w/w IBU Na in comparison with 1% w/w IBU Na (p-value < 0.01, One-way ANOVA, n = 3).

Table 3.6. Encapsulation efficiency of IBU Na in the PLGA scaffolds. The values are represented as means and standard deviations of % encapsulation efficiency (n = 3).

Scaffold	Encapsulation efficiency (%)
PLGA-IBU Na 1%	46.92 ± 6.92
PLGA-IBU Na 2%	55.11 ± 2.23
PLGA-IBU Na 5%	64.51 ± 1.69

3.5.2.6 Superficial drug distribution determined by ToF-SIMS

ToF-SIMS is a sensitive, in-depth surface analytical methodology, which is used to analyse surface chemistry, polymer components and drug distribution in the scaffold.[148,149] The top nanometre layer of the scaffolds is bombarded with high energy Bi^{3+} clusters under ultra-high vacuum atmosphere. Later, the secondary ion fragments were ejected from the surface of material and analysed based on their atomic mass to charge (*m/z*) ratios.

Polymers typically have unique chemical fingerprint species for identification. PLGA was identified by the peak at *m/z* = 43 ($[C_2H_3O]^+$), *m/z* = 71 ($[C_3H_3O_2]^-$), *m/z* = 73 ($[C_3H_5O_2]^-$), *m/z* = 87 ($[C_3H_3O_3]^-$), and *m/z* = 89 ($[C_3H_5O_3]^-$).[150] Due to PLGA and IBU Na can share some similar chemical fractions when ionised, for example, $[C_2H_3O]^+$, *m/z* = 43, therefore the peak at *m/z* = 43 cannot be used for identifying IBU Na. As a result, sodium ion ($[Na]^+$, *m/z* = 23) and $[C_{13}H_{17}O_2]^-$ at *m/z* = 205[151] from IBU Na was selected to confirm the presence of the drug on the surface of fibres (Figure 3.13, 3.14 and 3.15).

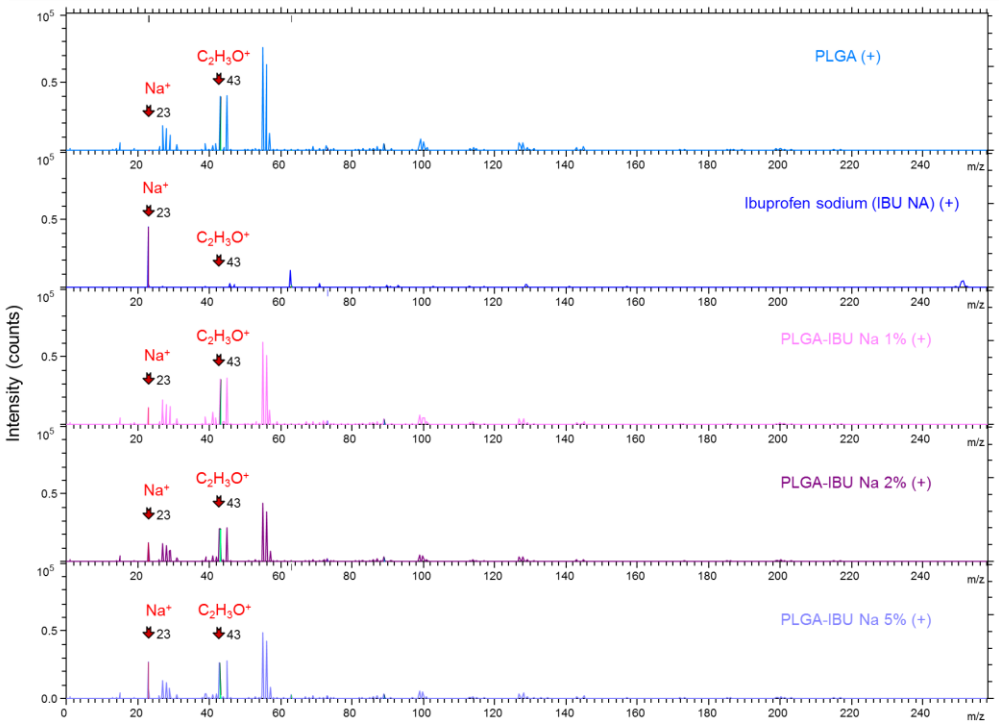


Figure 3.13. Representative positive ToF-SIMS spectra of the surface of electrospun scaffolds. The peak at *m/z* = 23, $[Na]^+$, represents IBU Na; and the peak at *m/z* = 43, $[C_2H_3O]^+$, represents PLGA

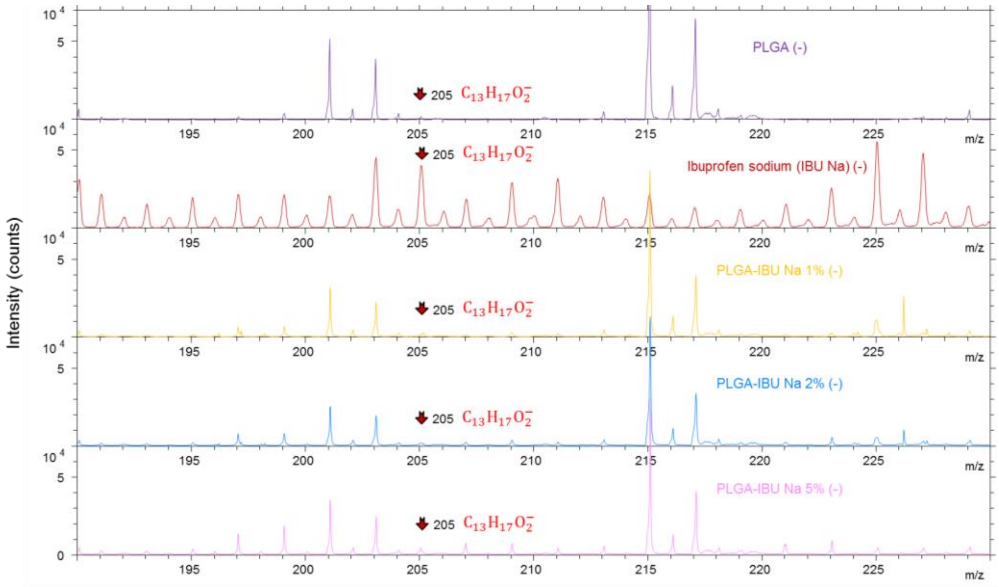


Figure 3.14. Representative negative ToF-SIMS spectra of the surface of electrospun scaffolds. The peak at *m/z* = 205, $[C_{13}H_{17}O_2]^-$, represents IBU Na.

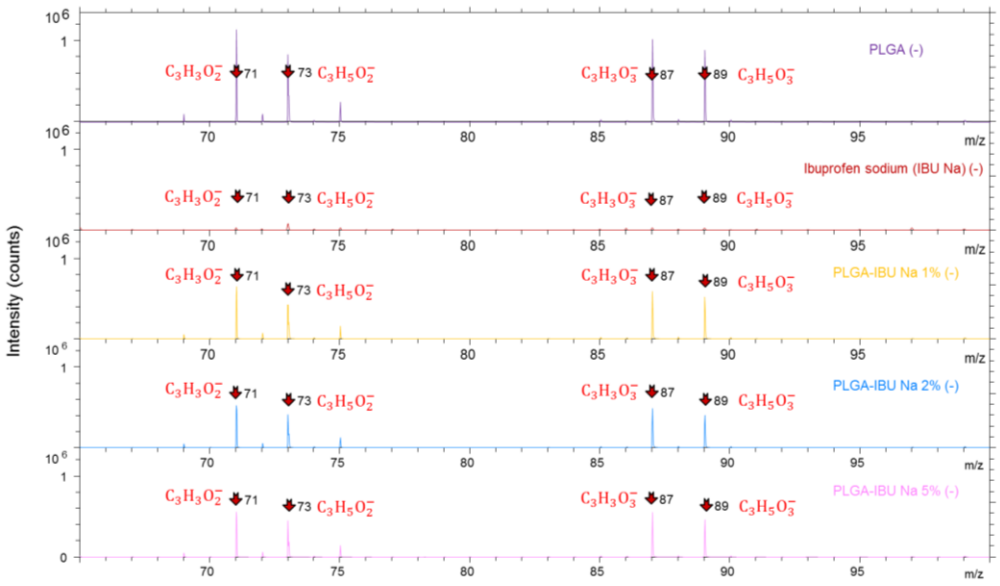


Figure 3.15. Representative negative ToF-SIMS spectra of the surface of electrospun scaffolds. The peak at *m/z* = 71, $[C_3H_3O_2]^-$; *m/z* = 73, $[C_3H_5O_2]^-$; *m/z* = 87, $[C_3H_3O_3]^-$; and *m/z* = 89, $[C_3H_5O_3]^-$, represents PLGA.

The relative comparison of total ion intensity of $[Na]^+$ and $[C_{13}H_{17}O_2]^-$ between the scaffolds (Figure 3.16) implies that the surface of electrospun PLGA-IBU Na scaffolds contained more IBU Na when drug loading was increased.

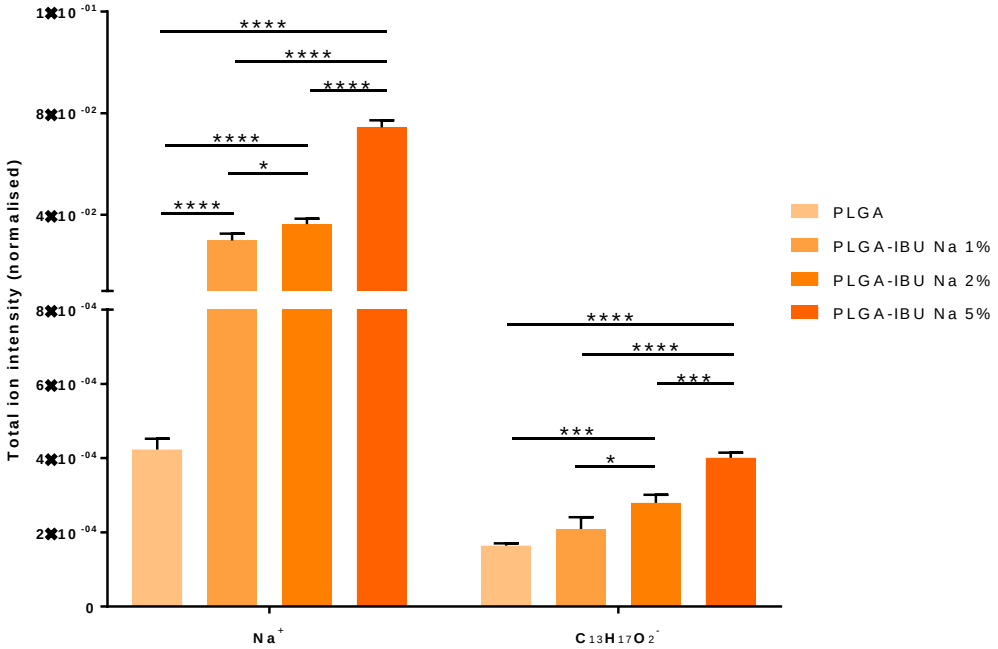


Figure 3.16. Normalised total ion intensity of $[Na]^+$ and $[C_{13}H_{17}O_2]^-$. The values are means and standard deviations of the total ion intensity obtained from three different areas in one scaffold sample (n = 3). Data are normalised to the total ion counts. *, *** and **** define a significant difference between the scaffolds at *p*-value < 0.05, < 0.001 and < 0.0001, respectively.

The secondary ion images (Figure 3.17 and 3.18) show a homogeneous distribution of IBU Na throughout the electrospun fibres with an increasing intensity when drug loading was higher.

As the fibre diameter of the scaffolds are approximately 1 μm and the lateral resolution of secondary ion images are circa 1.95 μm per pixel, the fibrous structure of the scaffolds are not clearly illustrated. However, the increased intensity of IBU Na can be observed with the higher drug loadings.

To observe the distribution of drug in the fibres, imaging the fibres at cross-section should generate the mapping of drug distribution in each individual fibre, providing additional information in conjunct with imaging at only lateral section. Nevertheless, high lateral resolution mode must be carried out to ensure that the resolution is high enough to observe the cross-section of each fibre clearly.

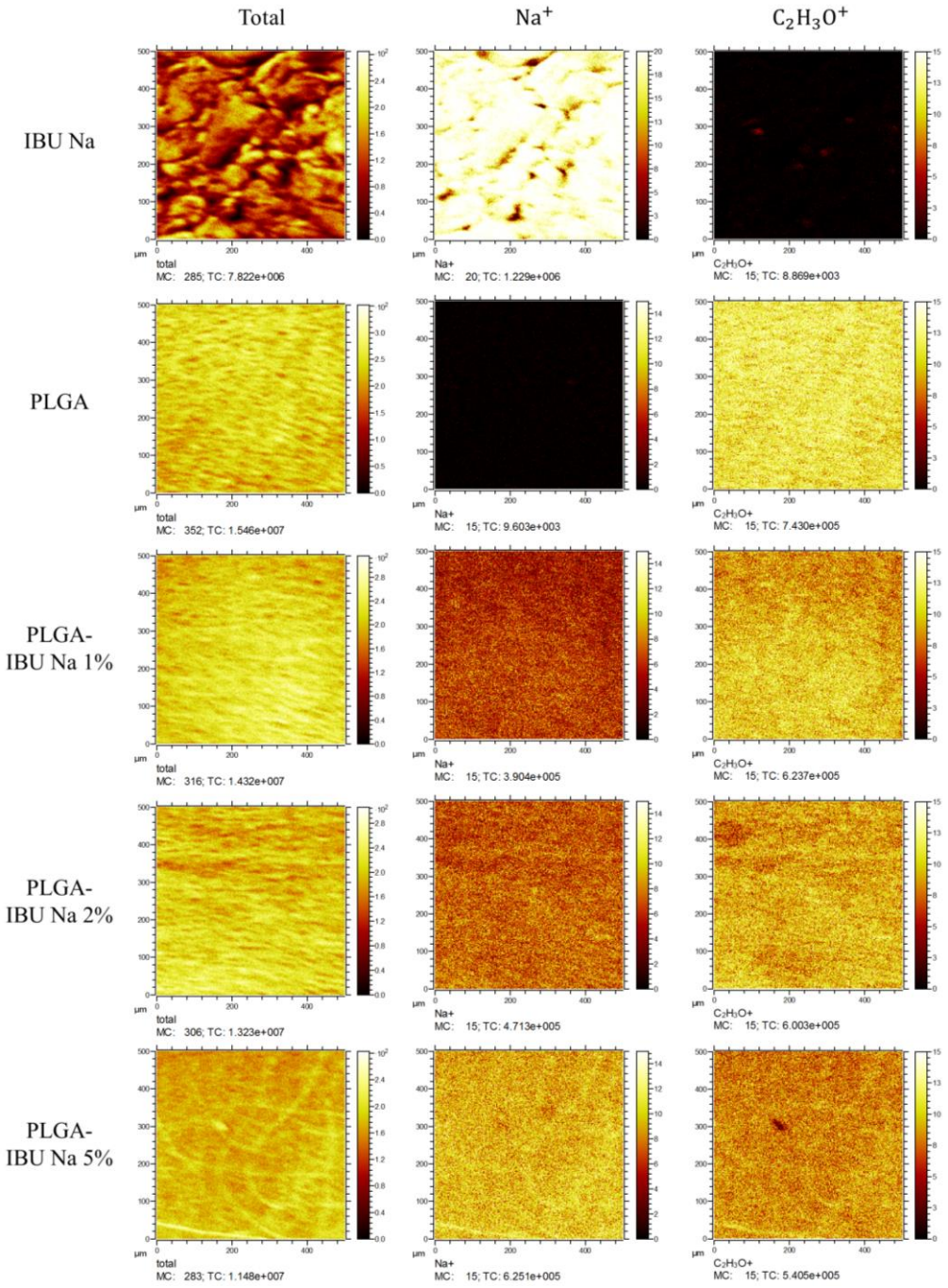


Figure 3.17. The 2D images show the distribution of $[C_2H_3O]^+$, representing PLGA, $[Na]^+$, representing (IBU Na); and the total ions on the top surface of scaffolds. The images are acquired with a 2D surface imaging mode and normalised to the total ion counts.

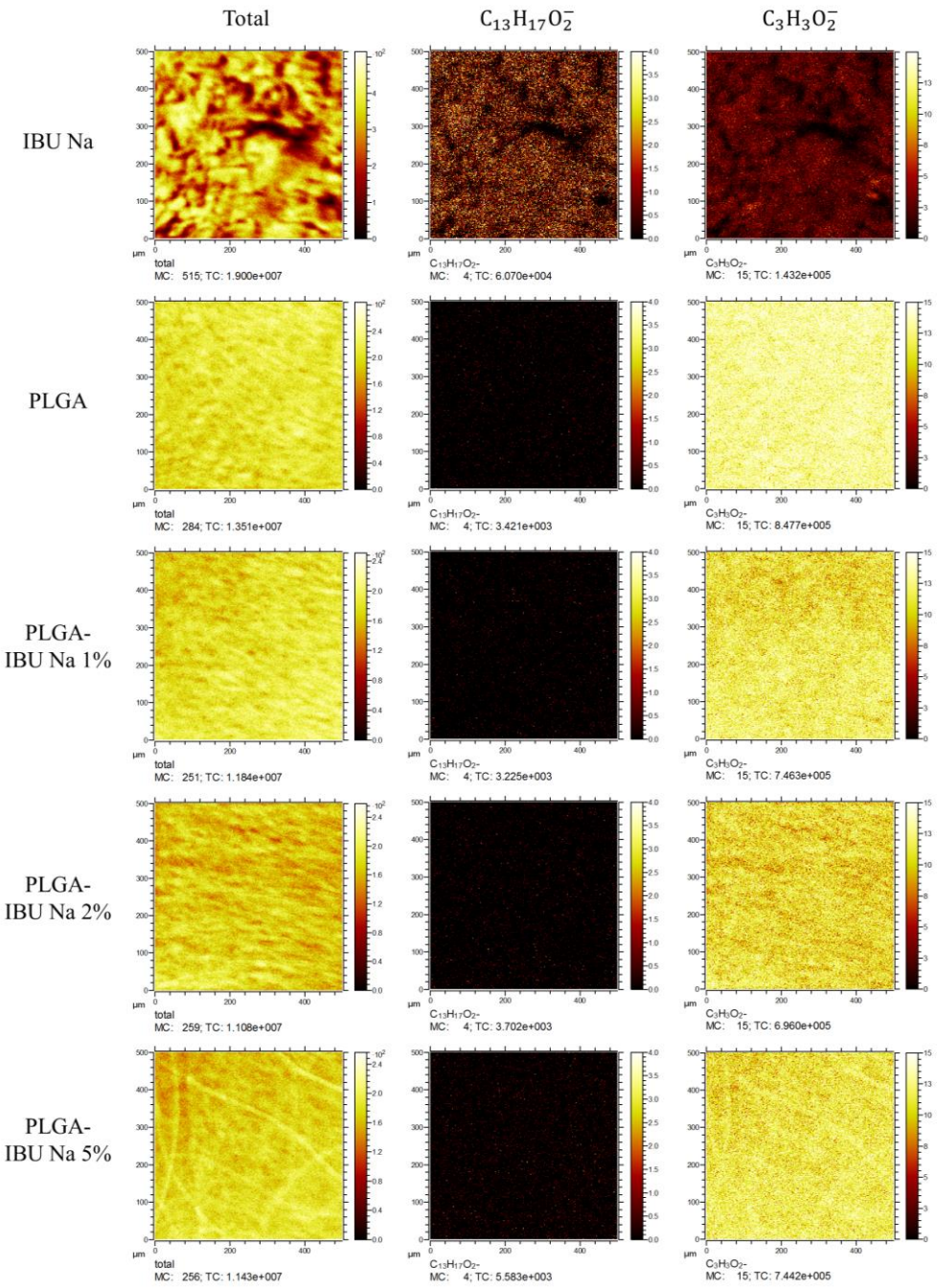


Figure 3.18. The 2D images show the distribution of $[C_3H_3O_2]^-$, representing PLGA, $[C_{13}H_{17}O_2]^-$, representing (IBU Na); and the total ions on the top surface of scaffolds. The images are acquired with a 2D surface imaging mode and normalised to the total ion counts.

3.5.2.7 Drug release profiles of IBU Na from the PLGA scaffolds

The initial rapid burst release of IBU Na into phosphate buffer solution (pH 7.4) was observed within the first 30 minutes of the study (Figure 3.19). The release of IBU Na gradually increased and reached the plateau within 24 hours before a lag phase. A tri-phasic drug release profile was observed in PLGA-IBU Na 1% scaffolds. It could be that the remaining IBU Na is encapsulated in the intra-structure of individual fibres and released once the scaffolds degraded.

Additionally, the results reveal that higher drug loadings of IBU Na led to an increase in cumulative drug release although it was non-linear relationship. As shown in Table 3.7, IBU Na was released up to 59.54 ± 1.76% from PLGA-IBU Na 5% scaffolds in 60 days. Whilst, less cumulative release was observed in PLGA-IBU Na 2% and PLGA-IBU Na 1% scaffolds at 45.50 ± 11.00% and 35.39 ± 5.18%, respectively.

Considering the location and intensity of IBU Na in Figure 3.16, 3.17 and 3.18, it was obvious that more drug molecules had accumulated on the top surface of scaffolds when amount of drug loading was increased. These hydrophilic drug molecules were ready to be released from the scaffolds. Therefore, a larger burst release was observed from the PLGA scaffolds with higher loading amounts of IBU Na.[136,152]

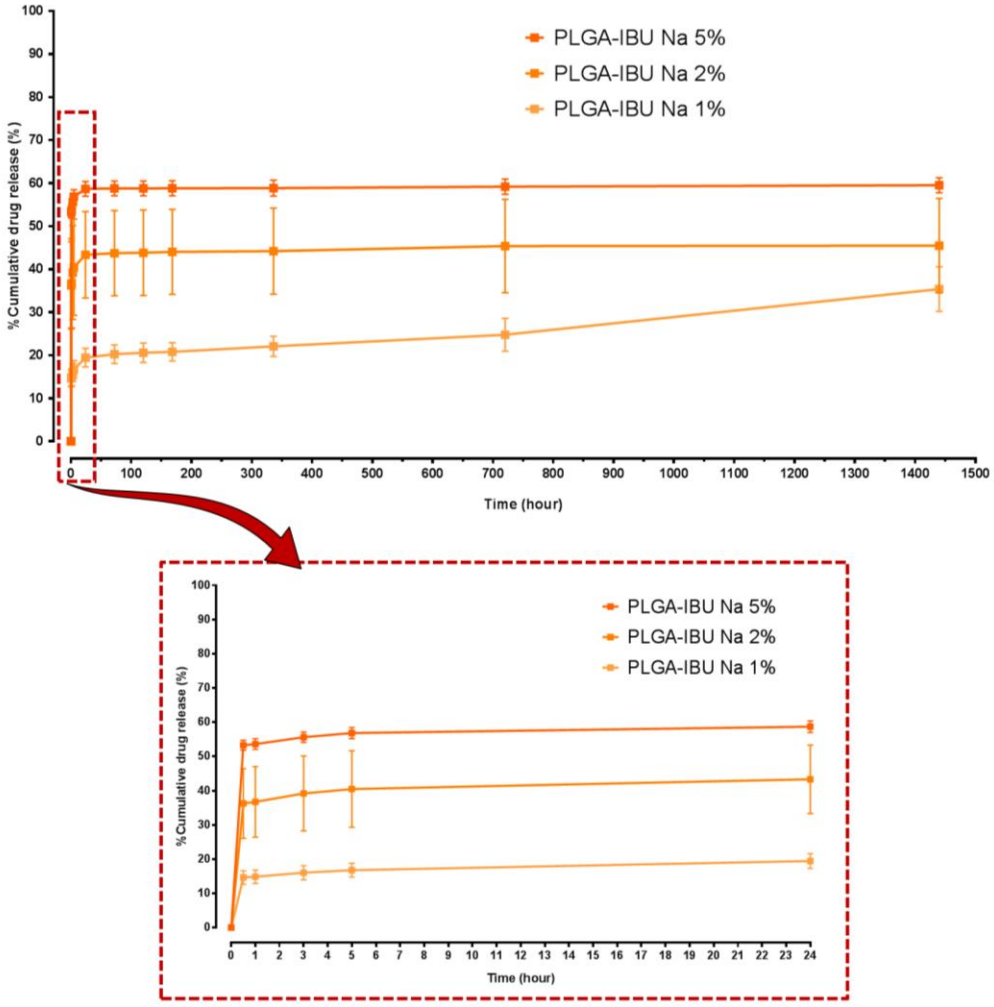


Figure 3.19. Cumulative drug release of IBU Na from PLGA scaffolds in PBS solutions over 60 days (1,440 hours, upper graph) and within the first 24 hours (lower graph). The values represent means and standard deviations of triplicate samples.

Table 3.7. % cumulative drug release of IBU Na from the PLGA scaffolds over 60 days in PBS solutions. The values represent means and standard deviations of % encapsulation efficiency (n = 3).

Scaffold	Cumulative drug release in 60 days (%)
PLGA-IBU Na 1%	35.39 ± 5.18
PLGA-IBU Na 2%	45.50 ± 11.00
PLGA-IBU Na 5%	59.54 ± 1.76

Multiple factors have been reported to cause the burst release of hydrophilic small drug molecules,[153] for example, high drug solubility in media, poor partitioning, and low compatibility between drug and hydrophobic polymers. Hydrophilic drugs with low solubility in non-polar solvent-polymer system have poor partition with polymer. Hence, they preferentially stay on the surface of fibres, resulting in the initial burst release.

Moreover, high ionic strength of the drug itself can influence drug distribution in the fibres. Previous study by Hadjiargyrou *et al*. found that cefoxitin sodium was localised at the surface of fibres due to its high ionic strength, resulting in the burst release of drug.[154]

Conductivity can be employed to estimate ionic strength of a sample as they have a linear relationship. According to the conductivity values measured from PLGA-IBU Na solutions. It can draw to a conclusion that IBU Na is a drug with high ionic strength due to sodium ions. Therefore, IBU Na is more likely to localise at the surface of fibres.

Ionic strength of a solution indicates the concentration of ionic charge in the solution. IBU Na dissociates to give two ions in HFIP: IBU^- and Na^+. During electrospinning, high voltage was applied to the polymer-drug solution, resuting in gathering of positive charges on the surface of polymer-drug jet (*see* Figure 3.20). These positive charges will then attract the negative ions (IBU^-) to migrate to the surface of polymer-drug jet. Sodium ions (Na^+) simultaneously

follow IBU^- to the surface of polymer-drug jet due to the Culombic forces. As a result, IBU Na localises at the surface of PLGA fibres.

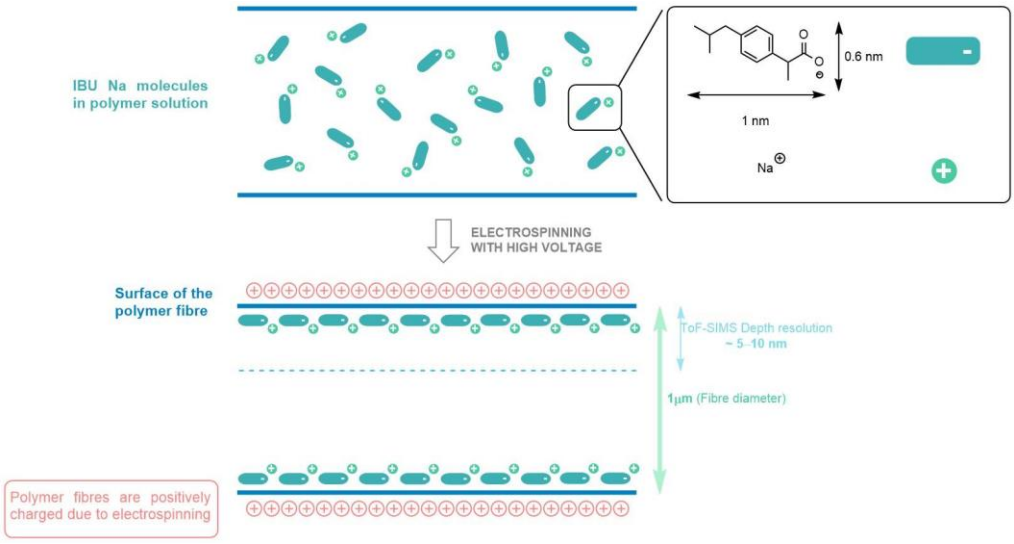


Figure 3.20. Dissociation and migration of ibuprofen sodium to the surface of polymer-drug jet during electrospinning.[155]

The profile of drug release from biodegradable materials generally exhibits as a triphasic release profile: initial burst release, lag phase and second burst release (*see* Figure 3.21).[156,157] An initial burst release is a result of dissolution and distribution of drug deposited at/near the surface of material. Next, the lag phase takes place when the release of drug is observed as a near-zero rate of release. The second burst release links to morphological changes of material. Li *et al* observed pore formation on PLGA-mPEG micro-particles that were incubated in PBS for 5 weeks.[157] Once the pore volume was higher, the uptake of water into micro-particles increased. This enhanced the diffusion of drug from micro-particles into PBS in a concentration gradient fashion. Finally, the second burst release of drug was observed.

The release of IBU Na from PLGA-IBU Na scaffolds is therefore more likely to be a triphasic drug release. The initial burst release of IBU Na was observed within the first 30 minutes after the scaffolds were incubated in PBS. The lag phase was then observed after the initial burst release until day 60 of the study. At day 60, the release of IBU Na from PLGA-IBU Na 1% was obviously increased when compared to day 30, implying that the early stage of second burst release has begun and the remaining drug will be released soon after.

The release of IBU Na can relate to morphological changes of the scaffolds. The morphology of PLGA-IBU Na scaffolds gradually changed from the initial stage over 60 days in PBS (*see* Figure 3.26). It was clearly seen that the morphology of the scaffolds remained unchanged within the first 7 days. This corresponds to the initial burst drug release that was due to the diffusion of drug at/near the surface of fibres not the degradation of the scaffolds. At day 60, the fibres were swollen, which resulted in the diffusion of IBU Na from within the fibres into PBS in a late stage of lag phase. The second burst release of IBU Na was expected to occur from day 90, as the morphology of PLGA-IBU Na scaffolds were changed considerably. However, the drug release study was not carried out after day 60. The second burst release may take longer time to occur and release the remaining drug from the scaffolds.

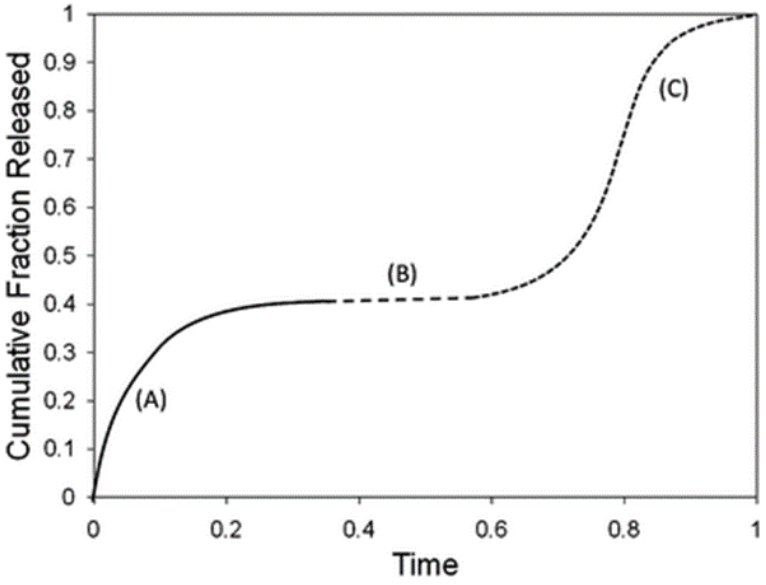


Figure 3.21 Triphasic drug release profile depicting: (A) initial burst release, (B) lag phase and (C) second burst release.[156]

3.5.2.8 PLGA-IBU Na interactions (hydrogen bond and Van der Waals)

The interactions between the drug (IBU Na) and the scaffold (PLGA 8515) were probed by ^{1}H NMR spectroscopy. The investigation started with recording the ^{1}H signals of IBU Na and PLGA8515 in d_6-DMSO separately. The ^{1}H NMR spectrum of IBU Na (Figure 3.22) shows 9 distinct chemical shifts, 7 of which belong to the molecule of IBU Na, and the rest of the signals correspond with water (at 3.33 ppm) and the residual NMR solvent (DMSO, at 2.50 ppm). The doublet peak at 0.84 ppm with an integration of 6 protons corresponds with the hydrogen atoms of the 2 methyl groups (a and c) on the isopropyl moiety. The doublet signal at 1.21 ppm with an integration of 3 protons belongs to the hydrogen atoms on the methyl group (h) adjacent to the aromatic ring. The signal at 1.77 ppm, which appears as a septet, is designated to the hydrogen atom at position b. The doublet of 2 protons at 2.36 ppm is a signal of the hydrogen atoms of the methylene group at position d. The quartet peak at 3.23 ppm of 1 proton well corresponds with the hydrogen atom at position g. The last two peaks at 6.96 and 7.16 ppm, which are a pair of doublets, are for the 4 aromatic protons (e and f) on a *para*-substituted benzene ring.

The ^{1}H spectrum of PLGA8515 in d_6-DMSO (Figure 3.23) clearly shows 3 peaks, which belong to the hydrogen atoms on polymer structure (a', b' and c'), and 2 peaks of water and residual NMR solvent (DMSO) at 3.33 and 2.50 ppm, respectively.

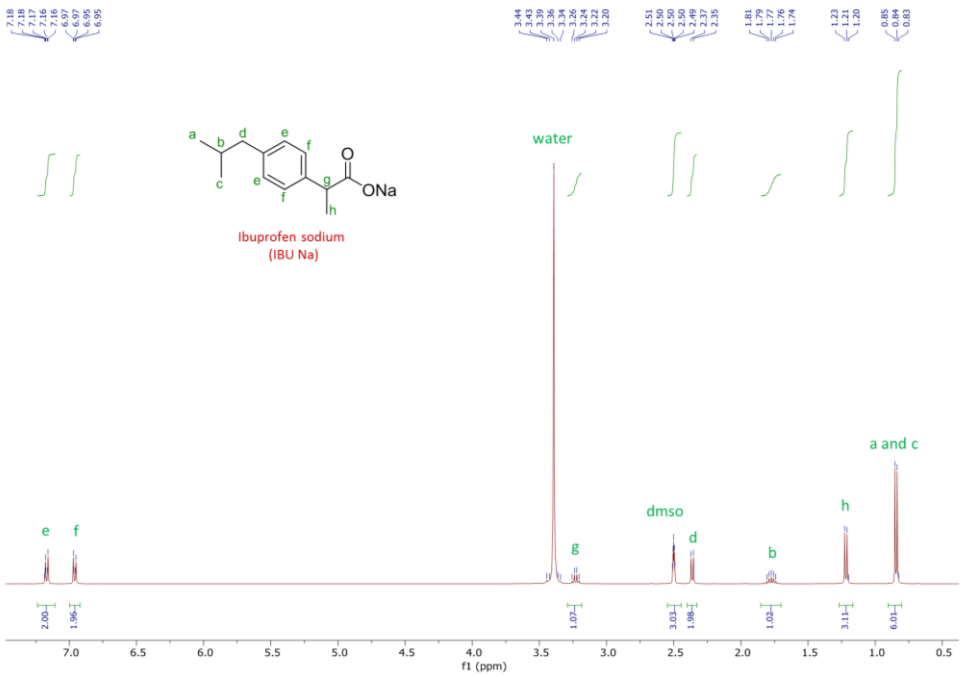


Figure 3.22. ^{1}H NMR spectrum of IBU Na in d_6-DMSO

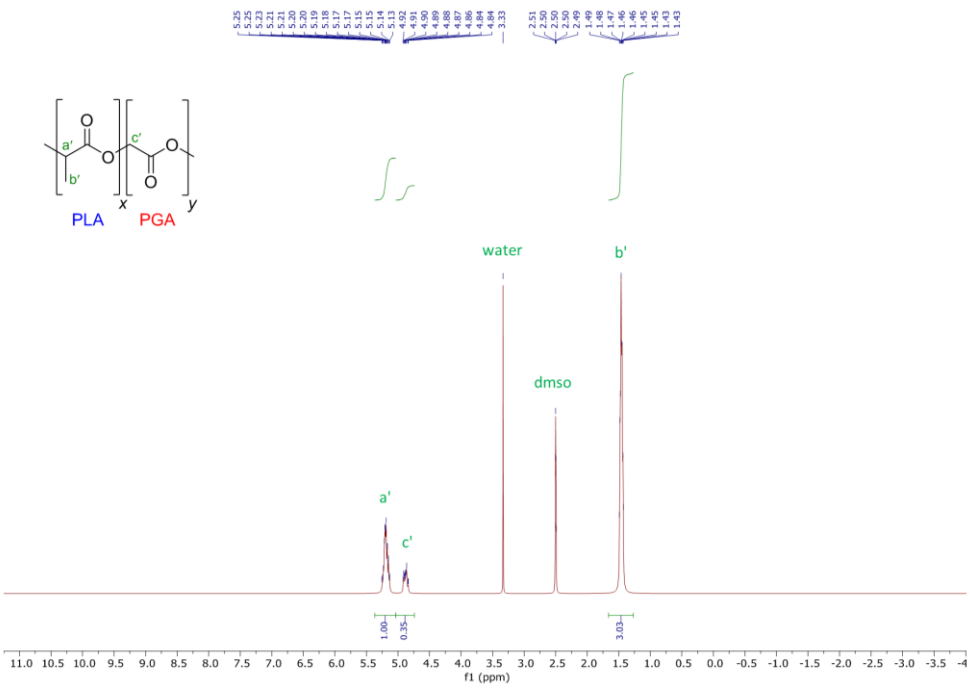


Figure 3.23. ^{1}H NMR spectrum of PLGA 8515 in d_6-DMSO

The ^{1}H NMR spectrum of a mixture of IBU Na and PLGA8515 in d_6-DMSO (blue, Figure 3.24) reveals some significant peak shifts of IBU Na, which indicates the interactions between the drug and the polymer scaffold. Since all NMR samples were prepared in the same NMR solvent at the same concentration, and the spectra were recorded on the same machine under identical conditions, the peak shifts are a result of changes in electronic environments. There are 3 apparent IBU Na peak shifts (red dotted lines, Figure 3.24). Interestingly, Theses 3 signals, corresponding to the hydrogen atoms next the ester group (f, g and h), shift to more deshielded regions (towards left hand side). This suggests the stage of more electron deficient environment when compared with the authentic sample (maroon). This could indicate that the ester group of IBU Na acts as an electron donor and interacts with the proximal polymer network. As a consequence, the overall electron density on the IBU Na molecule decreases. The peak shift effect can be observed more clearly on the hydrogen atoms closer to the ester unit, and gradually disappears when the hydrogen atoms are further way from the ester group.

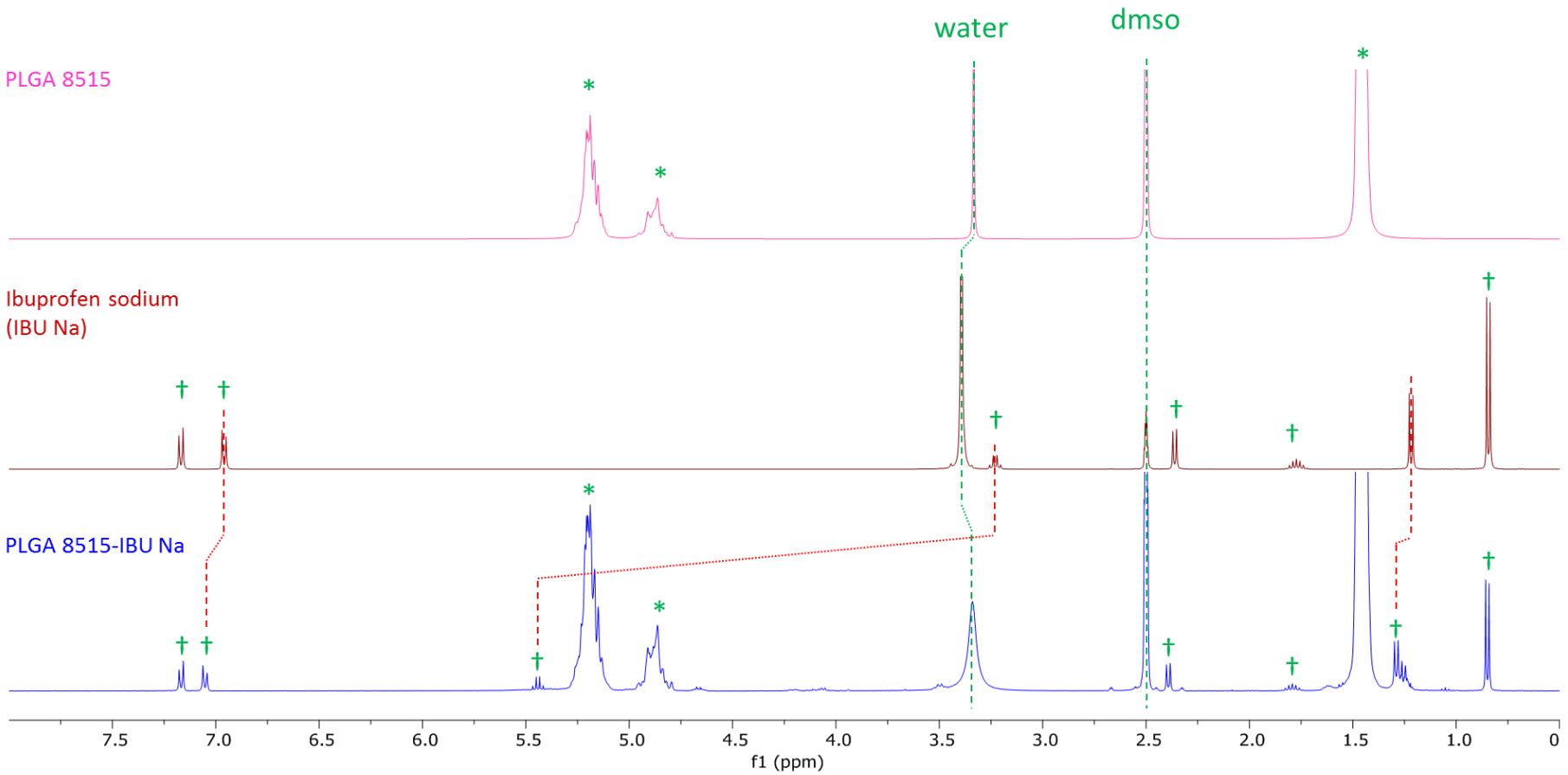


Figure 3.24. Significant peak shifts (red dotted lines) of IBU Na in PLGA8515-IBU Na 5% scaffolds indicative of molecular interactions between the polymer scaffold and the drug. * represents peaks of PLGA 8515, and † represents peaks of IBU Na.

3.5.2.9 Degradation profile of the scaffolds

The *in vitro* degradation of the scaffolds was studied by incubating the scaffolds in PBS solutions (pH 7.4) at 37 °C over time. At predetermined time points, % weight loss and fibre morphology were evaluated. The trend and level of weight loss over 90 days can be found in Figure 3.25 and Table 3.8. Figure 3.26 illustrates representative SEM images of the scaffolds over time.

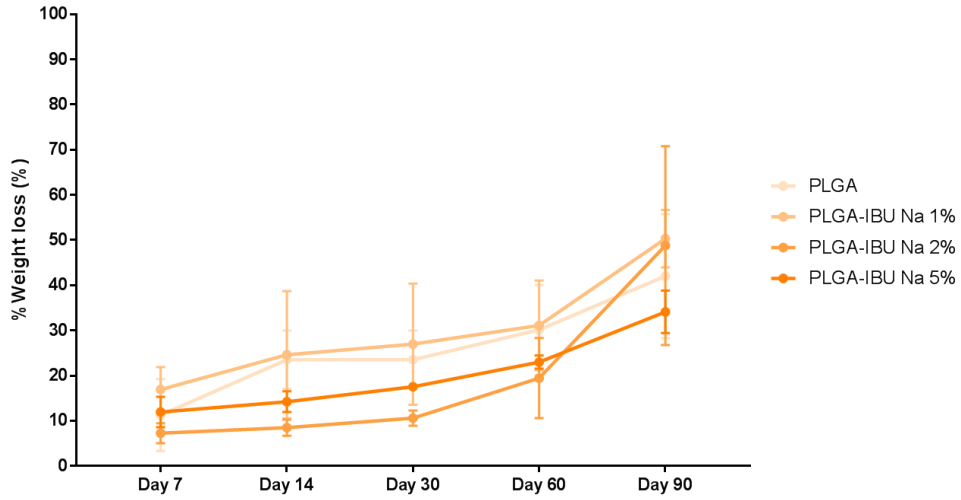


Figure 3.25. Degradation profile of the scaffolds in PBS solution (pH 7.4) shown as % weight loss. The values shown in the graph are mean ± SD of triplicate samples.

Table 3.8. % Weight loss of the scaffolds over time determined in the *in vitro* degradation study. The values are mean ± SD of triplicate samples.

Time point	% Weight loss			
	PLGA	PLGA-IBU Na 1%	PLGA-IBU Na 2%	PLGA-IBU Na 5%
Day 7	11.27 ± 7.95	16.92 ± 4.95	7.25 ± 2.20	11.94 ± 3.36
Day 14	23.52 ± 6.44	24.62 ± 14.05	8.47 ± 1.79	14.23 ± 2.29
Day 30	23.52 ± 6.44	26.97 ± 13.41	10.59 ± 1.67	17.54 ± 0.60
Day 60	30.12 ± 9.95	31.09 ± 9.95	19.45 ± 8.86	22.99 ± 1.44
Day 90	42.02 ± 13.73	50.32 ± 6.36	48.79 ± 22.05	34.12 ± 4.69

Although the change in morphology of the scaffolds was not obvious within 14 days of the study, the weight of the scaffolds decreased slightly by 8 to 24% of the initial weight. At 30 and 60 days of the study, the morphology of scaffolds changed. The fibres were swollen and fused together in most areas of the scaffolds. The further reduction of weight was also observed.

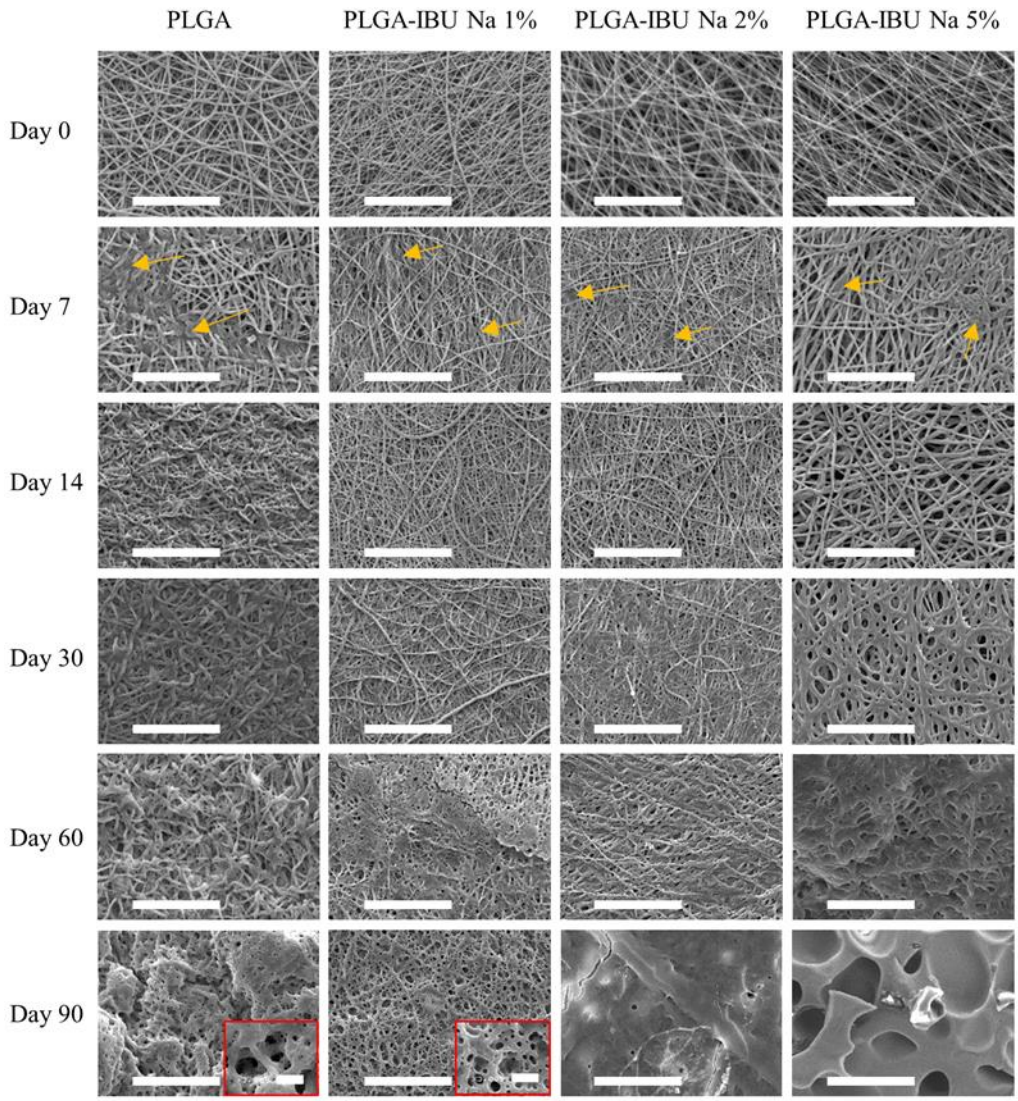


Figure 3.26. Representative SEM images showing morphological changes of the scaffolds over time. All images are illustrated at the magnification of 1,000X. The scale bar is 50 µm. Arrows are used to point areas where changes in morphology of the scaffolds were observed. SEM images in red windows are showed scaffolds' morphology at the magnification of 3,000X. The scale bar is 5 µm.

The degradation study was carried out further to day 90 when the morphology of the whole scaffolds drastically changed. Fusion of fibres in PLGA and PLGA-IBU Na 1% scaffolds created thick porous structures. While, PLGA-IBU Na 2% and PLGA-IBU Na 5% scaffolds lost their fibrous structural integrity, forming thick packed constructs. The scaffolds were eventually lost 34-50% of their weights at this time point.

The degradation of PLGA in aqueous environments occurs through hydrolysis of its ester linkages which can be describe in 4 steps.[125] Firstly, water penetrates into the amorphous region and disrupts the van der Waals forces and hydrogen bonds, causing a decrease in the glass transition temperature. Secondly, the initial degradation begins with the cleavage of covalent bonds, resulting in decreased molecular weight. Next, carboxylic end groups auto-catalyse the degradation process, and massive cleavage of the backbone covalent bonds continued which results in loss of mass and integrity. Lastly, the fragments are further cleaved to molecules that are soluble in the aqueous environment.

The degradation of PLGA8515 has been reported to be in the range of 4–6 months.[97] Nevertheless, the electrospun scaffolds fabricated from PLGA8515 degraded much faster than expected. This may be due to the high surface area and porous structure of the scaffolds that allows more water to infiltrate, and undergo ester hydrolysis, resulting in the faster degradation of PLGA.

IBU Na was likely to expedite the degradation of the scaffolds but not in a linear relation to the amount of drug loaded. It has been previously reported that

ibuprofen could accelerate the breakdown of ester linkages in PLGA backbone through acid catalysis, resulting in faster degradation.[90]

3.5.3 Cytotoxic concentration of IBU Na

To evaluate the cytotoxicity of IBU Na, mouse fibroblasts and primary human dermal fibroblasts were treated with different concentrations of IBU Na in cell culture media and cell viability was determined using PrestoBlue® assay.

As observed in Figure 3.27A and 3.27B, IBU Na exhibited a cytotoxic effect at the concentration of 10,000 µM in both cell types. Less than 25% of cells were viable after being treated with such drug concentration. In contrast, the viability of both mouse and primary human fibroblasts remained above 90% when cells were treated with IBU Na in the concentration range of 1–1,000 µM, which agrees with what has been reported the literature.[90]

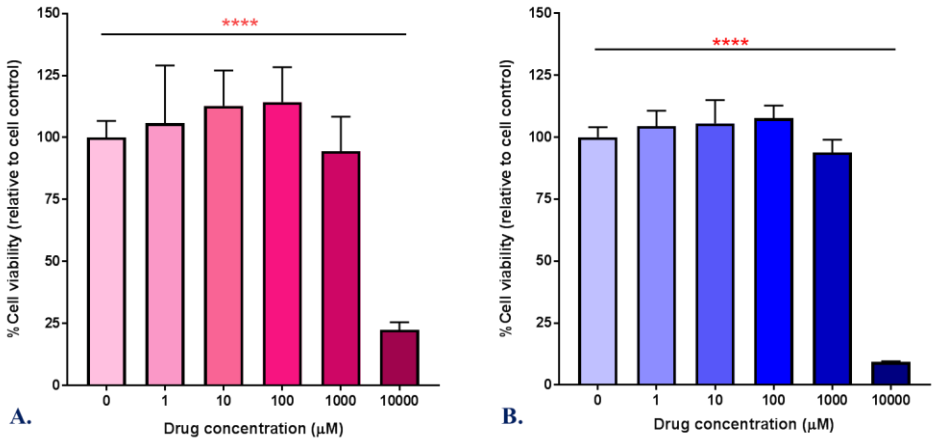


Figure 3.27. Cytotoxic effect of IBU Na was evaluated by PrestoBlue® assay to assess metabolic activity of cells after being treated with complete cell culture media containing IBU Na at different concentrations ranging from 0 to 10,000 µM for 24 hours. **** defines a statistical significant difference when compared to cell control (*p*-value < 0.0001). (A) Mouse fibroblasts (n = 6/concentration) and (B) Primary human dermal fibroblasts (n = 3/concentration).

3.5.4 Cell proliferation study

3.5.4.1 Cellular metabolic activity by PrestoBlue® assay

The metabolic activity of mouse fibroblasts proliferating on the scaffolds was studied using PrestoBlue® assay. Tissue culture plastic (TCP) served as a 2D control while PLGA scaffolds were used as a 3D control for IBU Na-loaded scaffolds. The metabolic activity of cells determined by PrestoBlue® assay can imply the number of viable cells on the scaffolds as only viable cells can reduce non-fluorescent, cell permeable resazurin (blue colour) into highly fluorescent resorufin (red colour). The results in Figure 3.28 shows that mouse fibroblasts could proliferate on the scaffolds as fluorescence intensity was increasing over time. The significant difference in cell proliferation was observed on day 3 between PLGA and PLGA-IBU Na 5% scaffolds. At day 5 of the study, lower cellular metabolic activity was noticed from PLGA-IBU Na 2% and PLGA-IBU Na 5% scaffolds when compared to PLGA scaffolds. At 7 days of cell culture on the scaffolds, the highest cellular metabolic activity was observed from PLGA scaffolds when compared to all IBU Na-loaded scaffolds. However, the comparable cellular metabolic activity among the scaffolds was observed on day 14 of cell culture.

Figure 3.29 illustrates the fold change in fluorescence intensity at different time points in relative to the fluorescence intensity of day 1, representing the increase in metabolic activity of 3T3 cells. The results agree with the pattern observed in Figure 3.26 that the metabolic activity of 3T3 cells on the scaffolds was increasing over time. The proliferation of 3T3 cells was significantly lower when the loadings of IBU Na into PLGA scaffolds were higher.

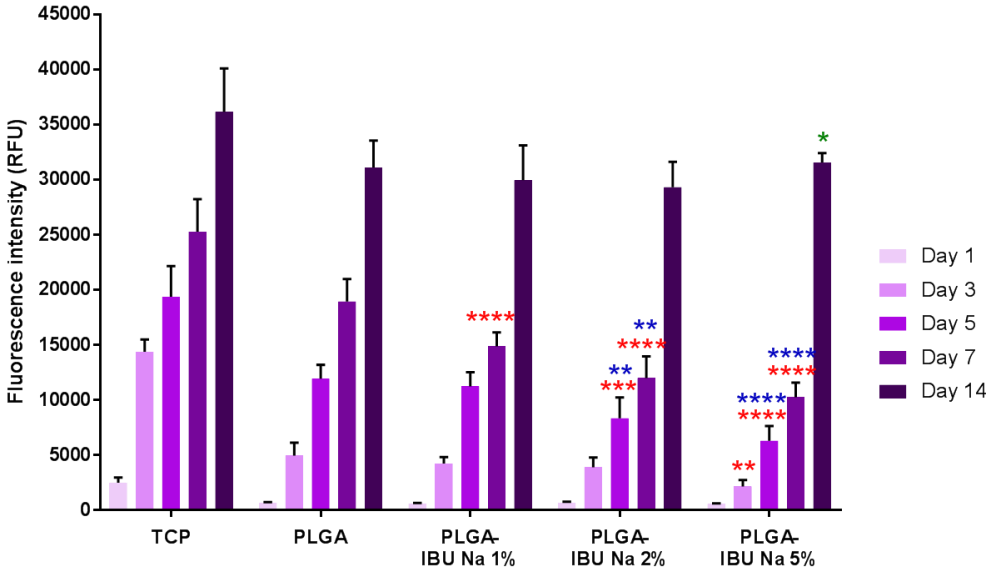


Figure 3.28. Cell proliferation on TCP, PLGA, PLGA-IBU Na 1%, PLGA-IBU Na 2% and PLGA-IBU Na 5% electrospun scaffolds determined by cellular metabolic activity of mouse fibroblasts (3T3 cells) over 14 days using PrestoBlue® assay. The values are shown as means and standard deviations (n = 6). *, **, *** and **** define a significant difference between the scaffolds at the same time point at *p*-value < 0.05, < 0.01, < 0.001 and < 0.0001, respectively. Red, blue and green asterisks were used to indicate the significance when compared to PLGA, PLGA-IBU Na 1% and PLGA-IBU Na 2% scaffolds, respectively.

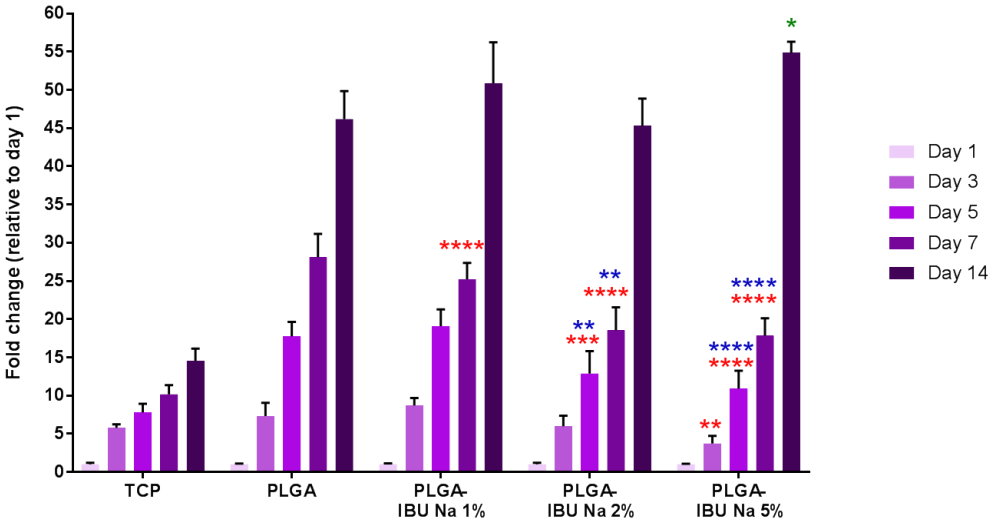


Figure 3.29. Fold change in cell proliferation on TCP, PLGA, PLGA-IBU Na 1%, PLGA-IBU Na 2% and PLGA-IBU Na 5% electrospun scaffolds determined by cellular metabolic activity of mouse fibroblasts (3T3 cells) over 14 days using PrestoBlue® assay. The values are shown as means and standard deviations (n = 6). *, **, *** and **** define a significant difference between the scaffolds at the same time point at *p*-value < 0.05, < 0.01, < 0.001 and < 0.0001, respectively. Red, blue and green asterisks were used to indicate the significance when compared to PLGA, PLGA-IBU Na 1% and PLGA-IBU Na 2% scaffolds, respectively

Metabolic activity of cells was lower on the electrospun scaffolds in comparison with TCP on day 1. This was due to cell loss from the seeding step on the 3D structures. Moreover, the release of IBU Na into cell culture media may affect cell viability after seeding. If IBU Na was totally released, the concentration of IBU Na in cell culture media was estimated to be 180, 465 and 1,860 µM in PLGA-IBU Na 1%, PLGA-IBU Na 2% and PLGA-IBU Na 5% scaffolds, respectively. Although the concentration did not reach the cytotoxic dose (10,000 µM), seeding cells on the drug-enriched surface of fibres may reduce the cell viability.

Riggin *et al*. (2017) found that the release of ibuprofen (acid form) from PLGA7525 electrospun scaffolds in serum was faster and higher than in PBS.[136] It potentially is the case that the release of IBU Na was accelerated by serum in cell culture media, resulting in less drug content in the fibres in the later days of the study. As a consequence, cells could proliferate more on IBU Na-loaded fibres.

3.5.4.2 LIVE/DEAD® assay

Images taken from the LIVE/DEAD® assay have been pooled in Figure 3.30, 3.31 and 3.32 to confirm the presence and proliferation of mouse fibroblasts on the scaffolds in a timely manner. The increasing number of viable cells was indicated by higher intensities of green fluorescence that were visualised on the electrospun fibres, supporting biocompatibility of the scaffolds.

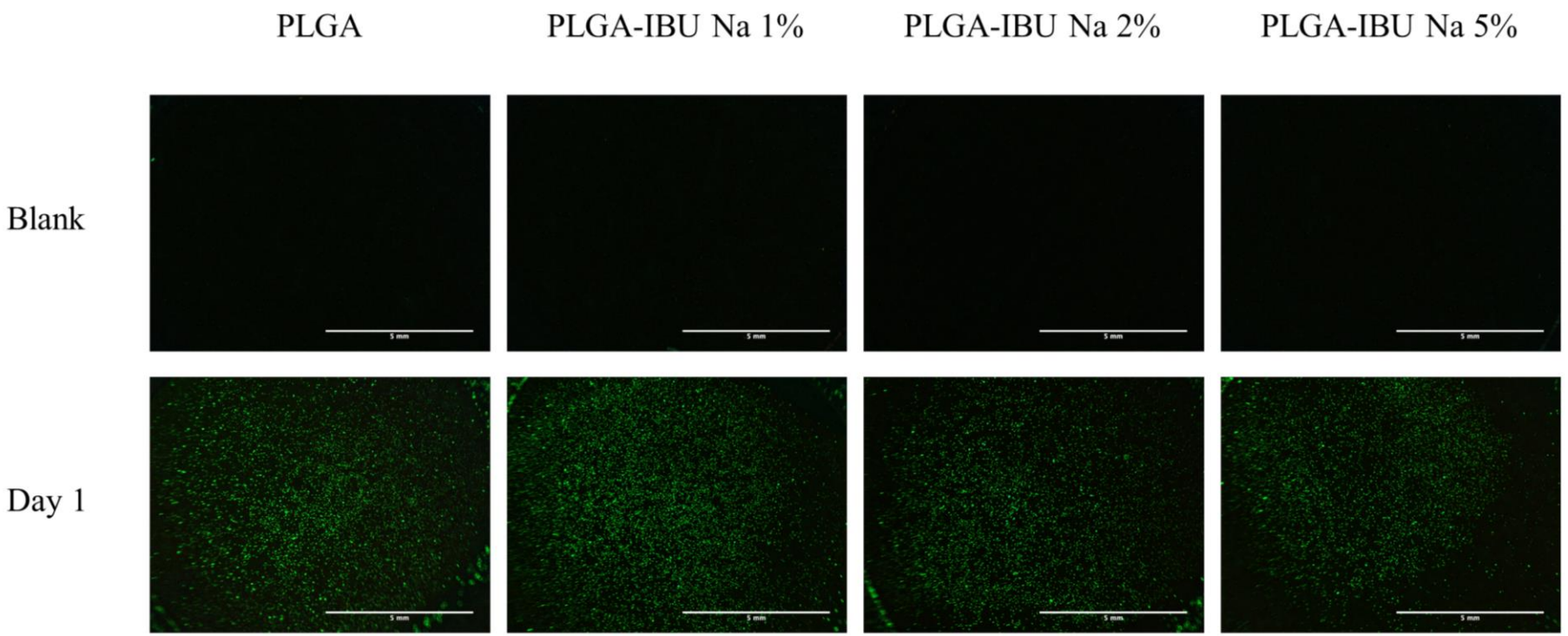


Figure 3.30. Representative fluorescent images obtained from the LIVE/DEAD® assay illustrating the blank scaffolds (without cells), and the presence of viable (green) and dead (red) mouse fibroblasts on the surface of the electrospun scaffolds on day 1 of cell culture. All images are shown at the magnification of 2X and the scale bar is 5 mm.

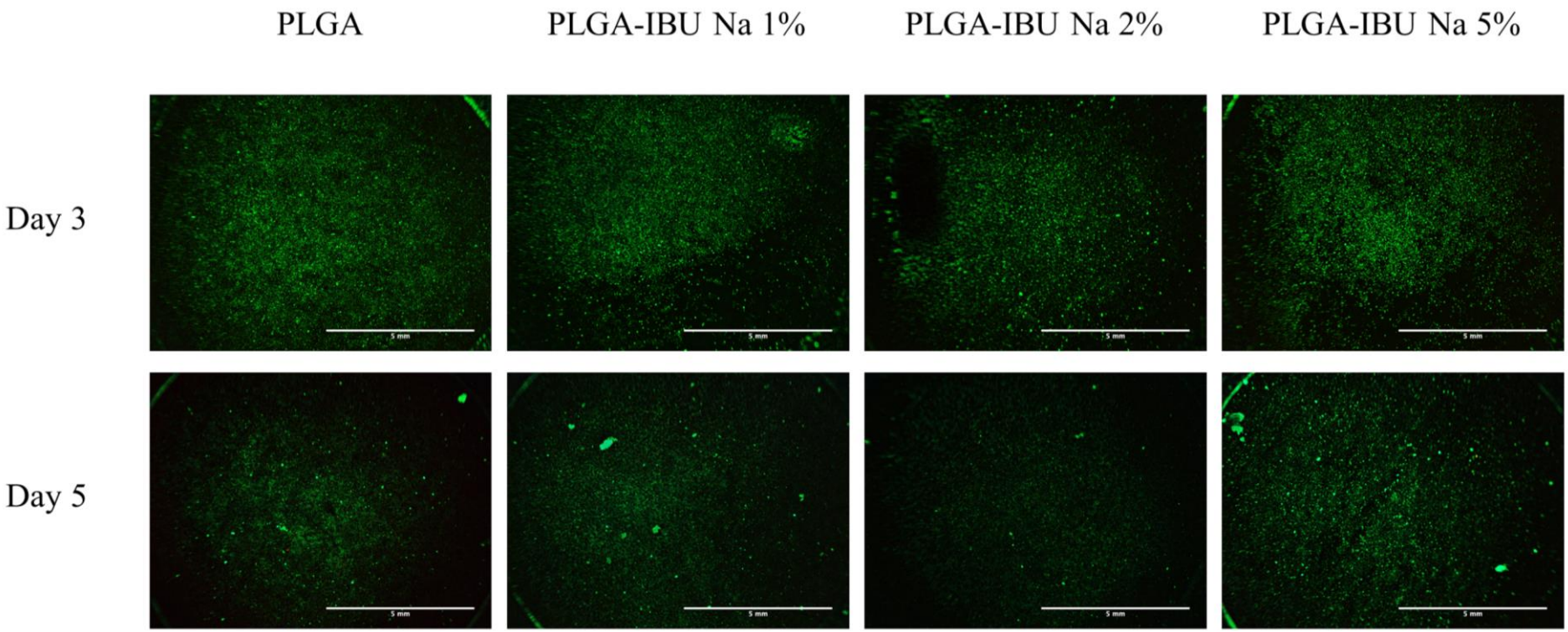


Figure 3.31. Representative fluorescent images obtained from the LIVE/DEAD® assay illustrating the presence of viable (green) and dead (red) mouse fibroblasts on the surface of the electrospun scaffolds on day 3 and day 5 of cell culture. All images are shown at the magnification of 2X and the scale bar is 5 mm.

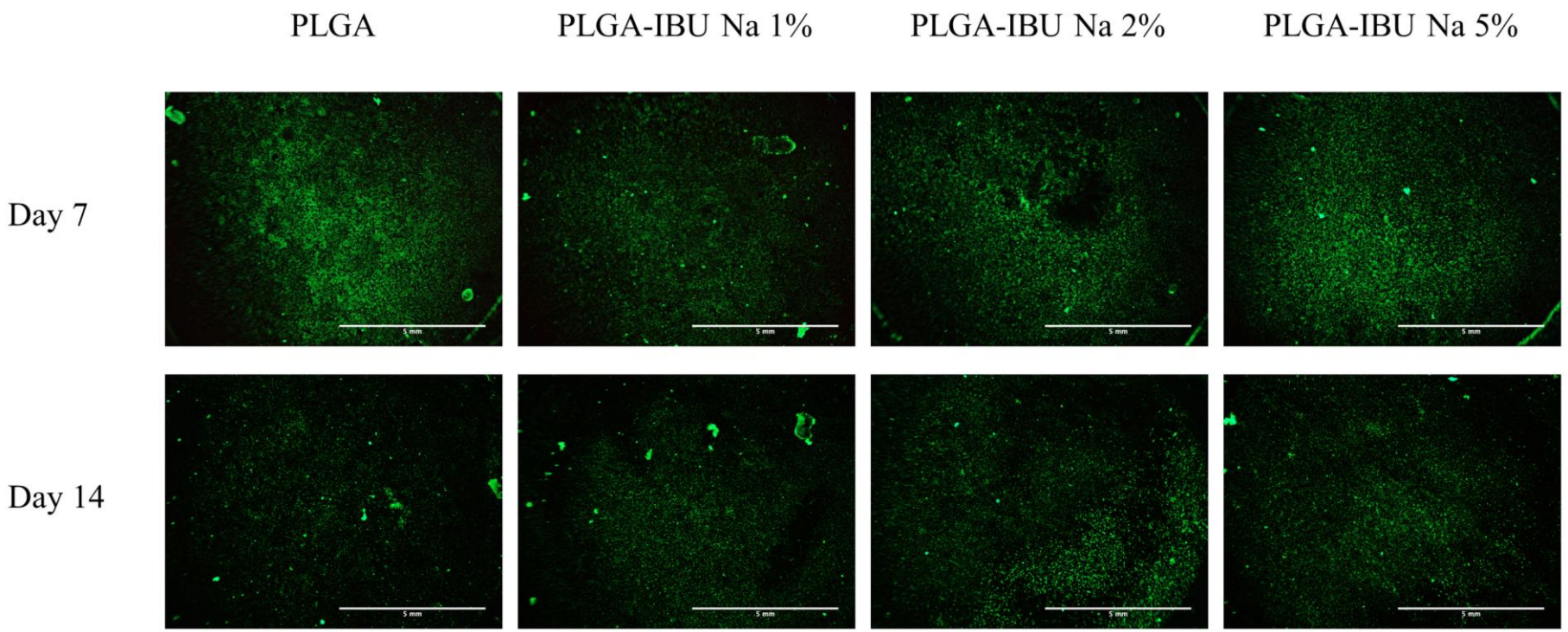


Figure 3.32. Representative fluorescent images obtained from the LIVE/DEAD® assay illustrating the presence of viable (green) and dead (red) mouse fibroblasts on the surface of the electrospun scaffolds on day 7 and day 14 of cell culture. All images are shown at the magnification of 2X and the scale bar is 5 mm.

3.5.4.3 Cell morphology

The morphology of mouse fibroblasts cultured on the scaffolds was revealed by SEM imaging (Figure 3.33). On day 1 post-seeding, a rounded morphology of mouse fibroblasts was observed. Cells attached to the scaffolds by wrapping themselves around the nearby fibres.

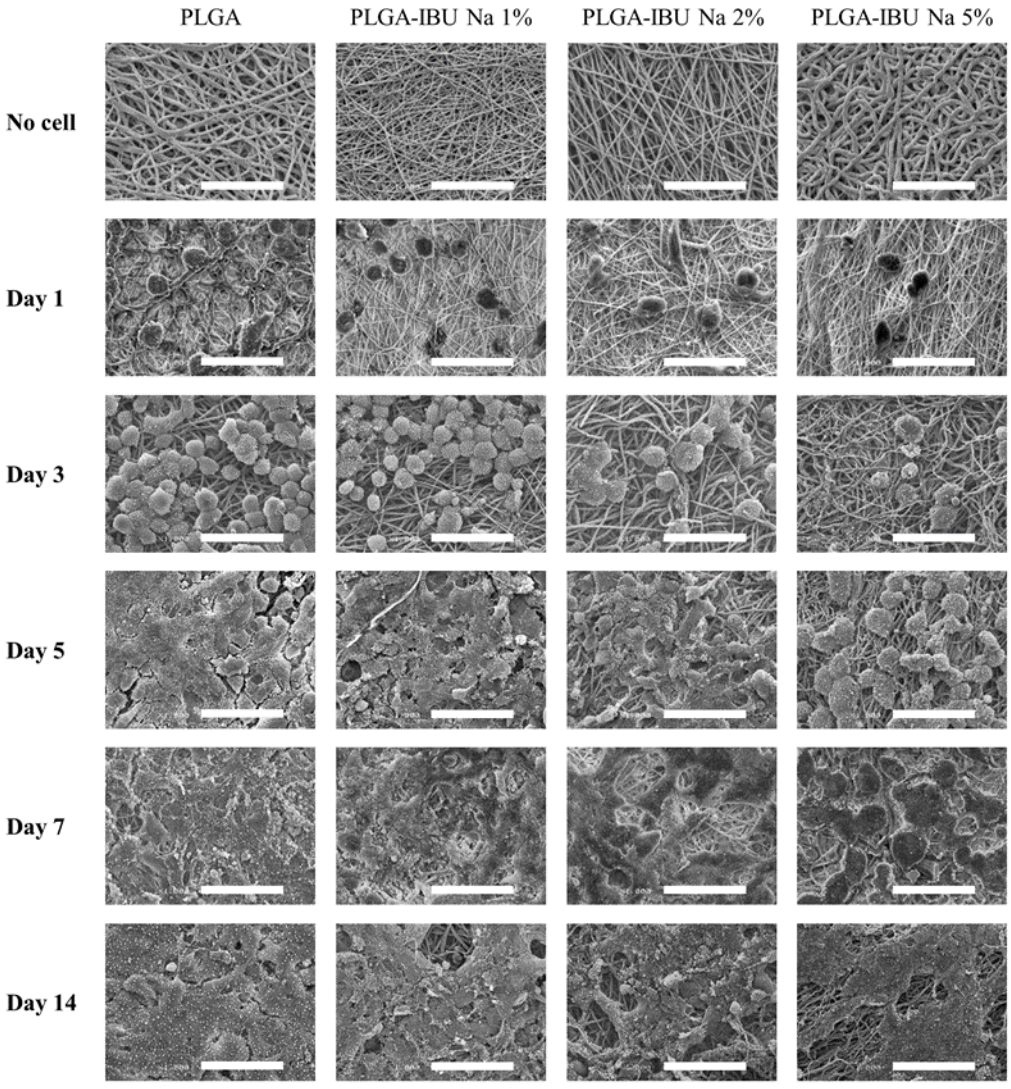


Figure 3.33. Representative SEM images showing cell morphology of mouse fibroblasts on the electrospun scaffolds at the magnification of 1,000X (scale bar 50 µm).

The number of cells on the scaffolds increased over time, indicating the ability of the scaffolds to support cell proliferation. Nevertheless, the scaffolds with higher drug loadings retarded the proliferation of cells when compared to lower drug loaded-scaffolds and blank PLGA scaffolds.

Once cells were reaching approximately 70–80% confluence, they started forming a cluster of cells. At day 5 of cell culture, the morphology of mouse fibroblasts on PLGA, PLGA-IBU Na 1% and PLGA-IBU Na 2% scaffolds gradually changed into a spindle-liked morphology. At day 7 of cell culture, the surface area of the scaffolds was almost fully covered by fibroblasts especially PLGA and PLGA-IBU Na 1% scaffolds. Therefore, new dividing cells were growing on top of previous cell monolayers and forming stacks of cell layers.

The morphology of 3T3 cells on the scaffolds was rounded. This was due to random orientation of fibres in the scaffolds.[158] The size of pores between these fibres is small, resulting in a decrease in cell contact area. Hence, cells do not elongate on fibres but adhere to several nearby fibres and spread in all directions. As a result, a rounded morphology with random orientation of cells was observed. In addition, PLGA lacks of cell recognition site for cell attachment. Although cell adhesion occurs, the spreading of cells on the surface of PLGA scaffolds requires longer time.[159–161]

Furthermore, hydrophobicity of the scaffolds can prevent cell-material interactions. Asadian *et al* reports that human foreskin fibroblasts seeded on PCL fibres are rounded and have poor interaction with fibres.[162] Whilst,

fibroblasts that are seeded on the surface modified PCL fibres (plasma surface treatment) have spread morphology. This was due to the increasing hydrophilicity after plasma surface treatment. PLGA and PLGA-IBU Na scaffolds in this study have hydrophobic surface. Therefore, the cell-material interaction is poor and the morphology of 3T3 cells is rounded.

3.5.4.4 Cell infiltration into the structure of electrospun scaffolds

Figure 3.34 represents the images taken by a confocal microscope, showing the location of cell nuclei (blue colour). It is evident that mouse fibroblasts could not infiltrate into the structure of the electrospun scaffolds. Although the electrospun scaffolds have a porous structure and the ability to promote cell proliferation, mouse fibroblasts only adhered and proliferated on the surface of the scaffolds. This finding was also confirmed with the SEM images of the cross-sectional region of the scaffold, shown in Figure 3.35A–C. Cells proliferated and formed cell stacks on the top surface of the scaffolds without infiltrating into the structure.

This potentially relates to the shrinkage of the scaffolds when immersed in an aqueous environment as the inter-fibre pores were too small for cell infiltration.[163,164] Cells also prefer to live in the nutrient-rich environment, where the scaffold-cell media interface is.

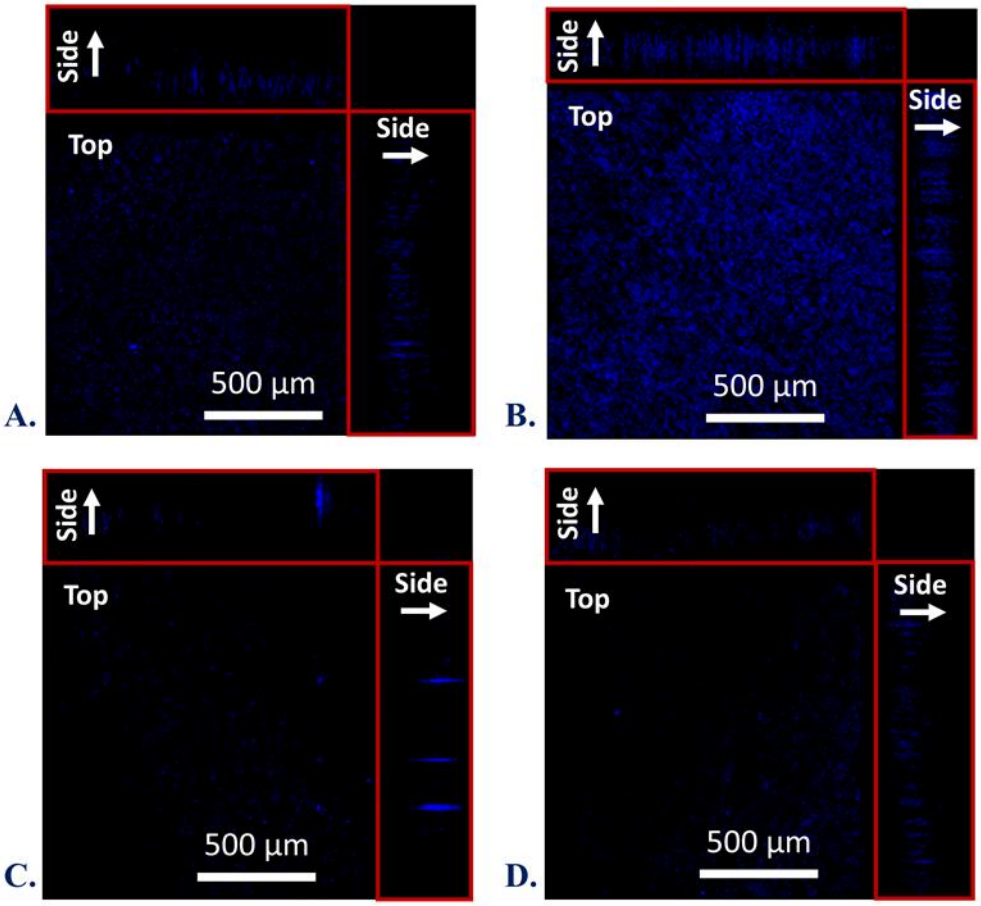


Figure 3.34. Confocal micrographs of mouse fibroblasts (3T3 cells) adhered and proliferated on various electrospun scaffolds at day 14 of cell culture. (A) PLGA, (B) PLGA-IBU Na 1%, (C) PLGA-IBU Na 2% and (D) PLGA-IBU Na 5%. All images were taken at the magnification of 10X. The scale bar is 500 µm. Red windows show cell infiltration from side view.

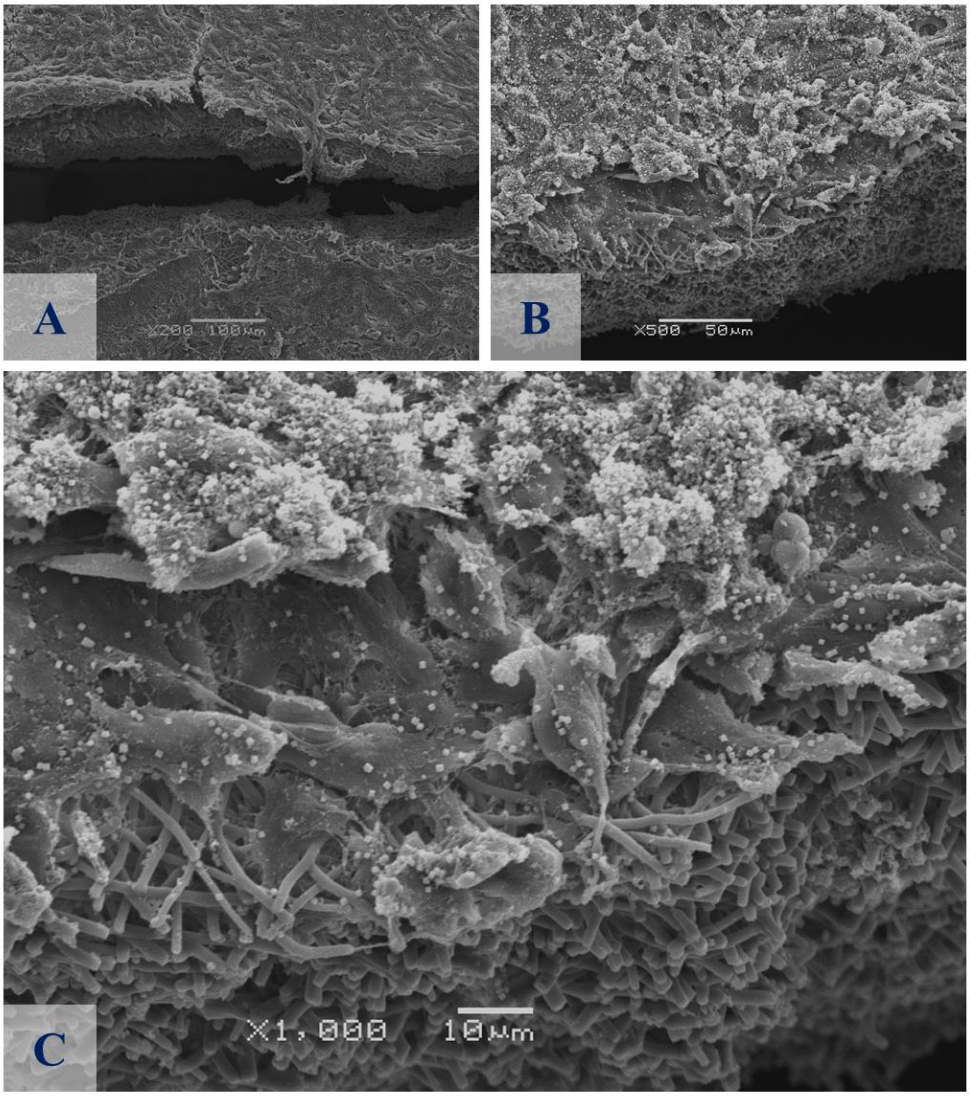


Figure 3.35. Representative SEM images of mouse fibroblasts on the PLGA scaffolds after being cultured for 14 days at various magnifications; (A) 200X (scale bar 100 µm), (B) 500X (scale bar 50 µm), and (C) 1,000X (scale bar 10 µm).

Due to limited resources, primary human dermal fibroblasts have not been examined with the scaffolds developed in this chapter. However, similar outcomes observed in the study with mouse fibroblasts are predicted. This is due to the similar cell response in a same manner found in the cytotoxicity study. Additionally, the study from the MacNeil research group has demonstrated the compatibility and ability of PLGA scaffolds loaded with 1–10% w/w ibuprofen (acid form) to promote the proliferation of primary human dermal fibroblasts.[90]

Table 3.9. Summary of scaffolds' properties

Property	PLGA	PLGA-IBU Na 1%	PLGA-IBU Na 2%	PLGA-IBU Na 5%
Fibre diameter (µm)	1.20 ± 0.28	1.14 ± 0.22	1.11 ± 0.20	0.98 ± 0.23
Porosity (%)	55.83 ± 0.27	77.53 ± 0.53	79.00 ± 1.22	78.05 ± 0.77
Water contact angle (static)	93.93 ± 10.01	93.33 ± 6.50	100.29 ± 7.81	N/A
Water contact angle (advancing)	103.57 ± 3.68	102.63 ± 1.12	109.68 ± 4.31	N/A
Water contact angle (receding)	22.52 ± 1.57	26.73 ± 2.78	28.10 ± 0.38	N/A
Contact angle hysteresis	81.04 ± 2.61	75.90 ± 3.65	81.58 ± 4.23	N/A
Ultimate tensile strength (MPa)	4.11 ± 0.45	5.15 ± 0.74	2.34 ± 0.11	1.43 ± 0.29
Strain at break (%)	285.31 ± 13.10	107.09 ± 24.74	156.87 ± 8.19	4.50 ± 0.42
Young's modulus (MPa)	155.29 ± 11.34	96.09 ± 39.73	26.37 ± 3.58	41.35 ± 5.16
Encapsulation efficiency (%)	N/A	46.92 ± 6.92	55.11 ± 2.23	64.51 ± 1.69
Cumulative drug release in 60 days (%)	N/A	35.39 ± 5.18	45.50 ± 11.00	59.54 ± 1.76
Drug localisation	N/A	Surface	Surface	Surface
Drug-polymer interaction	N/A	Weak	Weak	Weak
Cumulative weight loss in 90 days (%)	42.02 ± 13.73	50.32 ± 6.36	48.79 ± 22.05	34.12 ± 4.69
Cell proliferation on the scaffolds	Yes	Yes	Yes	Yes
Cell infiltration	No	No	No	No

N/A: not applicable

3.6 Conclusion

Prolonged inflammation is a significant underlying cause of delayed wound healing in chronic skin wounds. In addition, it causes pain, affecting patients' quality of life both physically and psychologically, and also wound management. Electrospun scaffolds produced from biocompatible and biodegradable materials have been widely studied and used as dressings to support wound healing. To modulate the inflammation, NSAIDs such as ibuprofen have been incorporated into the electrospun scaffolds, serving as a local drug delivery system.

In this chapter, anti-inflammatory drug-loaded electrospun scaffolds were fabricated from biocompatible and biodegradable PLGA polymer blended with IBU Na at different drug loadings. Incorporation of IBU Na affected the properties of PLGA solutions by decreasing viscosity and increasing conductivity. These changes resulted in a smaller fibre diameter.

Other properties of PLGA scaffolds were also affected by the incorporation of IBU Na. Firstly, porosity of the scaffolds was increased in IBU Na-loaded PLGA scaffolds as the drug generated repulsive forces between fibres. The mechanical strength, strain at break and elasticity of the scaffolds were found to drop after the addition of IBU Na. At 5% drug loading, the scaffolds lost their plasticity and became brittle. However, the mechanical strength of these scaffolds were in the range reported for the human skin. The surface of these scaffolds exhibited hydrophobic properties as their contact angles were greater than 90 degrees when determined by static water contact angle measurement,

excluding PLGA-IBU Na 5% scaffolds; such scaffolds were completely wetted by water. The hydrophobic surface of the scaffolds was the result of surface roughness.

The ability of the scaffolds to be drug carrier was evaluated by various studies. Higher drug loadings of IBU Na into PLGA scaffolds resulted in both higher encapsulation efficiency and cumulative drug release. These are due to the deposition of IBU Na on the top surface of fibres as well as the loose interaction between the drug and PLGA as confirmed by ToF-SIMS and NMR analysis, respectively. Weight of the scaffolds reduced by 34–50% after the incubation in PBS for 90 days and PLGA-IBU Na 2% and PLGA-IBU Na 5% scaffolds completely lost their fibrous structure.

The scaffolds have been shown to be promising in terms of supporting cell proliferation of mouse fibroblasts as the higher metabolic activity of cells as determined by PrestoBlue® assay and the presence of more viable cells as dertermined by LIVE/DEAD® assay were observed. Higher drug loadings of IBU Na led to the initial lower cellular metabolic activity and less number of cells on the scaffolds when compared to PLGA scaffolds without or with less amount of drug. However, all PLGA-IBU Na scaffolds could promote cell proliferation after 14 days. Although successful cell attachment and proliferation were achieved, cell infiltration was not observed with these scaffolds. Taking all into account, the fabrication of IBU Na loaded PLGA scaffolds was successful. The characterisation confirmed that the scaffolds were able to release drug whilst promote cell proliferation of fibroblasts.

Chapter 4

Fabrication and Characterisation of Doxycycline Hydrochloride-loaded PCL Electrospun Scaffolds

4.1 Introduction

Matrix metalloproteinases (MMPs) are a family of zinc-dependent enzymes, degrading ECM components.[165] Humans have 23 types of MMPs which can be sub-classified into 6 groups: collagenases, gelatinases, stromelysins, matrilysins, membrane-type MMPs, and other non-classified MMPs (Table 4.1).[166]

In normal physiology, MMPs maintain homeostasis of the skin by degrading or remodelling ECM to allow the migration of cells, the deposition of new ECM components, and the formation of new tissue.[167] The expression of MMPs in keratinocytes and dermal fibroblasts are not constitutive, but can be induced temporarily in response to exogenous signals such as inflammatory cytokines, growth factors, oxidative stress, UV radiation and hormones (*e.g.* IL-1, IL-6, TNF-α, TGF-β, EGF, PDGF, and bFGF).[165,168,169]

The activity of MMPs are counterbalanced and highly regulated by their natural inhibitors known as tissue inhibitors of metalloproteinases (TIMPs).[165,169]

Table 4.1. Classification of matrix metalloproteinases (MMPs), their biological effects and substrates[170]

MMP classification			Biological effect	Group of substrates for enzymes
Group	**Traditional classification**	**Numerical classification**		
Collagenases	Collagenase-1	MMP-1	• Migration of keratinocytes • Re-epithelialization • Cell migration • Platelet aggregation • Cell proliferation • Pro-inflammatory effect	• Collagen (I, II, III, VII, VIII, X) • Casein • Entactin • Pro-MMP-1, -2, -9 • Serpins
	Collagenase-2	MMP-8	• The activation of osteoclasts • The enhancement of collagen affinity • β-FGF release • Anti-inflammatory activity	• Collagen (I–III, V, VII, VIII, X) • Gelatin • Aggrecan • Fibronectin
	Collagenase-3	MMP-13	• Cell migration	• Collagen (I, II, III, IV) • Gelatin
Gelatinases	Gelatinase A	MMP-2	• Enhancement of collagen affinity • Cell proliferation • Migration of epithelial cells • Anti-inflammatory activity • An increase in the bioavailability of TGF-β	• Gelatin • Collagen (I , IV–VI, X, XI, XIV) • Elastin • Fibronectin
	Gelatinase B	MMP-9	• Enhancement of collagen affinity • Pro-inflammatory effect • Anti-inflammatory activity	• Gelatin • Collagen (IV, V, VII, X, XIV) • Elastin • Fibrillin

MMP classification			Biological effect	Group of substrates for enzymes
Group	Traditional classification	Numerical classification		
Stromelysins	Stromelysin-1	MMP-3	• Migration of cells • Epithelial cells apoptosis • The collagen affinity enhancement • Cell proliferation • Pro-inflammatory effect • Anti-inflammatory activity	• Laminin • Aggregan • Gelatin • Fibronectin
	Stromelysin-2	MMP-10	• Degradation of COL-IV, COL-XVIII, perlecan in cancers	• Collagens (III–V) • Gelatin • Casein • Aggregan • Elastin • MMP-1,-8
	Stromelysin-3	MMP-11	• Release of α1-proteinase inhibitor • Decrease cancer cell sensitivity to NK cells	• Fibronectin • Laminin • Aggregan • Gelatin
Matrilysins	Matrilysin-1	MMP-7	• Collagen affinity enhancement • An increase in the bioavailability of IGF-1 and TGF-β • Cell differentiation • Vasoconstriction • Cell growth	• Collagen (IV–X) • Fibronectin • Laminin • Gelatin • Pro-MMP-9
	Matrilysin-2	MMP-26	• Unknown	• Gelatin • Collagen IV • Pro-MMP-9

MMP classification			Biological effect	Group of substrates for enzymes
Group	**Traditional classification**	**Numerical classification**		
Membrane-type MMPs (MT-MMP)	MT-MMP-1	MMP-14	• Anti-inflammatory activity • Cell migration • Epithelial cell migration	• Collagen (I, II, III) • Gelatin • Fibronectin • Laminin • Aggrecan • Tenascin
	MT-MMP-2	MMP-15	• Adhesion and cell flattering reduction	• Fibronectin • Laminin • Aggrecan • Perlecan
	MT-MMP-3	MMP-16	• Adhesion and cell flattering reduction	• Collagen III • Gelatin • Casein
	MT-MMP-4	MMP-17	• Unknown	• Fibrinogen • TNF precursor
	MT-MMP-5	MMP-24	• Unknown	• Proteoglycans
Other non-classified MMPs	Metalloelastase	MMP-12	• Unknown	• Elastin • Gelatin • Collagen I, IV • Fibronectin • Laminin

In chronic wounds, it has been found that the level of MMPs increases while the level of TIMPs decreases.[171–173] The increased levels of MMPs can lead to the aggressive degradation of new ECM and prolonged inflammation, negatively affecting wound healing.[71] To modulate the inflammation in chronic wounds, synthetic inhibitors of MMPs have been developed in the past decades.

Doxycycline hydrochloride (DOX HCl) is a semisynthetic, chemically modified analogue of tetracyclines (Figure 4.1). At sub-antimicrobial dose, it exerts a non-specifically inhibiting activity towards MMPs which is independent from its antibacterial property.[174–176] Doxycycline is currently approved by the U.S. Food and Drug Administration (FDA) to be used for the prevention of periodontitis[177] and the treatment of rosacea[178].

By chelating with the active zinc ion and secondarily binding to the inactive calcium ion of MMPs, DOX HCl causes the conformational changes and loss of enzymatic activity.[179,180] Moreover, doxycycline also has shown potential to inhibit the activity of TNF-α converting enzyme (TACE) and prevents the secretion of TNF-α at wound sites.[22]

Owing to the inhibiting activity of doxycycline towards MMPs, it has been used to improve the inflammation in many applications; for example, acne vulgaris[181,182], rosacea[181,183], periodontitis[184] and diabetic foot ulcers[185]. Chin *et al.* reported that topical doxycycline at the concentration of 50, 500 and 5000 mM significantly reduced the activity of proteases by 44%, 75% and 89%, respectively in diabetic foot ulcers.[22] In addition, Serra *et al.* found that oral

administration of 20 mg doxycycline twice a day for 3 months increased the healing rate through the inhibition of MMP-9, improving the wound healing in chronic venous leg ulcers.[186]

As both oral and topical administrations of doxycycline have been shown to accelerate the wound healing through the inhibition of MMPs. Doxycycline has also been incorporated into electrospun scaffolds to treat diseases in which inflammation is the underlying cause of delayed healing. For example, PCL-DOX HCl fibres for periodontitis treatment[187,188] and doxycycline loaded-PLA fibres for aortic aneurysm treatment[189,190]. However, there are no DOX HCl loaded-electrospun scaffolds that have been designed for modulating the inflammation in chronic skin wounds. Hence, the fabrication, characterisation, as well as the evaluation of such electrospun scaffolds for dermal fibroblast proliferation are set as overarching aims in this chapter.

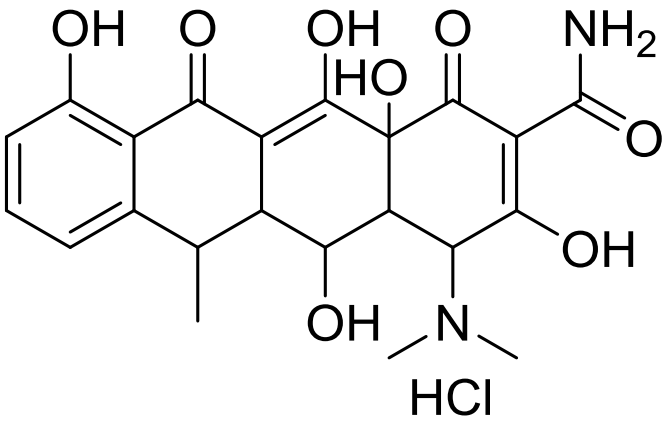


Figure 4.1. Chemical structure of doxycycline hydrochloride

Poly(ε-caprolactone) (PCL) is a biodegradable and biocompatible polymer with a linear aliphatic polyester structure (Figure 4.2).[191] This hydrophobic semi-crystalline polymer has been widely used in several biomedical fields and approved by the U.S. FDA for the production of medical devices.[191,192] Owing to its slow degradation, good biocompatibility and high mechanical property[188], PCL was chosen for producing the electrospun scaffolds.

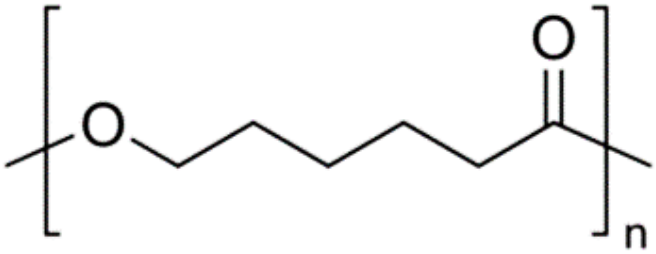


Figure 4.2. Chemical structure of poly(ε-caprolactone)

Electrospun PCL scaffolds have been proven to effectively promote cell proliferation as well as deliver doxycycline for improving periodontitis both *in vitro* and *in vivo* (clinical study).[187,188] Considering the pathology of the disease, a prolonged inflammation caused by excessive MMPs is an underlying cause, which is similar to most of chronic skin wounds. Therefore, this chapter aimed to develop PCL scaffolds loaded with DOX HCl to promote the proliferation of dermal fibroblasts.

4.2 Aims and Objectives

The aims of this chapter were to investigate the feasibility of fabricating DOX HCl-loaded fibrous PCL scaffolds using conventional electrospinning. The electrospun scaffolds were characterised with various techniques to study their properties and to explore cell-scaffold interactions with mouse fibroblasts and primary human dermal fibroblasts (Figure 4.3).

The aims were achieved with the following objectives:

1. Manufacture of DOX HCl-loaded electrospun scaffolds from biocompatible and biodegradable PCL with different drug loadings.
2. Characterisation of the electrospun fibres in terms of fibre diameter, porosity, water contact angle, mechanical properties, drug encapsulation efficiency, drug release, drug localisation, drug-polymer interaction and degradation.
3. Investigation of the ability of the scaffolds to promote cell proliferation using mouse fibroblasts and primary human dermal fibroblasts.

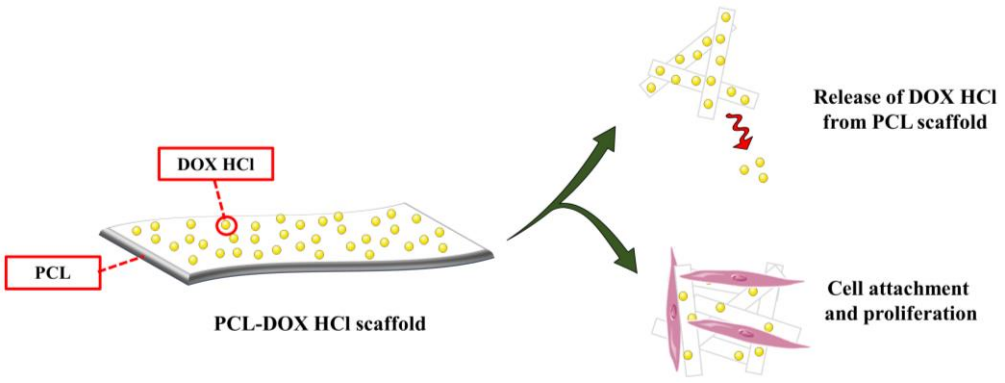
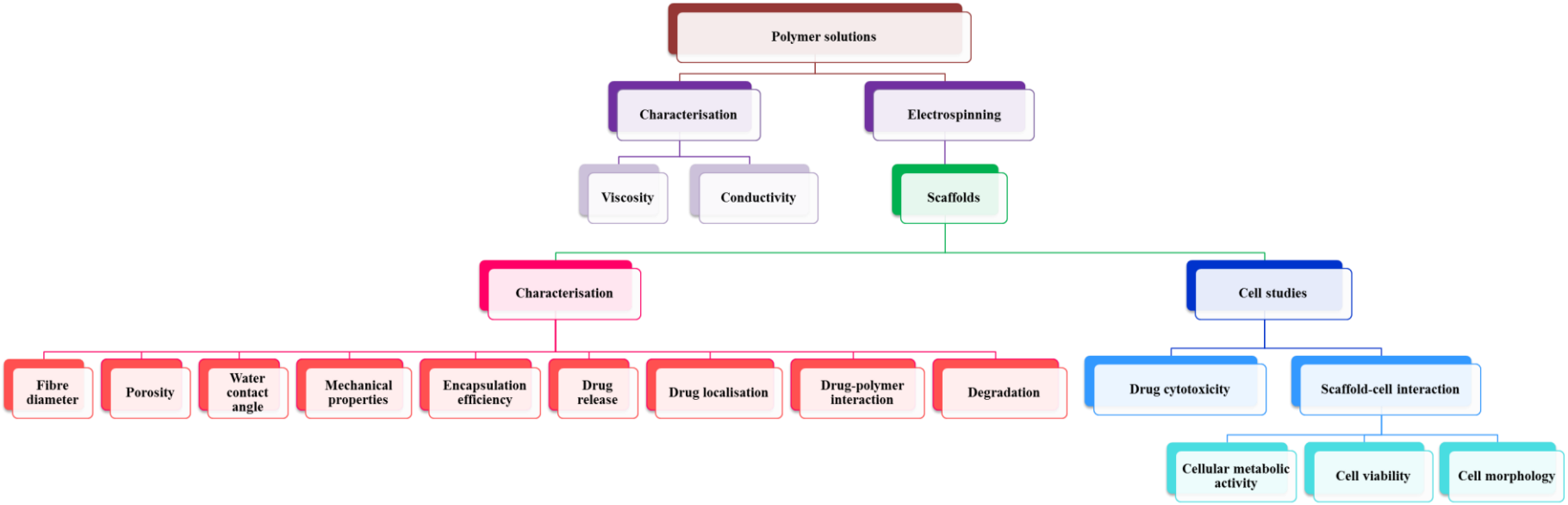


Figure 4.3. Diagram illustrating the application of electrospun scaffolds to deliver DOX HCl and support cell proliferation.

4.3 Experimental overview



4.4 Materials and Methods

4.4.1 Preparation of polymer and polymer-drug solutions for electrospinning

Poly(ε-caprolactone) (PCL, Mn 800 kDa, Sigma-Aldrich, UK) was dissolved in hexafluoroisopropanol (HFIP, analytical grade, Fluorochem, UK) by magnetic stirring overnight to form 10% w/v polymer solution for electrospinning.

For drug-loaded electrospun scaffolds, doxycycline hydrochloride (DOX HCl, 98% GC grade, Sigma-Aldrich, UK) was added to the PCL solutions at the concentrations of 1, 2 and 5% w/w relative to the weight of polymer. The vials containing the solutions were covered with aluminium foil to protect from ambient light. The polymer-drug solutions were mixed overnight on a magnetic stirrer and then used for electrospinning next day. All PCL-DOX HCl solutions were clear and no drug precipitation was observed.

4.4.2 Fabrication of PCL and DOX HCl-loaded PCL scaffolds using electrospinning technique

Electrospun scaffolds were fabricated using a climate-controlled electrospinning apparatus (IME Technologies, Netherlands). A 5 mL syringe wrapped with aluminium foil was charged with the polymer solution, and then connected to a plastic tubing. The other end of the tubing was fitted with a blunt tipped stainless steel needle (internal diameter: 0.8 mm). The polymer solution was injected at a constant flow rate of 2 mL h^{-1} using a programmable syringe pump (Harvard Apparatus, USA), and was horizontally electrospun with 14 kV. The voltage

was supplied by a high voltage power supply. Electrospun scaffolds were collected on an aluminium foil sheet, wrapping around a spinning grounded aluminium-rotating collector (150 rpm). The gap distance was set at 10 cm. The electrospinning processes were all performed in dark at 20 °C and 30% relative humidity. All scaffolds were placed in a vacuum oven at 25 °C for 24 h to remove residual solvent.

4.4.3 Characterisation of the scaffolds

See Chapter 2 General Methods

4.4.4 Cell studies

See Chapter 2 General Methods

4.5 Results and Discussion

The attempt to fabricate DOX HCl-loaded electrospun scaffolds initially started with PLGA8515 polymer, which was previously used in manufacturing the IBU Na-loaded electrospun scaffolds (*see* Chapter 3). However, preliminary studies revealed that the release of DOX HCl from the PLGA scaffolds in PBS was very limited (*see* Appendix). The cumulative drug release was less than 1% within 24 h, and no further significant drug release was detected after 90 days.

There was a report showing that the higher concentration of PLGA5050 led to a slower rate of release of DOX HCl from the electrospun scaffolds.[193] Using high

polymer concentrations results in the formation of dense polymer matrix structures. Such frameworks require a longer time to degrade.[194] The release of the entrapped drug is delayed, as this process relies on the degradation of the polymer network. Furthermore, higher ratios of PLA to PGA and a higher molecular weight of PLGA led to the lower initial level during the burst releasing. These two factors also affected the more sustained release profile of drug release, when compared to the lower ratios and molecular weight PLGA.[195]

The observations were consistent with what have been reported; the rate of releasing DOX HCl from the electrospun PLGA scaffolds was reduced, when using high ratio of PLA:PGA (85:15) at high concentration (40% w/v). PLGA8515 was therefore dismissed from the study.

Other biocompatible and biodegradable polymers were screened for fabricating DOX HCl-loaded electrospun scaffolds. The candidates were PLGA5050, PLA and PCL polymers. Similarly, it was found that PLGA5050 and PLA scaffolds released very small amount of DOX HCl (*see* Appendix). Although PLGA5050 degraded faster than PLGA8515, the erosion and degradation of PLGA5050 did not result in the release of DOX HCl as much as reported in the literature.[193] DOX HCl remained within the scaffolds while simultaneously degraded along with the polymer (degradation of DOX HCl was indicated by the colour change from yellow to brown-black, *see* Appendix).

The degradation of doxycycline undergoes *via* epimerisation, when DOX is exposed to light, heat (> 70 °C), humidity and hydrogen peroxide.[190,196–198] The

common degradation products of DOX are metacycline and oxytetracycline.[198,199] Redelsperger *et al* reported that the solution of doxycycline in water stored in tinted bottles at 37 °C was stable up to 7 days.[200] Therefore, when apply DOX HCl-loaded electrospun scaffolds at wound sites, a backing layer should be placed on top of the electrospun scaffolds to prevent the degradation of DOX HCl induced by light.

PCL was the only candidate in this study that potentially released DOX HCl into PBS. As a result, PCL was considered as the most suitable polymer for fabricating DOX HCl-loaded electrospun fibres in this study. The electrospun scaffolds were all fabricated from 10% w/v PCL solutions in HFIP with or without DOX HCl to obtain uniform fibres. DOX HCl was blended at different drug loadings: 1, 2 and 5% w/w.

4.5.1 Characterisation of polymer solution properties (viscosity and conductivity)

The measurement revealed that the viscosity of PCL solutions was 3.08 ± 0.09 Pa·s. Incorporating DOX HCl into PCL solutions led to a slight decrease in viscosity (Figure 4.4A). The decrease in viscosity and the amount of DOX HCl loaded were however not in a linear relationship.

The lowest conductivity was observed in PCL solutions as expected (0.71 ± 0.05 $\mu S \cdot cm^{-1}$). Figure 4.4B shows that the addition of DOX HCl significantly increased the conductivity of PCL solutions by approximately 25–103 fold, depending on drug loadings. The greater conductivity values were observed with

higher drug loadings. This is due to the fact that drug molecules provide more ions into the solutions.

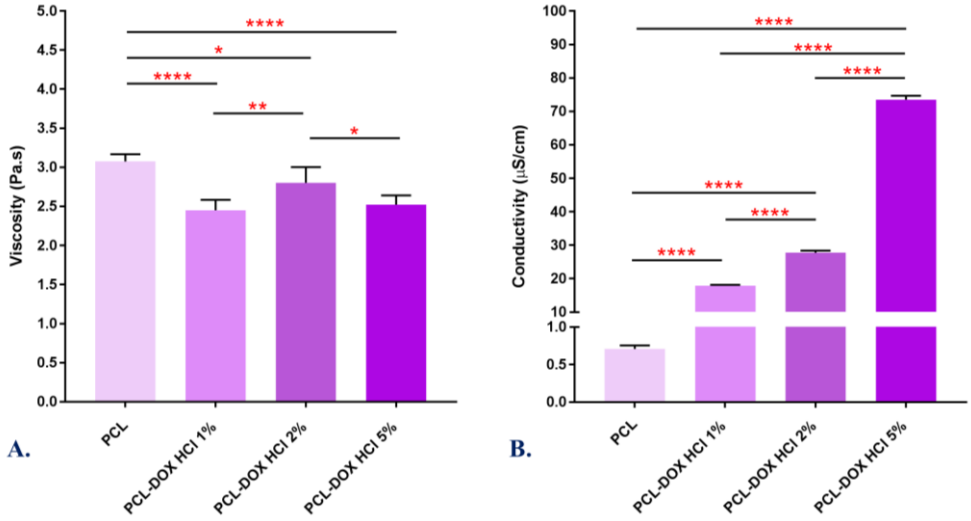


Figure 4.4. Means and standard deviations of (A) viscosity and (B) conductivity of polymer solutions. The viscosity of solutions was averaged from six measurements (n = 6) and the conductivity of solutions were averaged from ten measurements (n = 10). *, **, **** define statistical significance at *p*-value < 0.05, < 0.01 and < 0.0001, respectively.

Table 4.2. Viscosity and conductivity values of polymer and polymer-drug solutions. The viscosity and conductivity values reported were the means and standard deviations obtained from six and ten measurements, respectively.

Solution	Viscosity (Pa·s)	Conductivity ($\mu S \cdot cm^{-1}$)
PCL	3.08 ± 0.09	0.71 ± 0.05
PCL-DOX HCl 1%	2.45 ± 0.13	17.88 ± 0.25
PCL-DOX HCl 2%	2.80 ± 0.20	27.72 ± 0.64
PCL-DOX HCl 5%	2.52 ± 0.12	73.46 ± 1.18

4.5.2 Characterisation of the electrospun scaffolds

4.5.2.1 Scaffold morphology and fibre diameter

Figure 4.5 shows that the scaffolds were made of smooth rounded nanofibres. The addition of DOX HCl improved size distribution of fibre diameter to be narrower (histograms in Figure 4.5). In addition, no drug crystals were observed on the surface of fibres. This could indicate that crystalline DOX HCl has transformed to its amorphous state and molecularly dispersed in PCL matrix after electrospinning.[188,201]

PCL scaffolds had the biggest fibres at 638 ± 135 nm, followed by PCL-DOX HCl 1% scaffolds at 466 ± 86 nm (Figure 4.6A). The smallest fibre diameters were observed from PCL-DOX HCl 2% and PCL-DOX HCl 5% scaffolds at 353 ± 72 and 382 ± 71 nm, respectively.

The average fibre diameters of PCL and PCL-DOX HCl electrospun scaffolds are smaller than those of PLGA and PLGA-IBU Na electrospun scaffolds in Chapter 3 due to different polymer concentration and higher conductivity. These two parameters have a counterbalanced effect on fibre diameter. If the scaffolds are prepared by using the same process and environmental parameters, higher polymer concentrations will provide more viscoelastic force to resist the stretching repulsive force by charge when compared to the lower polymer concentrations.[202] As a result, the bigger fibre diameter will be obtained. Whist, polymer solutions with higher conductivity are subjected to a greater stretching repulsive force from increased charge density when compared to polymers solutions with lower conductivity. Hence, the fibre diameter will be smaller.[202]

The concentrations of PCL and PLGA solutions in HFIP are 10% w/v and 25% w/v, respectively. The presence of PLGA decreased the conductivity of pure HFIP solution from 0.75 ± 0.10 $\mu S \cdot cm^{-1}$ to 0.16 ± 0.001 $\mu S \cdot cm^{-1}$. Whereas, the conductivity of solutions remained at 0.71 ± 0.05 $\mu S \cdot cm^{-1}$ in the presence of PCL. Additionally, the viscosity of PCL solutions is higher than those of PLGA solutions at the given concentrations (3.08 ± 0.09 Pa·s versus 0.60 ± 0.01 Pa·s). PLGA solutions are less viscous and conductive. While, PCL solutions are more viscous and conductive.

According to the results, the average fibre diameter of PLGA scaffolds is approximately 1 μm whereas the fibre diameter of PCL scaffolds is approximately 600 nm. These are the outcome of counterbalanced effect of polymer concentrations and conductivity. It should be noted here that the effect of these two parameters on the average fibre diameter of PCL and PLGA may not be the same, because they are different polymers, which they have their own unique properties.

For drug-loaded fibres, it was found that the viscosity of the solutions are comparable between PCL and PLGA solutions. Therefore, conductivity will have more influence on the average fibre diameter of the scaffolds. The addition of DOX HCl into PCL solutions increased conductivity in a greater magnitude in comparison with the effect of IBU Na addition into PLGA solutions at the same drug loading. As a result, the average fibre diameter of PLGA-IBU Na scaffolds is bigger than those of PCL-DOX HCl scaffolds due to lower stretching repulsive force as mentioned above.

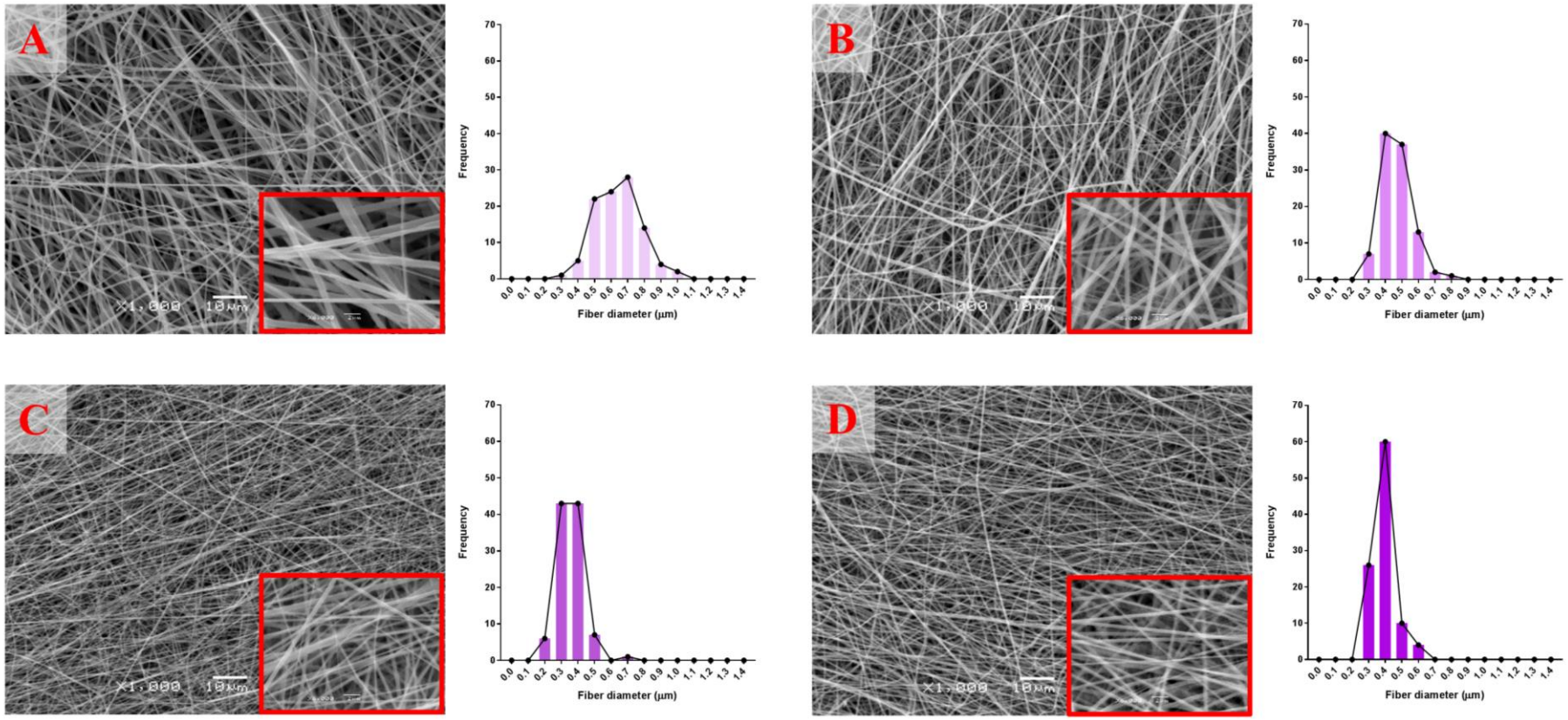


Figure 4.5. Representative SEM images and histograms for fibre diameter distribution of (A) PCL, (B) PCL-DOX HCl 1%, (C) PCL-DOX HCl 2% and (D) PCL-DOX HCl 5% scaffolds. SEM images were all shown at the magnification of 1,000X (scale bar 10 µm) for the big images, and 6,000X (scale bar 2 µm) for the small images (red windows).

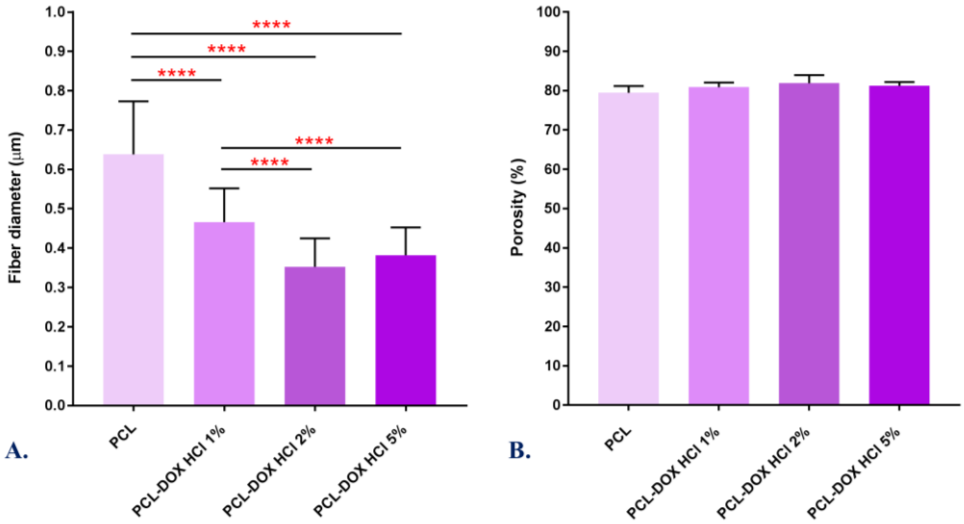


Figure 4.6. (A) Fibre diameter and (B) total porosity of PCL, PCL-DOX HCl 1%, PCL-DOX HCl 2% and PCL-DOX HCl 5% electrospun scaffolds. Fibre diameter was measured from representative SEM images of the scaffolds using ImageJ software (n = 100 fibres). Total porosity of the scaffolds was determined by gravimetric method in triplicate. Values are shown as mean and standard deviation. **** defines statistical significance at *p*-value < 0.0001.

Table 4.3. Means and standard deviations of fibre diameter (n = 100) and total porosity (n = 3) of PCL, PCL-DOX HCl 1%, PCL-DOX HCl 2% and PCL-DOX HCl 5% electrospun scaffolds.

Scaffold	Fibre diameter (nm)	Porosity (%)
PCL	638 ± 135	79.45 ± 1.72
PCL-DOX HCl 1%	466 ± 86	80.90 ± 1.17
PCL-DOX HCl 2%	353 ± 72	81.89 ± 2.08
PCL-DOX HCl 5%	382 ± 71	81.22 ± 0.98

Both viscosity and conductivity of polymer solutions have an influence on fibre diameter of the electrospun scaffolds.[72] In this study, the viscosity of the solutions was slightly different. The differences in fibre diameters were a result of changes in conductivity after adding DOX HCl. As previously mentioned in Chapter 3, the addition of electrolytes or ionic salts into polymer solutions results in increased number of charged species on the surface of polymer solutions.[203,204] These charges provide more elongation capacity to the polymer jet while being electrospun. Hence, obtaining smaller fibre diameters.[204]

4.5.2.2 Total porosity

The total porosity of all scaffolds were approximately 80% (Figure 4.6B). Although there were differences in fibre diameter between the scaffolds, there were no statistically significant differences in the total porosity of the scaffolds.

Unlike PLGA-IBU Na scaffolds, the porosity of PCL-DOX HCl scaffolds are not significantly different from the porosity of PCL scaffolds. This is because PCL-DOX HCl scaffolds have smaller fibre diameter when compared to that of PCL scaffolds. Soliman *et al* observed that bigger fibre diameter reduces the porosity of PCL electrospun scaffolds.[205] If the fibre diameter of PCL-DOX HCl scaffolds is in the same range as the PCL scaffolds, the higher porosity of the scaffolds may be observed as the drug increases surface charge density and creates a repulsive Coulombic force between fibres.[134]

4.5.2.3 Mechanical properties

The stress-strain curves in Figure 4.7A illustrates that PCL scaffolds were more ductile when compared to all PCL-DOX HCl scaffolds. PCL scaffolds underwent plastic, non-reversible deformation before a gradual breakage. In contrast, PCL-DOX HCl 1%, PCL-DOX HCl 2% and PCL-DOX HCl 5% scaffolds were more brittle as they broke after being stretched at earlier strain.

The ultimate tensile strength and Young's modulus of all PCL-DOX HCl scaffolds were significantly higher than PCL scaffolds (Figures 4.7B and 4.7D). However, dramatic decrease in % strain at break was observed in all PCL-DOX

HCl scaffolds (Figure 4.7C). The results suggest that increasing the amount of DOX HCl into PCL scaffolds from 1% w/w to 5% w/w did not lead to an extensive change in mechanical properties of the resulting scaffolds.

The degree of crystallinity of the polymer constituting the fibres affects the mechanical properties of electrospun scaffolds.[206] The amorphous and crystalline regions of fibres account for elasticity and strength of the scaffolds, respectively.[206]

Bosworth *et al* observed a gradual increase in tensile strength of PCL electrospun scaffolds when incubated in PBS over 90 days.[207] The increasing tensile strength is a result of hydrolysis of the ester linkages in the amorphous regions of polymer, leading to the rearrangement of polymer chains.[207] This results in a more ordered structure and higher degree of crystallinity.[207] Furthermore, the increase in crystallinity of PCL fibres resulted in decreased elongation at break.[208]

As DOX HCl is an acidic salt form of doxycycline[193] and PCL is a semi-crystalline polymer that has hydrolysable ester linkages[191]. DOX HCl hydrolyses the ester linkages in an amorphous region of the polymer.[209] Therefore, the overall crystallinity of PCL is increased, resulting in the higher mechanical strength and Young's modulus of the scaffolds.[207,210]

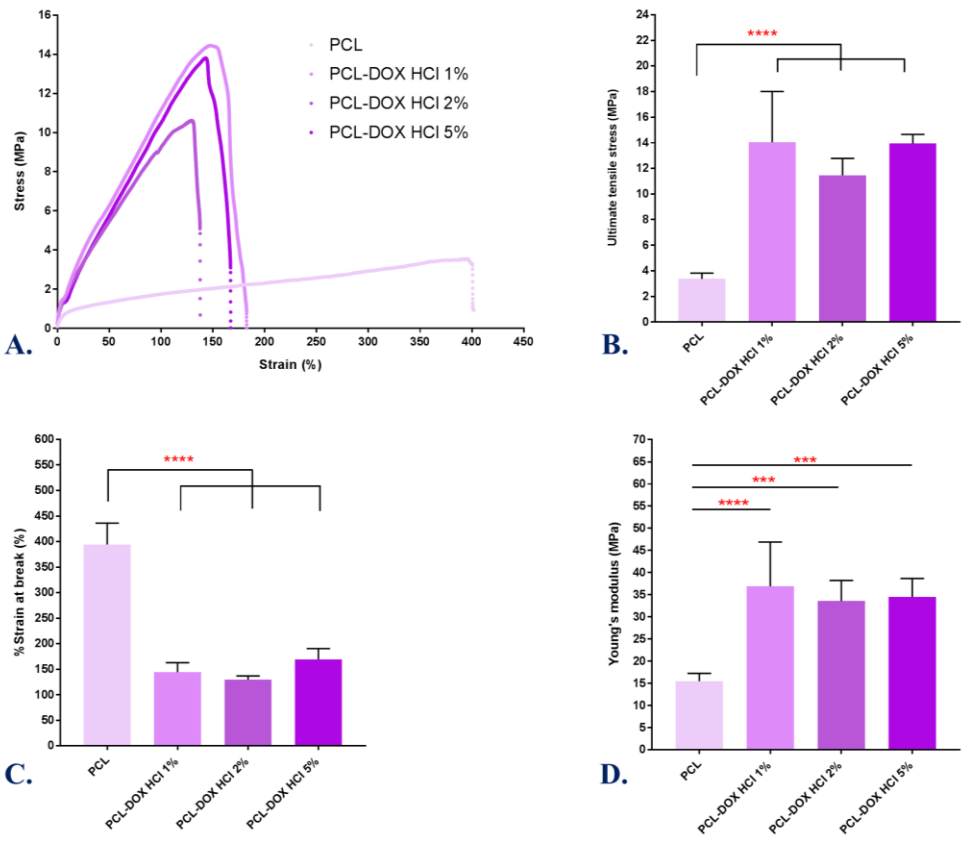


Figure 4.7. Mechanical properties of electrospun scaffolds were evaluated by a uniaxial tensile test. Each scaffold was tested in sextuplicate (n = 6). (A) Representative stress-strain curves, (B) Ultimate tensile strength, (C) % Strain at break and (D) Young's modulus. The values are shown as means and standard deviations. *** and **** define statistical significance at *p*-value < 0.001 and < 0.0001, respectively.

Table 4.4. Means and standard deviations of ultimate tensile strength, % strain at break and Young's modulus of PCL, PCL-DOX HCl 1%, PCL-DOX HCl 2%, and PCL-DOX HCl 5% scaffolds (n = 6).

Scaffold	Ultimate tensile strength (MPa)	% Strain at break (%)	Young's modulus (MPa)
PCL	3.37 ± 0.45	394.17 ± 41.82	15.48 ± 1.75
PCL-DOX HCl 1%	14.04 ± 3.97	144.16 ± 18.75	36.89 ± 10.00
PCL-DOX HCl 2%	11.46 ± 1.32	129.48 ± 7.31	33.58 ± 4.64
PCL-DOX HCl 5%	13.95 ± 0.71	169.18 ± 21.22	34.49 ± 2.18

4.5.2.4 Water contact angle

The results obtained from the static mode of the sessile drop method (Figure 4.8) show that PCL, PCL-DOX HCl 1% and PCL-DOX HCl 2% scaffolds possessed a water contact angle higher than 90° but less than 150°. This implies that these scaffolds are hydrophobic but not yet super-hydrophobic.[201,211] Whereas, PCL-DOX HCl 5% scaffolds possessed a water contact angle of 87.77 ± 6.85°, being more hydrophilic and wettable when compared to the others.[201]

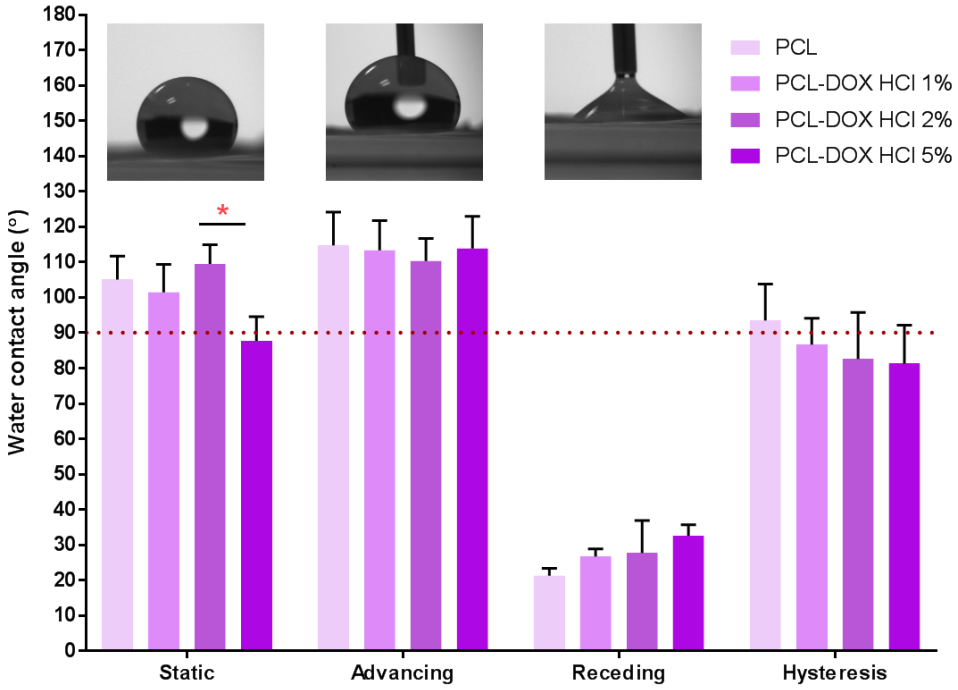


Figure 4.8. Water contact angles of electrospun scaffolds were determined by static and dynamic modes of a sessile drop method. Values represent means and standard deviations of static water contact angle, advancing water contact angle, receding water contact angle, and contact angle hysteresis (the difference between advancing and receding water contact angles) (n = 3). The small figures shown are the representative images of water droplet on electrospun scaffolds when tested by static and dynamic modes: static water contact angle (left), advancing water contact angle (middle) and receding water contact angle (right). * defines a statistical significance at *p*-value < 0.05.

Table 4.5. Water contact angles of electrospun scaffolds were determined by static and dynamic modes of a sessile drop method. The values represent means and standard deviations of static water contact angle, advancing water contact angle, receding water contact angle, and contact angle hysteresis (the difference between advancing and receding water contact angles) (n = 3).

Scaffold	Static contact angle (°)	Advancing contact angle (°)	Receding contact angle (°)	Contact angle hysteresis (°)
PCL	105.11 ± 6.64	114.78 ± 9.38	21.29 ± 2.09	93.49 ± 10.31
PCL-DOX HCl 1%	101.45 ± 7.93	113.35 ± 8.45	26.70 ± 2.21	86.65 ± 7.51
PCL-DOX HCl 2%	109.48 ± 5.49	110.36 ± 6.34	27.71 ± 9.20	82.65 ± 13.17
PCL-DOX HCl 5%	87.77 ± 6.85	113.91 ± 9.09	32.61 ± 3.11	81.30 ± 10.88

Poor wettability of PCL scaffolds is due to the hydrophobic nature of PCL.[201] Previous studies have observed that when the amount of water soluble DOX or tetracycline in the scaffolds increased, the hydrophilicity of the scaffolds also improved.[201,212] In our study, PCL scaffolds became more hydrophilic when loaded with 5% w/w DOX HCl.

As discussed in Chapter 3, the scaffolds fabricated by electrospinning have an inhomogeneous surface or surface roughness due to gas trapped between fibres.[144,145] This results in reduced liquid-solid interaction, showing as high values of water contact angle. Consequently, the sessile drop method was implemented in a dynamic mode to determine wettability of the scaffolds using advancing and receding water contact angles (Figure 4.8). No significant difference in both advancing and receding water contact angles between the scaffolds was observed. Contact angle hysteresis, which is the difference between advancing and receding water contact angles, has been used to determine the roughness of surface.[142,146] According to the results, contact angle

hysteresis of all scaffolds was greater than 80°, indicating poor wettability of the scaffolds from surface roughness. However, these scaffolds are not super-hydrophobic materials as their contact angle hysteresis values are larger than 10°.[211]

4.5.2.5 Drug encapsulation efficiency

Table 4.6 reveals that the encapsulation of DOX HCl in PCL electrospun scaffolds was successfully achieved at 89% or greater. The loading of DOX HCl at 5% w/w resulted in a significant higher encapsulation efficiency when compared to drug loading of 1% w/w (*p*-value < 0.05, One-way ANOVA, n = 3).

Table 4.6. % encapsulation efficiency of DOX HCl in PCL electrospun scaffolds. The values are means and standard deviations of triplicate samples.

Scaffold	Encapsulation efficiency (%)
PCL-DOX HCl 1%	89.87 ± 2.97
PCL-DOX HCl 2%	92.14 ± 1.84
PCL-DOX HCl 5%	96.20 ± 2.14

The encapsulation efficiency of DOX HCl in PCL fibres is higher than those of IBU Na in PLGA fibres. This is possibly due to the higher molecular weight of PCL when compared to PLGA (80 kDa *versus* 63 kDa). Xue found that PLGA with higher molecular weights can encapsulate more drug in microspheres as a result of increased viscosity of polymer solution.[213] The viscous polymer solutions retard the diffusion of drug from PLGA matrix to the environment. Hence, the encapsulation efficiency is increased.

4.5.2.6 Superficial drug distribution determined by ToF-SIMS

ToF-SIMS was conducted to investigate the accumulation of drug molecules at the top surface of fibres. PCL was identified by the ions at *m/z* 115 $[C_6H_{11}O_2]^+$ and at *m/z* 113 $[C_6H_9O_2]^-$ (Figures 4.9 and 4.12, respectively).[149,214] While, DOX HCl was identified using the ions at *m/z* 445 $[C_{22}H_{25}N_2O_8]^+$, *m/z* 443 $[C_{22}H_{23}N_2O_8]^-$ and *m/z* 35 $[Cl]^-$ (Figures 4.10, 4.11 and 4.13, respectively).[215]

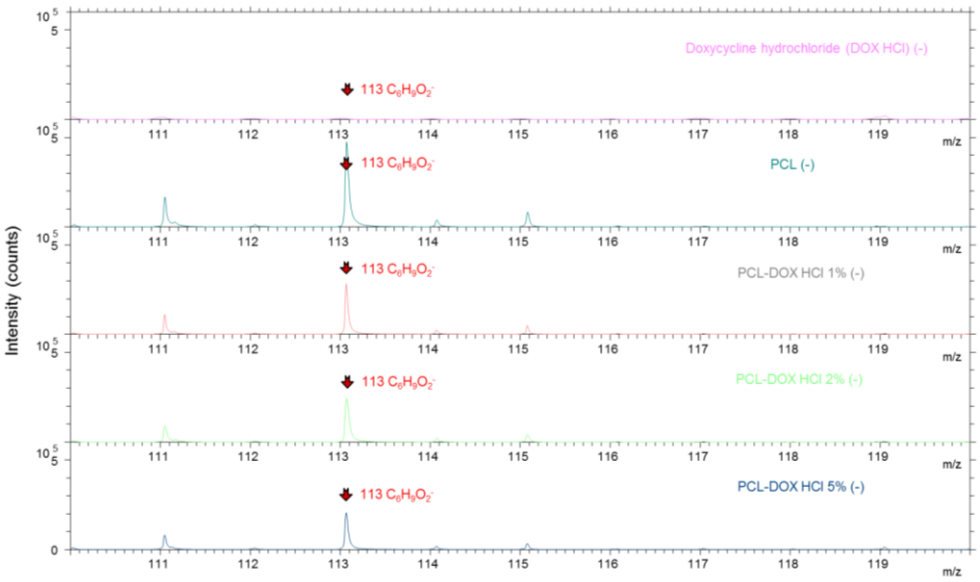


Figure 4.9. Representative negative ToF-SIMS spectra of the surface of electrospun scaffolds. The peak at *m/z* = 113, $[C_6H_9O_2]^-$, represents PCL.

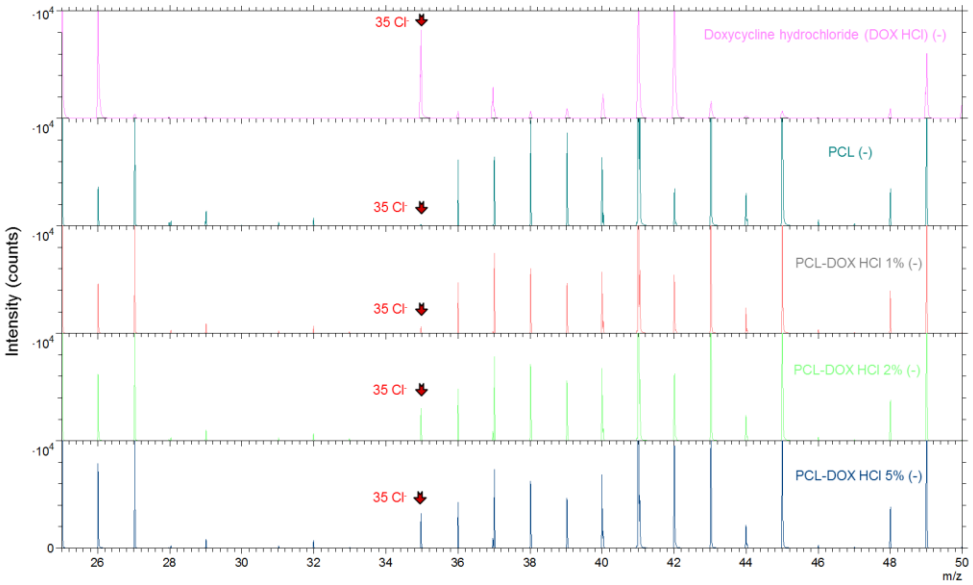


Figure 4.10. Representative negative ToF-SIMS spectra of the surface of electrospun scaffolds. The peak at *m/z* = 35, $[Cl]^-$, represents DOX HCl.

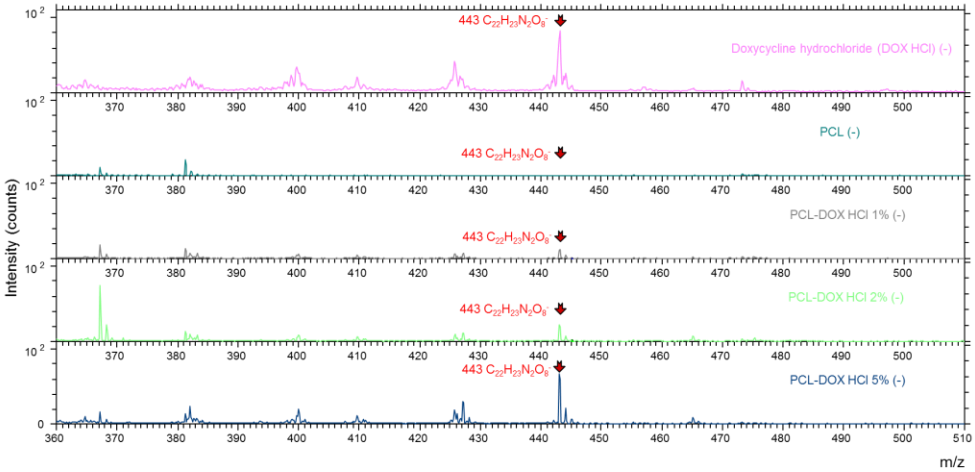


Figure 4.11. Representative negative ToF-SIMS spectra of the surface of electrospun scaffolds. The peak at *m/z* = 443, $[C_{22}H_{23}N_2O_8]^-$, represents DOX HCl.

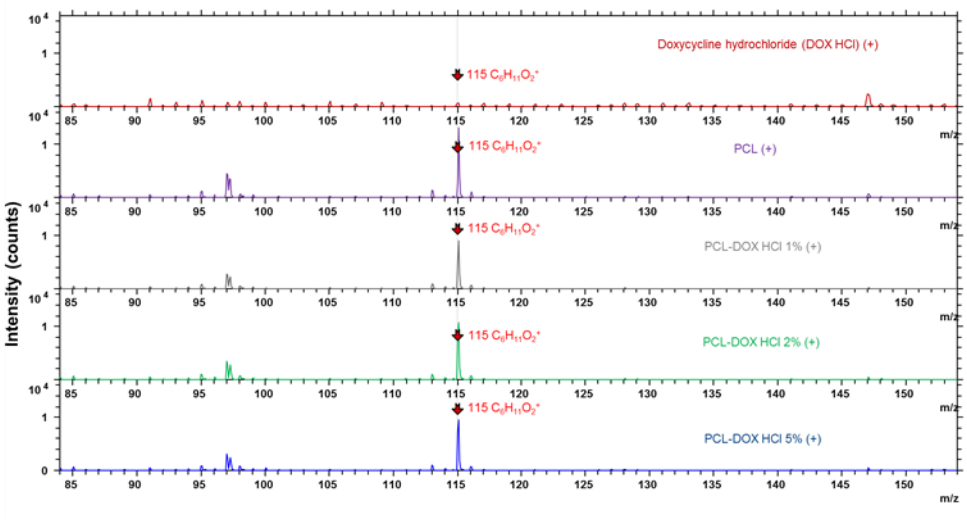


Figure 4.12. Representative positive ToF-SIMS spectra of the surface of electrospun scaffolds. The peak at *m/z* = 115, $[C_6H_{11}O_2]^+$, represents PCL.

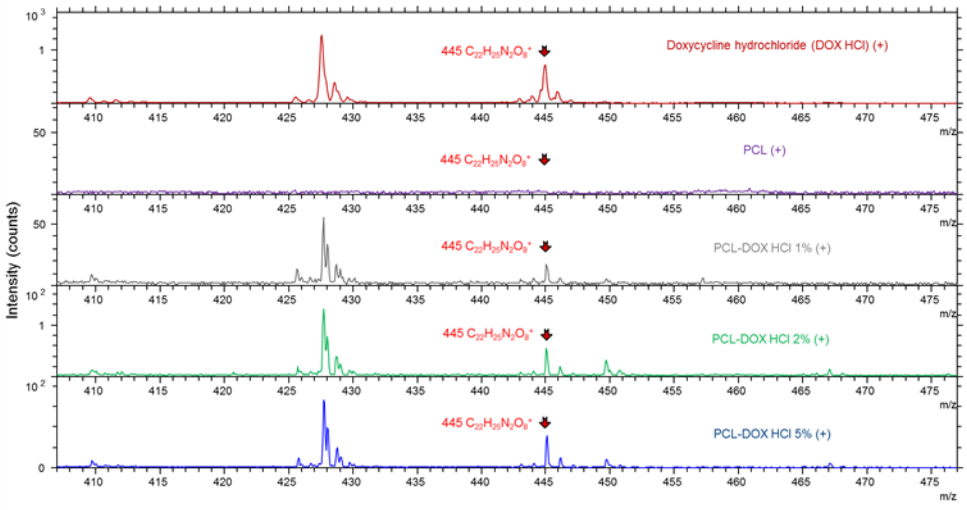


Figure 4.13. Representative positive ToF-SIMS spectra of the surface of electrospun scaffolds. The peak at *m/z* = 445, $[C_{22}H_{25}N_2O_8]^+$, represents DOX HCl.

The results show that DOX HCl distributed across the surfaces of the scaffolds—more DOX HCl was detected on the surface of higher % loading DOX HCl scaffolds (Figure 4.14). The total ion intensity of $[C_{22}H_{25}N_2O_8]^+$ observed in PCL-DOX HCl 1% scaffolds was not significantly different from blank PCL scaffolds. This is perhaps because the amount of DOX HCl was small, and some of DOX HCl is located deeper in the surface of the PCL network. Although $[Cl]^-$ is a common contaminant, it was observed that the total ion intensity of chloride ions increased with the higher drug loadings. This observation is similar to what have been observed in the case of positive molecular ion. This confirmed the presence of DOX HCl at the surface levels of the scaffolds.

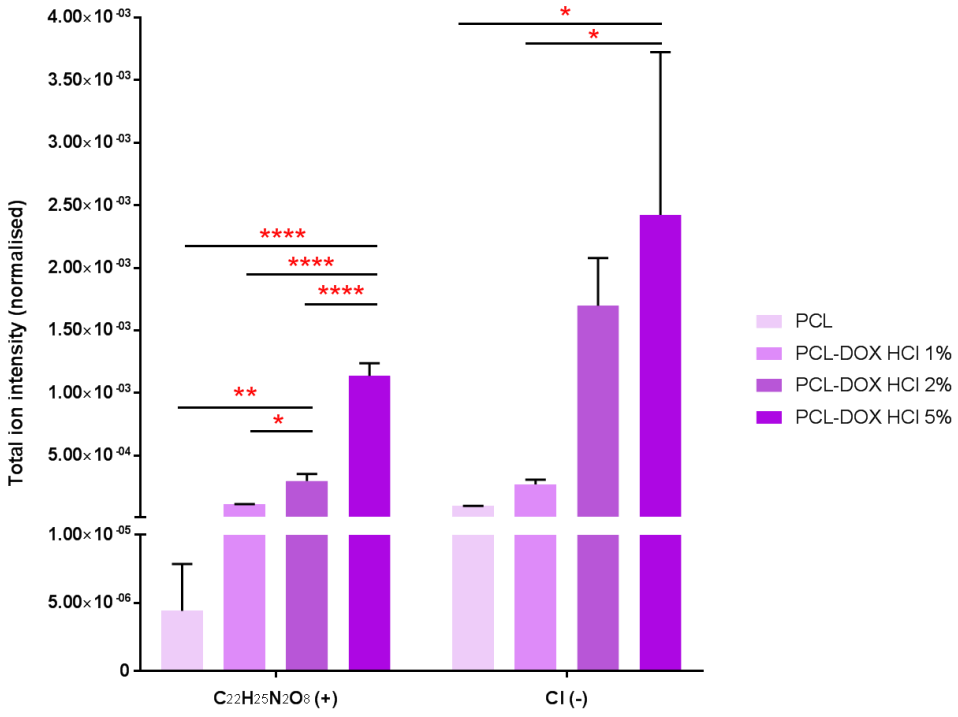


Figure 4.14. Normalised total ion intensity of $[C_{22}H_{25}N_2O_8]^+$ and $[Cl]^-$ for positive and negative charges. The values are means and standard deviations of the total ion intensity obtained from three different areas in one scaffold sample (n = 3). Data are normalised to the total ion counts. *, **, *** and **** define a significant difference between the scaffolds at *p*-value < 0.05, < 0.01, < 0.001 and < 0.0001, respectively.

The images for both positive and negative ions (Figures 4.15 and 4.16) show a homogeneous distribution of DOX HCl throughout the surface of electrospun PCL fibres with an increasing intensity when drug loading was higher.

Similar to the case of IBU Na in Chapter 3, DOX HCl is a small hydrophilic drug molecule with high ionic strength. In addition, the difference in hydrophilicity results in poor phase partition between DOX HCl and hydrophobic PCL. Therefore, drug molecules gathered at the surface of fibres.[153,154]

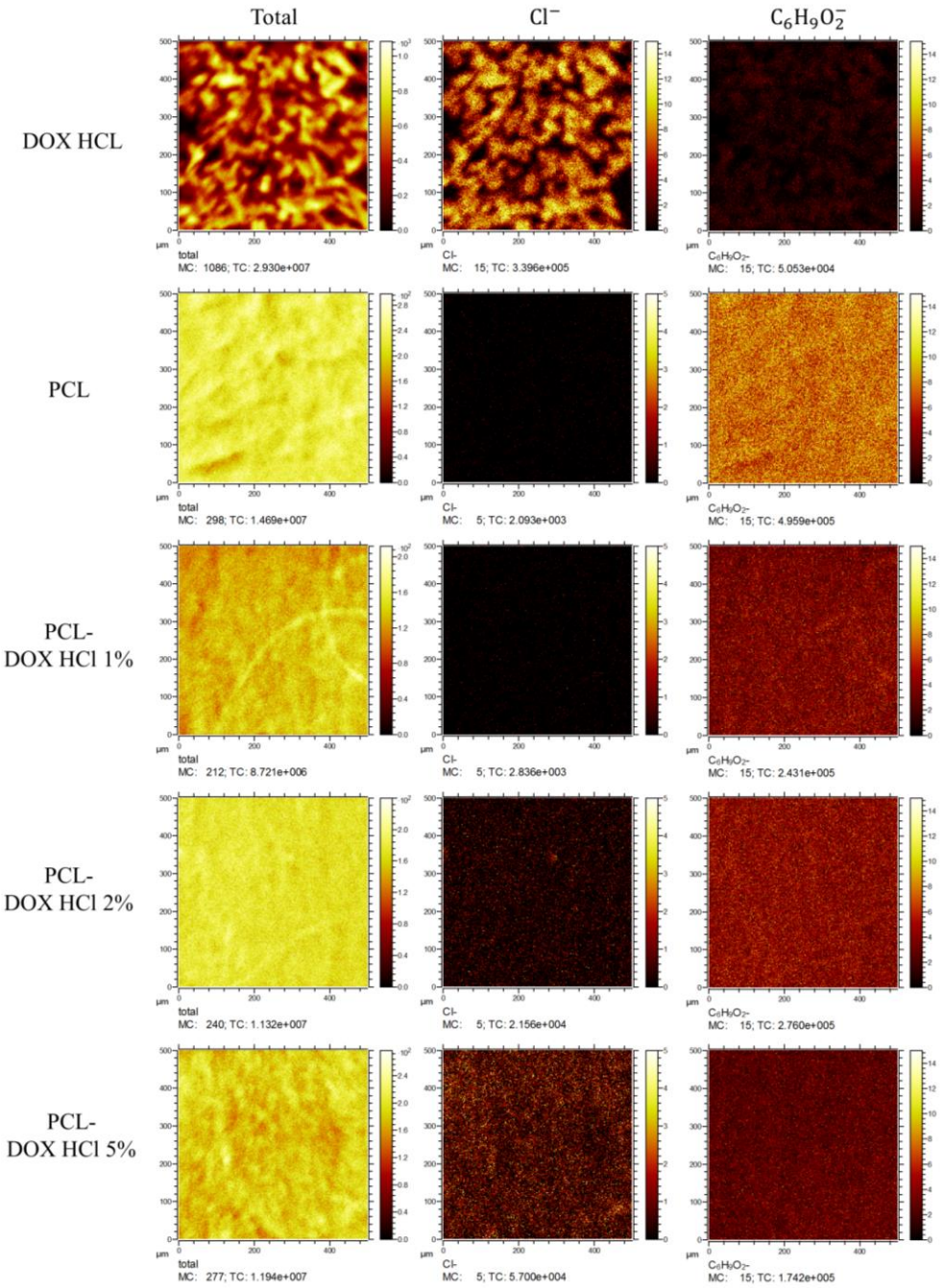


Figure 4.15. The 2D images show the distribution of $[C_6H_9O_2]^-$ (PCL), $[Cl]^-$ (DOX HCl), and total ions on the top surface of scaffolds. The images are acquired with a 2D surface imaging mode and normalised to the total ion counts.

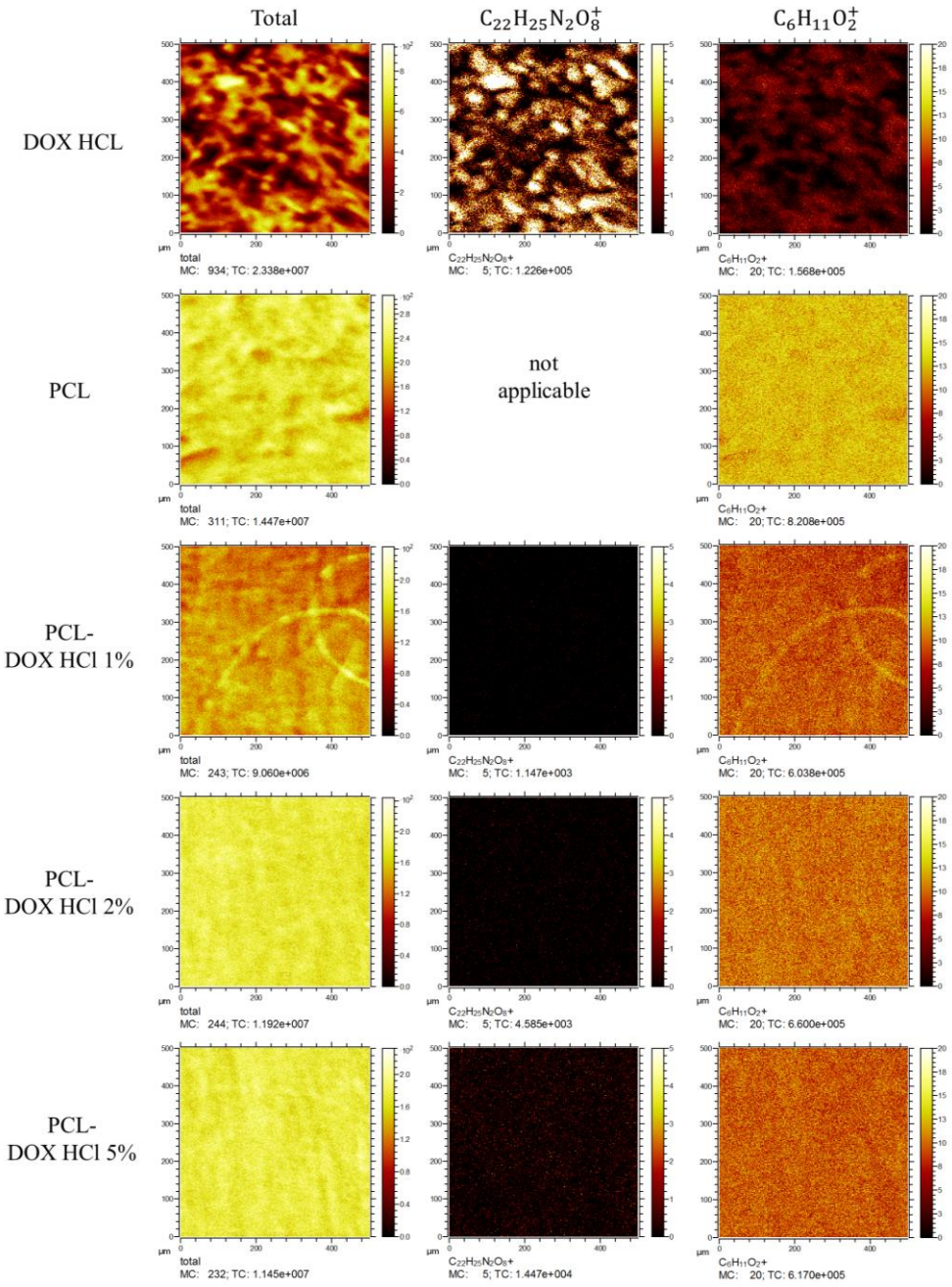


Figure 4.16. The 2D images show the distribution of $[C_6H_{11}O_2]^+$ (PCL), $[C_{22}H_{25}N_2O_8]^+$ (DOX HCl), and total ions on the top surface of scaffolds. The images are acquired with a 2D surface imaging mode and normalised to the total ion counts.

4.5.2.7 Drug release profiles of DOX HCl from PCL scaffolds

Figure 4.17 shows that the release of DOX HCl from PCL scaffolds in PBS was a rapid burst release regardless of drug loading. The average drug release reached approximately 99% within 30 minutes of the study in PCL-DOX HCl 2% and PCL-DOX HCl 5% scaffolds. Similarly, approximately 96% of drug were released from PCL-DOX HCl 1% scaffolds. Table 4.7 exhibits the averages and standard deviations of cumulative drug release over 30 days.

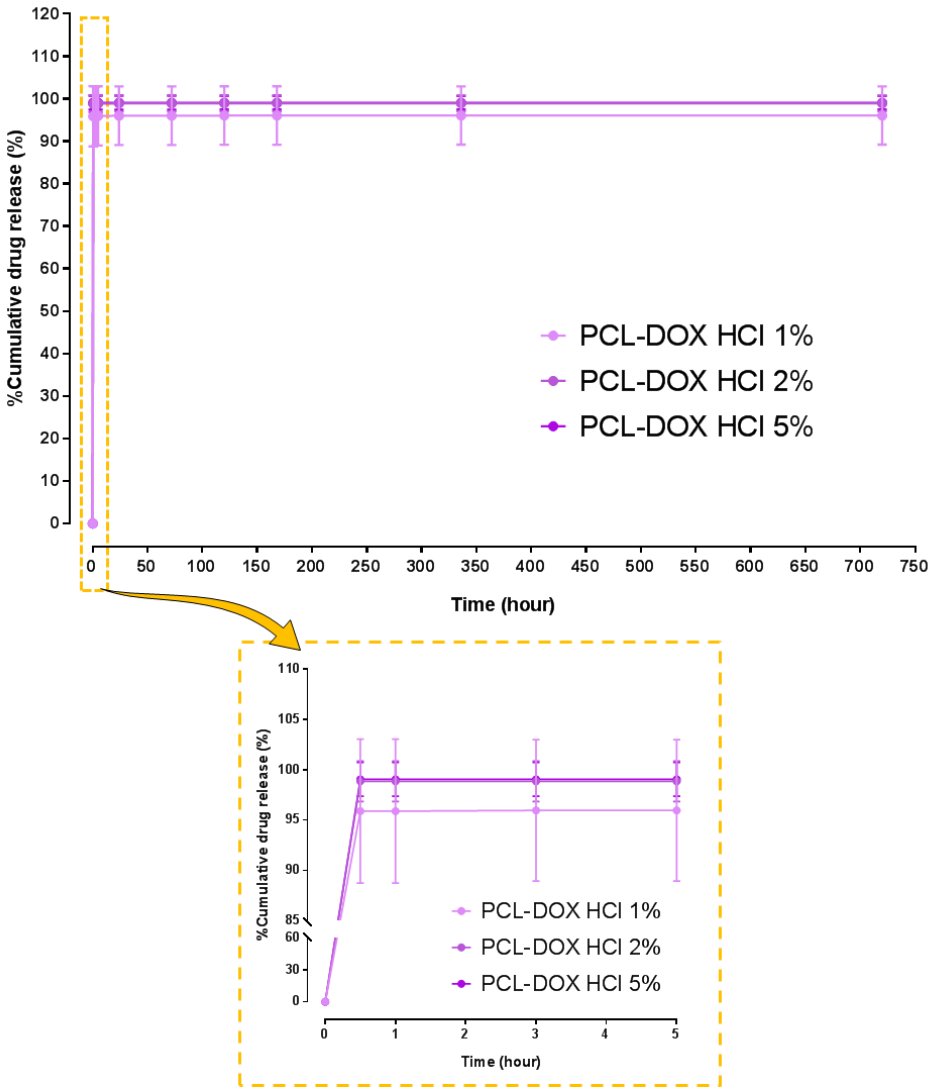


Figure 4.17. Cumulative drug release of DOX HCl from PCL scaffolds in PBS solutions over 30 days (720 hours, upper graph) and within the first 5 hours (lower graph). The values represent means and standard deviations of triplicate samples.

Table 4.7. % Cumulative drug release of DOX HCl from the PCL scaffolds over 30 days in PBS solutions. The values are represented as means and standard deviations of % encapsulation efficiency (n = 3).

Scaffold	Cumulative drug release in 30 days (%)
PCL-DOX HCl 1%	96.05 ± 6.84
PCL-DOX HCl 2%	98.93 ± 1.85
PCL-DOX HCl 5%	99.07 ± 1.61

Taking into account that hydrophilic DOX HCl molecules are highly accumulated at the surface of the scaffolds and hydrophobic PCL has a slow degradation profile. The initial burst release of DOX HCl should occur through diffusion, not an erosion of the polymer.[216]

The burst drug release is related to the accumulation of drug molecules on the surface of fibres. Together with the poor partitioning between hydrophilic DOX HCl and hydrophobic PCL, DOX HCl is to be readily released to the dissolution medium. There was a previous report observing that the microspheres fabricated from 20% w/v PCL concentration prolonged the release of DOX HCl when compared to microspheres made from 10% w/v PCL.[217] This is because the degradation products of PCL are acidic, hence can accelerate the further breakdown of PCL. The release of DOX HCl is therefore faster and less sustained in the microspheres fabricated from 10% w/v.

The release of DOX HCl from PCL-DOX HCl scaffolds is faster and higher than the release of IBU Na from PLGA-IBU Na scaffolds. This corresponds to more hydrophobicity of PCL in comparison with PLGA.[153,218] Therefore, the partition

of hydrophilic drugs like DOX HCl in PCL is more likely to be less than the partition of PLGA and IBU Na.

In addition, NMR spectra indicate that the molecules of PLGA interact with the molecules of IBU Na. Whilst, PCL and DOX HCl do not have molecular interactions. This results in less amount of IBU Na released from PLGA fibres into PBS when compared to the amount of DOX HCl released from PCL fibres at the same time point.

Moreover, it was reported that PCL polymer chains can uptake water more rapidly than PLGA because PCL polymer chains are in a rubbery state (lower T_g).[219] While, PLGA polymer chains are in a glassy state (higher T_g), retarding the mobility of water and drug.[219]

Jia *et al* observed the burst release of DOX HCl from PCL fibres.[188] The higher drug loadings leads to the greater encapsulation efficiency which results in more rapid burst drug release.

Riggin *et al* reported that the release profile of ibuprofen from PLGA fibres is in a triphasic pattern when incubated in PBS over 60 days.[136] In the first three days, approximately 20% of ibuprofen was rapidly released into PBS, followed by a lag phase during day 3 to day 10. After 10 days, ibuprofen was released at the rate of 1 μg/mg scaffold/day until reaching approximately 70% drug release on day 60.[218] Similarly, Canton *et al* demonstrated an initial burst release of

ibuprofen from PLGA electrospun scaffolds during the first 5 hours and then the release of ibuprofen remained constant over 7 days in water.[90]

4.5.2.8 Doxycycline hydrochloride-PCL interaction by NMR

The ^{1}H spectrum of an authentic sample of DOX HCl (crystallised in EtOH) is matched with the literature values (Figure 4.18).[220,221] Herein, only key signals are explained as some of the OH signals from the hydroxyl groups rapidly exchange with the deuterated solvent. This is due to their acidic character, leading to the broadness of signals.[221]

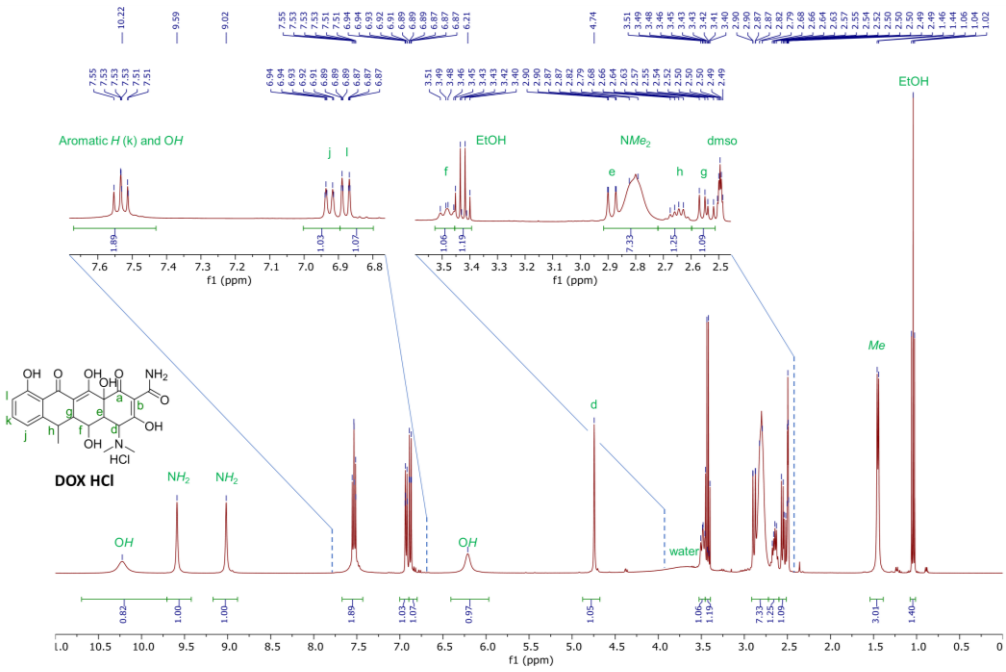


Figure 4.18. ^{1}H NMR spectrum of doxycycline hydrochloride (DOX HCl) in d_6-DMSO.

There are broad singlet signals of O*H* being observed at 11.48 (observed by COSY NMR), 10.22, 7.53 (obscured by the peak of the aromatic proton at position k), and 6.21 ppm. Next, there are 2 sharp singlets at 9.59 and 9.02 ppm,

which are the characteristic peaks of a primary amide (CONH_2) in the tetracycline drugs. A triplet at 7.53 ppm is assigned to the aromatic hydrogen at position k; another 2 aromatic hydrogen atoms (positions j and l) give the doublet peaks at 6.92 and 6.88 ppm, respectively. These aromatic proton signals will be later used to indicate the presence of DOX HCl in PCL-DOX HCl 5% scaffolds. The sharp singlet peak at 4.74 ppm belongs to the methine hydrogen (C*H*) at position d. Interestingly, this peak does not appear as a doublet even though it seemed to be able to couple with the nearby hydrogen (position e); this is due to the fact that the conformation of a doxycycline molecule sets the dihedral between the two hydrogen atoms to be ~ 90°, which minimises the effect of proton-proton coupling according to the Karplus equation.[222]

The methine hydrogen at position f gives a broad triplet signal at 3.48 ppm. This signal appears as a triplet because it couples to the adjacent hydrogen atoms at positions e and g. The doublet peak at 2.89 ppm correlates with the hydrogen atom at position e. The hydrogen atoms in the dimethyl amine unit (NMe_2) of doxycycline give rise to a broad singlet signal of 6 protons at 2.80 ppm. The methine hydrogen at position h results in a multiplet at a chemical shift of 2.65 ppm; this multiplet peak couples with the hydrogen atom at position g and 3 hydrogen atoms of the methyl group (Me).

A peak of double of doublets at 2.55 belongs to the hydrogen atom at position g; this peak is in the form of a double of doublets since it couples with hydrogen atoms at 2 different positions: f and h. The last key peak (doublet, 1.45 ppm,

coupling with the hydrogen atom at position h) is the signal of the methyl hydrogens (CH_3).

It is worth mentioning that there are a few signals in the spectrum which do not belong to doxycycline molecule: residual DMSO from the NMR solvent (2.50 ppm), residual water present in the solvent (very broad, 3.33 ppm), and the peaks of crystallising ethanol (a quartet at 3.43 ppm and a triplet at 1.04 ppm)

The spectrum shows 4 distinct proton signals of PCL in d_6-DMSO (Figure 4.19).

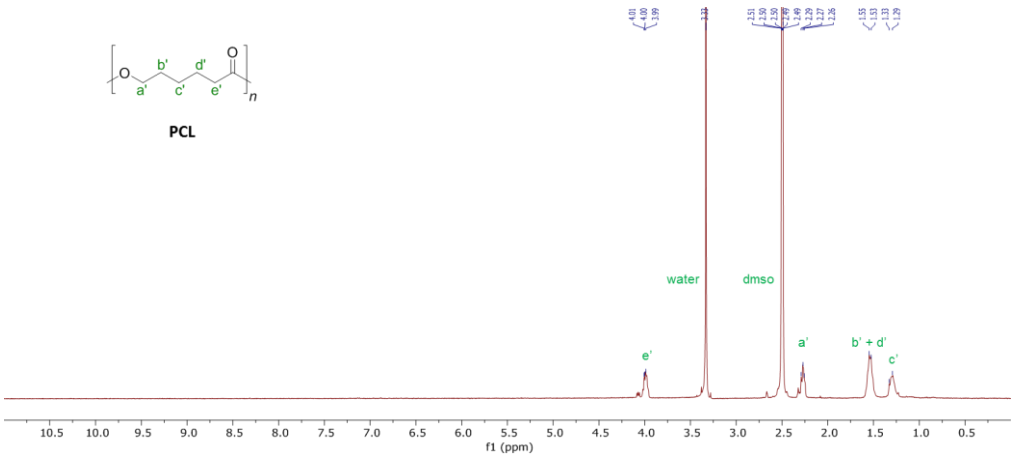


Figure 4.19. ^{1}H NMR spectrum of polycarbolactone (PCL) in d_6-DMSO.

The multiplet at about 4.00 ppm belongs to the 2 hydrogen atoms of the methylene group adjacent to the carbonyl unit (e'). The signal at 2.27 ppm (multiplet) corresponds with the methylene hydrogen atoms next the hydroxyl group (a'). The peak at 1.54 ppm is the result of the two overlap signals of the two methylene groups (4 hydrogen atoms) at positions b' and d'. The last signal (at 1.31 ppm) is assigned to the methylene hydrogen atoms at position c'. It is

worth nothing that the two massive signals at around 3.33 and 2.50 ppm are the signals of residual water and dimethyl sulfoxide, respectively.

Since the amount of DOX HCl is significantly less than PCL (polymer), not all the signals of the drug can be observed in the spectrum (Figure 4.20).

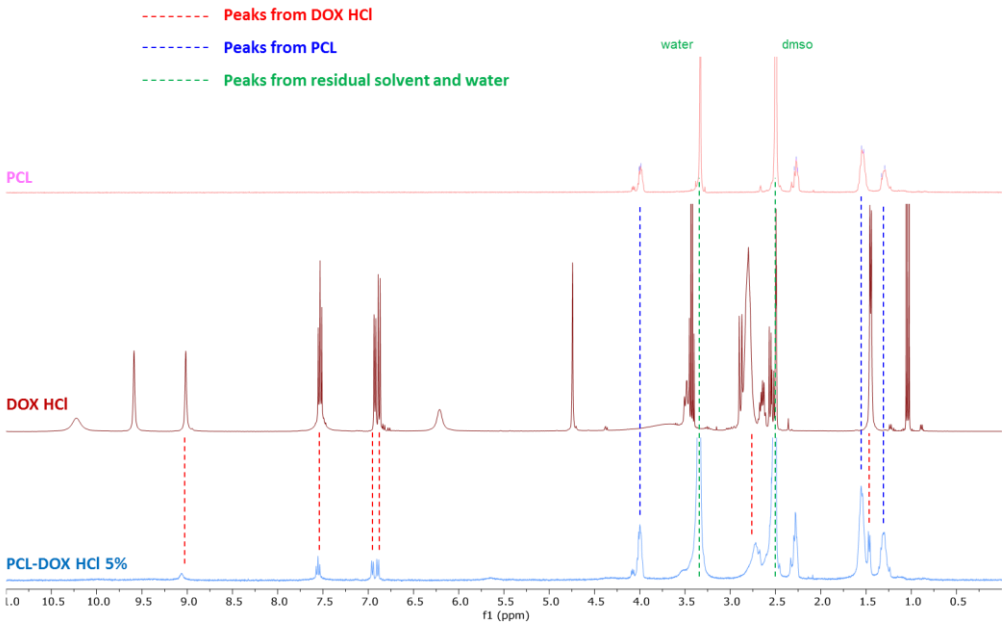


Figure 4.20. No peak shifts were observed in the ^{1}H NMR spectrum of PCL-DOX HCl 5%, which indicates no significant molecular interactions between the polymer scaffolds and the drug.

There are some peaks of DOX HCl being observed from the ^{1}H spectrum of PCL-DOX HCl 5%: 9.02, 7.53, 6.92, 6.88, 2.80, and 1.45 ppm (Figure 4.20, blue spectrum). Unlike the case of IBU Na/PLGA (*see* Chapter 3), there is no significant peak shift, which could suggest that there are no significant interactions between the drug and the polymer scaffolds. As a result, a burst release of doxycycline from the PCL-DOX HCl scaffolds was observed in the drug release experiments.

4.5.2.9 Degradation profiles of the scaffolds

The *in vitro* degradation of the scaffolds was determined by monitoring % weight loss and morphological changes (Figures 4.21 and 4.22). Within 14 days, PCL-DOX HCl scaffolds lose more than 30% of their initial weights. Whilst, blank PCL scaffolds degraded slower, losing approximately 12% of their weights. The degradation of the scaffolds gradually continued over time. On day 90, % weight loss of blank PCL scaffolds reached approximately 22%. Whereas, the weight of PCL-DOX HCl reduced by 37–50%. It was noticed that the morphology of the scaffolds was not significantly changed throughout the course of study (90 days). Only a small number of fibres were swollen and fused with nearby fibres.

Ha *et al.* explained that the slow degradation of PCL in aqueous solutions was due to its semi-crystalline and hydrophobic nature.[223] The degradation of PCL occurs slowly through the hydrolysis of labile ester linkages.[210,224] Initially, chain scission takes place, leading to a decrease in molecular weight. Later, the weight of the scaffold reduces and PCL breaks into small units. The rate of degradation of PCL scaffolds is likely to speed up with the increasing amount of DOX HCl. This is a result of weak acidity of DOX HCl, which accelerates the hydrolysis of ester linkages in PCL chains. Higher weight loss of PCL-DOX HCl scaffolds was therefore observed when compared to PCL scaffolds.

The degradation of PCL scaffolds were considered rapid when compared to the report from literatures that the degradation of PCL requires approximately 1–2 years.[225,226] This is possibly due to the protocol used in the degradation study

that the scaffolds were placed in the vacuum oven at 30 °C to remove remaining water in the scaffolds. The degradation of PCL may be accelerated by heat.[227] Hence, the percentage of weight loss was higher than expected. Nevertheless, Augustine *et al* also reported that PCL fibrous scaffolds lost approximately 18% of their weight after being incubated in simulated body fluid for 30 days.[228] Higher surface to volume ratio of electrospun scaffolds may increase rate of degradation by facilitating water penetration to reach PCL polymer chain which enhances hydrolysis of ester linkages in PCL backbone.[228]

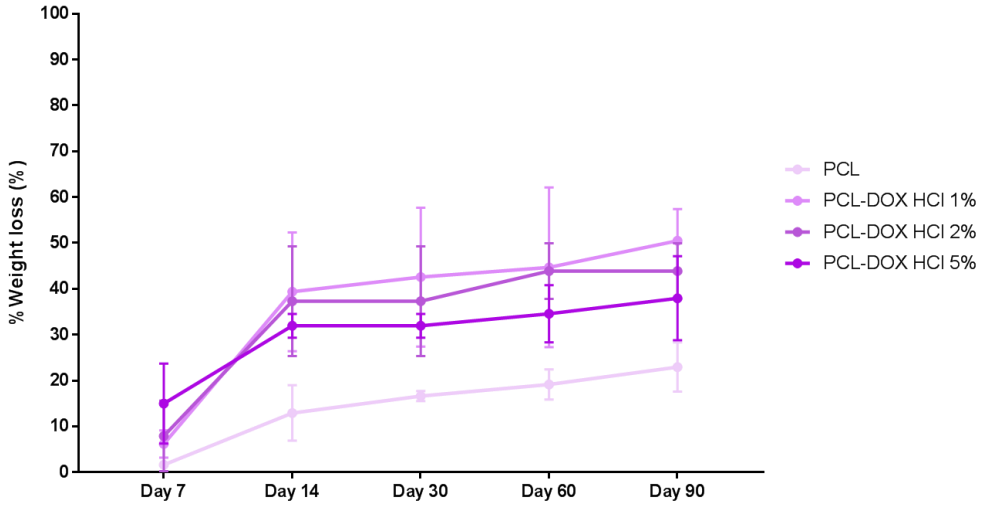


Figure 4.21. Degradation profiles of the scaffolds in PBS solution (pH 7.4) shown as % weight loss. The values shown in the graph are means and standard deviations of triplicate samples.

Table 4.8. % Weight loss of the scaffolds over time determined in the *in vitro* degradation study. The values are means and standard deviations of triplicate samples.

Time point	% Weight loss (mean ± SD)			
	PCL	PCL-DOX HCl 1%	PCL-DOX HCl 2%	PCL-DOX HCl 5%
Day 7	1.62 ± 0.84	6.15 ± 2.97	7.91 ± 7.70	14.99 ± 8.73
Day 14	12.92 ± 6.05	39.36 ± 12.95	37.30 ± 11.96	31.94 ± 2.59
Day 30	16.63 ± 1.10	42.55 ± 15.13	37.30 ± 11.96	31.94 ± 2.59
Day 60	19.16 ± 3.28	44.68 ± 17.42	43.86 ± 6.06	34.55 ± 6.23
Day 90	22.94 ± 5.37	50.49 ± 6.92	43.86 ± 6.06	37.95 ± 9.17

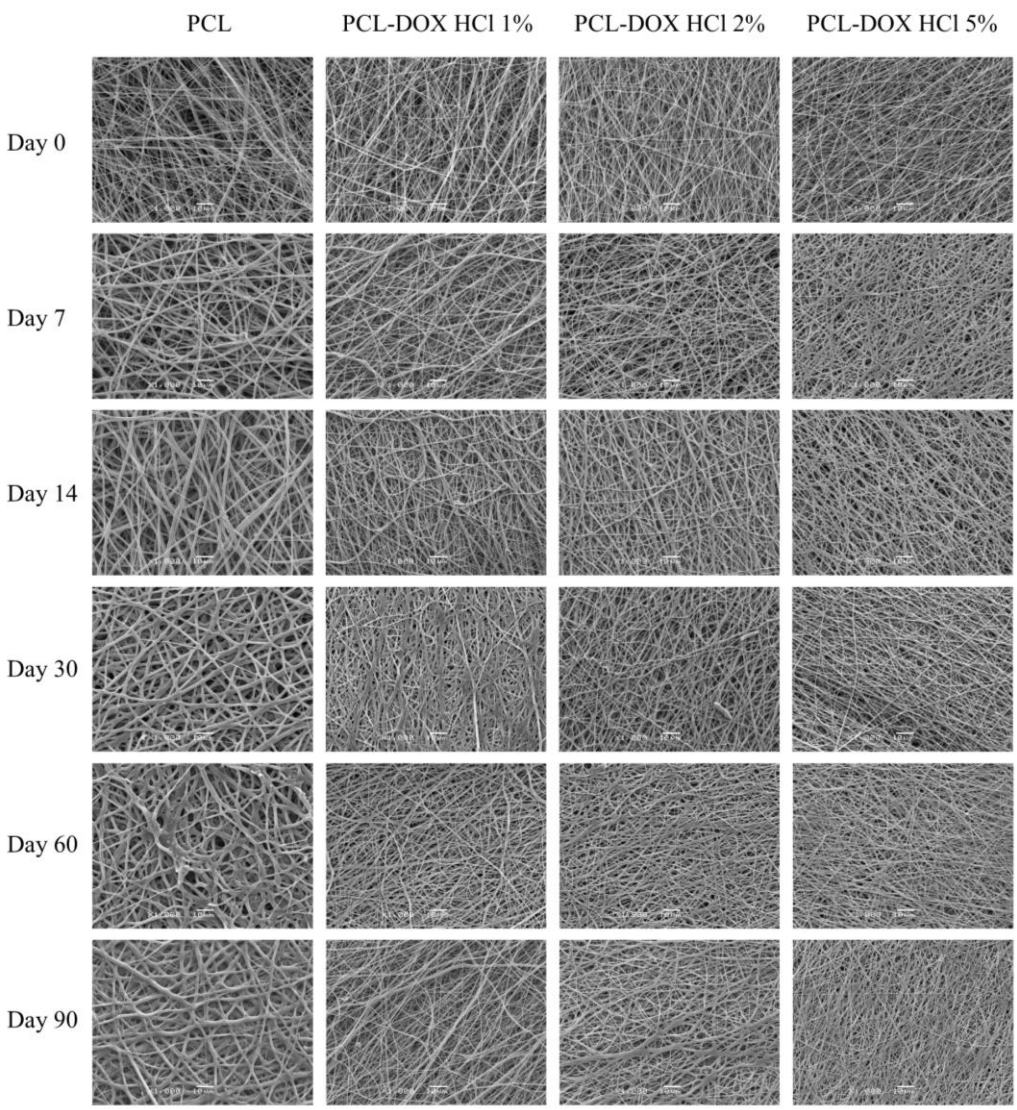


Figure 4.22. Representative SEM images showing morphological changes of the scaffolds over time. All images are illustrated at the magnification of 1,000X. The scale bar is 10 μm.

4.5.3 Drug cytotoxicity

In order to assess cytotoxicity of DOX HCl, mouse fibroblasts and primary human dermal fibroblasts were treated with different concentrations of DOX HCl in cell culture media for 24 hours and cellular metabolic activity was investigated using PrestoBlue® assay. A significant decline in cellular metabolic activity was observed when mouse fibroblasts were treated with 100 and 1,000 µM DOX HCl in cell culture media (Figure 4.23A). Whist, a significant drop in cellular metabolic activity of primary human dermal fibroblasts was observed at the concentration of 10 µM and higher (Figure 4.23B). According to the results, DOX HCl exhibited a distinct cytotoxic effect when mouse fibroblasts or primary human dermal fibroblasts were treated with DOX HCl at the concentrations of 100 and 1,000 µM as cell viability was less than 80% and 50%, respectively.

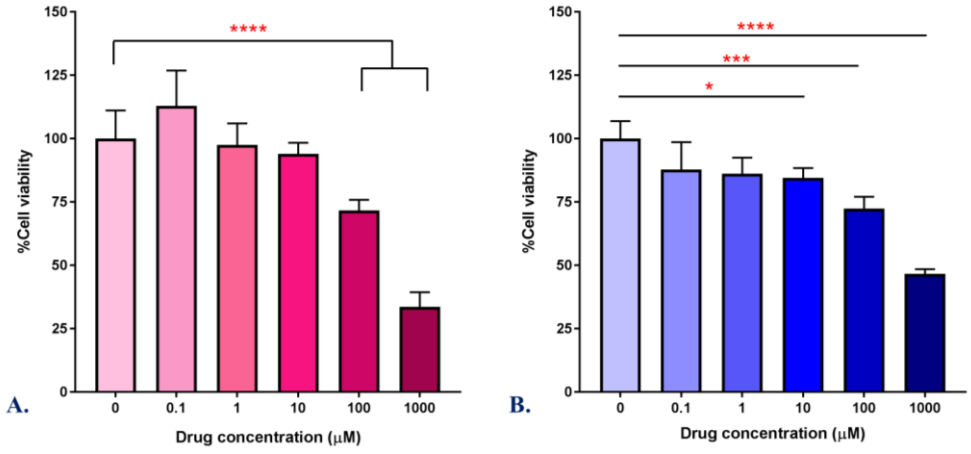


Figure 4.23. Cytotoxic effect of DOX HCl was evaluated by PrestoBlue® assay. Metabolic activity of cells was assessed after being treated with complete cell culture media containing DOX HCl at different concentrations ranging from 0 to 1,000 µM for 24 hours. *, ***, **** define significant difference when compared to cell control (0 µM) at *p*-value < 0.05, < 0.001 and < 0.0001, respectively. (A) Mouse fibroblasts (n = 6/concentration) and (B) Primary human dermal fibroblasts (n = 3/concentration).

4.5.4 Cell proliferation

4.5.4.1 Cellular metabolic activity by PrestoBlue® assay

The ability of the scaffolds to support cell proliferation was monitored using PrestoBlue® assay over 14 days. The higher fluorescence intensities correlate to the increasing numbers of cells. Overall, mouse fibroblasts proliferated on all scaffolds over time. A slower rate of proliferation and fewer number of cells were observed in all PCL-DOX HCl scaffolds on day 3 of cell culture and onwards when compared to blank PCL scaffolds (Figure 4.24). At day 14 of the study, the lowest cellular metabolic activity was observed in PCL-DOX HCl 5% scaffolds when compared to PCL, PCL-DOX HCl 1% and PCL-DOX HCl 2% scaffolds.

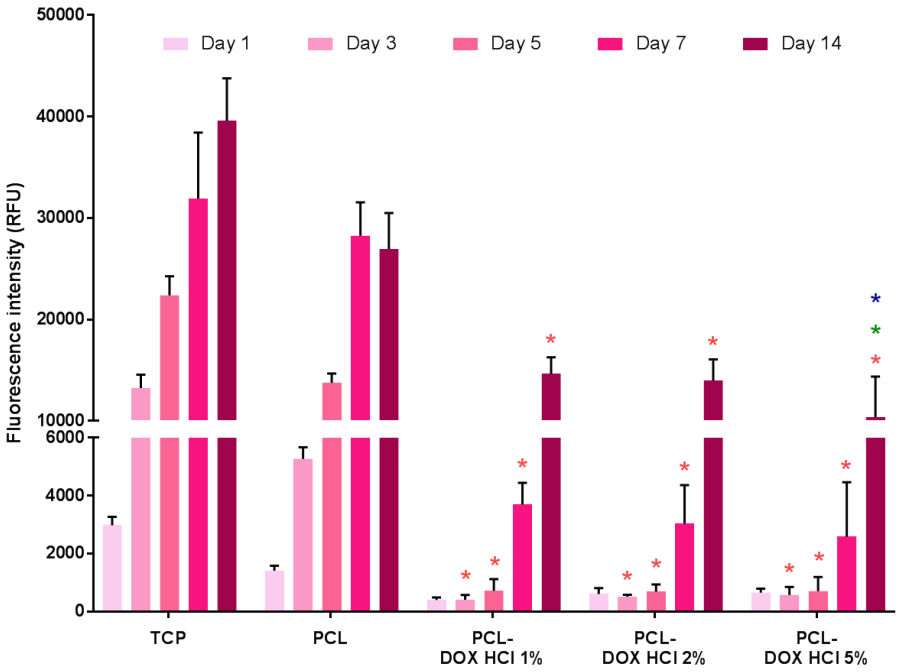


Figure 4.24. Cell proliferation on TCP, PCL, PCL-DOX HCl 1%, PCL-DOX HCl 2% and PCL-DOX HCl 5% electrospun scaffolds determined by cellular metabolic activity of mouse fibroblasts (3T3 cells) over 14 days using PrestoBlue® assay. The values are shown as means and standard deviations (n = 6). * defines a significant difference at *p*-value < 0.0001 when compared to PCL scaffolds at the same time point. * defines a significant difference at *p*-value < 0.001 when compared to PCL-DOX HCl 1% scaffolds at the same time point. * defines a significant difference at *p*-value < 0.01 when compared to PCL-DOX HCl 2% scaffolds at the same time point.

The similar proliferation profile was observed in primary human dermal fibroblasts (Figure 4.25). Cells adhered and grew on the scaffolds throughout 7 days of cell culture. However, the metabolic activity of cells was lower in all PCL-DOX HCl scaffolds when compared to the blank PCL scaffolds after 4 days of cell culture. After 7 days of cell culture, the proliferation of cells on PCL-DOX HCl scaffolds remained lower than PCL scaffolds in which PCL-DOX HCl 5% scaffolds had the lowest cell numbers presented as the lowest fluorescence intensity.

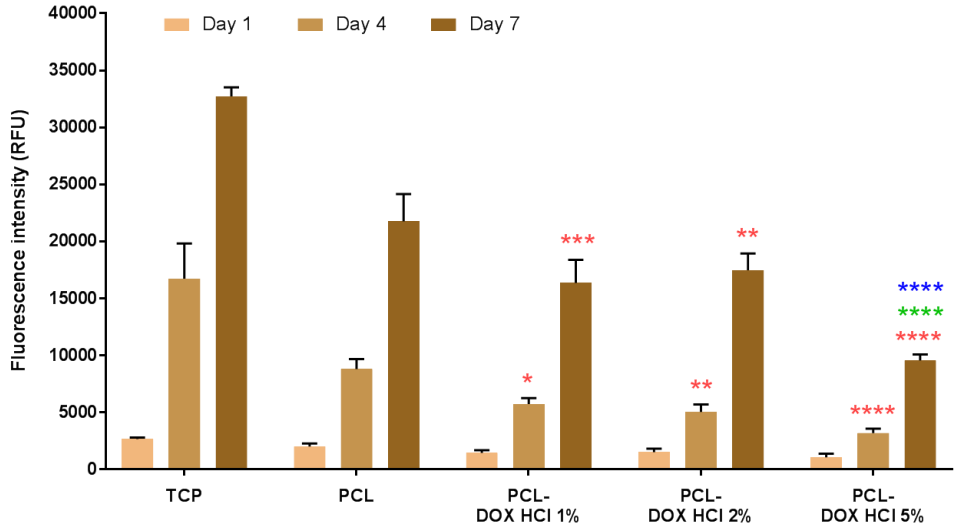


Figure 4.25. Cell proliferation on TCP, PCL, PCL-DOX HCl 1%, PCL-DOX HCl 2% and PCL-DOX HCl 5% electrospun scaffolds were determined by cellular metabolic activity of primary human dermal fibroblasts over 7 days using PrestoBlue® assay. Values shown as means and standard deviations (n = 3). *, **, *** and **** define a significant difference between the scaffolds at the same time point at *p*-value < 0.05, < 0.01, < 0.001 and < 0.0001, respectively. Red, blue and green asterisks were used to indicate the significance when compared to PCL, PCL-DOX HCl 1%, PCL-DOX HCl 2% scaffolds, respectively.

Cell proliferation on TCP, a 2D control, was higher than those on PCL electrospun scaffolds with or without DOX HCl. This probably relates to the hydrophobic property of PCL that negatively affects cell adhesion and penetration into the scaffolds.[224]

The addition of DOX HCl into PCL scaffolds retarded the proliferation of mouse fibroblasts and also primary human dermal fibroblasts. During the study, it was found that DOX HCl remained in the scaffolds by inspection–the yellow colour (drug colour) was clearly visible. Higher intensity of yellow colour was observed in the scaffolds with higher drug loadings (*see* Appendix). Moreover, the solubility of DOX HCl in cell culture media was less than that of in PBS. This is because cell culture media contains supplements. Therefore, there is less free water molecules that are available to dissolve DOX HCl.

When considering the conditions used in the proliferation study, the maximum concentrations of DOX HCl in cell culture media approximately 50, 100 and 250 μM could be obtained from PCL-DOX HCl 1%, PCL-DOX HCl 2% and PCL-DOX HCl 5% scaffolds, respectively. If DOX HCl was not completely released from the scaffolds and remained at the surface of the scaffolds, seeded cells would come into contact with a high amount of drug. The cytotoxicity of DOX HCl was therefore observed, as reflected in the reduction of the cellular metabolic activity.

4.5.4.2 LIVE/DEAD® assay

Fluorescence images confirm the presence of primary human dermal fibroblasts on the surface of the scaffolds (Figure 4.26). The number of viable cells (emitting green fluorescence) highly increased from day 1 to day 7. After 7 days of cell culture, the surface of scaffolds were fully covered with cells.

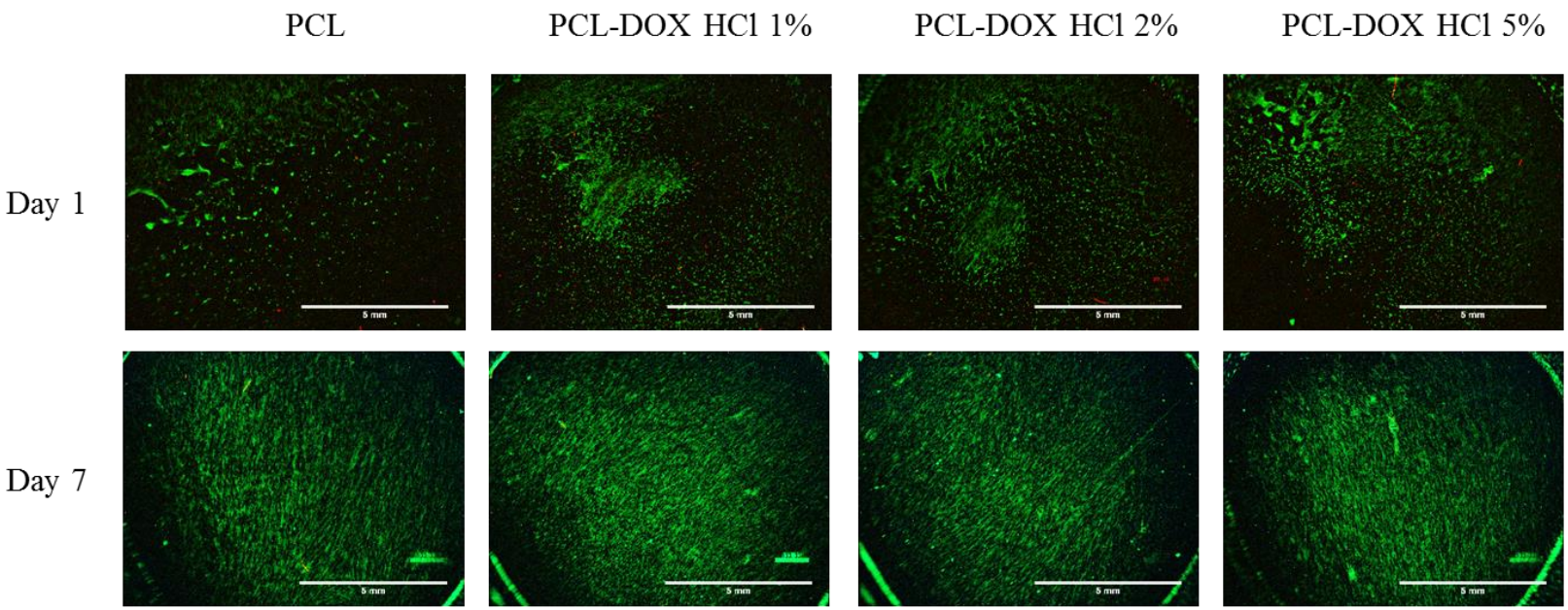


Figure 4.26. Fluorescent images obtained from LIVE/DEAD® assay illustrating the presence of viable (green) and dead (red) cells of primary human dermal fibroblasts on the surface of the electrospun scaffolds after 1 and 7 days of cell culture. Scale bar is 5 mm.

4.5.4.3 Cell morphology by SEM

SEM images in Figure 4.27 illustrates the morphology of cells that were cultured on the scaffolds. The morphology of mouse fibroblasts was rounded on all scaffolds until day 5 when the morphology of cells on PCL scaffolds became spindle-shaped. It was also noticed that higher DOX HCl in the scaffolds delayed the transformation of cell morphology from rounded to spindle shapes.

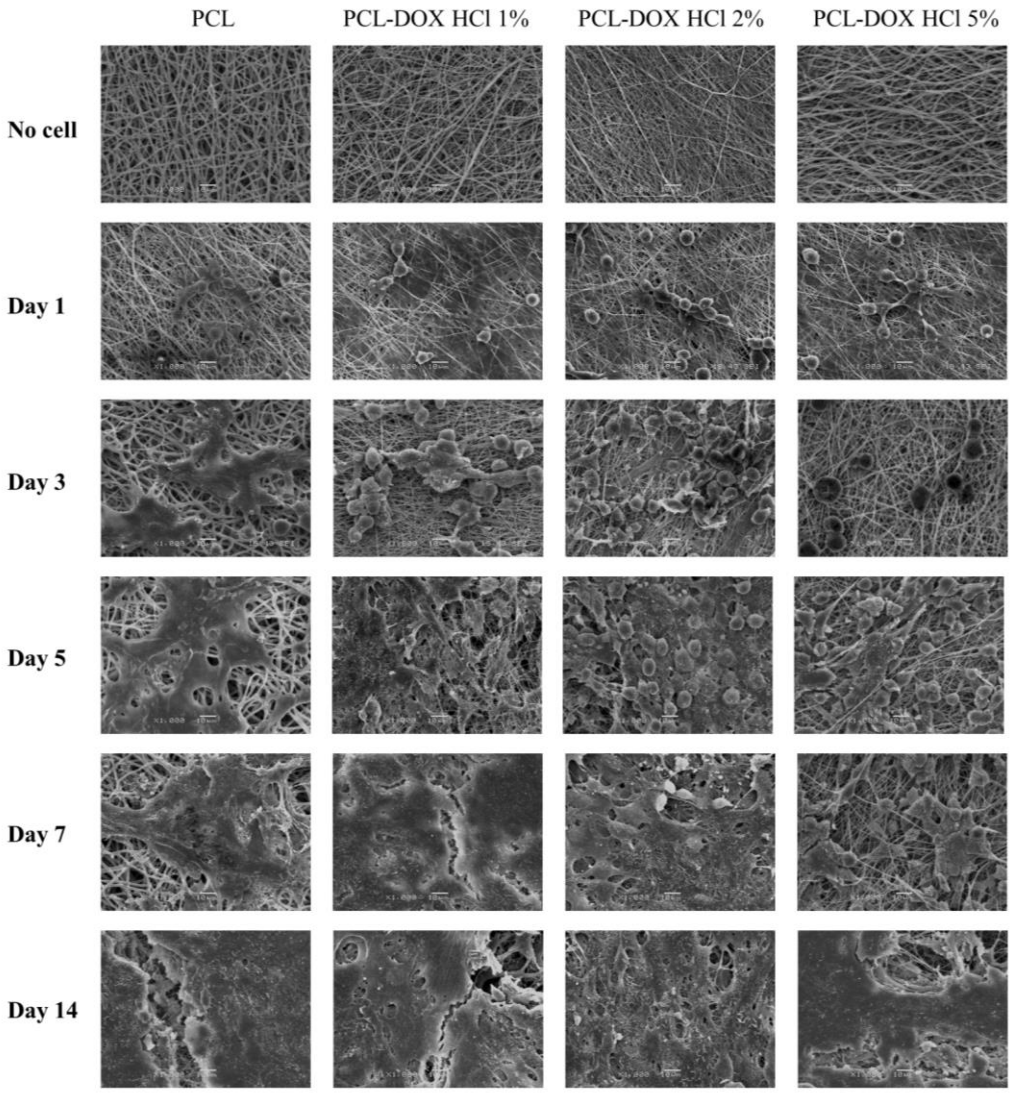


Figure 4.27. Representative SEM images showing cell morphology of mouse fibroblasts on the electrospun scaffolds at the magnification of 1,000X (scale bar 10 μm).

The morphology of primary human dermal fibroblasts was spindle shaped from day 1 of cell culture (Figure 4.28). Cells proliferated quickly and densely packed on the surface of the scaffolds within 7 days of cell culture.

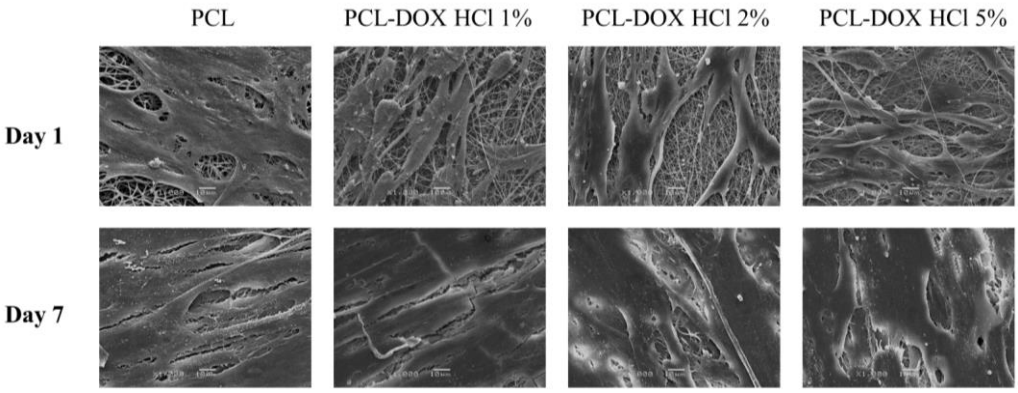


Figure 4.28. Representative SEM images showing cell morphology of primary human dermal fibroblasts on the electrospun scaffolds at the magnification of 1,000X (scale bar 10 μm).

The morphology of primary human dermal fibroblasts on the electrospun scaffolds were elongated since day 1 of cell culture, whereas mouse fibroblasts were rounded until day 5 of cell culture. This is perhaps because the compositions of cell culture media used for culturing these two cell types are different. Cell culture media used for primary human dermal fibroblasts contains fibroblast growth factor. Hence, the surface of scaffolds absorbs fibroblast growth factor, enhancing cell adhesion, elongation and proliferation.[229–232]

Table 4.9. Summary of scaffold properties

Property	PCL	PCL-DOX HCl 1%	PCL-DOX HCl 2%	PCL-DOX HCl 5%
Fibre diameter (nm)	638 ± 135	466 ± 86	353 ± 72	382 ± 71
Porosity (%)	79.45 ± 1.72	80.90 ± 1.17	81.89 ± 2.08	81.22 ± 0.98
Water contact angle (static)	105.11 ± 6.64	101.45 ± 7.93	109.48 ± 5.49	87.77 ± 6.85
Water contact angle (advancing)	114.78 ± 9.38	113.35 ± 8.45	110.36 ± 6.34	113.91 ± 9.09
Water contact angle (receding)	21.29 ± 2.09	26.70 ± 2.21	27.71 ± 9.20	32.61 ± 3.11
Contact angle hysteresis	93.49 ± 10.31	86.65 ± 7.51	82.65 ± 13.17	81.30 ± 10.88
Ultimate tensile strength (MPa)	3.37 ± 0.45	14.04 ± 3.97	11.46 ± 1.32	13.95 ± 0.71
Strain at break (%)	394.17 ± 41.82	144.16 ± 18.75	129.48 ± 7.31	169.18 ± 21.22
Young's modulus (MPa)	15.48 ± 1.75	36.89 ± 10.00	33.58 ± 4.64	34.49 ± 2.18
Encapsulation efficiency (%)	N/A	89.87 ± 2.97	92.14 ± 1.84	96.20 ± 2.14
Cumulative drug release in 30 days (%)	N/A	96.05 ± 6.84	98.93 ± 1.85	99.07 ± 1.61
Drug localisation	N/A	Surface/Matrix	Surface	Surface
Drug-polymer interaction	N/A	No	No	No
Cumulative weight loss in 90 days (%)	22.94 ± 5.37	50.49 ± 6.92	43.86 ± 6.06	37.95 ± 9.17
Cell proliferation on the scaffolds	Yes	Yes	Yes	Yes

N/A: not applicable

4.6 Conclusion

DOX HCl-loaded PCL electrospun scaffolds were fabricated to serve as a wound dressing and drug delivery system. The properties of polymer solutions before electrospinning and the produced scaffolds were characterised. The addition of DOX HCl increased conductivity of PCL solutions, hence reducing the fibre diameter of the electrospun scaffolds. The morphology of all scaffolds was smooth rounded nanofibres. Total porosity was high (around 80%), and consistent throughout the scaffold regardless of % drug loading. However, the mechanical properties of PCL-DOX HCl scaffolds were significantly different from the blank PCL scaffolds. The ultimate tensile strength and Young's modulus were increased with DOX HCl incorporation whereas % strain at break dramatically dropped. Large contact angle hysteresis indicated that the scaffolds had rough surface and exhibited hydrophobic property. The wettability of PCL-DOX HCl 5% scaffolds was the most hydrophilic among the other scaffolds (1% and 2% DOX HCl) as manifested by the small water contact angle (lower than 90°).

The encapsulation of DOX HCl in PCL electrospun scaffolds was successfully achieved. More than 89% of DOX HCl was encapsulated in the scaffolds for all drug loadings. The release of DOX HCl exhibited as a rapid burst release within 30 minutes with more than 96% drug released. ToF-SIMs analysis revealed that DOX HCl deposited on the surface of fibres with increasing amounts when drug loadings were higher. In addition, the spectra from NMR spectroscopic analysis also show weak interaction between PCL and DOX HCl. These findings support the observation of burst drug release in PBS. In terms of *in vitro* degradation, %

weight loss of PCL-DOX HCl scaffolds was significantly higher than PCL scaffolds due to drug acidity. Although morphological changes were not observed during the course of study.

Cytotoxicity of DOX HCl was screened both in mouse fibroblasts and primary human dermal fibroblasts. The significant decreases in cell viability by 25% and 50% were observed when cells were treated with 100 and 1,000 μM DOX HCl, respectively. Mouse fibroblasts could adhere to fibres and proliferate on the surface of the scaffolds over time, although their proliferation was slower when compared to TCP. This was due to the hydrophobicity of PCL. In addition, lower cellular metabolic activity was observed in all PCL-DOX HCl scaffolds when compared to blank PCL scaffolds. In this regard, it was a result of poor solubility of DOX HCl in cell culture media. Therefore, cells were in direct contact with DOX HCl-enriched surface of scaffolds when first seeded. The proliferation of fibroblasts on PCL-DOX HCl 5% scaffolds was considered the slowest, which is possibly due to more drug amount in the fibres. The growth of primary human dermal fibroblasts was rapid, and the surfaces of the scaffolds were fully covered by cells within 7 days. Moreover, the morphology of mouse fibroblasts transformed into spindle-shaped after 5–7 days of cell culture, whilst, primary human dermal fibroblasts showed a spindle shape morphology from day 1 of cell culture and throughout.

This chapter has shown fabrication of DOX HCl-loaded electrospun scaffolds. The scaffolds have been shown to be able to deliver DOX HCl while still supporting the proliferation of cells.

Chapter 5

Fabrication and Characterisation of Dual Drug-loaded Coaxial PCL/PLGA Electrospun Scaffolds

5.1 Introduction

A study involving 758 patients with leg ulceration found that the prolonged duration of non-healing wounds led to the higher number of pain-relating reports.[233] In order to manage wound pain, oral or topical administration of drug in the family of non-steroidal anti-inflammatory drugs (NSAIDs) and opioids is often selected for patients based on the severity of pain.[42,234] However, some patients did not respond to an oral analgesia.[235]

As mentioned in the previous chapters, chronic inflammation is associated with wound pain.[41,42,236] Therefore, treatment aimed at modulating chronic inflammation may accelerate the healing of wounds and reduce pain.

There are several drugs that exhibit anti-inflammatory effects involving several pharmacological pathways. In Chapter 3, the pharmacological effects of NSAIDs such as ibuprofen have been described. In short, NSAIDs inhibit the activity of cyclooxygenase (COX) enzymes, preventing the production of prostaglandins.[109,110] Moreover, they inhibit inducible nitric oxide synthase (iNOS) and scavenge reactive oxygen species.[111] In Chapter 4, drug analogues in the family of tetracycline such as doxycycline were introduced as they exhibit anti-inflammatory effect at low doses by inhibiting the activity of matrix

metalloproteinases (MMPs).[174–176,186] Furthermore, It was found that doxycycline can scavenge reactive oxygen species[237], and inhibit pro-inflammatory cytokines (TNF-α and IL-1β)[238,239], and then reduce the expression of NOS by promoting the degradation of NOS mRNA through post-transcriptional modification of iNOS[181]. In addition, doxycycline is able to inhibit the activity of phospholipase A_2 (PLA_2), which is an enzyme involving the release of arachidonic acid from phospholipids to generate the inflammatory mediators like prostaglandins.[181] Figure 5.1 summarizes the activities of ibuprofen and doxycycline that are related to their anti-inflammatory effects.

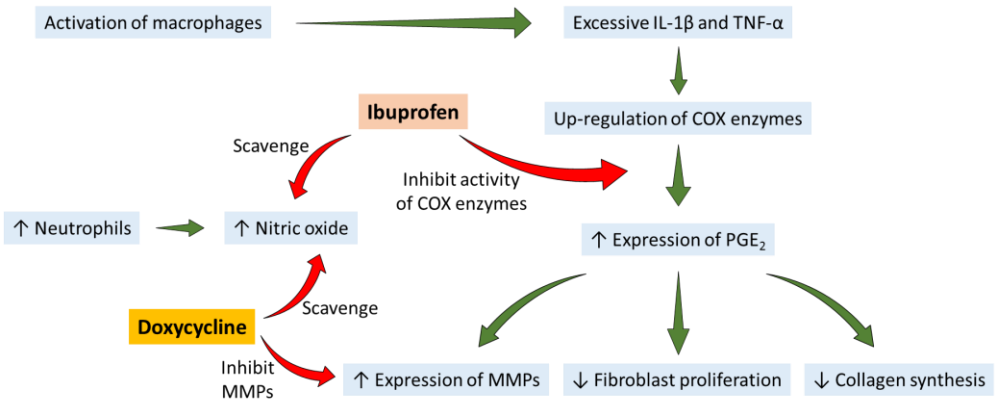


Figure 5.1. The activities of ibuprofen (IBU) and doxycycline (DOX)

Over several decades, the administration of sub-antimicrobial dose of doxycycline/tetracycline and NSAIDs has been studied in several animal and human disease models including periodontitis, rheumatoid arthritis, and osteoarthritis.[237,240–242] It has been observed that NSAIDs could potentiate the effects of tetracycline. Although NSAIDs do not directly inhibit MMPs, they modulate inflammation and reduce edema.[240] As a consequence, the uptake of doxycycline at the wound site increases.[240] It has also been reported that

administration of such a drug combination (tetracyclines and NSAIDs) synergistically suppressed the activity of MMPs, alleviated pain-associated inflammation, and reduced tissue destruction.[237]

According to the advantages of the two-drug combination regimen and the properties of electrospun scaffolds, a dual drug delivery system fabricated by the electrospinning technique was considered suitable for chronic wounds that require both the supportive structure and anti-inflammatory drugs. The electrospun scaffolds containing two drugs can be designed and produced by various techniques; monoaxial electrospinning (blending drugs with polymer solution, which will be electrospun using a monoaxial needle), coaxial electrospinning, and emulsion electrospinning.[243,244]

Coaxial electrospinning is modified from a standard electrospinning set-up (Figure 5.2). By using a coaxial nozzle, two polymer solutions are separately injected through inner and outer compartments, which will be met at the exit of the nozzle.[243,245] The droplet of polymer solutions are then elongated when electrostatic repulsion overcomes the surface tension of solutions, generating a core-shell structure in form of fibres.[243,246]

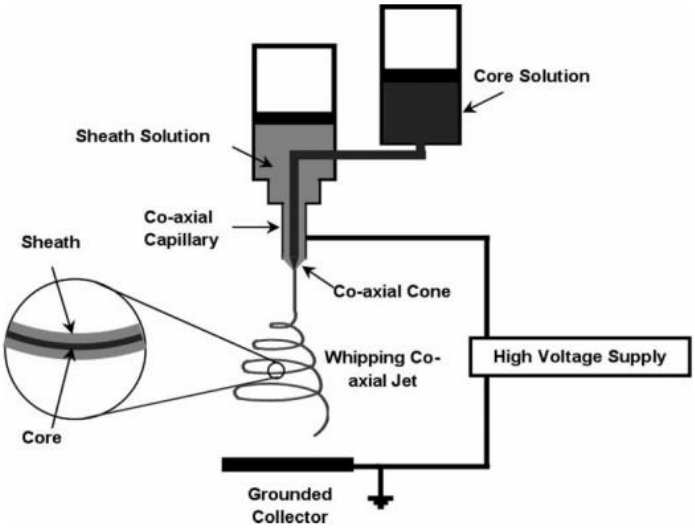


Figure 5.2. Schematic of coaxial electrospinning set-up[247]

The fabrication of fibres using coaxial electrospinning has benefits over a typical monoaxial electrospinning; it allows two drugs to be separated to core and shell parts.[248] In addition, better therapeutic effects and reduced toxicity could be obtained with coaxial fibres.[249] Moreover, loading drugs in different layers leads to different drug release profiles (*e.g.* fast release from shell and slow release from core).[250,251] However, other parameters such as polymer chemistry, drug concentration, solvents, electrospinning parameters (*e.g.* flow rate) and structure of the scaffolds also influence the release of drug from the scaffolds.[248,249,252,253]

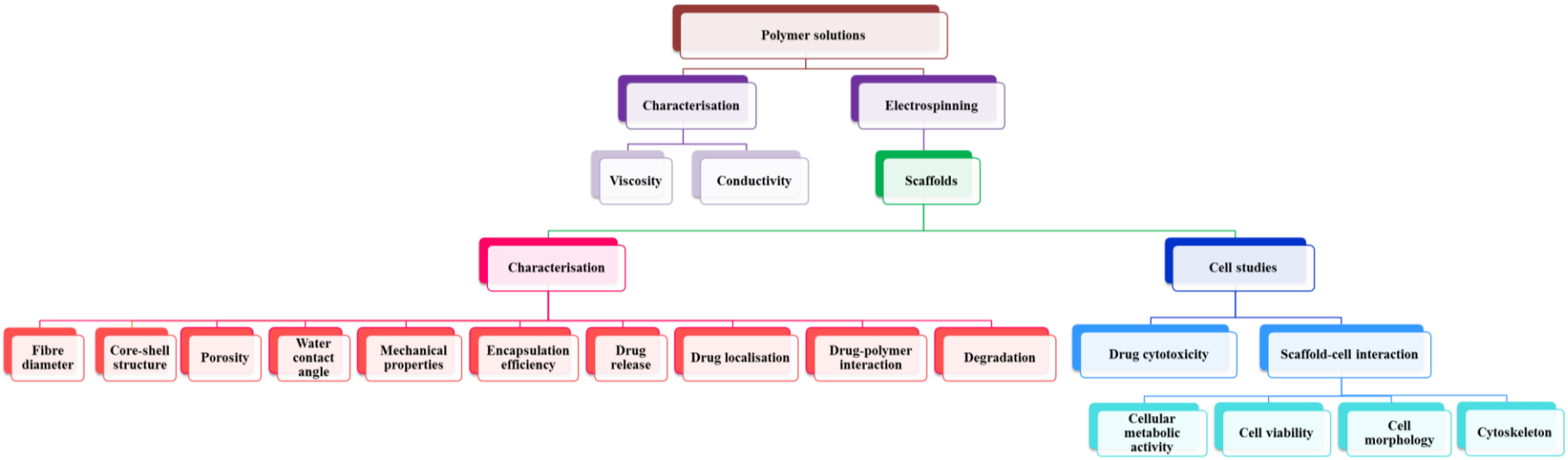
5.2 Aims and Objectives

The aims of this chapter were to investigate the fabrication of coaxial electrospun scaffolds containing IBU Na and DOX HCl. The scaffolds were characterised with various techniques to assess their properties. Lastly, the scaffolds were used in cell culture studies to investigate cell-scaffold interaction with mouse fibroblasts and primary human dermal fibroblasts.

The aims were achieved with the following objectives:

1. Manufacture coaxial electrospun scaffolds from biocompatible and biodegradable PLGA8515 and PCL, and incorporate DOX HCl and IBU Na into the scaffolds.
2. Characterise the electrospun scaffolds in terms of fibre diameter, total porosity, water contact angle, mechanical properties, drug encapsulation efficiency, drug release, drug localization, drug-polymer interaction and degradation.
3. Investigate cell proliferation, cell morphology and cytoskeleton on the coaxial electrospun scaffolds.

5.3 Experimental overview



5.4 Materials and Methods

5.4.1 Preparation of polymer and polymer-drug solutions

Core solutions

- PLGA8515 (MW 63 kDa, Evonik, UK) was dissolved in HFIP (Fluorochem, UK) by magnetic stirring overnight to obtain a 40% w/v polymer solution.
- PLGA8515-IBU Na 5% solution was prepared by dissolving IBU Na (5% w/w relative to PLGA dry weight) in the 40% w/v PLGA solution in HFIP. The solution was stirred overnight prior to the electrospinning fabrication.

Shell solutions

- PCL (Mn 800 kDa, Sigma-Aldrich, UK) was dissolved in HFIP (Fluorochem, UK) by magnetic stirring overnight to form a 10% w/v polymer solution.
- PCL-DOX HCl 1% solution was prepared by adding DOX HCl to the 10% w/v PCL solution at the concentration of 1% w/w relative to the weight of polymer. The vial of the solution was covered with aluminium foil to protect from light. The solution was mixed overnight using a magnetic stirrer and used for electrospinning next day.

5.4.2 Coaxial electrospinning set-up

Coaxial electrospinning was performed using a climate-controlled electrospinning apparatus (IME Technologies, Netherlands) in a horizontal orientation (Figure 5.3). Two polymer solutions were separately loaded into 5 mL syringes. The syringe of core solution was connected to one end of a tubing and the other end of the tubing was fitted with a stainless-steel core needle of the coaxial nozzle. Whilst, the syringe of the shell solution was connected to another tubing. The other end of the tubing was fitted with a sided stainless-steel needle of the shell part. The internal diameters of the nozzle at the exit are 0.4 mm and 1.2 mm for core and shell, respectively. The core and shell polymer solutions were pumped at a constant flow rate of 0.4 and 2 mL h^{-1} using a programmable syringe pump (Harvard Apparatus, USA), respectively. The polymer solutions were electrospun using 12 kV accelerating voltage supplied by a high voltage power supply. Electrospun scaffolds were collected on an aluminium foil sheet wrapped around a grounded aluminium-rotating collector (rotating at 150 rpm). The gap distance was set at 10 cm. The electrospinning processes were all performed at 20 °C and 30% relative humidity. All scaffolds were placed in a vacuum oven at 25 °C for 24 h to remove residual solvent.

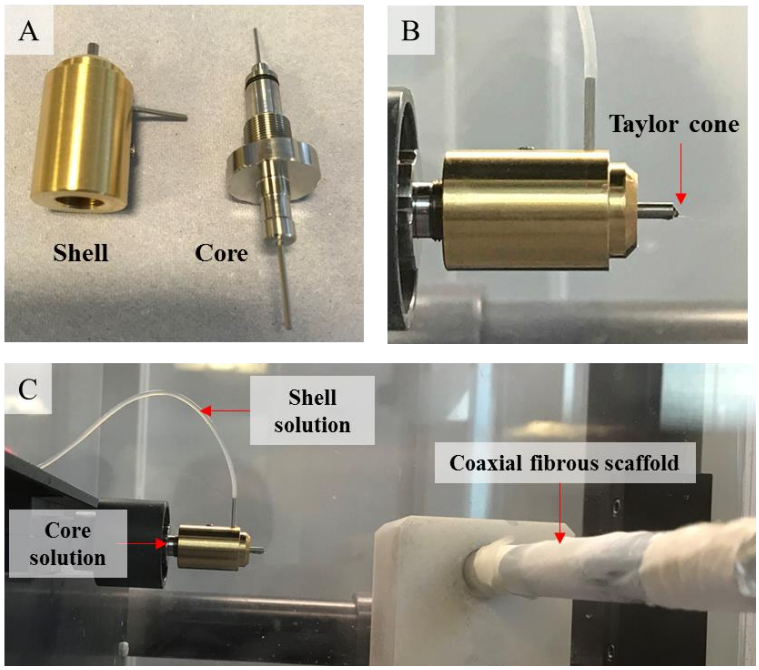


Figure 5.3. (A) Disassembled coaxial nozzle, (B) The formation of Taylor cone at the exit of the coaxial nozzle, and (C) The formation of scaffold using coaxial electrospinning technique

5.4.3 Transmission electron microscopy (TEM)

A sample was directly electrospun on a copper 300 mesh grid coated with holey carbon film (EM Resolutions Ltd., UK) for 15 seconds. Transmission electron microscopy (TEM) observations were performed using a FEI Tecnai G2 12 Biotwin (FEI Company, US), operated at an accelerating voltage of 100 kV.

5.4.4 Characterisation of the scaffolds

See chapter 2 General materials and methods

5.4.5 Cell studies

See chapter 2 General materials and methods

5.5 Results and Discussion

In order to produce coaxial fibres containing IBU Na and DOX HCl, the conditions used to fabricate single drug-loaded fibres in Chapters 3 and 4 were merged and modified for coaxial electrospinning. PCL and PLGA were selected as a carrier for DOX HCl and IBU Na, respectively, according to the suitability as discussed in the previous chapters.

The structure of coaxial fibres was designed in two different patterns: PCL as a core and PLGA as a shell, and vice versa. However, preliminary studies revealed that the release of DOX HCl from the PCL core was hindered (*see* Appendix). Less than 3% of DOX HCl was released over 30 days. It is perhaps because of the interaction between DOX HCl and PLGA. Although they were not blended together before electrospinning, DOX HCl has to diffuse through the PLGA shell. As a result, coaxial fibres made from PCL as a core and PLGA as a shell were excluded from the study.

In this chapter, coaxial fibres that consisted of PCL shell and PLGA core were manufactured and evaluated their potential to carry and release drugs (Figure 5.4). According to the findings in Chapter 4 and the goal to deliver the two drugs, DOX HCl was incorporated into the PCL shell at 1% w/w to avoid a cytotoxic effect seen at higher doses. Considering the small ratio of core to shell (1:5), PLGA core was loaded with 5% w/w IBU Na, which was the maximum acceptable drug loading found in Chapter 3.

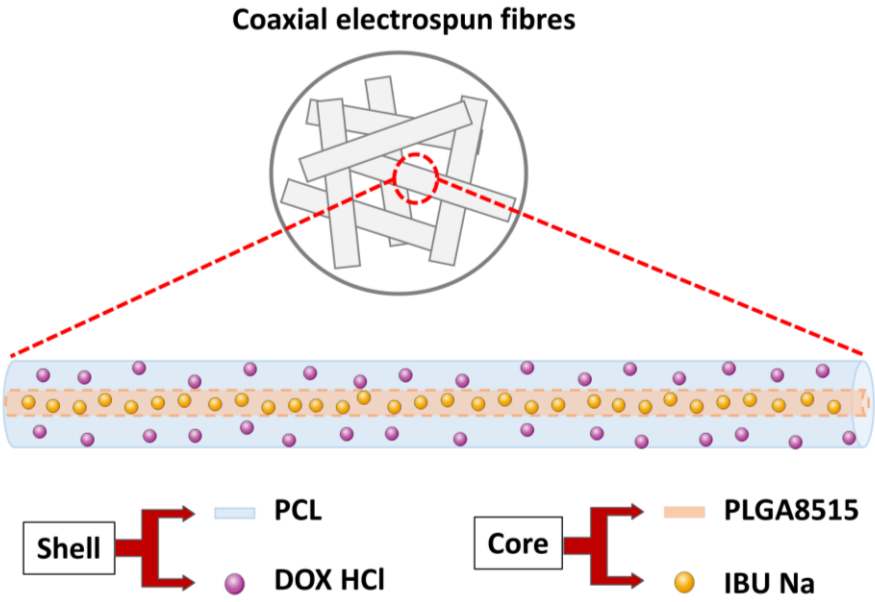


Figure 5.4. The structure of the coaxial fibre, polymers and drugs.

The work in this chapter shows investigation of the properties of the scaffolds when they contain

(i) no drug (PCL/PLGA scaffolds)

(ii) only DOX HCl in PCL shell (PCL-DOX HCl 1%/PLGA scaffolds),

and (iii) DOX HCl in PCL shell and IBU Na in PLGA core (PCL-DOX HCl 1%/PLGA-IBU Na 5% scaffolds).

5.5.1 The studies of polymer solution's properties

5.5.1.1 Viscosity

Similar to the results reported in Chapter 3 and Chapter 4, Figure 5.5A shows that PLGA solutions possessed higher viscosity than PLGA-IBU Na 5% solutions (2.16 ± 0.03 Pa·s *versus* 1.63 ± 0.03 Pa·s). In addition, the viscosity of PCL was significantly higher than the viscosity of PCL-DOX HCl 1% solutions (2.56 ± 0.10 Pa·s *versus* 2.33 ± 0.05 Pa·s). The reduction in viscosity was a result of drug's acidity that accelerates the hydrolysis of ester linkages in PCL and PLGA backbones.[90,124,125,191,193]

5.5.1.2 Conductivity

The conductivity of the polymer solutions dramatically increased when more electrolytes were added from drug molecules. Figure 5.5B shows that the conductivity of PCL solutions increased by approximately 20 fold when 1% w/w DOX HCl was incorporated (0.62 ± 0.01 $\mu S \cdot cm^{-1}$ *versus* 16.44 ± 0.16 $\mu S \cdot cm^{-1}$). A large increase in the conductivity by approximately 100 fold was also observed in PLGA solutions loaded with 5% w/w IBU Na (0.34 ± 0.02 $\mu S \cdot cm^{-1}$ *versus* 50.44 ± 0.22 $\mu S \cdot cm^{-1}$).

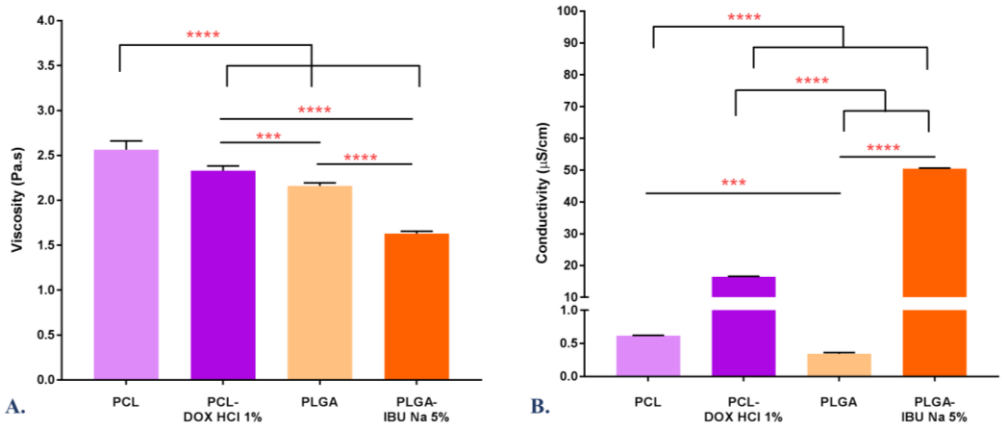


Figure 5.5. Means and standard deviations of (A) viscosity and (B) conductivity of polymer and polymer-drug solutions. The viscosity of solutions was averaged from six measurements (n = 6) and the conductivity of solutions were averaged from ten measurements (n = 10). *** and **** define statistical significance at *p*-value < 0.001 and < 0.0001, respectively.

Table 5.1. Viscosity and conductivity values of polymer and polymer-drug solutions. The average and standard deviation of viscosity were obtained from six measurements (n = 6). The average and standard deviation of conductivity were obtained from ten measurements (n = 10).

Solution	Viscosity (Pa·s)	Conductivity ($\mu S \cdot cm^{-1}$)
PCL	2.56 ± 0.10	0.62 ± 0.01
PCL-DOX HCl 1%	2.33 ± 0.05	16.44 ± 0.16
PLGA	2.16 ± 0.03	0.34 ± 0.02
PLGA-IBU Na 5%	1.63 ± 0.03	50.44 ± 0.22

5.5.2 The characterisation of scaffold properties

5.5.2.1 Fibre morphology and fibre diameter

Figure 5.6 illustrates representative SEM images of the coaxial electrospun scaffolds. All scaffolds were composed of smooth, round-shaped fibres with random orientations. No drug crystals were observed on the surface of fibres in all cases.

It was observed that loading DOX HCl (1% w/w) into PCL shell of the coaxial fibres led to a decrease in fibre diameter when compared to blank PCL/PLGA scaffolds (0.82 ± 0.21 µm *versus* 1.08 ± 0.34 µm, Figure 5.7). However, the size distribution of fibre diameter became narrower in PCL-DOX HCl 1%/PLGA scaffolds when compared to that of PCL/PLGA scaffolds (histograms in Figure 5.6). Conversely, incorporating DOX HCl into PCL shell and IBU Na into PLGA core did not significantly reduce the fibre diameter when compared to blank PCL/PLGA coaxial scaffolds (1.01 ± 0.29 µm *versus* 1.08 ± 0.34 µm) but the size distribution of PCL-DOX HCl 1%/PLGA-IBU Na 5% scaffolds was narrower.

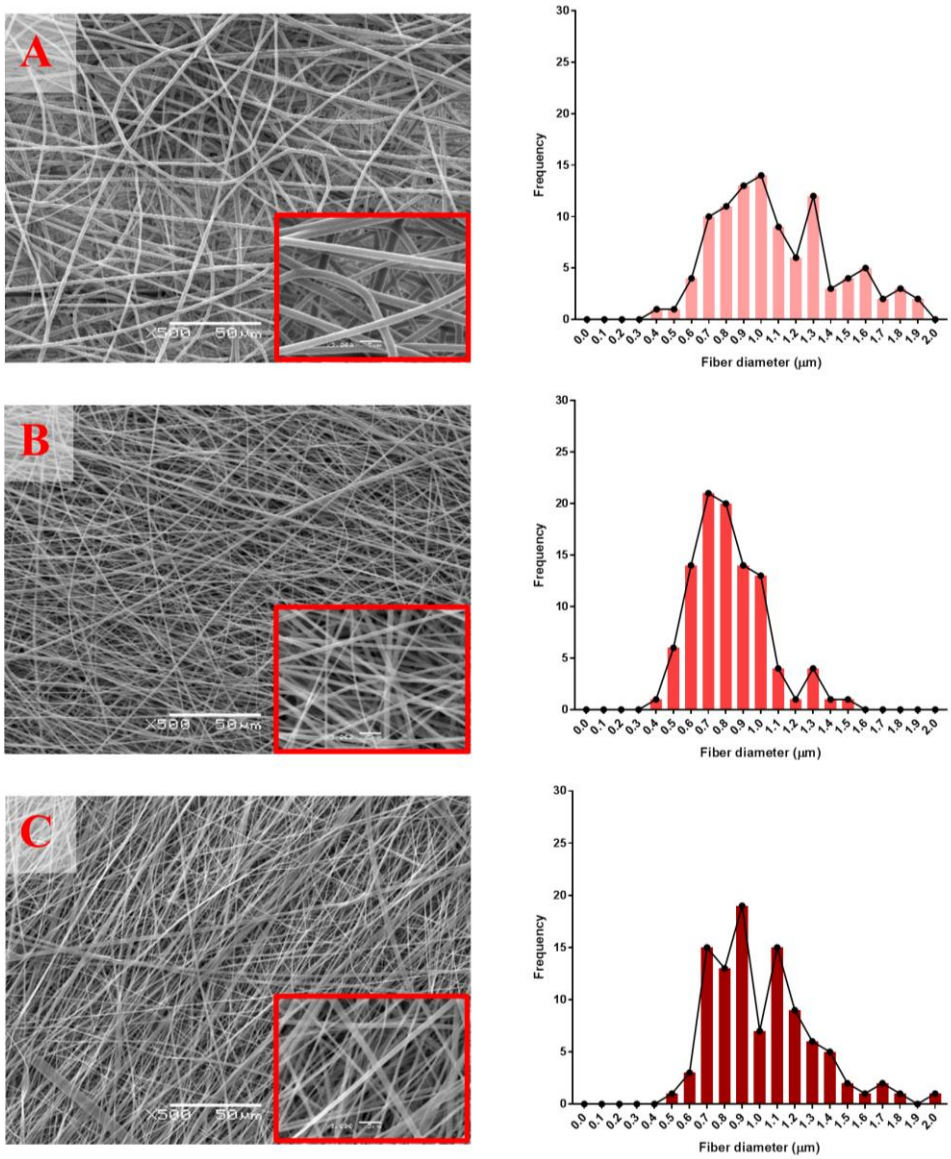


Figure 5.6. Representative SEM images and histograms for fibre diameter distribution of (A) PCL/PLGA, (B) PCL-DOX HCl 1%/PLGA, and (C) PCL-DOX HCl 1%/PLGA-IBU Na 5% scaffolds. All SEM images were shown at the magnification of 500X (scale bar of 50 μm) and 3,000X (scale bar 5 of μm) for the big and small images (red windows), respectively.

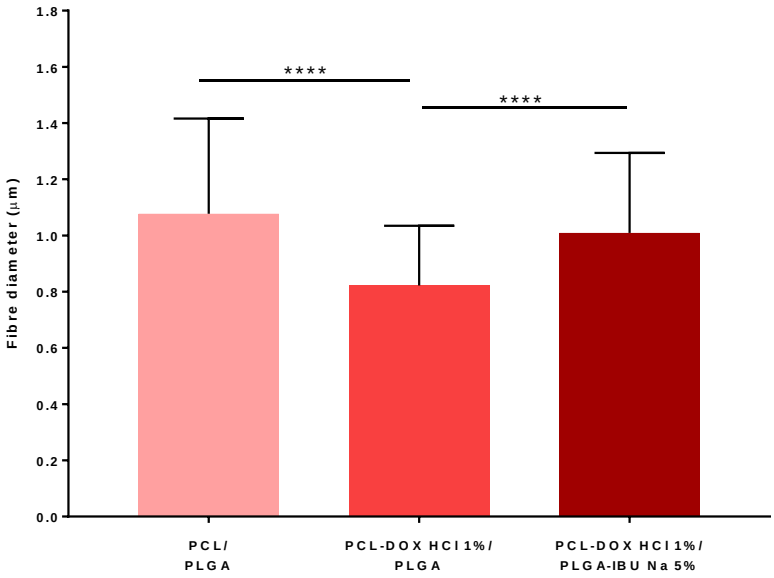


Figure 5.7. Means and standard deviations of fibre diameter of the scaffolds. Fibre diameter was measured from representative SEM images of the scaffolds using ImageJ software (n = 100 fibres). **** defines statistical significance at *p*-value < 0.0001.

Table 5.2. Means and standard deviations of fibre diameter of the scaffolds (n = 100)

Scaffold	Fibre diameter (μm)
PCL/PLGA	1.08 ± 0.34
PCL-DOX HCl 1%/PLGA	0.82 ± 0.21
PCL-DOX HCl 1%/PLGA-IBU Na 5%	1.01 ± 0.29

5.5.2.2 Determination of core-shell structure

The fabricated scaffolds were examined by TEM to confirm the existence of core-shell structure. Representative TEM images in Figure 5.8 show that the structure of electrospun scaffolds consisted of core and shell with a distinct boundary between them. The formation of core-shell structure was observed in all scaffolds regardless of the presence or absence of drugs.

In this study, the same solvent (HFIP) was used to prepare both shell and core solutions to ensure that they had low interfacial tension and neither polymers nor drugs precipitated at the tip of nozzle.[254–256] The formation of core-shell structure depends on various parameters either polymer solutions or electrospinning process. It was found that the shell solutions should have higher viscosity than the core solutions in order to overcome the interfacial tension between the core and shell solutions, and generates a stable Taylor cone.[254,257] In addition, high viscous shell solutions will be able to entrain the less viscous core solutions, leading to the successful formation of continuous core-shell structure.[255,257–259] Pleasingly, the obtained results agreed with the literature.[258,259] The shell solutions (either PCL or PCL-DOX HCl 1% solutions) had higher viscosity values when compared to the core solutions (either PLGA or PLGA-IBU Na 5% solutions).

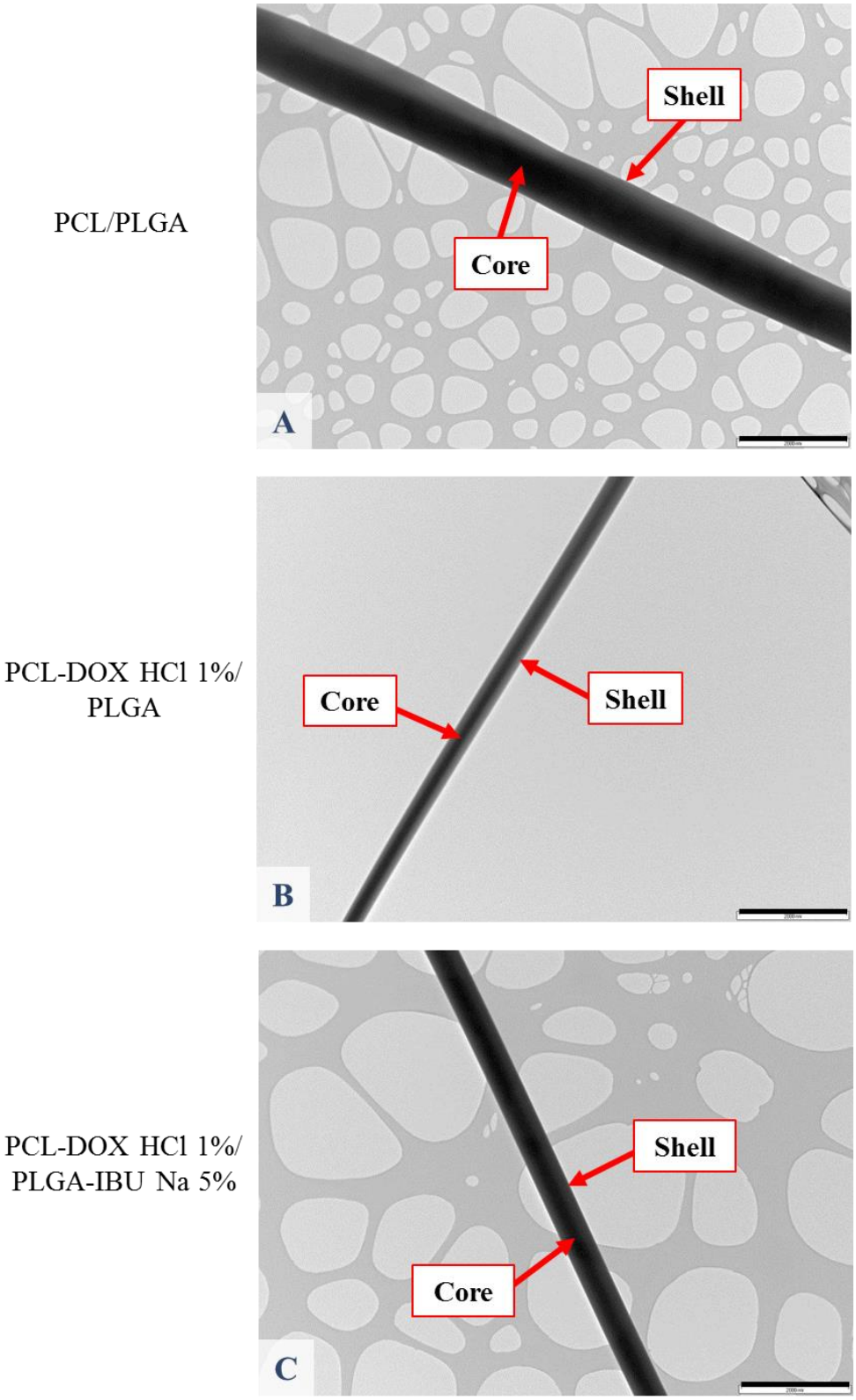


Figure 5.8. Representative TEM images illustrate the structure of coaxial electrospun fibres at the magnification of 8,200X (scale bar 2 µm).

The conductivity of the solutions also has an influence on the formation of core-shell fibres including their fibre diameters. The conductive shell solutions are required to provide enough surface charge density to facilitate the elongation through electrostatic force, and to enable fibre drawing to the collector.[72,254,255] The shell solutions with higher conductivity resulted in the production of the scaffolds with thinner fibre diameters.[254,260]

In contrast, the conductivity of the core solutions is not as important as that of the shell solutions.[254] However, the separation of core and shell may be incomplete if the core solutions have too low conductivity.[261] This is due to the weaker elongation forces under the electric field to drive the core solution during electrospinning.[261] Hence, the mixing of the core solution and the shell solution occurs. In addition, the conductivity of the core solutions affects their diameter. The core solutions with high conductivity is more stretched in the electric field, resulting in finer core diameters.[261]

5.5.2.3 Total porosity

The porosity of the scaffolds determined by the gravimetric method was comparable, ranging between 76% and 79% (Figure 5.9). Although the fibre diameter of PCL-DOX HCl 1%/PLGA scaffolds was significantly smaller than the other scaffolds and was expected to decrease the porosity of the scaffolds due to densely packing of fibres[205], such an effect was not observed in this study.

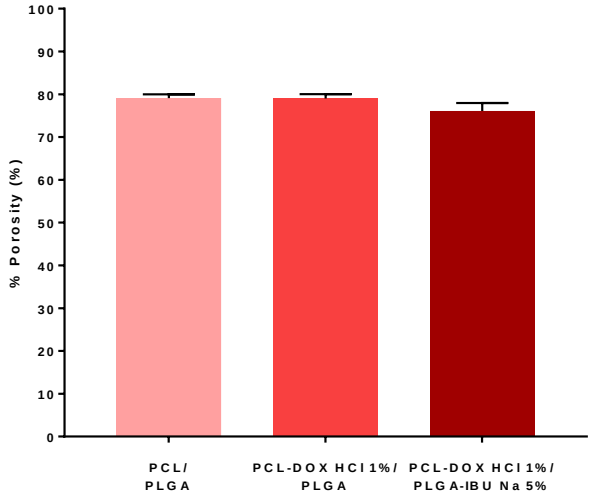


Figure 5.9. Total porosity of the scaffolds determined by gravimetric method in triplicate (n = 3). The values are shown as means and standard deviations.

Table 5.3. Means and standard deviations of total porosity of the scaffolds (n = 3)

Scaffold	Porosity (%)
PCL/PLGA	79.09 ± 0.91
PCL-DOX HCl 1%/PLGA	79.02 ± 0.99
PCL-DOX HCl 1%/PLGA-IBU Na 5%	76.09 ± 1.86

5.5.2.4 Mechanical properties

Stress-strain curves (Figure 5.10A) show that the coaxial electrospun scaffolds in this study were all ductile and possessed plasticity as the gradual deformation of the scaffolds against the stress was observed before the breakage. Incorporation of DOX HCl into the PCL shell significantly increased the ultimate tensile strength of the scaffolds by approximately 3.5 fold when compared to blank PCL/PLGA scaffolds (Figure 5.10B). Furthermore, the greater increase in the ultimate tensile strength was observed when both DOX HCl and IBU Na were added into the scaffolds (approximately 5.5 and 1.6 fold when compared to PCL/PLGA and PCL-DOX HCl 1%/PLGA scaffolds, respectively).

Both semi-crystalline PCL and amorphous PLGA are polyester polymers that can be hydrolysed by acid. Weakly acidic drugs like DOX HCl and IBU Na could break down ester linkages initially in an amorphous region of the polymers.[209] Hence, the crystalline region of PCL[207,210] and PLGA[262] remained, improving the mechanical strength of the scaffolds. Furthermore, smaller fibre diameter of the electrospun scaffolds was reported to enhance crystallinity and molecular orientation within an amorphous phase of the fibres, resulting in improved mechanical strength.[263–265]

Figures 5.10C and 5.10D show the significant lower strain at break and higher Young's modulus of PCL-DOX HCl 1%/PLGA scaffolds when compared to PCL/PLGA scaffolds. The results agreed with the previous studies that the smaller fibre diameters correlated to the higher Young's moduli.[265–268] This is

perhaps due to the increase in crystallinity of PCL. However, the effect of higher crystallinity on Young's modulus was not distinct in PCL-DOX HCl 1%/PLGA-IBU Na 5% scaffolds.

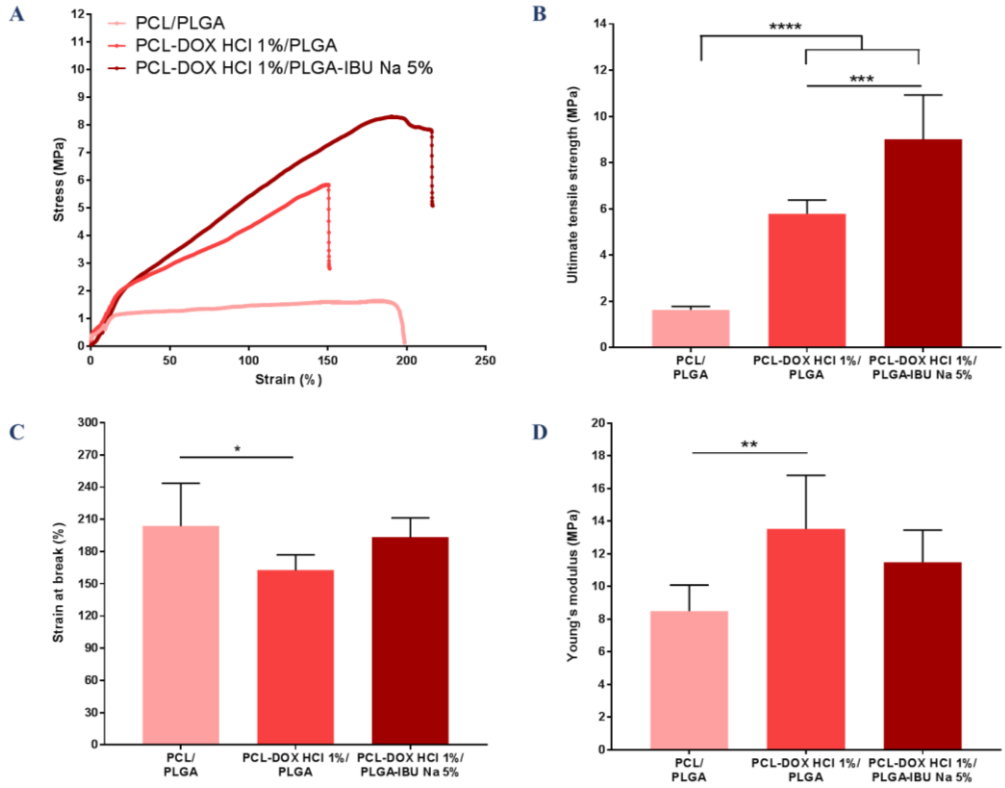


Figure 5.10. Mechanical properties of electrospun scaffolds evaluated by a uniaxial tensile test. Each scaffold was tested in sextuplicate (n = 6). (A) Representative stress-strain curves, (B) Ultimate tensile strength, (C) % Strain at break and (D) Young's modulus. The values are shown as means and standard deviations. *, **, *** and **** define statistical significance at *p*-value < 0.05, < 0.01, < 0.001 and < 0.0001, respectively.

Table 5.4. Means and standard deviations of ultimate tensile strength, % strain at break and Young's modulus of the scaffolds (n = 6).

Scaffold	Ultimate tensile strength (MPa)	% Strain at break (%)	Young's modulus (MPa)
PCL/PLGA	1.63 ± 0.15	203.70 ± 39.84	8.49 ± 1.59
PCL-DOX HCl 1%/ PLGA	5.79 ± 0.59	162.47 ± 14.58	13.52 ± 3.29
PCL-DOX HCl 1%/ PLGA-IBU Na 5%	9.01 ± 1.92	193.19 ± 18.17	11.48 ± 1.97

5.5.2.5 Water contact angle

Water contact angle measurements were carried out to investigate the wettability of the scaffolds. The results from a static mode showed that PCL/PLGA and PCL-DOX HCl 1%/PLGA scaffolds had poor wettability as their water contact angles were higher than 90 degrees (Figure 5.11).[142,269] Meanwhile, PCL-DOX HCl 1%/PLGA-IBU Na 5% scaffolds exhibited complete wettability as the water contact angle was zero degree (the scaffolds absorbed water).[269] The change in wettability of the scaffolds from being hydrophobic to hydrophilic should be a result of the incorporated drugs. As both IBU Na and DOX HCl are hydrophilic drugs and are located on the surface of fibres. The hydrophilicity of the scaffolds was therefore higher.[143,201,212]

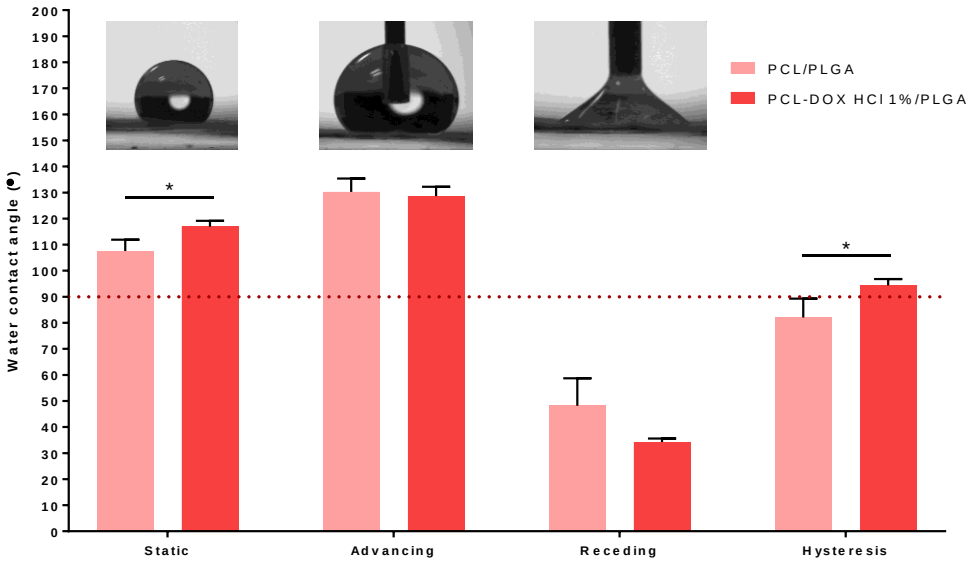


Figure 5.11. Water contact angles of electrospun scaffolds determined by static and dynamic modes of a sessile drop method. The values represent means and standard deviations of static water contact angle, advancing water contact angle, receding water contact angle, and contact angle hysteresis (the difference between advancing and receding water contact angles) (n = 3). The small figures shown are the representative images of water droplet on electrospun scaffolds when tested by static and dynamic modes: static water contact angle (left), advancing water contact angle (middle) and receding water contact angle (right). * defines a statistical significance at *p*-value < 0.05.

Table 5.5. Water contact angles of electrospun scaffolds determined by static and dynamic modes of a sessile drop method. The values represent means and standard deviations of static water contact angle, advancing water contact angle, receding water contact angle, and contact angle hysteresis (the difference between advancing and receding water contact angles) (n = 3).

Scaffold	Static contact angle (°)	Advancing contact angle (°)	Receding contact angle (°)	Contact angle hysteresis (°)
PCL/PLGA	107.57 ± 4.37	130.26 ± 5.14	48.19 ± 10.52	82.07 ± 7.21
PCL-DOX HCl 1% /PLGA	116.94 ± 2.19	128.63 ± 3.62	34.28 ± 1.30	94.35 ± 2.43
PCL-DOX HCl 1% /PLGA-IBU Na 5%	N/A	N/A	N/A	N/A

N/A: not applicable

The measurements of the advancing and receding water contact angles were carried out to investigate the surface roughness of the scaffolds through contact angle hysteresis values. Contact angle hysteresis values of the scaffolds were large (82–94%), indicating that the surfaces of the scaffolds were rough. This should relate to the structure of the scaffolds that are formed by multiple layers of fibres. The gaps between fibres not only create rough topography on the surface of the scaffolds, but also trap some air within the structure.[270] The water contact angles are increased accordingly due to the replacement of liquid-solid interface by gas-liquid interface.[142,146]

The greater hydrophobicity of PCL-DOX HCl 1%/PLGA scaffolds may relate to the higher crystallinity of PCL shell after blending with DOX HCl and also more ordered alignment of fibres in the finished scaffolds in comparison with PCL/PLGA scaffolds. Areias *et al.* explained in their study that fibre alignment and degree of crystallinity had a strong influence on hydrophobicity of the

electrospun scaffolds.[271] The electrospun scaffolds with more aligned fibres and higher crystallinity tend to be more hydrophobic.

5.5.2.6 Drug encapsulation efficiency

Table 5.6 presents the values of encapsulation efficiency of DOX HCl and IBU Na in the coaxial scaffolds. Overall, both drugs were successfully entrapped in the fibres at levels of more than 70%. It was observed that the scaffolds that were loaded with only DOX HCl had higher amounts of encapsulated DOX HCl when compared to the scaffolds that were loaded with both DOX HCl and IBU Na (90.61 ± 3.35% *versus* 75.06 ± 6.17%).

In addition, fabricating the scaffolds as coaxial PCL/PLGA scaffolds improved the encapsulation of IBU Na when compared to PLGA-IBU Na 5% scaffolds manufactured by monoaxial electrospinning in Chapter 3 (72.59 ± 3.57% *versus* 64.51 ± 1.69%). This could be a result of having PCL shell wrapping around PLGA core, reducing the loss of IBU Na.

Table 5.6. % Encapsulation efficiency of DOX HCl and IBU Na in the scaffolds. The values are means and standard deviations of triplicate samples (n = 3).

Scaffold	Encapsulation efficiency (%)	
	DOX HCl	IBU Na
PCL-DOX HCl 1%/ PLGA	90.61 ± 3.35	N/A
PCL-DOX HCl 1%/ PLGA-IBU Na 5%	75.06 ± 6.17	72.59 ± 3.57

N/A: not applicable

5.5.2.7 Drug-drug interaction by NMR spectroscopic analysis

^{1}H NMR spectroscopy was used to probe whether there are intermolecular interactions between IBU Na and DOX HCl molecules when these drugs are present in the same medium. This was done by comparing the ^{1}H spectrum of a solution of IBU Na and DOX HCl in d_6-DMSO and the ^{1}H spectrum of each drug in d_6-DMSO. It turns out that a number of peak shifts were observed (Figure 5.12), which suggests the existence of molecular interactions between the drugs.

First, it is clear that the NH_2 amide peaks (2 singlets at 9.59 and 9.02 ppm) of DOX HCl (maroon spectrum) shifted to 9.21 ppm and appeared as one singlet peak (green spectrum). This is indicative of a change in electronic environment around the amide group of DOX HCl when IBU Na is present in the same solution. Interestingly, the quartet signal at 3.32 ppm of IBU Na (α proton next to the carboxylic group) also moved upwards to 3.44 ppm; this likewise indicates an electronic surrounding perturbation. Such peak shifts could be an indication of hydrogen bonding between the amide moiety of DOX HCl and the carboxylic group of IBU Na. Additionally, there are aromatic peak shifts (6.92 and 6.88 ppm of DOX HCl moving to 6.68 and 6.59 ppm, respectively; and 7.16 and 6.96 ppm of IBU Na shifting to 7.18 and 7.08, respectively) signifying π-π interaction, or so called 'π-stacking' between the drugs.[272,273]

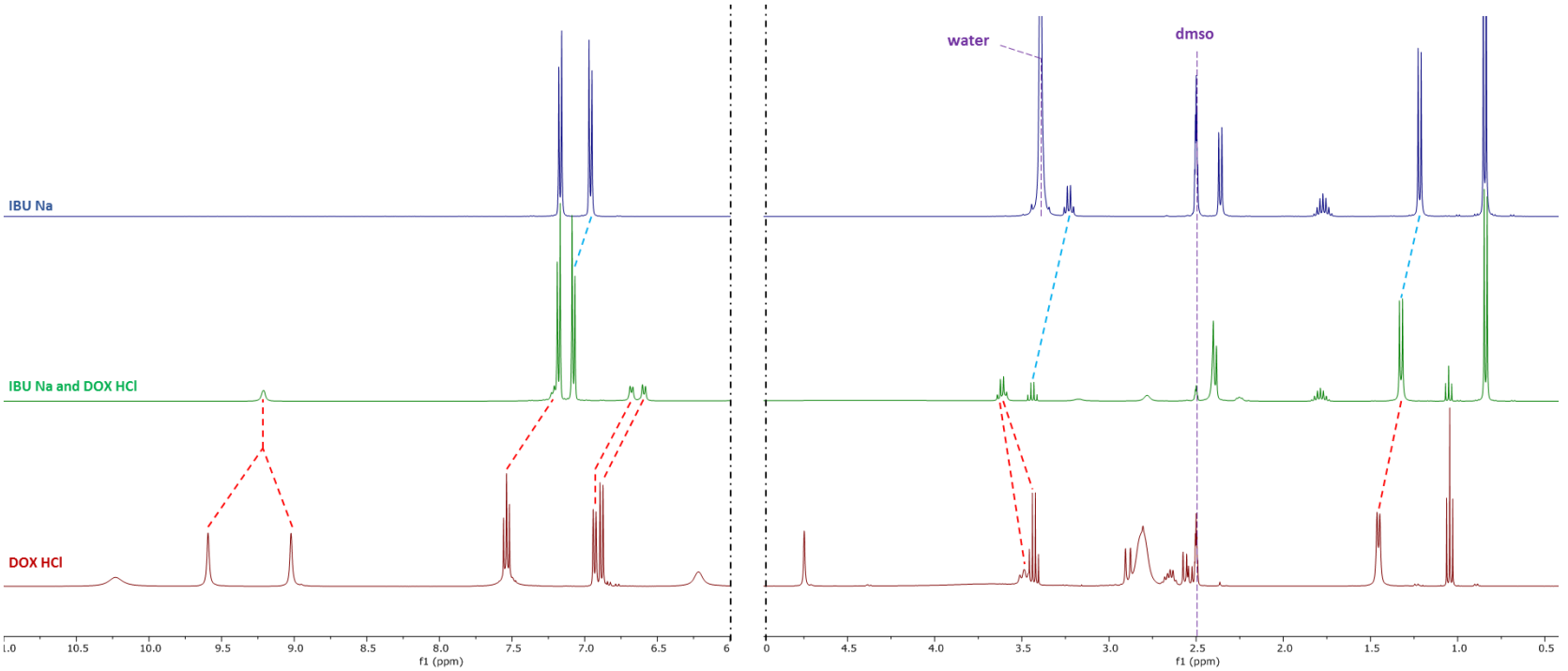


Figure 5.12. ^{1}H NMR spectra (0.00—11.00 ppm)[1] of IBU Na (blue), DOX HCl (maroon), and a mixture of IBU Na and DOX HCl (green) in d_6-DMSO. Several significant peak shifts of IBU Na (blue dotted lines) and DOX HCl (red dotted lines) are observed when both drugs are in the same solution.

[1] 5.00—6.00 ppm is omitted due to no signal appears within the range

5.5.2.8 Superficial drug distribution determined by ToF-SIMS

The accumulation of IBU Na and DOX HCl at the top surface of fibres was determined by ToF-SIMS analysis. Table 5.7 summarises the ions that are the fingerprint of polymers and drugs.

Table 5.7. Positive and negative ions used to identify polymers and drugs[149–151,214,215]

Polymer/Drug	Positive ions	Negative ions
PCL	*m/z* 115, $[C_6H_{11}O_2]^+$	*m/z* 113, $[C_6H_9O_2]^-$
PLGA	*m/z* 89, $[C_3H_5O_3]^+$	*m/z* 143, $[C_{10}H_7O]^-$
DOX HCl	*m/z* 445, $[C_{22}H_{25}N_2O_8]^+$	*m/z* 35, $[Cl]^-$ *m/z* 443, $[C_{22}H_{23}N_2O_8]^-$
IBU Na	*m/z* 23, $[Na]^+$	*m/z* 205, $[C_{13}H_{17}O_2]^-$

The spectra in Figures 5.13 and 5.14 show the positive and negative ions used to identify IBU Na, respectively. Although, sodium ions are the common contaminant, it was clearly seen that the intensity of sodium ions was distinct in the sample containing IBU Na. Therefore, the presence of sodium ions was investigated to confirm the localisation of IBU Na.

The intensity of the ions at *m/z* 205 ($[C_{13}H_{17}O_2]^-$) may present in the sample of DOX HCl. However, the magnitude of intensity was considered lower than the sample of IBU Na. Hence, these ions were also used to track the existence of IBU Na on the surface of the scaffolds and to confirm the results obtained from analysing sodium ions.

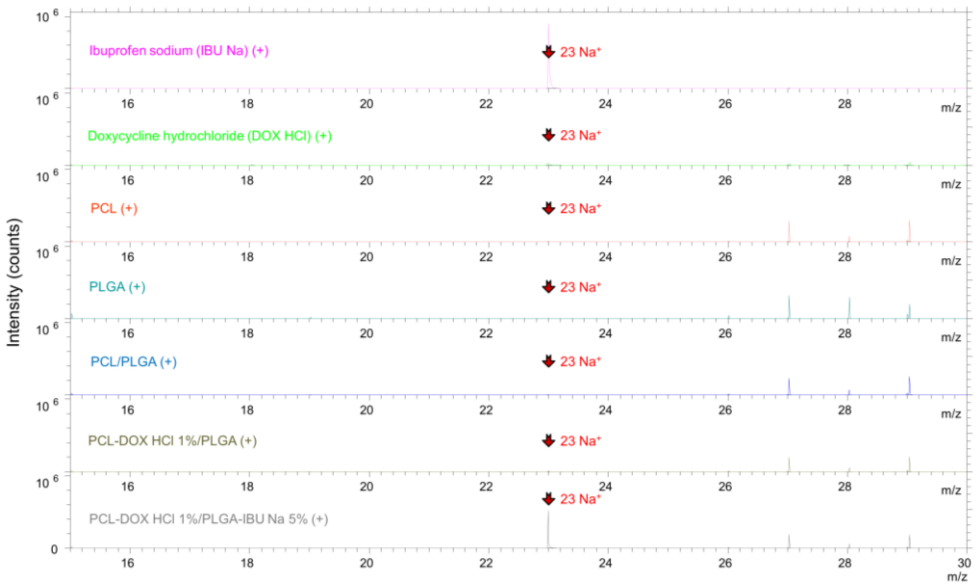


Figure 5.13. Representative positive ToF-SIMS spectra of the surface of electrospun scaffolds. The peak at *m/z* = 23, $[Na]^+$, represents IBU Na.

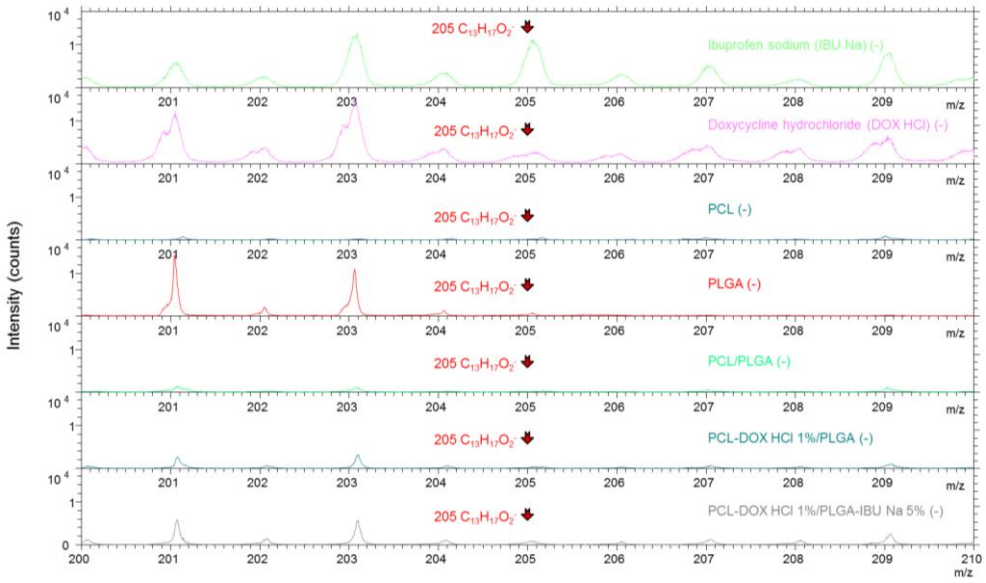


Figure 5.14. Representative negative ToF-SIMS spectra of the surface of electrospun scaffolds. The peak at *m/z* = 205, $[C_{13}H_{17}O_2]^-$, represents IBU Na.

Figures 5.15 and 5.16 show the representative spectra with negative ions that were used to identify DOX HCl. Obviously, the ions at *m/z* 443, $[C_{22}H_{23}N_2O_8]^-$ are the characteristic fingerprint of DOX HCl. Additionally, chloride ions at *m/z* 35 was also observed to be a good candidate to identify the presence of DOX HCl.



Figure 5.15. Representative negative ToF-SIMS spectra of the surface of electrospun scaffolds. The peak at *m/z* = 35, $[Cl]^-$, represents DOX HCl.

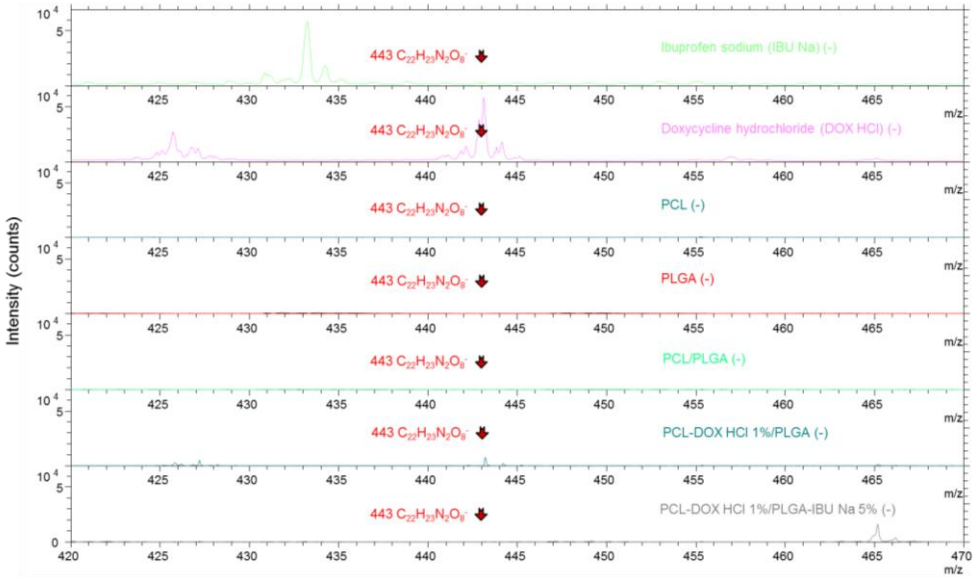


Figure 5.16. Representative negative ToF-SIMS spectra of the surface of electrospun scaffolds. The peak at *m/z* = 443, $[C_{22}H_{23}N_2O_8]^-$, represents DOX HCl.

The following spectra illustrate the positive and negative ions that are the fingerprint of PCL and PLGA (Figures 5.17 and 5.18).

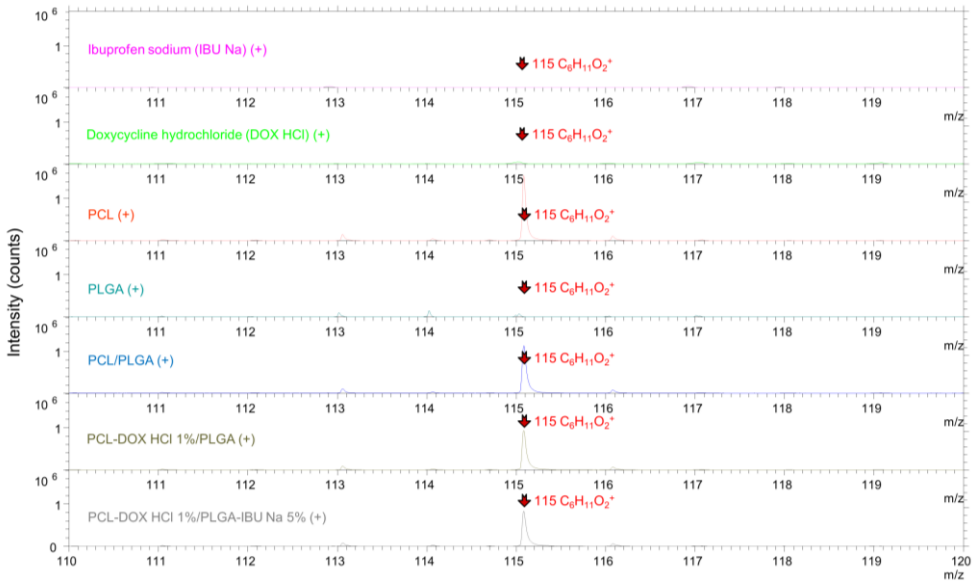


Figure 5.17. Representative positive ToF-SIMS spectra of the surface of electrospun scaffolds. The peak at *m/z* = 115, $[C_6H_{11}O_2]^+$, represents PCL.

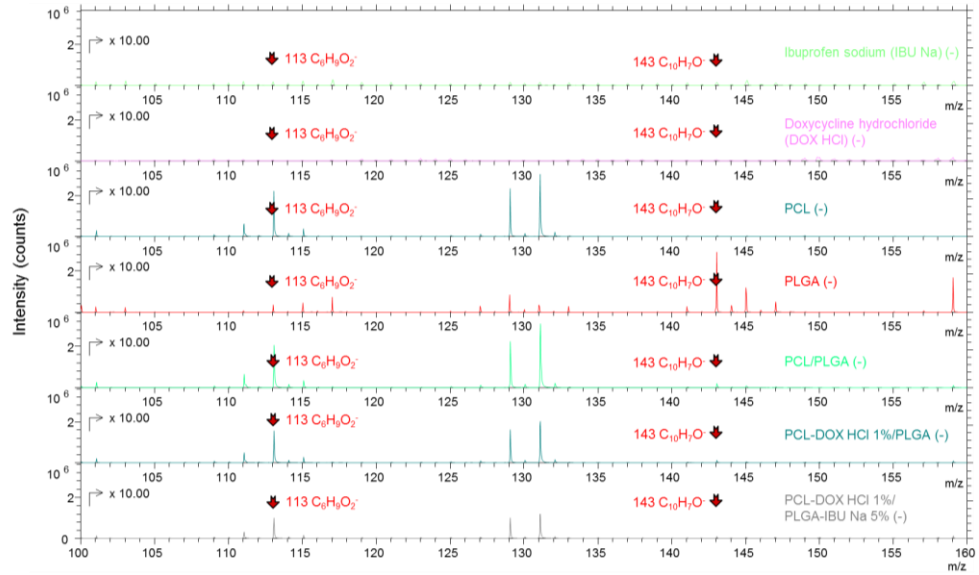


Figure 5.18. Representative negative ToF-SIMS spectra of the surface of electrospun scaffolds. The peak at *m/z* = 113, $[C_6H_9O_2]^-$, represents PCL. The peak at *m/z* = 143, $[C_{10}H_7O]^-$, represents PLGA.

It is worth noting that the signals of positive ions at *m/z* 445, ($[C_{22}H_{25}N_2O_8]^+$) for DOX HCl and at *m/z* 89 ($[C_3H_5O_3]^+$) for PLGA were too low for the software to generate the spectra. Similarly, the data for the total ion intensity of drugs on the surfaces of the scaffolds could be obtained but the images showing the distribution of some ions were unable to generate if the signal was too low.

The results shown in Figure 5.19 imply that DOX HCl located on the surface of PCL-DOX HCl 1%/PLGA scaffolds as the ion intensities of $[C_{22}H_{25}N_2O_8]^+$ and $[C_{22}H_{23}N_2O_8]^-$ were higher than those of blank PCL/PLGA scaffolds. In contrast, these two ions could not confirm the presence of DOX HCl at the surface of PCL-DOX HCl 1%/PLGA-IBU Na 5% scaffolds. Therefore, chloride ion was investigated to confirm the deposition of DOX HCl on the surface of such scaffolds. It was clearly that the ion intensity of chloride ion in PCL-DOX HCl 1%/PLGA-IBU Na 5% scaffolds was greater than both blank PCL/PLGA and PCL-DOX HCl 1%/PLGA scaffolds. As illustrated in the ^{1}H NMR analysis (Figure 5.12), DOX HCl had strong interactions with IBU Na. The ions of $[C_{22}H_{25}N_2O_8]^+$ and $[C_{22}H_{23}N_2O_8]^-$ are more likely to interact with ions from IBU Na, leading to the lower detected ion intensities. Whereas, chloride ions are more freely and less interact with the ions from IBU Na. Hence, higher ion intensity of $[Cl]^-$ was observed in PCL-DOX HCl 1%/PLGA-IBU Na 5% scaffolds, confirming the presence of DOX HCl at the surface of the scaffolds.

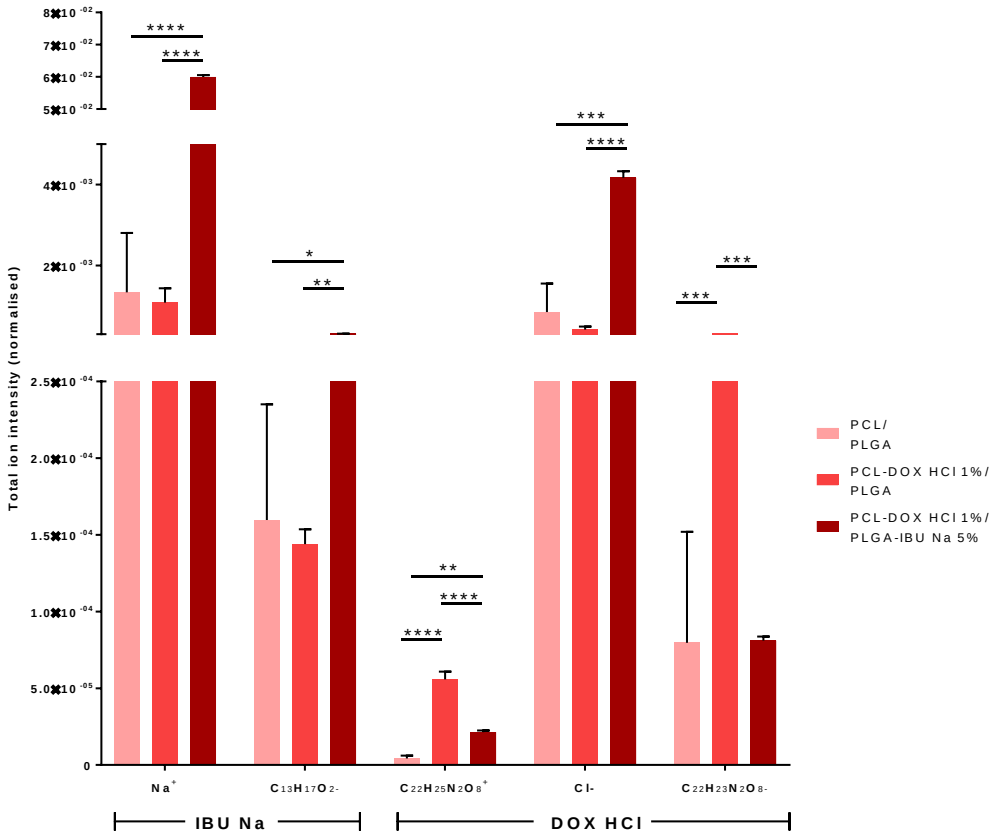


Figure 5.19. Normalised total ion intensity of $[Na]^+$ and $[C_{13}H_{17}O_2]^-$ for IBU Na, and $[C_{22}H_{25}N_2O_8]^+$, $[Cl]^-$, $[C_{22}H_{23}N_2O_8]^-$ for DOX HCl. The values are means and standard deviations of the total ion intensity obtained from three different areas in one scaffold sample (n = 3). Data are normalised to the total ion counts. *, **, *** and **** define a significant difference between the scaffolds at *p*-value < 0.05, < 0.01, < 0.001 and < 0.0001, respectively.

The significant higher ion intensities of $[Na]^+$ and $[C_{13}H_{17}O_2]^-$ identified that IBU Na distributed on the surface of PCL-DOX HCl 1%/PLGA-IBU Na 5% scaffolds (Figure 5.19). The presence of IBU Na on the surface of the coaxial fibres could be related to several factors. Hydrophilic IBU Na has poor partition with hydrophobic PLGA. Hence, IBU Na deposits mostly at the surface of PLGA core due to phase separation. At the interface between PLGA core and PCL shell, IBU Na meets DOX HCl. As these two drugs have strong intermolecular interactions, DOX HCl induces the mobility of IBU Na from PLGA core to PCL shell during electrospinning. As the solvent used in the

preparation of the core and shell solutions is HFIP, the mixing of core and shell solution could occur.[254] Lastly, phase separation between hydrophobic PCL and both drugs takes place, which leads to the presence of IBU Na and DOX HCl and the surface of coaxial fibres.

The images for both positive and negative ions (Figures 5.20 and 5.21) show a homogeneous distribution of DOX HCl and IBU Na throughout the surface of coaxial PCL/PLGA fibres. However, the image for $[C_{22}H_{23}N_2O_8]^-$ was unable to obtain due to low intensity.

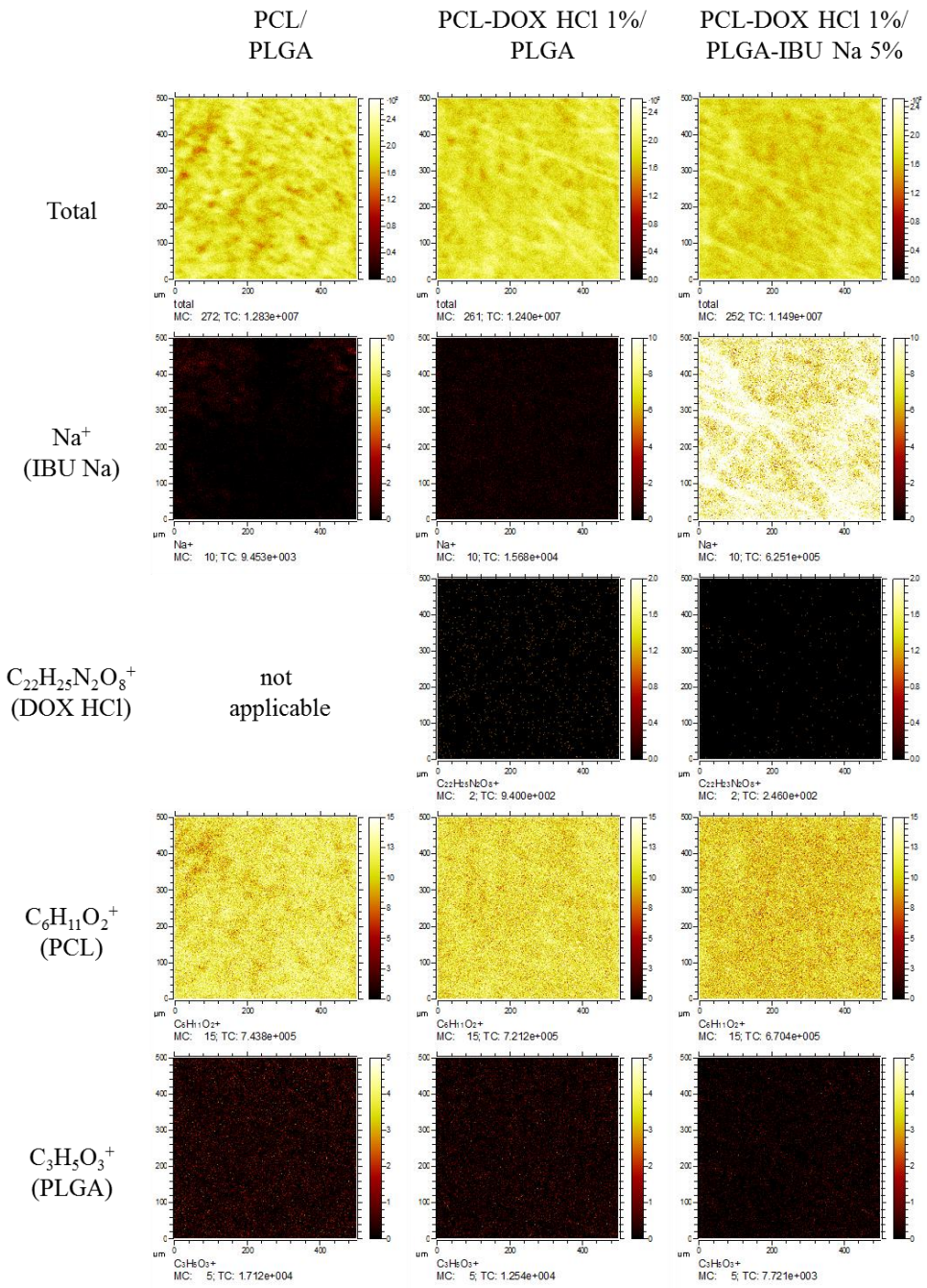


Figure 5.20. The 2D images show the distribution of $[Na]^+$ (IBU Na), $[C_{22}H_{25}N_2O_8]^+$ (DOX HCl), $[C_6H_{11}O_2]^+$ (PCL), $[C_3H_5O_3]^+$ (PLGA) and total ions on the top surface of scaffolds. The images are acquired with a 2D surface imaging mode and normalised to the total ion counts.

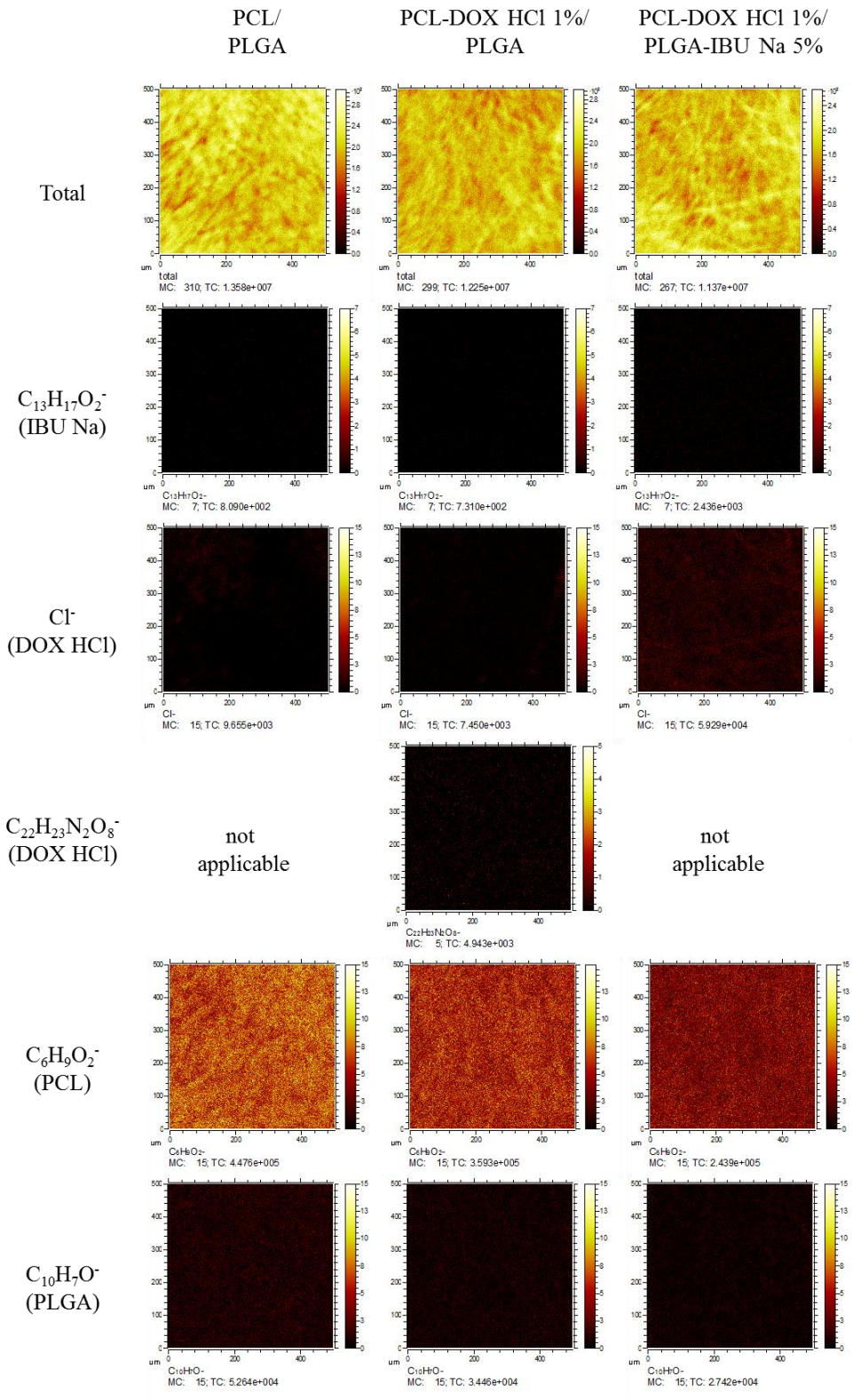


Figure 5.21. The 2D images show the distribution of $[C_{13}H_{17}O_2]^-$ (IBU Na), $[Cl]^-$ (DOX HCl), $[C_{22}H_{23}N_2O_8]^-$ (DOX HCl), $[C_6H_9O_2]^-$ (PCL), $[C_{10}H_7O]^-$ (PLGA) and total ions on the top surface of scaffolds. The images are acquired with a 2D surface imaging mode and normalised to the total ion counts.

5.5.2.9 Drug release profiles

The results from the drug release study revealed that the release of DOX HCl and IBU Na in a PBS was rapid with burst release occurring within the first 30 minutes (Figure 5.22). Both DOX HCl and IBU Na are hydrophilic small drug molecules. Therefore, the partition of drugs and hydrophobic polymers, like PCL and PLGA, was poor after electrospinning.[153,154,274] Drugs deposited at the top surface of fibres as reported in ToF-SIMS analysis (Figure 5.19). As a result, drug molecules at the surface of fibres disassociated from the scaffolds rapidly once the scaffolds were immerged in the medium (PBS).

It was noted that the cumulative release of DOX HCl from PCL-DOX HCl 1%/PLGA scaffolds was lower than that of PCL-DOX HCl 1%/PLGA-IBU Na 5% scaffolds (74.92 ± 5.30% *versus* 96.90 ± 5.01%). As mentioned earlier, DOX HCl had the interaction with PLGA, retarding the release of DOX HCl as observed in PLGA-DOX HCl scaffolds. Although, DOX HCl was not directly blended with PLGA in manufacturing of the coaxial scaffolds, DOX HCl and PLGA are met at the interface of PCL shell and PLGA core. Therefore, some molecules of DOX HCl may be trapped in the scaffolds, resulting in lower drug release.

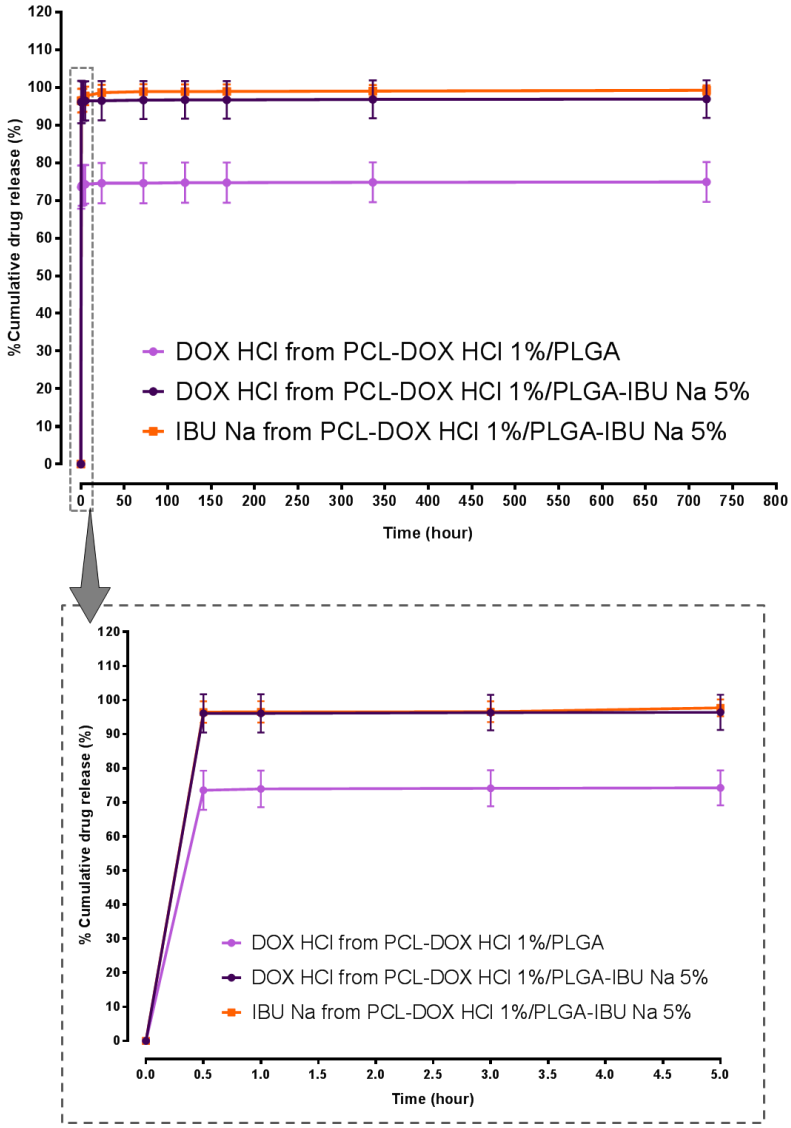


Figure 5.22. Cumulative drug release of DOX HCl and IBU Na from the scaffolds in PBS solutions over 30 days (720 hours, upper graph) and within the first 5 hours (lower graph). The values represent means and standard deviations of triplicate samples.

Table 5.8. Cumulative drug release of DOX HCl and IBU Na from the scaffolds over 30 days in PBS solutions. The values are means and standard deviations of % cumulative drug release (n = 3).

Scaffold	% Cumulative drug release in 30 days	
	DOX HCl	IBU Na
PCL-DOX HCl 1%/ PLGA	74.92 ± 5.30	N/A
PCL-DOX HCl 1%/ PLGA-IBU Na 5%	96.90 ± 5.01	99.26 ± 1.28

N/A: not applicable

The previous study observed that the release of acyclovir from the PLGA shell of coaxial scaffolds was higher and faster when the concentration of bovine serum albumin (BSA) in the core increased (acyclovir release: 3%, 16.5% and 56% for BSA concentrations of 0 mg/mL, 40 mg/mL and 150 mg/mL, respectively).[248] According to the high affinity between acyclovir and BSA, the distribution of acyclovir in the fibres perhaps changed with an increasing amount of BSA, resulting in faster drug release. Similarly, these results showed a strong drug interaction between DOX HCl and IBU Na as described earlier in the NMR spectroscopic analysis (Figure 5.12), this could potentially be the case that IBU Na accelerates the release of DOX HCl by enhancing the distribution of DOX HCl in the PCL shell to be more closer to the surface of fibres.

The release of IBU Na was considered complete as 99.26% of drug was detected in a PBS within the first 24 hours of the study. Interestingly, the release of IBU Na from the coaxial fibres was higher than the fibres produced by monoaxial electrospinning in Chapter 3. Typically, the release of drug encapsulated in the coaxial fibres is more likely to be less burst and more sustained.[153,275–278] However, there was a case where ibuprofen[279] in the core was completely released into the dissolution medium in the same manner as fibres manufactured from monoaxial electrospinning.

The diffusion of core solution to shell solution occurs during coaxial electrospinning due to the fast drawing and drying processes.[280] IBU Na in the core solution dissociates into ions, moving toward the shell solution under high electric field as discussed previously in Chapter 3.[281] In addition, HFIP is the

solvent for both shell and core. IBU Na can travel from the core solution to the shell solution until the evaporation of solvent is complete.[282] Consequently, some drug molecules could travel from the core to the shell, and results in the burst release of drug.[280] Moreover, using the same solvent for the core and shell solutions may cause the solutions to mix at the tip of nozzle, leading to the presence of the drug that is supposed to be in the core at the surface of the shell.[275]

5.5.2.10 Degradation profile of the scaffolds

The degradation of the coaxial electrospun scaffolds in PBS was monitored over 90 days using weight loss and morphological change as key parameters. According to % weight loss, the coaxial scaffolds gradually degraded over time (Figure 5.23). PCL/PLGA scaffolds loaded with single and dual drugs degraded faster and in a greater extent when compared to blank PCL/PLGA scaffolds.

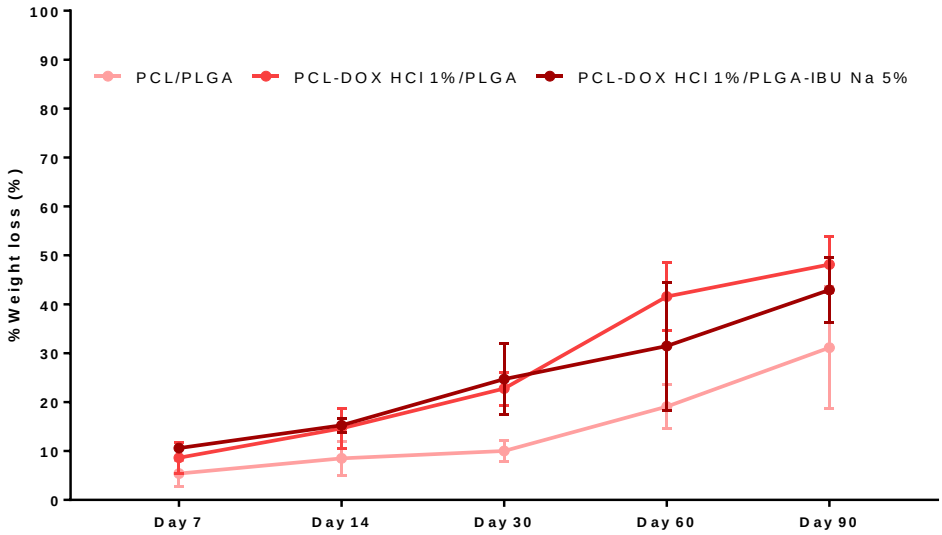


Figure 5.23. Degradation profiles of the scaffolds in PBS (pH 7.4) shown as % weight loss. The values shown in the graph are means and standard deviations of triplicate samples.

Table 5.9. % Cumulative weight loss of the scaffolds after being immerged in PBS at different time points. The values are means and standard deviations of triplicate samples (n = 3).

Time point	% Weight loss		
	PCL/PLGA	PCL-DOX HCl 1%/ PLGA	PCL-DOX HCl 1%/ PLGA-IBU Na 5%
Day 7	5.39 ± 2.68	8.62 ± 3.14	10.58 ± 0.53
Day 14	8.49 ± 3.47	14.63 ± 4.05	15.28 ± 1.44
Day 30	10.02 ± 2.21	22.76 ± 3.36	24.70 ± 7.17
Day 60	19.07 ± 4.51	41.59 ± 7.01	31.46 ± 13.08
Day 90	31.12 ± 12.45	48.13 ± 5.72	42.91 ± 6.70

Nevertheless, significant changes in scaffold morphology were not observed (Figure 5.24). The scaffolds were able to retain their integrity as a fibrous structure up to 90 days. Only the fusion of adjacent fibres in the blank PCL/PLGA scaffolds was observed on day 90 of the study.

The outer structure of the coaxial fibres was made of PCL shell. As a result, the morphological change predominantly depends on the degradation of PCL. Bosworth *et al.* (2010) observed increases in molecular mass loss and crystallinity but no change in surface morphology of PCL electrospun fibres in the degradation study over 90 days in a PBS.[207] Bosworth *et al.* (2010) suggested that the degradation of PCL scaffolds undergo *via* the hydrolysis in the polymer bulk, leading to a reduction in the scaffold mass. Whilst, the morphology change requires enzymatic degradation. As the study was carried out in PBS without enzymes, only mass loss could be detected.

PCL and PLGA polyesters are both susceptible to acid-catalysed hydrolysis. The faster degradation of drug-loaded PCL/PLGA coaxial fibres should be a result of incorporated DOX HCl and IBU Na that have acidic property and hydrolyse the ester bonds in the polymer chains.

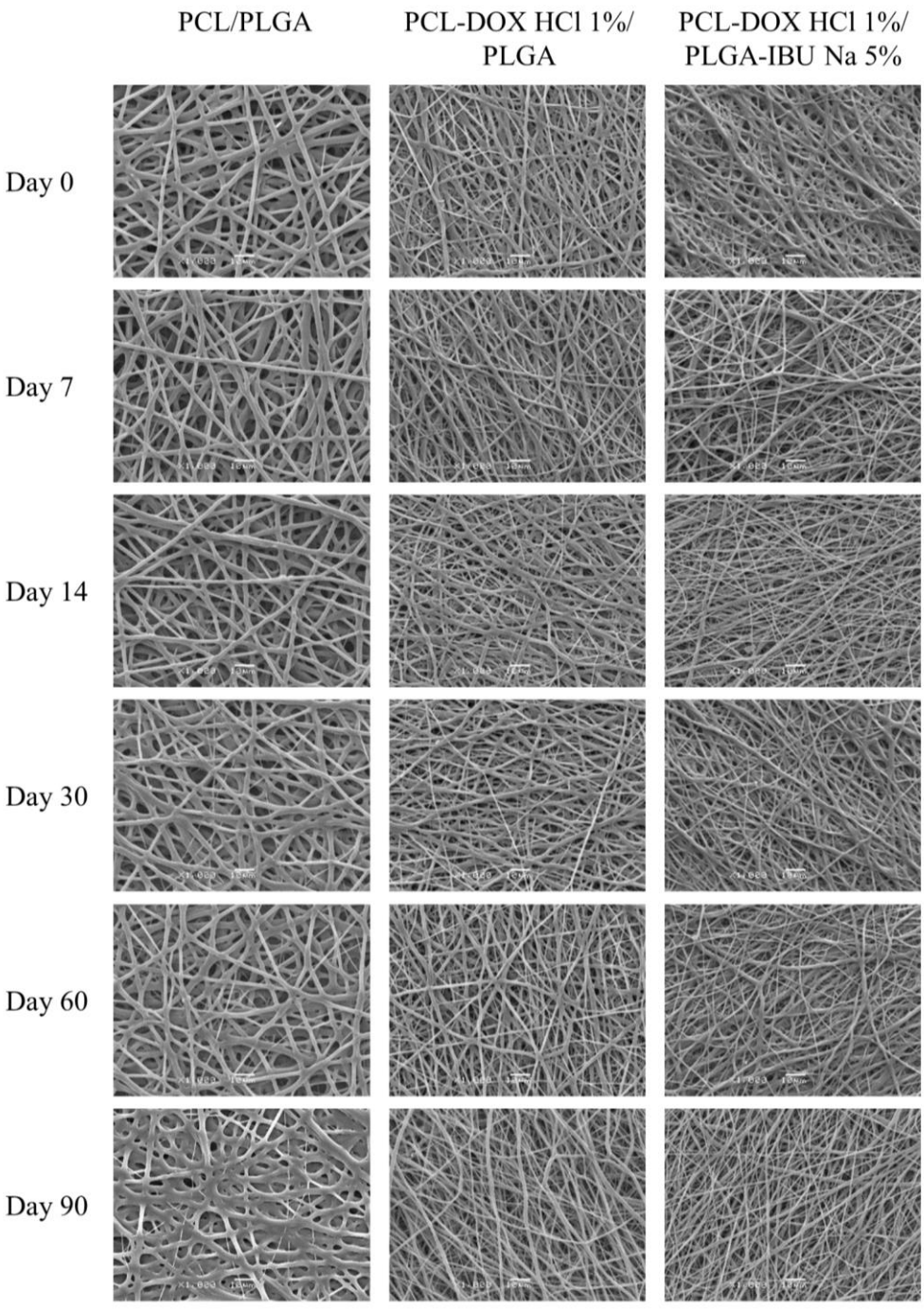


Figure 5.24. Representative SEM images showing morphological changes of the scaffolds over time. All images are illustrated at the magnification of 1,000X. The scale bar is 10 μm.

5.5.3 Drug cytotoxicity

The cytotoxic effect of drug mixtures was assessed in mouse fibroblasts and primary human dermal fibroblasts. DOX HCl and IBU Na in different concentrations were mixed and added to cell culture media. Cells were incubated with the mixtures of drugs in cell culture media for 24 hours before the metabolic activity of cells was determined by PrestoBlue® assay.

Figure 5.25 illustrates significant decreases in cell viability of mouse fibroblasts after cells were treated with the mixture of DOX HCl (0.1, 1 and 10 µM) and IBU Na (10, 100 and 1,000 µM) in cell culture media when compared to the control (no drugs).

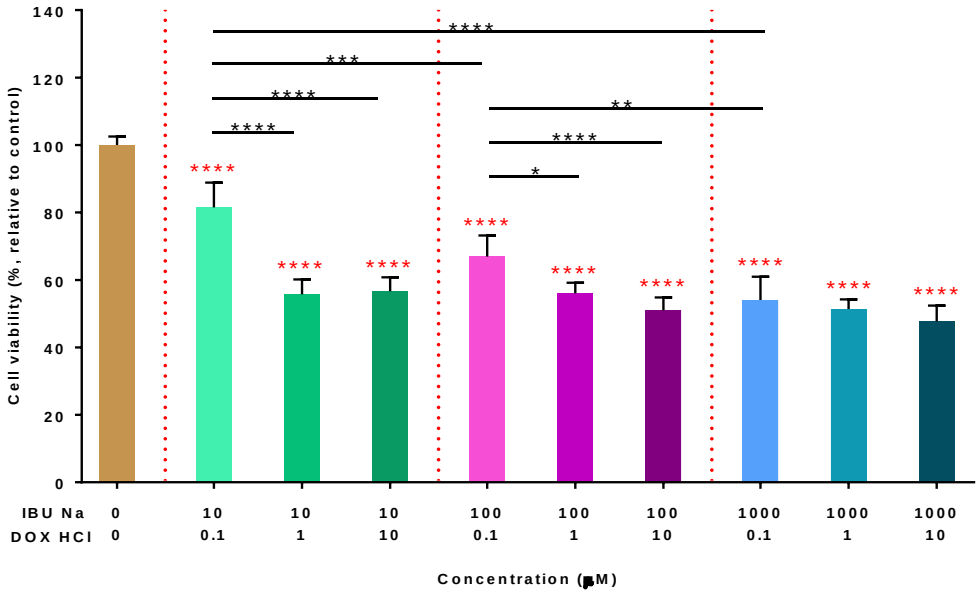


Figure 5.25. Cytotoxic effect of DOX HCl and IBU Na mixtures in mouse fibroblasts (3T3 cells) evaluated by PrestoBlue® assay (n = 3/concentration). Metabolic activity of cells was assessed after being treated with complete cell culture media containing different concentrations of DOX HCl (0.1, 1 and 10 µM) and IBU Na (10, 100 and 1,000 µM) for 24 hours. *, **, *** and **** define significant difference at *p*-value < 0.05, < 0.01, < 0.001 and < 0.0001, respectively. Red asterisks indicate the significant difference when the condition was compared to cell control (0 µM DOX HCl and 0 µM IBU Na).

The viability of mouse fibroblasts dropped to 81.50 ± 7.40% when treated with 10 µM IBU Na and 0.1 µM DOX HCl. The greater reduction in cell viability was observed at higher concentrations of DOX HCl. Only 55.75 ± 4.42% and 56.66 ± 4.14% of cells were viable when cell culture media contained 10 µM IBU Na and 1 µM DOX HCl or 10 µM DOX HCl, respectively.

The similar outcomes were observed in the group of 100 µM IBU Na. Cell viability decreased to 66.96 ± 6.24%, 56.01 ± 3.17% and 50.99 ± 3.80% in the group of cells treated with drug mixtures containing 100 µM IBU Na and 0.1, 1 and 10 µM DOX HCl, respectively.

Cell culture media containing 1,000 µM IBU Na, % reduced cell viability to 54.09 ± 6.89%, 51.34 ± 2.87% and 47.68 ± 4.70% when co-incubated with 0.1, 1 and 10 µM DOX HCl, respectively.

The results for primary human dermal fibroblasts were different from those of mouse fibroblasts. The distinct decreases in cell viability were observed only in the group of cells treated with 1,000 µM IBU Na and DOX HCl (0.1, 1, 10 and 100 µM) when compared to cell control (Figure 5.26). Cell viability in this group ranged between 25–77%.

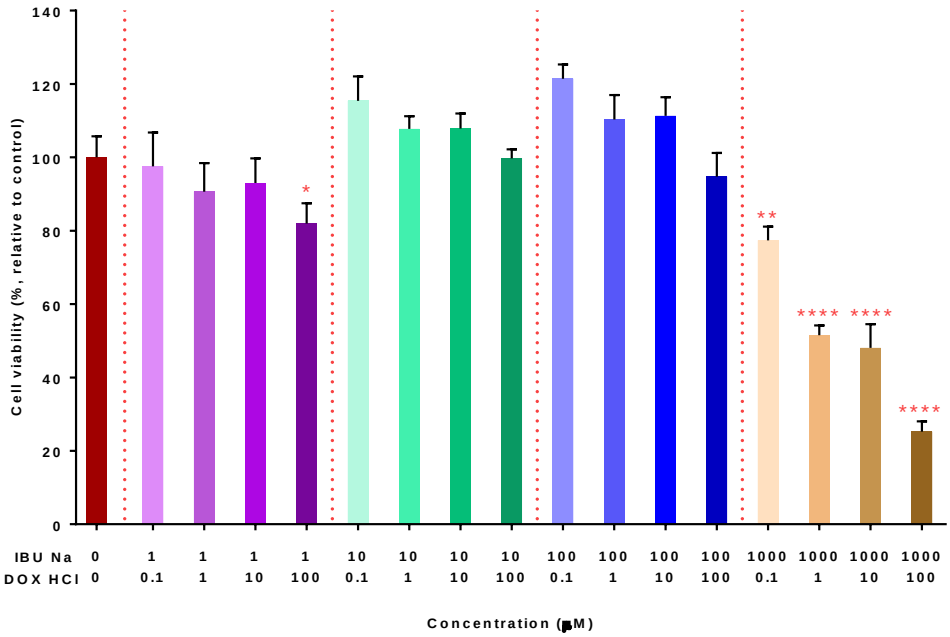


Figure 5.26. Cytotoxic effect of DOX HCl and IBU Na mixtures in primary human dermal fibroblasts evaluated by PrestoBlue® assay (n = 3/concentration). Metabolic activity of cells was assessed after being treated with complete cell culture media containing different concentrations of DOX HCl (0.1, 1, 10 and 100 µM) and IBU Na (1, 10, 100 and 1,000 µM) for 24 hours. *, ** and **** define significant difference when the condition was compared to cell control (0 µM DOX HCl and 0 µM IBU Na) at *p*-value < 0.05, < 0.01 and < 0.0001, respectively.

Table 5.10 summarises the effect of different concentrations of IBU Na on cell viability when the concentration of DOX HCl was kept constant, and vice versa. Interestingly, the proliferation of primary human dermal fibroblasts was promoted if cells were treated with higher concentrations of IBU Na (10 and 100 µM) in comparison with the lowest IBU Na concentration at 1 µM when the concentration of DOX HCl was fixed.

The effect of increasing concentrations of DOX HCl on cell viability was significant only when the concentration of IBU Na was 1,000 µM as described above.

Table 5.10. The effect of different concentrations of IBU Na on cell viability when the concentration of DOX HCl was fixed, and vice versa (n = 3).

Concentration (µM)				Cell viability	Significance level
Condition 1		Condition 2			
IBU Na	DOX HCl	IBU Na	DOX HCl		
1	0.1	10	0.1	↑	*
		100		↑	***
		1,000		↓	**
	1	10	1	↑	*
		100		↑	*
		1,000		↓	****
	10	100	10	↑	*
		1,000		↓	****
	100	10	100	↑	*
		1,000		↓	****
10	0.1	1,000	0.1	↑	****
	1		1	↓	****
	10		10	↓	****
	100		100	↓	****
100	0.1	1,000	0.1	↓	****
	1		1	↓	****
	10		10	↓	****
	100		100	↓	****
1,000	0.1	1,000	1	↓	***
			10	↓	****
			100	↓	****
	1		100	↓	***
	10			↓	**

5.5.4 Cell proliferation on the coaxial electrospun scaffolds

5.5.4.1 Cellular metabolic activity by PrestoBlue® assay

Mouse fibroblasts were seeded on the coaxial electrospun scaffolds to investigate the ability of the scaffolds to promote cell proliferation. The results from PrestoBlue® assay shown in Figure 5.27 revealed that the addition of drug(s) into PCL/PLGA scaffolds retarded the proliferation of cells when compared to blank PCL/PLGA scaffolds, resulting in lower cellular metabolic activity throughout the study. The concentration of drugs in cell culture media would achieve approximately 50 μM DOX HCl and 400 μM IBU Na if the release from the scaffolds was complete. It is more likely that cell viability will be decreased with drug-loaded scaffolds. However, the data suggests that cells could adapt and grow on the scaffolds over time.

As discussed in Chapter 4, the release of DOX HCl from the scaffolds in cell culture media was not complete within 24 hours as observed in PBS. The drug at the surface of the scaffolds directly exposed to seeded cells, hence, exhibiting cytotoxicity.

On day 14 of cell culture, a higher number of cells was observed in PCL-DOX HCl 1%/PLGA-IBU Na 5% scaffolds when compared to PCL-DOX HCl 1%/PLGA scaffolds. It was potentially due to the faster release of drugs from the scaffolds when both DOX HCl and IBU Na were loaded into the scaffolds. Hence, the scaffolds became more biocompatible.

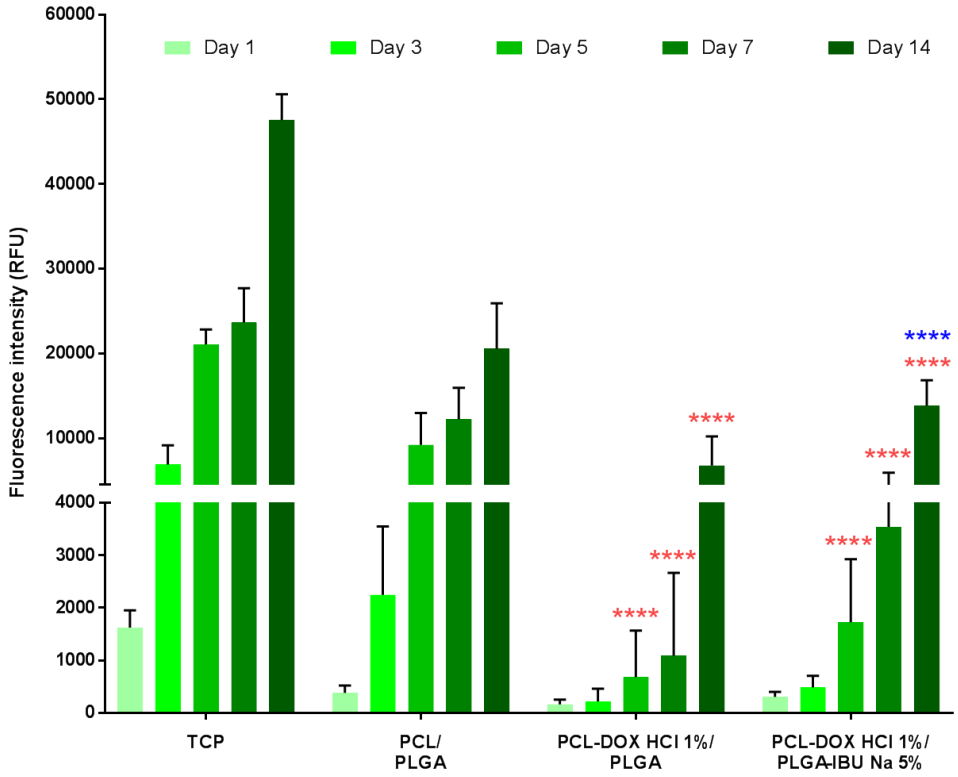


Figure 5.27. Cell proliferation on TCP, PCL/PLGA, PCL-DOX HCl 1%/PLGA, and PCL-DOX HCl 1%/PLGA-IBU Na 5% electrospun scaffolds determined by cellular metabolic activity of mouse fibroblasts (3T3 cells) over 14 days using PrestoBlue® assay. Values shown are means and standard deviations (n = 6). **** defines a significant difference at the same time point at *p*-value < 0.0001. * and * define a significant difference when compared to PCL/PLGA and PCL-DOX HCl 1%/PLGA scaffolds, respectively

The proliferation of primary human dermal fibroblasts on the scaffolds was investigated through cellular metabolic activity. The results in Figure 5.28 showed that primary human dermal fibroblasts were able to attach and proliferate on the coaxial electrospun scaffolds over 14 days of cell culture. The incorporation of DOX HCl alone or with IBU Na into PCL/PLGA scaffolds did not retard the cell growth. Although slightly lower cellular metabolic activity was observed on day 7 with PCL-DOX HCl 1%/PLGA scaffolds when compared to blank PCL/PLGA scaffolds, metabolic activity of cells became comparable when the culture underwent to day 14. Higher metabolic activity of cells in PCL-DOX HCl 1%/PLGA-IBU Na 5% scaffolds when compared to

PCL-DOX HCl 1%/PLGA scaffolds on day 7 was perhaps due to the faster drug release from the scaffolds. Hence, cells could grow more rapidly.

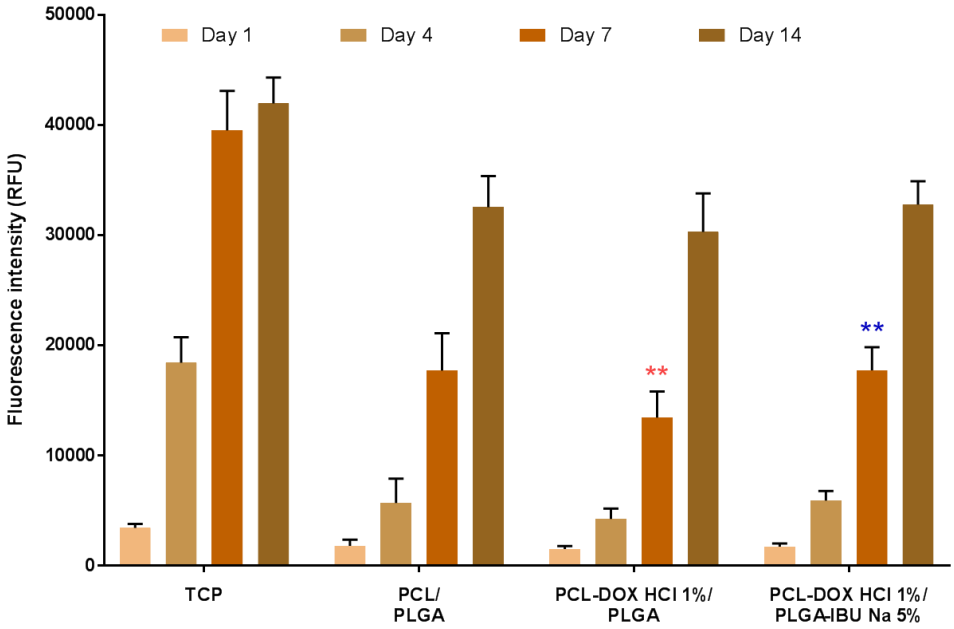


Figure 5.28. Cell proliferation on TCP, PCL/PLGA, PCL-DOX HCl 1%/PLGA, and PCL-DOX HCl 1%/PLGA-IBU Na 5% electrospun scaffolds determined by cellular metabolic activity of primary human dermal fibroblasts over 14 days using PrestoBlue® assay. Values shown are mean and standard deviation (n = 3, two independent experiments). ** defines a significant difference at the same time point at *p*-value < 0.01. * and * define a significant difference when compared to PCL/PLGA and PCL-DOX HCl 1%/PLGA scaffolds, respectively

5.5.4.2 LIVE/DEAD® assay

Representative images obtained from LIVE/DEAD® assay (Figure 5.29) confirmed the presence of primary human dermal fibroblasts on the scaffolds. The number of viable cells, which emitted green fluorescence, increased from day 1 to day 7.

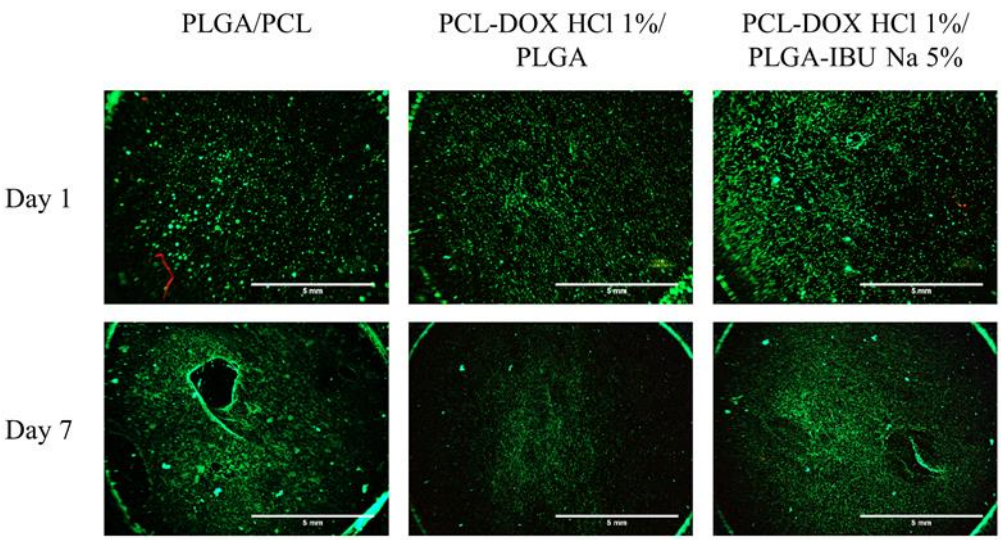


Figure 5.29. Fluorescent images obtained from LIVE/DEAD® assay illustrating the presence of viable (green) and dead (red) cells of primary human dermal fibroblasts on the surface of the electrospun scaffolds after 1 and 7 days of cell culture. The images were taken at the magnification of 2X (scale bar 5 mm).

5.5.4.3 Cell morphology by SEM

The morphology of cells after growing on the scaffolds was observed through SEM images. Round-shaped cell morphology of mouse fibroblasts was observed in all scaffolds (Figure 5.30). Mouse fibroblasts could adhere and proliferate on the scaffolds, but their morphology did not change to spindle-shaped even though the culture continued to day 14. This is attributed to the poor cell-material interaction due to the hydrophobicity of PCL.[283]

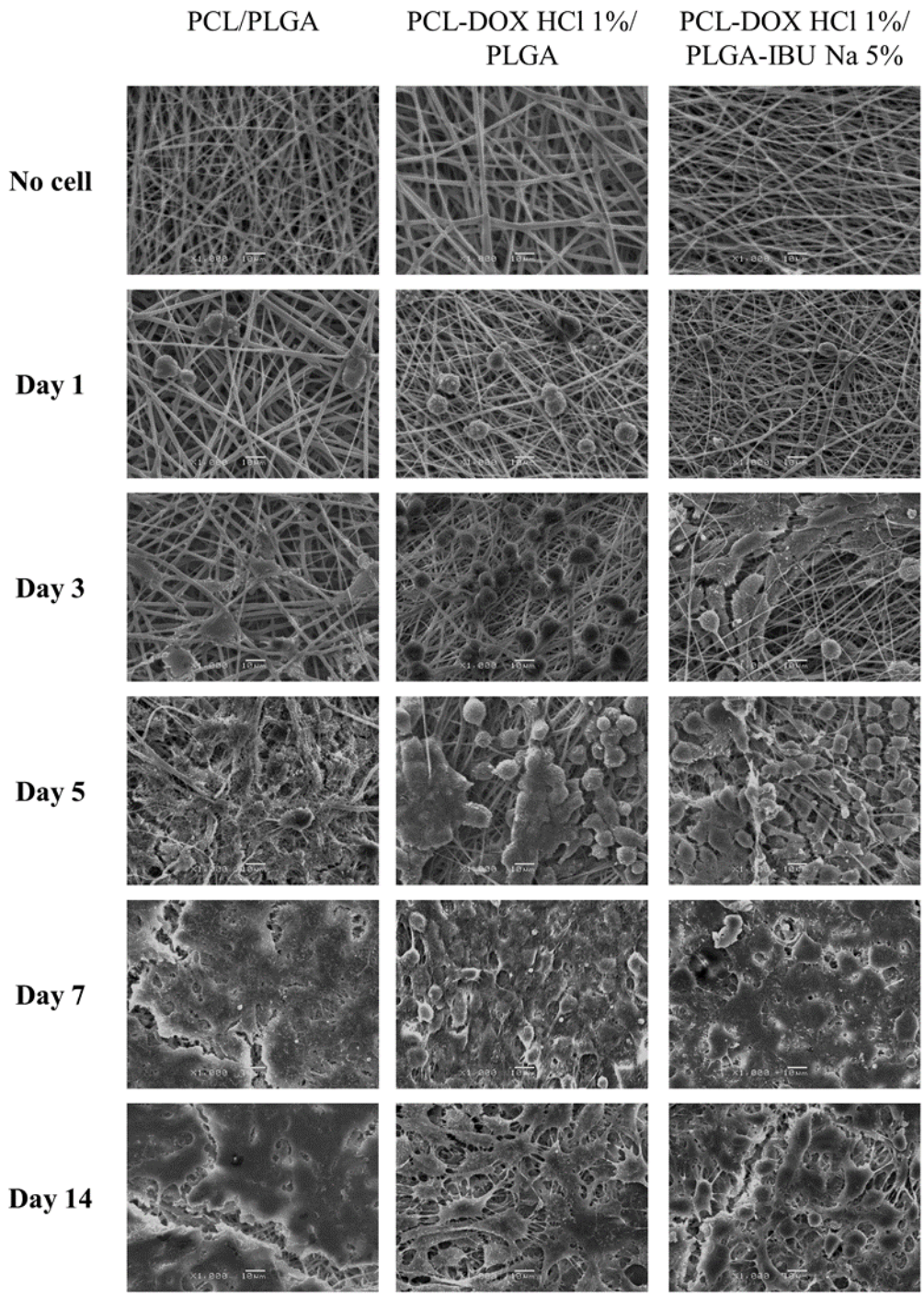


Figure 5.30. Representative SEM images showing cell morphology of mouse fibroblasts on the electrospun scaffolds at the magnification of 1,000X (scale bar 10 μm).

Figure 5.31 presents representative SEM images of primary human dermal fibroblasts on the scaffolds. Spindle cell morphology was observed when cells grew on the surface of the scaffolds for 14 days. Additionally, higher cell density, stack of cell layers, and more aligned orientation of cells were developed over time.

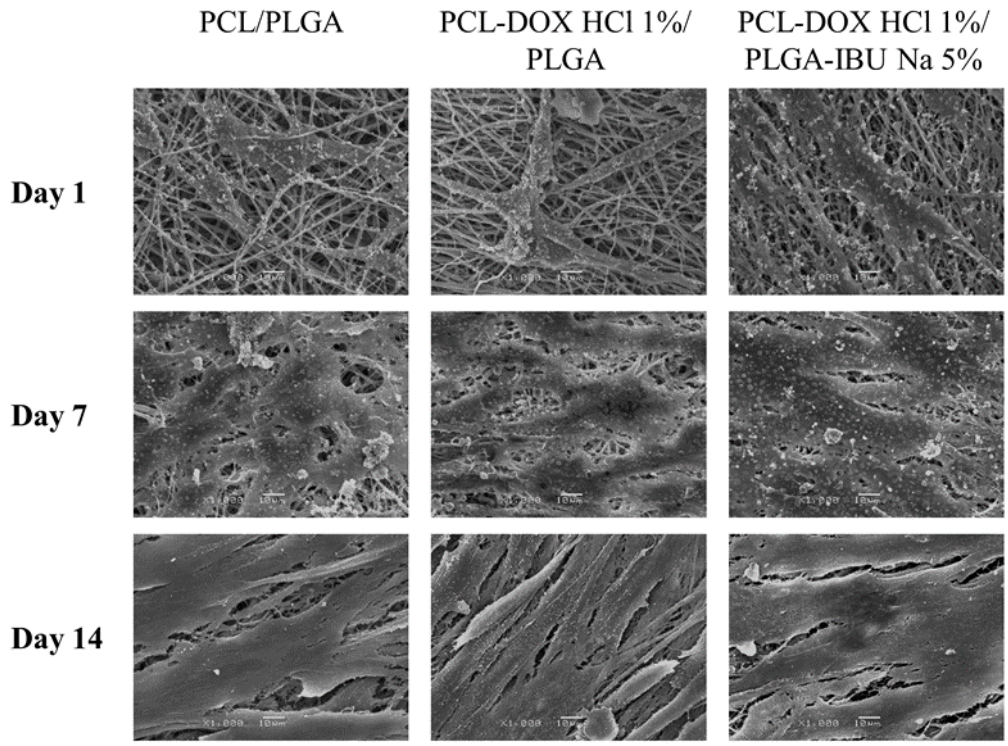


Figure 5.31. Representative SEM images showing cell morphology of primary human dermal fibroblasts on the electrospun scaffolds at the magnification of 1,000X (scale bar 10 µm).

Primary human dermal fibroblasts were in an elongated shape since day 1 of cell culture. In constrast, mouse fibroblasts were remained in a rounded shape until day 5 of cell culture before their morphology gradually became more spread. This is because of the presence of fibroblast growth factor in cell culture media used for culturing primary human dermal fibroblasts. The surface of scaffolds absorbs fibroblast growth factor, which promotes cell adhesion, elongation and proliferation.[229–232]

5.5.4.4 Cytoskeletal architecture of primary human dermal fibroblasts

The cytoskeletal arrangement of primary human dermal fibroblasts on the scaffolds was evaluated after 14 days of culture by staining F-actin with phalloidin and the cell nuclei were stained with Hoechst 33258. As shown in Figure 5.32, cells exhibited highly ordered spindle-shaped cytoskeletons when grown on the coaxial scaffolds. This result confirmed that cells could attach and spread on the surface of the scaffolds.

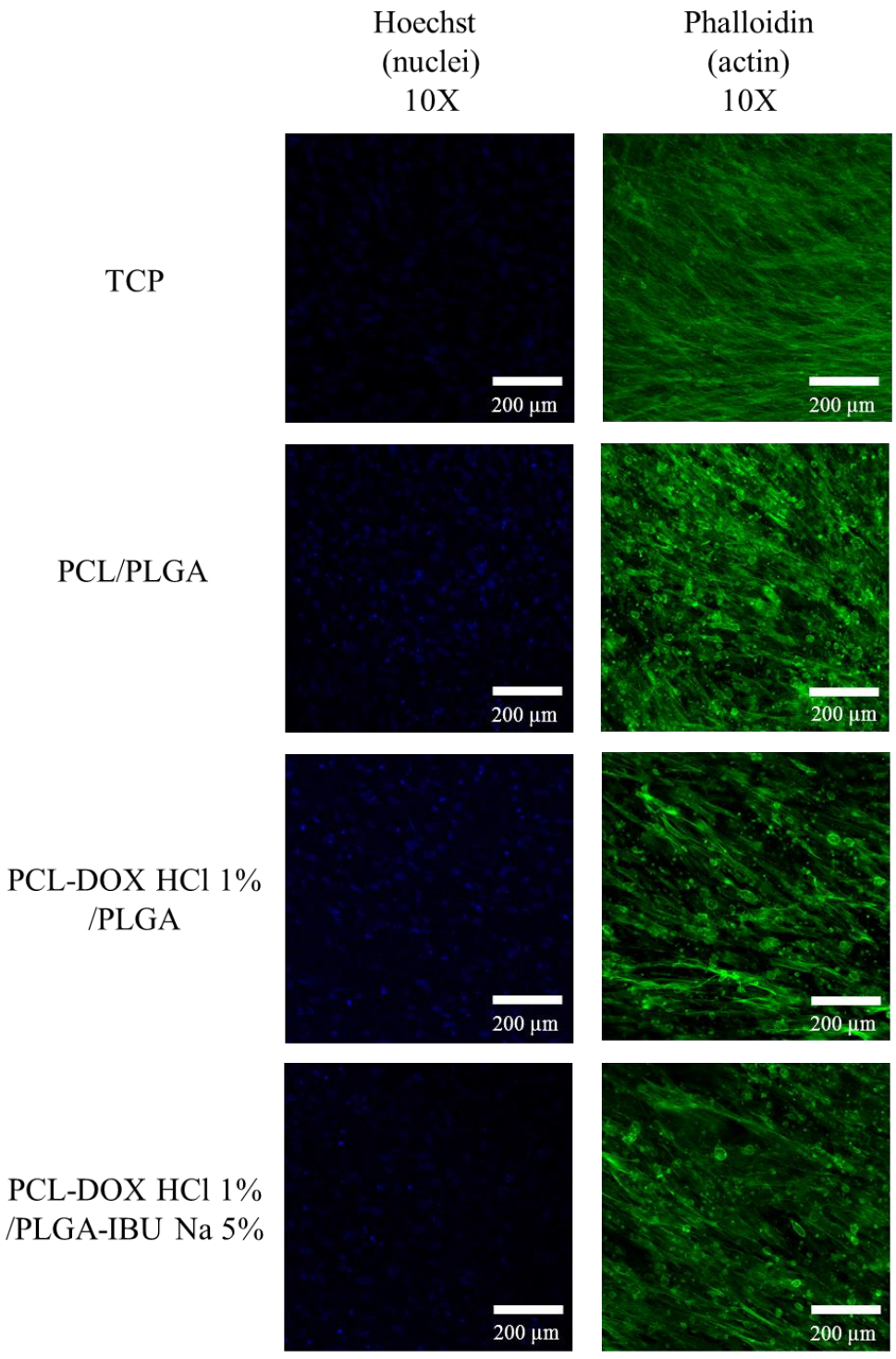


Figure 5.32. Representative confocal images of primary human dermal fibroblasts grown on tissue culture plastic (TCP) and the scaffolds for 14 days. Cell nuclei were stained with Hoechst, emitting blue fluorescence. F-actin were stained with Phalloidin, emitting green fluorescence. The images were taken at the magnification of 10X (scale bar 200 µm).

Table 5.11. Summary of scaffolds' properties

Property	PCL/ PLGA	PCL-DOX HCl 1%/ PLGA	PCL-DOX HCl 1%/ PLGA-IBU Na 5%
Fibre diameter (µm)	1.08 ± 0.34	0.82 ± 0.21	1.01 ± 0.29
Porosity (%)	79.09 ± 0.91	79.02 ± 0.99	76.09 ± 1.86
Water contact angle (static)	107.57 ± 4.37	116.94 ± 2.19	N/A
Water contact angle (advancing)	130.26 ± 5.14	128.63 ± 3.62	N/A
Water contact angle (receding)	48.19 ± 10.52	34.28 ± 1.30	N/A
Contact angle hysteresis	82.07 ± 7.21	94.35 ± 2.43	N/A
Ultimate tensile strength (MPa)	1.63 ± 0.15	5.79 ± 0.59	9.01 ± 1.92
Strain at break (%)	203.70 ± 39.84	162.47 ± 14.58	193.19 ± 18.17
Young's modulus (MPa)	8.49 ± 1.59	13.52 ± 3.29	11.48 ± 1.97
Encapsulation efficiency (%), DOX HCl	N/A	90.61 ± 3.35	75.06 ± 6.17
Encapsulation efficiency (%), IBU Na	N/A	N/A	72.59 ± 3.57
Cumulative drug release in 30 days (%), DOX HCl	N/A	74.92 ± 5.30	96.90 ± 5.01
Cumulative drug release in 30 days (%), IBU Na	N/A	N/A	99.26 ± 1.28
Drug localization	N/A	Surface	Surface
Drug-polymer interaction	N/A	No	No
Cumulative weight loss in 90 days (%)	31.12 ± 12.45	48.13 ± 5.72	42.91 ± 6.70
Cell proliferation on the scaffolds	Yes	Yes	Yes

N/A: not applicable

5.6 Conclusion

The work in this chapter has shown the potential of coaxial electrospinning to fabricate fibrous scaffolds for delivering drugs and simultaneously promoting cell proliferation. The structure of the scaffolds consisted of two distinct parts: outer PCL shell and inner PLGA core. According to the drug release profiles, DOX HCl and IBU Na were blended into PCL shell and PLGA core, respectively. The morphology of the coaxial electrospun scaffolds was rounded fibrous scaffolds with smooth surface and random orientation. The sharp boundary between the PCL shell and PLGA core was observed in all scaffolds. The scaffolds were highly porous and exhibited hydrophobic properties except PCL-DOX HCl 1%/PLGA-IBU Na 5% scaffolds that were completely wet as a result of hydrophilic drugs loaded. Incorporation of DOX HCl with/without IBU Na improved the mechanical strength of the scaffolds by dramatically increasing ultimate tensile strength. However, these drugs accelerated the degradation of the scaffolds as reflected in the greater weight loss was observed in all drug-loaded scaffolds.

Approximately 90% of DOX HCl was encapsulated in the PCL-DOX HCl 1%/PLGA scaffolds. However, the encapsulation of DOX HCl decreased to 75% when IBU Na was loaded to PLGA core. Within the same scaffolds, 72% of IBU Na was entrapped after electrospinning. The release of DOX HCl and IBU Na from the scaffolds was rapidly burst as observed in PLGA-IBU Na scaffolds and PCL-DOX HCl scaffolds in Chapters 3 and 4, respectively. The initial burst release occurred from the drug molecules that deposited on the uttermost top surface of fibres illustrated in images from the ToF-SIMS analysis.

The scaffolds were able to support cell proliferation of mouse fibroblasts and primary human dermal fibroblasts but in a different manner. The coaxial PCL/PLGA scaffolds that contained DOX HCl alone impeded the proliferation of mouse fibroblasts. While the coaxial PCL/PLGA scaffolds containing both DOX HCl and IBU Na could support cell proliferation after 7 days of cell culture. Only round-shaped cell morphology was observed although the number of cells was higher.

Primary human dermal fibroblasts exhibited a different behaviour when seeded on the scaffolds. The spindle shaped morphology which is the characteristic of fibroblast cells was observed in all scaffolds. In addition, cell proliferation on the blank PCL/PLGA scaffolds and drug-loaded scaffolds was considered comparable throughout the study. In addition, the cytoskeleton of cells was highly ordered, existed in aligned spindle arrangements. This confirmed that primary human dermal fibroblasts could adhere and spread themselves on the scaffolds.

It can be concluded that coaxial PCL/PLGA scaffolds were not only capable of carrying DOX HCl and IBU Na, but could also promote the proliferation of primary human dermal fibroblasts.

Chapter 6

Investigation of Doxycycline Hydrochloride- and Ibuprofen Sodium-doped Scaffolds in Simulated Cytokine-induction Inflammation Environments

6.1 Introduction

This part of the study aimed to investigate the performance of test materials under highly controlled conditions. The efficacy studies allow the investigation of advantages and disadvantages of test materials to occur through the testing with various techniques.[284]

There are various *in vitro* and *in vivo* approaches to assess the anti-inflammatory effects of scaffold materials.[115,285–289] Although the *in vitro* models are not able to mimic or represent the environment of wounds with the complexity as the *in vivo* models, they are less expensive, often more reproducible and minimize use of animal of models.[289–291] Moreover, they can provide a simple, rapid screening to observe effects of test materials on specific markers under controlled conditions.[289–291] Importantly, the differences between the skin of the mouse and human should be also taken into account.[292] The efficacy of materials presented in the mouse skin model may not be observed in the human skin.[292]

The *in vitro* inflammation models can be prepared in a variety of ways (*e.g.* 2D cells, 3D cells, skin equivalent and full thickness skin biopsies) with single cell type or co-culture of multiple cell types.[90,289,292–295] In general, cells are seeded and an inflammatory response triggered by single or mixed stimulants. The common stimulants used for creating the inflammation environment are cytokines (*e.g.* TNF-α, IL-1β and IFN-γ), bacterial endotoxin–lipopolysaccharide (LPS), and radiation (*e.g.* ultraviolet (UV) A and UVB).[292,293,296–298] After the stimulation, it is expected that cells secrete or express typical inflammation mediators such as prostaglandin E_2 (PGE_2), nitric oxide and matrix metalloproteinases (MMPs).[299–306]

In human fibroblasts, PGE_2 is constitutively generated by cyclooxygenase (COX)-1 enzyme with comparatively higher levels produced by inducible COX-2 enzyme in response to pro-inflammatory cytokines.[302,307] The expression of COX-2 enzyme is regulated by the activation of nuclear factor kappa B (NF-κB).[307]

In the inflammation phase, inducible nitric oxide synthase is upregulated by pro-inflammatory cytokines in fibroblasts, resulting in the increase in NO production.[308] High levels of NO results in cell senescence and apoptosis, leading to dysregulation in wound healing.[309] While, low levels of NO functions as a vasodilator and neurotransmitter agent.[308] Furthermore, NO at low levels exhibits anti-microbial and anti-proliferative effects as well as promoting angiogenesis.[308,309]

MMP enzymes contribute to the breakdown of extracellular matrix (ECM) to allow the migration of inflammatory cells into the injured area.[310,311] In human dermal fibroblasts, MMP-1 enzyme is one of the most abundant expressed MMPs.[311] After 24 h stimulation with 10 ng/mL TNF-α, the expression of MMP-1 was increased by 100 fold when compared to the untreated control.[311] In addition, it has been reported that IL-1β can also induce the expression of MMP-1 enzyme in dermal fibroblasts.[312–315]

Therefore, the quantification of these markers in cell supernatant can be used to determine the efficacy of test materials against the stimuli-induced inflammation.

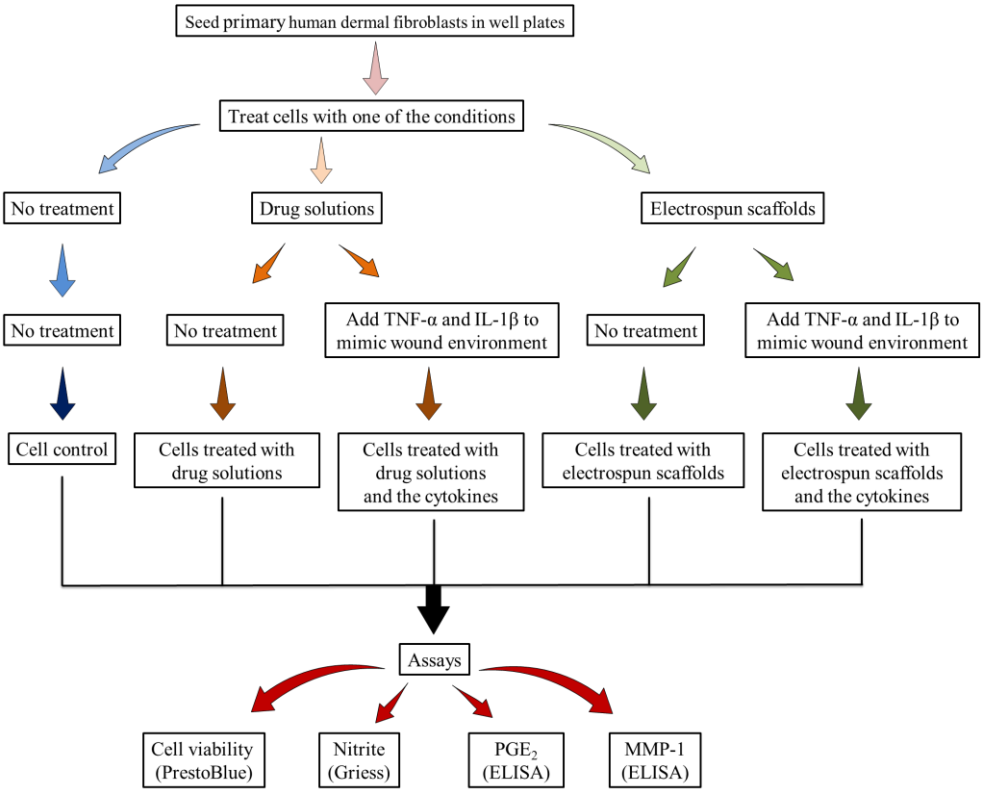
6.2 Aims

The aims of this chapter were to investigate and compare the efficacy of PCL-DOX HCl scaffolds that were fabricated with different drug loadings as described in Chapter 4 on the production/expression of inflammatory mediators: nitrite, MMP-1 enzyme and PGE_2. In addition, the effect of the coaxial PCL/PLGA scaffolds containing DOX HCl with/without IBU Na fabricated in Chapter 5 on the production of the inflammatory mediators were assessed and compared to observe, if IBU Na has the synergistic effect with DOX HCl to inhibit cytokine-induced MMP-1 expression.

The aims were achieved with the following objectives:

1. Assess the effect of DOX HCl solutions with different concentrations on cell viability, the expression of MMP-1, and the production of nitrite and PGE_2 both in the presence and absence of TNF-α and IL-1β.
2. Evaluate the effect of PCL-DOX HCl scaffolds with different drug loadings on cell viability, the expression of MMP-1, and the production of nitrite and PGE_2 both in the presence and absence of TNF-α and IL-1β.
3. Assess the effects of DOX HCl solution, IBU Na solution and the mixture of DOX HCl and IBU Na on cell viability, the expression of MMP-1, and the production of nitrite and PGE_2 both in the presence and absence of TNF-α and IL-1β.
4. Investigate and compare the effect of coaxial PCL/PLGA scaffolds that contain only DOX HCl and contain both DOX HCl and IBU Na on cell viability, the expression of MMP-1, and the production of nitrite and PGE_2 both in the presence and absence of TNF-α and IL-1β.

6.3 Experimental overview



6.4 Methods

6.4.1 Cell seeding

Primary human dermal fibroblasts were seeded in 24-well tissue culture plates at the cell density of 20,000 cells/well and 1 mL of fresh cell culture media were added to each well. The formulation of cell culture media can be found in Table 6.1. Cells were incubated in the incubator under 37 °C and 5% CO_2 for 24 hours before the exposure to the conditions.

Table 6.1. The formulation of cell culture media for primary human dermal fibroblasts used in the efficacy testing

Component	Final concentration
rh bFGF	5 ng/mL
L-glutamine	7.5 mM
rh Insulin	5 mg/mL
Fetal Bovine Serum	2%
Penicillin	10 units/mL
Streptomycin	10 µg/mL
Amphotericin B	25 ng/mL

6.4.2 Conditions

After PrestoBlue® assay, the PrestoBlue® solution was removed and 1 mL of D-PBS (without calcium and magnesium) were gently added to wash any residual PrestoBlue® reagent in the well. Later, drug solutions in cell culture media (total volume: 1.9 mL) or the electrospun scaffolds that were pre-incubated in 1.9 mL cell culture media for 24 hours were transferred to treat cells in the wells. Meanwhile, the cell control was treated with 1.9 mL cell culture media. After 2 hours of pre-incubation with drug solutions or the scaffolds, the mixture of 10

ng/mL TNF-α and 10 ng/mL IL-1β (R&D systems, UK), were added to cell culture media in order to mimic the environment of chronic wounds (final volume: 2 mL/well). Cells were further incubated with the cytokines for 48 hours before cell culture media were collected for the assays including the expression of MMP-1, and the production of nitrite and PGE_2.

6.4.3 Assays

6.4.3.1 Cell viability by PrestoBlue® assay

At 24 h post cell seeding, cell culture media was removed from the wells and replaced by 1 mL of PrestoBlue® solution in cell culture media (1 PrestoBlue:9 cell culture media). Cells were incubated with PrestoBlue® solution in the incubator for an hour before an aliquot (150 µL) from each well was taken and transferred to a flat-bottomed 96-well plate for fluorescence reading by a plate reader (Tecan Infinite M2000) at excitation/emission wavelength of 560/590 nm. PrestoBlue® solution in cell culture media was used as a 'no cell control' and its fluorescence was deducted from each sample's fluorescence to account for background fluorescence. PrestoBlue® assay was repeated again when the stimulation with the cytokines has been finished to investigate the effect of the conditions on cell viability.

6.4.3.2 Detection of nitrite by Griess assay

The measurement of nitrite by the Griess assay has been performed to indirectly assess the production of NO. As NO is unstable and converted to nitrate and nitrite.[309] Nitrate can also be reduced further to nitrite by nitrate reductase. Therefore, the total level of nitrite can be used to estimate the production of NO in cell supernatant.[309]

The Griess assay (Promega) is based on the chemical reaction using sulfanilamide and *N*-1-napthylethylenediamine dihydrochloride (NED) under acidic conditions (in the presence of phosphoric acid) to investigate the formation of nitric oxide (NO) *via* the detection of nitrite (NO_2^-)—a stable breakdown product of NO.

At the end of the experiment, 50 µL of cell supernatant was collected from each well and transferred to a 96-well plate. Sulfanilamide (50 µL) was then added to each well and incubated in dark for 5–10 minutes at room temperature. Cell supernatant in each well turned into clear colourless solution at this step. Later, 50 µL of NED solution was added to the well and incubated in dark for 5–10 minutes at room temperature. The purple/magenta colour would develop if there was nitrite in cell supernatant. Within 30 minutes, the absorbance of the solutions was measured by the plate reader at the wavelength of 520 nm. To quantify the concentration of nitrite, the absorbance of sample was compared to the standard curve.

6.4.3.3 MMP-1 ELISA assay

To quantify the level of MMP-1 in cell supernatant, the assay was performed using Human MMP-1 ELISA Kit (EHMMP1, Thermo Scientific, UK) with the recommended manufacturer's protocol. This assay uses the human MMP1 solid-phase sandwich ELISA (enzyme-linked immunosorbent assay). MMP-1 enzymes in cell supernatant bind to the immobilised antibody (capture antibody) in the coated 96-well plate. After washing in wash buffer, biotinylated anti-Human MMP1 antibody (detection antibody) was added to bind with another epitope on MMP-1. The unbound biotinylated antibody was removed by the washes and then HRP-conjugated streptavidin was pipetted to the wells. After incubating for 45 minutes at room temperature, the wells were washed again, and followed by addition of a solution of TMB substrate to develop a blue colour, which is proportional to the concentration of MMP-1. Finally, the stop solution was added, and the colour of the solution changed from blue to yellow. The absorbance of the samples was then measured at 450 nm and 550 nm. The values obtained at 550 nm were subtracted from the values obtained at 450 nm to correct for the optical imperfections in the microplate. The concentration of MMP-1 in the sample was calculated by comparing with a standard curve.

6.4.3.4 PGE_2 ELISA assay

To quantify the level of PGE_2 in cell supernatant, the assay was performed using Parameter™ PGE_2 Assay (R&D Systems, UK) with the manufacturer's protocol. The assay is based on the competitive binding of PGE_2 in the sample with horseradish peroxidase (HRP)-labelled PGE_2 for binding sites on a mouse monoclonal antibody. The first incubation (1 hour) allowed PGE_2 present in the sample to bind with the antibody. During the second incubation (2 hours), the remaining sites of the antibody was bound to HRP-labelled PGE_2. Later, the unbound materials were removed in the washing step. The bound enzyme activity was determined using the intensity of the colour developing after the addition of a substrate solution and stop solution consecutively. The intensity of the colour is inversely proportional to the concentration of PGE_2 in the sample. The absorbance of the solutions was measured by the plate reader at 450 nm and 570 nm. The readings at 570 nm were subtracted from the readings at 450 nm to correct for optical imperfections in the plate. PGE_2 concentration in the sample was determined using a standard curve.

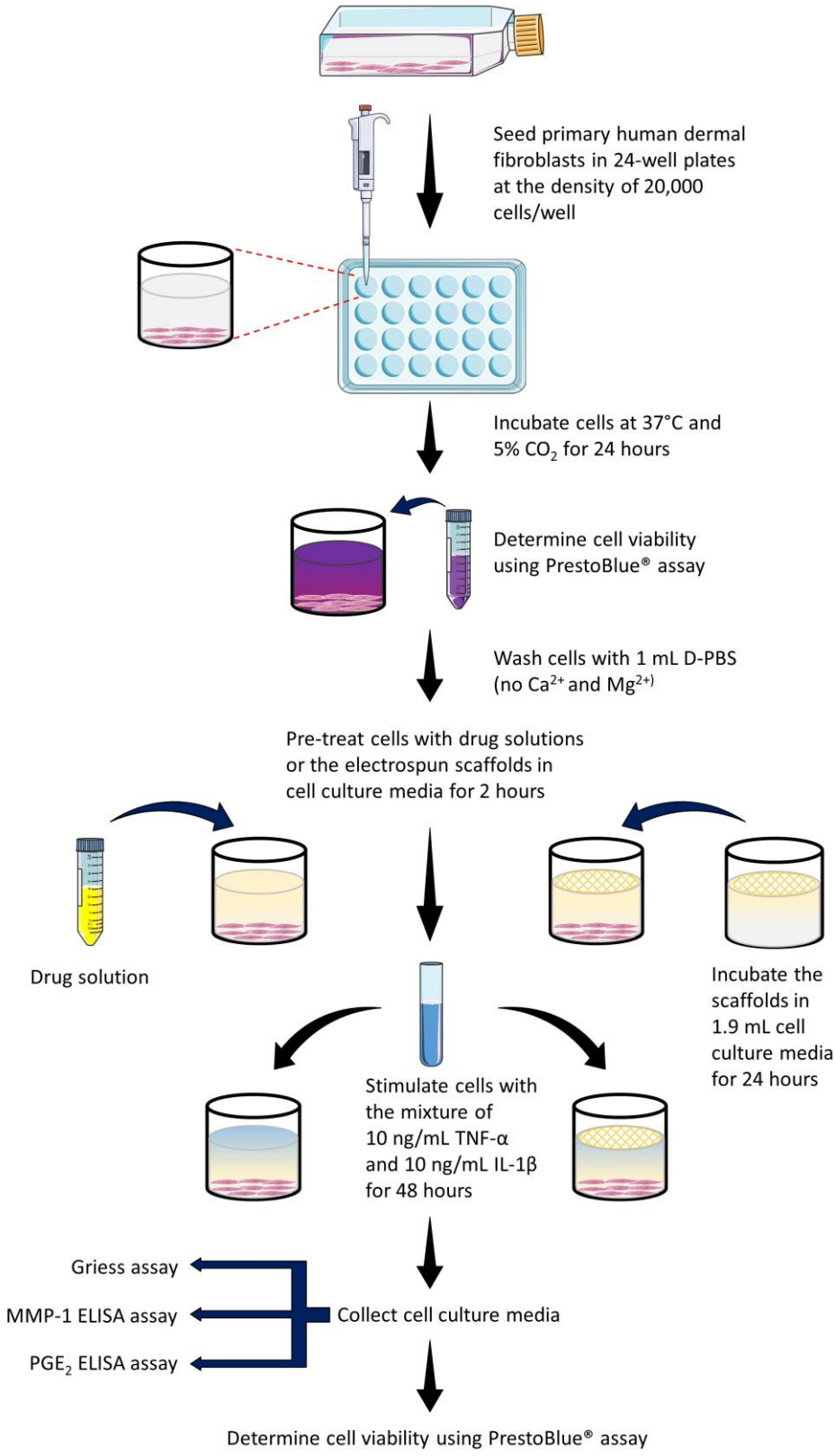


Figure 6.1. A schematic outlining the experimental procedure to perform the efficacy testing.

6.5 Results and Discussion

In order to assess the efficacy of the electrospun scaffolds fabricated in Chapters 4 and 5 against the cytokine-induced inflammation, the production/expression of the inflammatory mediators was determined. After cell seeding, primary human dermal fibroblasts were pre-treated with the electrospun scaffolds in order to allow drugs to exhibit their pharmacological effects before exposure to the cytokines. It is worth noting that the scaffolds were submerged in cell culture media and floated above the cell monolayer (indirect contact). As a consequence, the effect of drug released from the scaffolds without direct cell-scaffold interaction would merely be obtained.

The chosen cytokines to induce the inflammation in this work were TNF-α and IL-1β as chronic wounds have the excessive levels of these two cytokines.[22,316–320] The concentration of each cytokine at 10 ng/mL and 48-h exposure time to the cytokines were selected based on literatures.[298,306,321–323] Cell culture media was collected for the assays, including the expression of MMP-1, and the production of nitrite and PGE_2.

The results in this Chapter are divided into 2 main sections: the efficacy testing of PCL-DOX HCl scaffolds and the efficacy testing of the coaxial electrospun scaffolds. Each of the sections is further subcategorised into 2 subsections: the efficacy testing of drug solutions and the efficacy testing of the scaffolds.

6.5.1 Evaluation of the PCL-DOX HCl scaffolds

6.5.1.1 DOX HCl solutions

The representative concentrations of DOX HCl for the efficacy test were selected based on the amount of drug encapsulated in the scaffolds. If DOX HCl is completely released from PCL-DOX HCl 1%, PCL-DOX HCl 2% and PCL-DOX HCl 5% scaffolds, the concentrations of DOX HCl in cell culture media will be approximately 50, 100 and 250 µM, respectively.

6.5.1.1.1 Cell viability

Figure 6.2 shows that the mixture of 10 ng/mL TNF-α and 10 ng/mL IL-1β did not affect the viability of cells when compared to the cell control. In contrast, DOX HCl exhibited cytotoxic effect, decreasing the viability of primary human dermal fibroblasts in a dose-dependent manner. Higher concentrations of DOX HCl led to the lower cell viability regardless of the absence of the cytokines (cell viability: 69.78 ± 10.98%, 48.31 ± 6.67% and 28.60 ± 4.40% for 50 µM, 100 µM and 250 µM DOX HCl, respectively); or the presence of the cytokines (cell viability: 81.34 ± 3.75%, 63.93 ± 6.57% and 43.70 ± 8.25% for 50 µM, 100 µM and 250 µM DOX HCl, respectively).

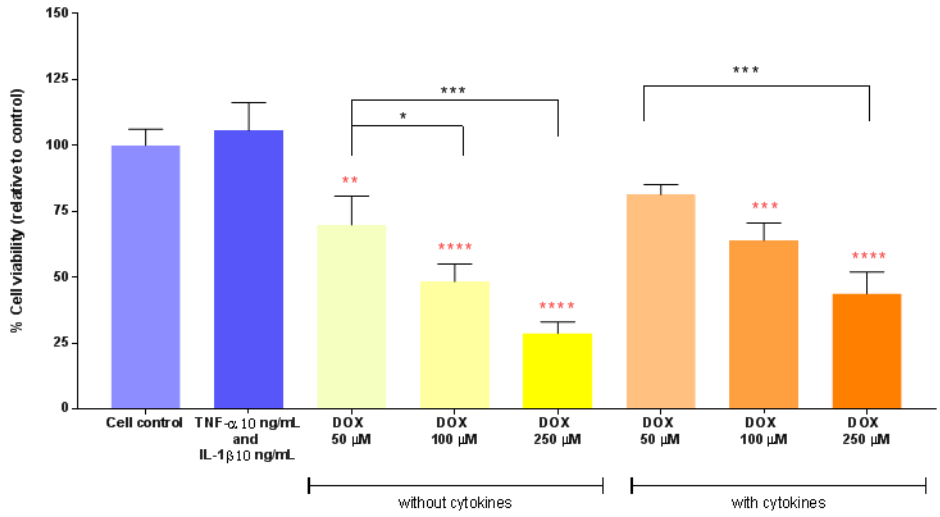


Figure 6.2. % Cell viability of primary human dermal fibroblasts when treated with the mixture of 10 ng/mL TNF-α and 10 ng/mL IL-1β, DOX HCl solutions (50, 100 and 250 µM), or pre-treated with DOX HCl solutions (50, 100 and 250 µM) for 2 hours before the exposure to the cytokines. The values are means and standard deviations of triplicate samples (n = 3). *, **, *** and **** define statistical significance at *p*-value < 0.05, < 0.01, < 0.001 and < 0.0001, respectively. Red asterisks are used to identify the significant difference when compared to the cell control. Black asterisks are used to identify the significant difference between two conditions.

In this study, primary human dermal fibroblasts were subjected to inflammation by exposure to the mixture of 10 ng/mL TNF-α and 10 ng/mL IL-1β. Previous studies reported that TNF-α promoted the proliferation of human fibroblasts.[323,324] TNF-α in the range of 0–200 ng/mL did not seem to exhibit a cytotoxic effect on human dermal fibroblasts after 72-h culture.[325] In addition, the proliferation of human dermal fibroblasts was promoted by IL-1β in a dose-dependent manner.[326,327] Although such effects were not observed in this work, the mixture of 10 ng/mL TNF-α and 10 ng/mL IL-1β could at least maintain a comparable cell viability to the cell control, and did not exhibit any cytotoxic effect.

Conversely, DOX HCl solutions exhibited the cytotoxic effect on primary human dermal fibroblast in a dose-dependent fashion.[328] The exposure to the cytokines after DOX HCl pre-treatment tended to antagonise the cytotoxic effect of drug, showing as approximately 20% higher in cell viability at the same drug concentration. It was possibly due to the down-regulation of TNF-α and IL-1β expression by doxycycline.[176] Hence, the addition of external TNF-α and IL-1β into cell culture media compensated the cytokines in the system. The DOX HCl-mediated cytotoxicity was therefore reduced.

6.5.1.1.2 Nitrite production

The results in Figure 6.3 revealed that the production of nitrite by primary human dermal fibroblasts was not significantly induced by the mixture of 10 ng/mL TNF-α and 10 ng/mL IL-1β. In contrast, DOX HCl at the concentrations of 50, 100 and 250 μM all significantly promoted the production of nitrite with respect to the cell control. The induction of nitrite production by DOX HCl was found to be dependent on the drug concentration. Interestingly, primary human dermal fibroblasts that were pre-treated with 250 μM DOX HCl before the exposure to the cytokines produced relatively less nitrite when compared to cells that were treated only with 250 μM DOX HCl.

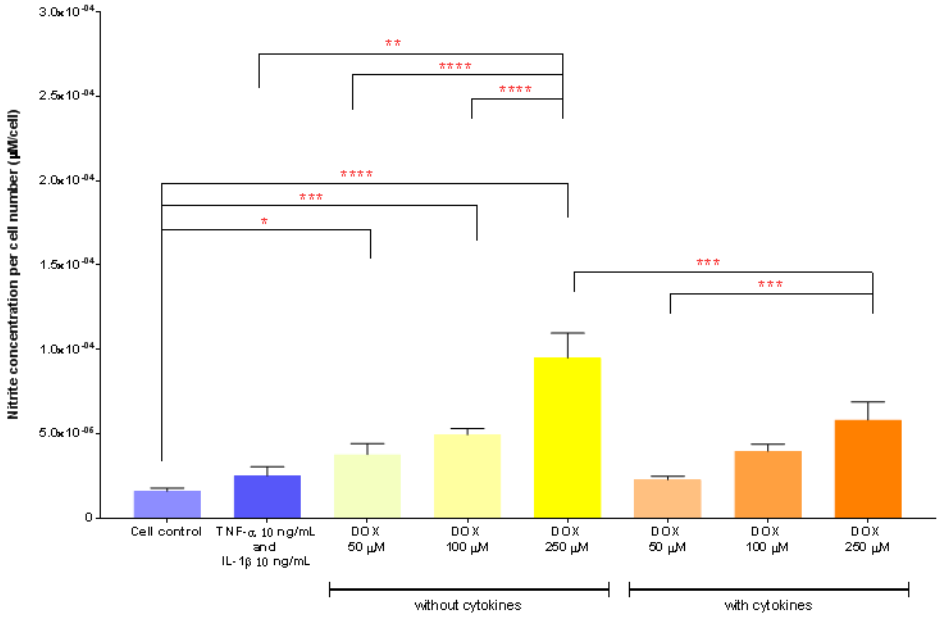


Figure 6.3. Normalised concentration of nitrite produced by primary human dermal fibroblasts when treated with the mixture of 10 ng/mL TNF-α and 10 ng/mL IL-1β, DOX HCl solutions (50, 100 and 250 µM), or pre-treated with DOX HCl solutions (50, 100 and 250 µM) for 2 hours before the exposure to the cytokines. The values are means and standard deviations of triplicate samples (n = 3). *, *** and **** define statistical significance at *p*-value < 0.05, < 0.001 and < 0.0001, respectively.

Although hydrocortisone hemisuccinate and ascorbic acid which are anti-inflammatory and anti-oxidant agents were removed from cell culture media to avoid their interfering effects on cytokine-mediated inflammation, serum and basic fibroblast growth factor (bFGF) were remained to support cell growth.[290]

It was more likely that bFGF exhibited anti-inflammatory effect and antagonised the effect of TNF-α and IL-1β. The previous studies observed that bFGF suppressed cytokine-induced iNOS mRNA expression in bovine corpus luteum.[329] Therefore, the inflammation in the surrounding tissues did not take place.[329] In addition, bFGF inhibited cytokine-induced synthesis of complement protein factor B (alternative pathway of complement activation to initiate the inflammation[330]) in human fibroblasts and exhibited anti-inflammatory effect.[331]

The inhibiting effect of bFGF was also found in myocytes as it completely inhibited cell apoptosis induced by hydrogen peroxide or LPS.[332] Moreover, bFGF decreased LPS-induced iNOS expression.[332] Taking all into account, bFGF antagonise the stimulation of nitrite production by TNF-α and IL-1β. Hence, the level of nitrite remained unchanged when compared to the cell control even though the cells were stimulated with the cytokines for 48 hours.

Moreover, it was observed that the production of reactive oxygen species (ROS) was not induced by the single exposure to TNF-α although high concentration of TNF-α (100 ng/mL) was used to stimulate human dermal fibroblasts.[325] In contrast, repetitive exposures to 10 or 100 ng/mL TNF-α for a total of 10 consecutive treatments every 2 days increased the production of ROS by 20% and 40% when compared to those of untreated cells, respectively.[325] This was perhaps because TNF-α induces the premature senescence of cells.[325]

DOX HCl enhanced the production of nitrite in a dose-dependent fashion. This agreed with the previous study—the greater cytotoxicity effect at higher concentrations of test sample resulted in the higher production of nitrite.[333] Additionally, lower nitrite production was observed in cells exposed to the cytokines after DOX HCl pre-treatment when compared to those of cells treated with only DOX HCl. This was related to the lower cytotoxicity after exposure to the cytokines as discussed above regarding cell viability. However, it is worth noting that these differences were not statistically significant.

6.5.1.1.3 The expression of MMP-1 enzyme

The effects of the cytokines, DOX HCl solutions and the combination on the expression of MMP-1 enzyme were investigated (Figure 6.4). It was clearly seen that the mixture of TNF-α and IL-1β strongly enhanced the expression of MMP-1 by approximately 8.24 fold with respect to the cell control. Whereas, DOX HCl (50, 100 and 250 µM) did not promote the expression of MMP-1 when compared to the cell control. The results also showed that DOX HCl was able to reduce cytokine-induced MMP-1 expression—higher level of DOX HCl more efficiently dropped the level of MMP-1. The expression of MMP-1 decreased from 1.01 ± 0.43 $pg \cdot mL^{-1} \cdot cell^{-1}$ to 0.43 ± 0.06, 0.19 ± 0.03 and 0.08 ± 0.01 $pg \cdot mL^{-1} \cdot cell^{-1}$ for 50 µM, 100 µM and 250 µM DOX HCl, respectively.

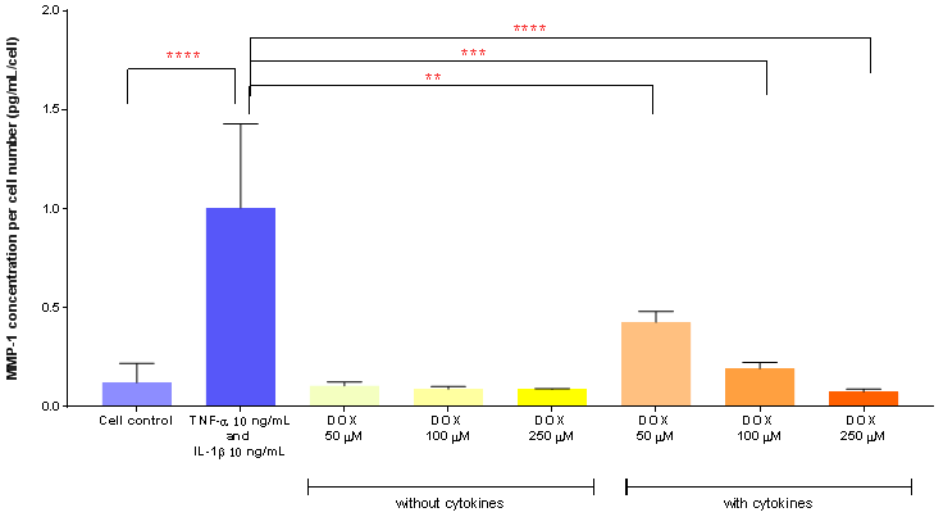


Figure 6.4. Normalised concentration of MMP-1 enzyme expressed by primary human dermal fibroblasts when treated with the mixture of 10 ng/mL TNF-α and 10 ng/mL IL-1β, DOX HCl solutions (50, 100 and 250 µM), or pre-treated with DOX HCl solutions (50, 100 and 250 µM) for 2 hours before the exposure to the cytokines. The values are means and standard deviations of triplicate samples (n = 3). **, *** and **** define statistical significance at *p*-value < 0.01, < 0.001 and < 0.0001, respectively.

The expression of MMP-1 enzyme was upregulated in the presence of 10 ng/mL TNF-α and 10 ng/mL IL-1β. It was previously reported that IL-1β alone showed a stimulatory effect on the expression of MMP-1 in human dermal fibroblasts.[312–315] Similarly, several studies reported the increase in MMP-1 expression *via* TNF-α stimulation.[305,306,311,313–315,325,334] When TNF-α was combined with IL-1β, their stimulatory effects on MMP-1 expression remained unchanged.[335] They could upregulate the expression of MMP-1 in dermal fibroblasts when compared to untreated cells.[336] Furthermore, the expression of MMP-1 in human dermal fibroblasts was also promoted by bFGF.[337]

DOX HCl at the concentrations of 50, 100 and 250 µM themselves neither induced nor reduced the expression of MMP-1. All concentrations of DOX HCl (50, 100 and 250 µM) showed the potential to prevent cytokine-induced MMP-1 expression.[338,339]

6.5.1.1.4 The production of PGE_2

Similar to the production of nitrite, the mixture of 10 ng/mL TNF-α and 10 ng/mL IL-1β was unable to stimulate the production of PGE_2 in primary human dermal fibroblasts (Figure 6.5). Whilst, 250 µM DOX HCl could induce the production of PGE_2 by approximately 4.98 folds (referenced with the cell control). Moreover, it was observed that the production of PGE_2 in cells that were exposed to the cytokines after 250 µM DOX HCl pre-treatment was slightly lower than those of cells exposed to 250 µM DOX HCl only (0.71 ± 0.22 $pg \cdot mL^{-1} \cdot cell^{-1}$ *versus* 0.91 ± 0.20 $pg \cdot mL^{-1} \cdot cell^{-1}$).

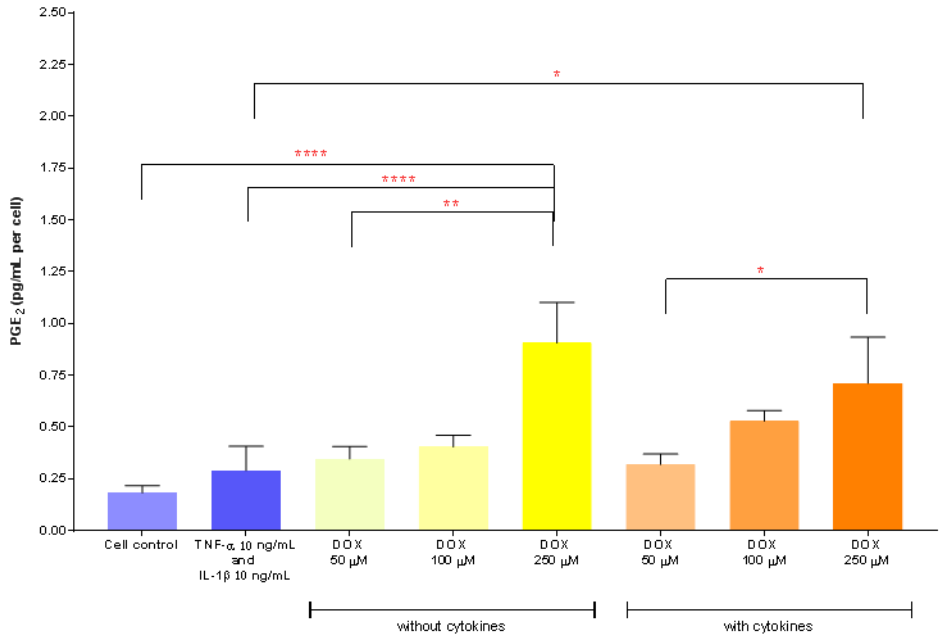


Figure 6.5. Normalised concentration of PGE_2 produced by primary human dermal fibroblasts when treated with the mixture of 10 ng/mL TNF-α and 10 ng/mL IL-1β, DOX HCl solutions (50, 100 and 250 µM), or pre-treated with DOX HCl solutions (50, 100 and 250 µM) for 2 hours before the exposure to the cytokines. The values are means and standard deviations of triplicate samples (n = 3). *, **, *** and **** define statistical significance at *p*-value < 0.05, < 0.01, < 0.001 and < 0.0001, respectively.

Although it was reported in the literature that TNF-α and IL-1β promoted the production of PGE_2[306,340,341], such an effect was not observed in this study. The previous studies found that the expression of COX-2 enzyme was reduced by approximately 50% in proliferative fibroblasts when compared to quiescent fibroblasts.[342] Quiescent fibroblasts expressed high level of COX-2 enzyme in response to TNF-α, IL-1β, and LPS.[343,344] This perhaps relates to the release of cytoguardin, an anti-inflammatory factor released by proliferative fibroblasts but not in quiescent fibroblasts.[342] Cytoguardin could inhibit the expression of COX-2 enzyme in human foreskin fibroblasts that was stimulated by TNF-α, IL-1β, bFGF and LPS.[345] The inhibition of COX-2 expression by cytoguardin was reported that was involved with blocking the activation of NF-κB induced by pro-inflammatory mediators.[346]

The increase in PGE_2 production was observed in those cells treated with DOX HCl. The higher concentrations of DOX HCl led to the higher production of PGE_2 which could be related to the greater cytotoxicity (Figure 6.2). The upregulated COX-2 gene expression and increased PGE_2 production were observed when cells were facing with cell death-inducing conditions.[347]

It was observed that doxycycline was capable of decreasing the production of TNF-α, IL-1β and NO both in the *in vitro* and the *in vivo* studies.[348,349] However, doxycycline induced the upregulation of COX-2 expression, resulting in the increase in PGE_2 production.[348,349]

Table 6.2. Summary of cell viability, the expression of MMP-1 enzyme and the production of nitrite and PGE_2 by primary human dermal fibroblasts after being treated under the specific conditions.

Condition	Cell viability (%)	Nitrite ($pM \cdot cell^{-1}$)	MMP-1 ($pg \cdot mL^{-1} \cdot cell^{-1}$)	PGE_2 ($pg \cdot mL^{-1} \cdot cell^{-1}$)
Cell control	100.00 ± 6.15	15.88 ± 1.88	0.12 ± 0.10	0.18 ± 0.03
TNF-α and IL-1β (T+I)	105.60 ± 10.59	25.11 ± 5.28	1.01 ± 0.42	0.29 ± 0.12
50 µM DOX HCl	69.78 ± 10.98	37.62 ± 6.57	0.11 ± 0.02	0.35 ± 0.06
100 µM DOX HCl	48.31 ± 6.67	49.45 ± 3.62	0.09 ± 0.01	0.40 ± 0.06
250 µM DOX HCl	28.60 ± 4.40	94.96 ± 14.79	0.09 ± 0.01	0.91 ± 0.20
50 µM DOX HCl +T+I	81.33 ± 3.75	22.73 ± 2.05	0.43 ± 0.06	0.32 ± 0.05
100 µM DOX HCl +T+I	63.93 ± 6.57	39.72 ± 4.06	0.19 ± 0.03	0.53 ± 0.05
250 µM DOX HCl +T+I	43.70 ± 8.25	58.21 ± 10.68	0.08 ± 0.01	0.71 ± 0.22

6.5.1.2 PCL-DOX HCl scaffolds

To determine the effect of the electrospun scaffolds on the production/expression of the inflammatory mediators, PCL, PCL-DOX HCl 1%, PCL-DOX HCl 2% and PCL-DOX HCl 5% scaffolds fabricated in Chapter 4 were assessed using the same experimental set up as DOX HCl solutions.

6.5.1.2.1 Cell viability

To test the effect of DOX HCl released from PCL electrospun scaffolds, an indirect cell viability study was performed on primary human dermal fibroblasts. The cytotoxic effects of DOX HCl were tested by the PrestoBlue® assay to assess the metabolic activity of cells exposed to the scaffolds with different drug loadings. To demonstrate that the cytotoxicity was caused by the released DOX HCl and not by the material used for fabricating the electrospun scaffolds, blank PCL electrospun scaffolds were tested in parallel with PCL-DOX HCl scaffolds.

As shown in Figure 6.6, blank PCL electrospun scaffolds showed good biocompatibility with primary human dermal fibroblasts. Conversely, the viability of primary human dermal fibroblasts significantly decreased in the presence of PCL-DOX HCl 2% and PCL-DOX HCl 5% scaffolds when compared to the cell control. The higher loadings of DOX HCl into PCL scaffolds led to the greater reduction in cell viability (77.35 ± 9.50%, 60.32 ± 5.71 and 34.09 ± 3.59% for PCL-DOX HCl 1%, PCL-DOX HCl 2% and PCL-DOX HCl 5% scaffolds, respectively).

Interestingly, percentage cell viability was not significantly different from the cell control when cells were pre-treated with PCL-DOX HCl 2% scaffolds and followed by the exposure to the cytokines (82.91 ± 16.41%). Whilst, the significant reduction in cell viability was still observed in the case of the cells that were pre-treated with PCL-DOX HCl 5% scaffolds, followed by the exposure to the cytokines (57.46 ± 5.39%).

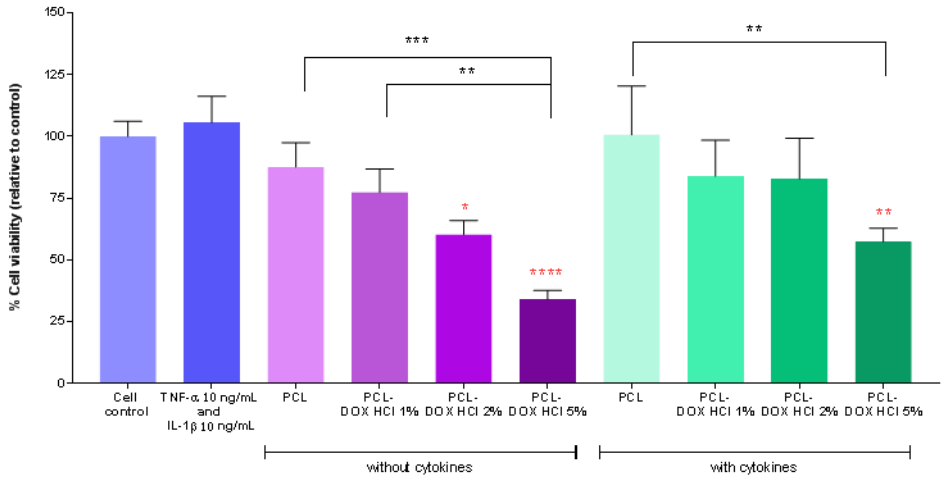


Figure 6.6. % Cell viability of primary human dermal fibroblasts when treated with the mixture of 10 ng/mL TNF-α and 10 ng/mL IL-1β, the scaffolds in cell culture media, or pre-treated with the scaffolds in cell culture media for 2 hours before the exposure to the cytokines. The values are means and standard deviations of triplicate samples (n = 3). *, **, *** and **** define statistical significance at *p*-value < 0.05, < 0.01, < 0.001 and < 0.0001, respectively. Red asterisks are used to identify the significant difference when compared to the cell control. Black asterisks are used to identify the significant difference between two conditions.

Although the results showed that blank PCL scaffolds did not significantly cause cytotoxicity to primary human dermal fibroblasts, lower cell viability was observed. This is possibly because the scaffolds exhibited as a hydrophobic barrier between cell culture media above them and the cell monolayer. Hence, less nutrients could reach the cell monolayer with respect to the cell control. Similarly, PCL-DOX HCl 1% scaffolds did not exhibit the significant

cytotoxicity. However, they showed slightly decreased the viability of cells in comparison with blank PCL scaffolds. This could be a result of DOX HCl release. As discussed in Chapter 4, DOX HCl was not completely released into cell culture media. Therefore, the concentration of DOX HCl may not reach 50 μM, resulting in higher cell viability than those of cells treated with 50 μM DOX HCl solution (Figure 6.2).

The viability of primary human dermal fibroblasts decreased in the presence of PCL-DOX HCl 2% and PCL-DOX HCl 5% scaffolds. This was because the concentration of released DOX HCl reached the cytotoxic level (Figure 6.2). However, the concentrations of DOX HCl were likely to be less than 100 and 250 μM for PCL-DOX HCl 2% and PCL-DOX HCl 5% scaffolds, respectively due to the incomplete drug release from the scaffolds in cell culture media. As a result, higher cell viability was noticed when compared to those of cells treated with 100 and 250 μM DOX HCl solutions (Figure 6.2).

Lastly, the proliferative effect of TNF-α and IL-1β on fibroblasts tended to antagonise with the cytotoxic effect of DOX HCl as approximately 20% higher in cell viability was observed.[324,326]

6.5.1.2.2 Nitrite production

Figure 6.7 demonstrates that PCL and PCL-DOX HCl 1% scaffolds did not significantly promote the production of nitrite. Whilst, PCL-DOX HCl 2% and PCL-DOX HCl 5% scaffolds led to 2.5- and 4.6-fold increase in nitrite production when compared to the cell control, respectively. This could relate to the cytotoxicity of high drug concentrations in cell supernatant that enhanced the production of nitrite.[333] Furthermore, it was observed that the nitrite production induced by PCL-DOX HCl 5% scaffolds significantly decreased in the presence of TNF-α and IL-1β (70 ± 10 pM·cell^{-1} *versus* 40 ± 7 pM·cell^{-1}). As mentioned earlier, TNF-α and IL-1β had the stimulatory effect on cell proliferation.[324,326] Hence, the cytotoxic effect of PCL-DOX HCl 5% scaffolds reduced, resulting in higher cell viability and lower nitrite production.

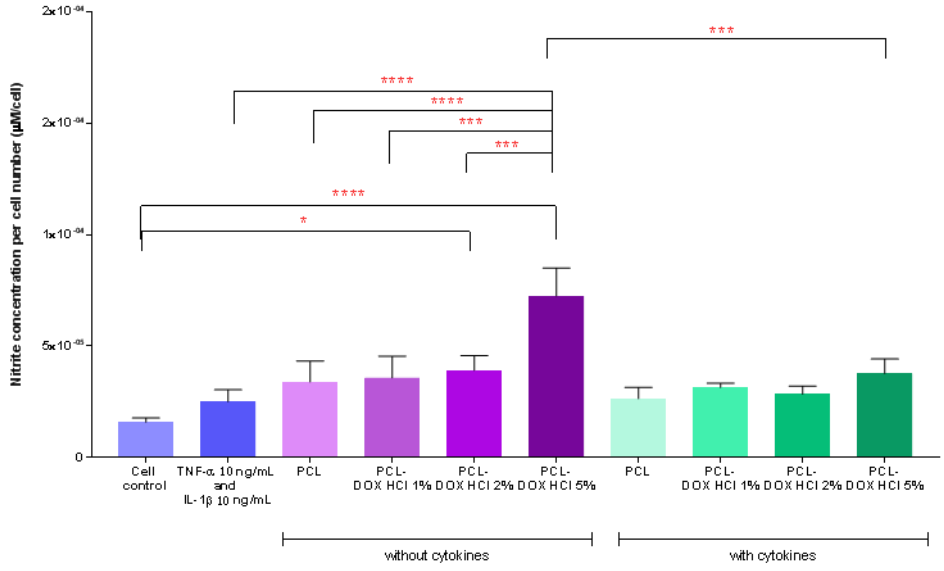


Figure 6.7. Normalised concentration of nitrite produced by primary human dermal fibroblasts when treated with the mixture of 10 ng/mL TNF-α and 10 ng/mL IL-1β, the scaffolds in cell culture media, or pre-treated with the scaffolds in cell culture media for 2 hours before the exposure to the cytokines. The values are means and standard deviations of triplicate samples (n = 3). *, *** and **** define statistical significance at *p*-value < 0.05, < 0.001 and < 0.0001, respectively.

6.5.1.2.3 The expression of MMP-1 enzyme

Figure 6.8 demonstrates that all scaffolds did not induce the expression of MMP-1 enzyme in primary human dermal fibroblasts. Furthermore, the scaffolds including blank PCL scaffolds could significantly decrease the cytokine-induced MMP-1 expression (1.7–8.8-fold reduction). Although the decrease in MMP-1 expression by PCL-DOX HCl 1% scaffolds was not significant, it was more likely that the scaffolds could reduce the expression of MMP-1 enzyme in the same manner as blank PCL scaffolds (0.57 ± 0.07 pg·mL^{-1}·cell^{-1} and 0.60 ± 0.05 pg·mL^{-1}·cell^{-1} for PCL and PCL-DOX HCl 1% scaffolds, respectively). In addition, PCL-DOX HCl 5% scaffolds completely inhibited the cytokine-induced MMP-1 expression as the level of MMP-1 was comparable to those of the cell control.

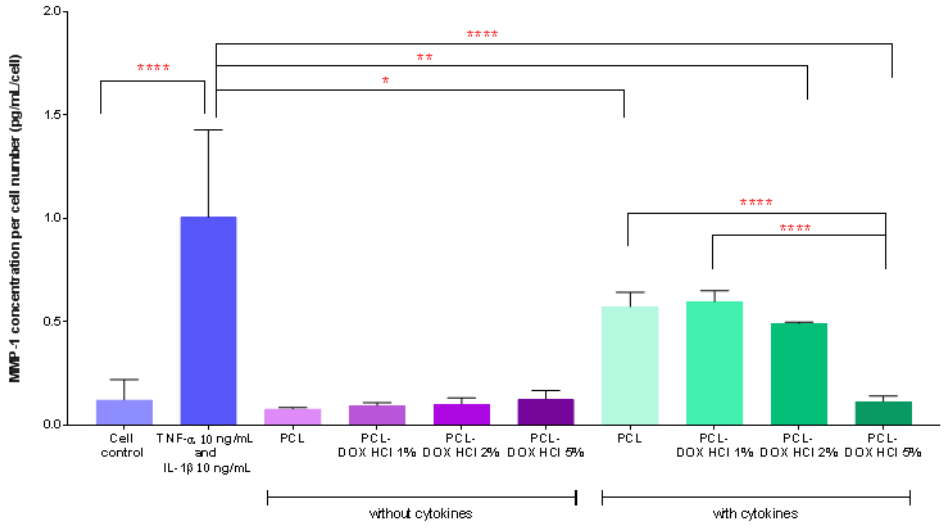


Figure 6.8. Normalised concentration of MMP-1 enzyme expressed by primary human dermal fibroblasts when treated with the mixture of 10 ng/mL TNF-α and 10 ng/mL IL-1β, the scaffolds in cell culture media, or pre-treated with the scaffolds in cell culture media for 2 hours before treated with the cytokines. The values are means and standard deviations of triplicate samples (n = 3). *, ** and **** define statistical significance at *p*-value < 0.05, < 0.01 and < 0.0001, respectively.

According to the results, blank PCL scaffolds could reduce the expression of MMP-1 enzyme stimulated by TNF-α and IL-1β. This might be due to the scaffolds retaining some of cytokines containing cell culture media, resulting in less expression of MMP-1. In addition, PCL-DOX HCl 1% scaffolds were unable to prevent the cytokine-induced MMP-1 expression in a higher magnitude than blank PCL scaffolds, even though they contained DOX HCl. This confirmed that the concentration of released DOX HCl from these scaffolds was lower than 50 µM. Otherwise, the significant decrease in MMP-1 expression would have been observed as seen in the cells treated with 50 µM DOX HCl solution (Figure 6.4).

Whilst, PCL-DOX HCl 2% and PCL-DOX HCl 5% scaffolds significantly reduced the cytokine-induced MMP-1 expression. The results suggested that the concentration of DOX HCl released from PCL-DOX HCl 2% scaffolds was less than 100 µM. This corresponds to the higher cytokine-induced MMP-1 expression when cells were pre-treated with PCL-DOX HCl 2% scaffolds in comparison with 100 µM DOX HCl solution (0.49 ± 0.01 pg·mL^{-1}·cell^{-1} *versus* 0.19 ± 0.03 pg·mL^{-1}·cell^{-1}). The concentration of DOX HCl released from PCL-DOX HCl 5% scaffolds may not achieved 250 µM, yet high enough to inhibit the cytokine-induced MMP-1 expression as observed in the pre-treatment with 250 µM DOX HCl solution (0.11 ± 0.03 pg·mL^{-1}·cell^{-1} *versus* 0.08 ± 0.01 pg·mL^{-1}·cell^{-1}).

.

6.5.1.2.4 The production of PGE_2

The production of PGE_2 was enhanced in the presence of PCL-DOX HCl 5% scaffolds when compared to the cell control (0.49 ± 0.17 pg·mL^{-1}·cell^{-1} *versus* 0.18 ± 0.04 pg·mL^{-1}·cell^{-1}, Figure 6.9). This was due to the induction of COX-2 expression and PGE_2 production by doxycycline.[349]

The exposure to the cytokines after the pre-treatment with PCL-DOX HCl 5% scaffolds did not reduce the production of PGE_2 stimulated by the presence of PCL-DOX HCl 5% scaffolds as observed in the case of 250 µM DOX HCl solution in Figure 6.5.

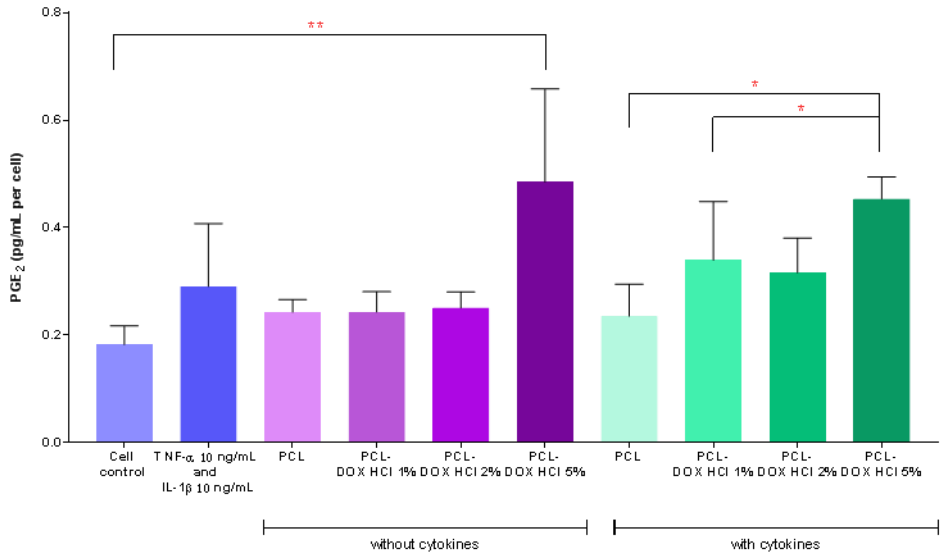


Figure 6.9. Normalised concentration of PGE_2 produced by primary human dermal fibroblasts when treated with the mixture of 10 ng/mL TNF-α and 10 ng/mL IL-1β, the scaffolds in cell culture media, or pre-treated with the scaffolds in cell culture media for 2 hours before treated with the cytokines. The values are means and standard deviations of triplicate samples (n = 3). * and ** define statistical significance at *p*-value < 0.05 and < 0.01, respectively.

Table 6.3. Summary of cell viability, the expression of MMP-1 enzyme and the production of nitrite and PGE_2 by primary human dermal fibroblasts after being treated under the specific conditions.

Condition	Cell viability (%)	Nitrite ($pM \cdot cell^{-1}$)	MMP-1 ($pg \cdot mL^{-1} \cdot cell^{-1}$)	PGE_2 ($pg \cdot mL^{-1} \cdot cell^{-1}$)
Cell control	100.00 ± 6.15	15.88 ± 1.88	0.12 ± 0.10	0.18 ± 0.03
TNF-α and IL-1β (T+I)	105.60 ± 10.59	25.11 ± 5.28	1.01 ± 0.42	0.29 ± 0.12
PCL	87.65 ± 9.85	33.93 ± 9.40	0.08 ± 0.01	0.24 ± 0.02
PCL-DOX HCl 1%	77.35 ± 9.50	35.74 ± 9.76	0.10 ± 0.01	0.24 ± 0.04
PCL-DOX HCl 2%	60.32 ± 5.71	39.17 ± 6.56	0.10 ± 0.03	0.25 ± 0.03
PCL-DOX HCl 5%	34.09 ± 3.59	72.52 ± 12.54	0.12 ± 0.04	0.49 ± 0.17
PCL +T+I	100.61 ± 19.85	26.42 ± 5.13	0.57 ± 0.07	0.24 ± 0.06
PCL-DOX HCl 1% +T+I	83.95 ± 14.51	31.45 ± 1.90	0.60 ± 0.05	0.34 ± 0.11
PCL-DOX HCl 2% +T+I	82.91 ± 16.41	28.46 ± 3.66	0.49 ± 0.01	0.32 ± 0.06
PCL-DOX HCl 5% +T+I	57.46 ± 5.39	37.71 ± 6.52	0.11 ± 0.03	0.45 ± 0.04

6.5.2 Evaluation of the coaxial electrospun scaffolds

6.5.2.1 DOX HCl solution, IBU Na solution and the mixture of drugs

The coaxial PCL/PLGA electrospun scaffolds were designed to contain DOX HCl with/without IBU Na as described in Chapter 5. To observe the effect of each drug and their combination without the effect of the materials constituting the scaffolds on the production/expression of the inflammatory mediators, cells were pre-treated with DOX HCl solution (50 µM), IBU Na solution (400 µM) and their combination in cell culture media before the exposure to the mixture of 10 ng/mL TNF-α and 10 ng/mL IL-1β. The given concentrations of DOX HCl and IBU Na were the maximum concentrations if the drugs were completely released.

6.5.2.1.1 Cell viability

It was observed that DOX HCl solution (50 µM), IBU Na solution (400 µM) and their combination did not significantly affect the viability of primary human dermal fibroblasts (Figure 6.10).

Interestingly, the exposure to the cytokines after the pre-treatment of 400 µM IBU Na increased the viability of cells by approximately 89% when compared to the cells treated only with 400 µM IBU Na or the cytokines (185.82 ± 15.14% *versus* 96.40 ± 5.79% and 129.20 ± 13.37%, respectively).

However, the viability of cells reduced with the pre-treatment of 50 µM DOX HCl and 400 µM IBU Na followed by the exposure to the cytokines (90.45 ± 9.21%). It implied that DOX HCl retarded the proliferation of cells.

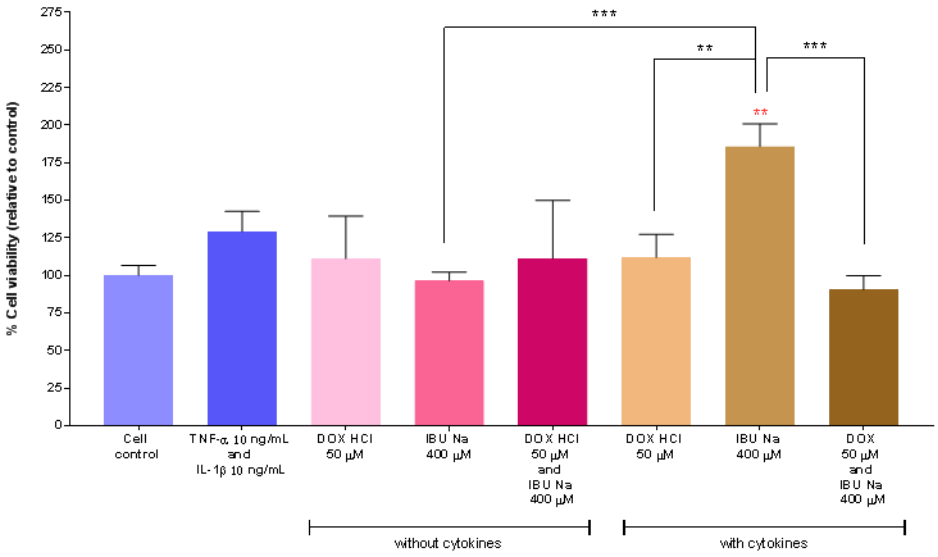


Figure 6.10. % Cell viability of primary human dermal fibroblasts when treated with the mixture of 10 ng/mL TNF-α and 10 ng/mL IL-1β, DOX HCl solution (50 µM), IBU Na solution (400 µM), the mixture of DOX HCl solution (50 µM) and IBU Na solution (400 µM) or pre-treated with the drug solutions for 2 hours before the exposure to the cytokines. The values are means and standard deviations of triplicate samples (n = 3). ** and *** define statistical significance at *p*-value < 0.01 and < 0.001, respectively. Red asterisks are used to identify a significant difference when compared to the cell control. Black asterisks are used to identify a significant difference between two conditions.

It is worth noting that the response of cells to 50 µM DOX HCl was different from the previous study. In the earlier experiment, cell viability decreased to 69.78 ± 10.98% in the presence of 50 µM DOX HCl (Figure 6.2). Whereas, the viability of cells was observed at 111.18 ± 28.26% in the current study. It could correspond to multiple factors. For instance, primary cells themselves may behave differently in each experiment.[350]

The cytotoxic effect was not observed in the presence of 400 μM IBU Na. This agreed with the results in Chapter 3 that the concentration of IBU Na in the range of 1–1,000 μM was not cytotoxic to primary human dermal fibroblasts.

Furthermore, TNF-α and IL-1β promoted cell proliferation in conjunction with 400 μM IBU Na pre-treatment, but not in the case of 50 μM DOX HCl and the drug combination. The literature reported the observation that ibuprofen at the concentrations of 1 and 10 μM augmented the stimulatory effect of IL-1β on the proliferation of human synovial fibroblasts.[327] Thus perhaps ibuprofen inhibits the production of PGE_2 which is a growth inhibitor.[327]

It can be referred to the results that DOX HCl counterbalanced the effect of IBU Na. This is perhaps due to drug interaction between IBU Na and DOX HCl observed in Chapter 5. Furthermore, DOX HCl inhibited the release of TNF-α *via* its inhibitory effect on the activity of TNF-α converting enzyme.[22] Therefore, the viability of cells was lower in the presence of both drugs.

6.5.2.1.2 Nitrite production

Figure 6.11 reveals that 400 µM IBU Na slightly increased the production of nitrite with respect to the cell control (60 ± 4 pM·cell^{-1} *versus* 70 ± 3 pM·cell^{-1}). Nevertheless, it was observed that the production of nitrite decreased when primary human dermal fibroblasts were pre-treated with 400 µM IBU Na and followed by the exposure to the cytokines in comparison with treated with 400 µM IBU Na alone (70 ± 3 pM·cell^{-1} *versus* 40 ± 2 pM·cell^{-1}). This could relate to the synergistic effect of IBU Na and the cytokine on the promoting of cell proliferation.

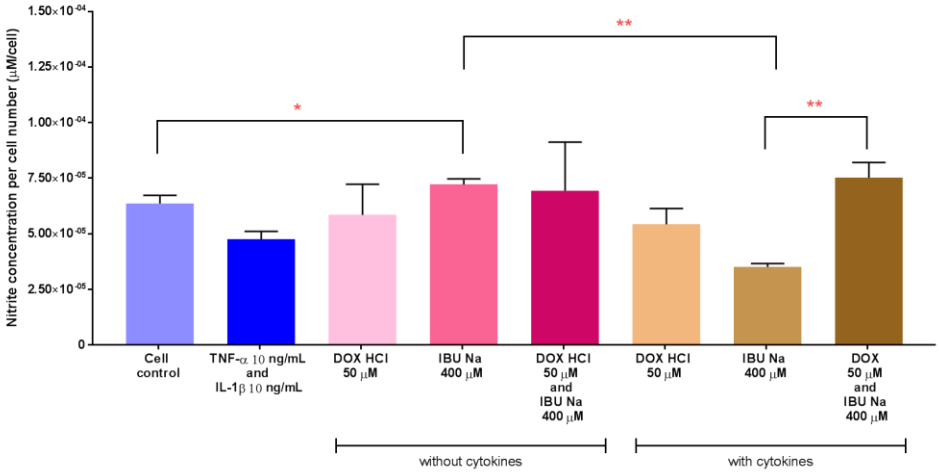


Figure 6.11. Normalised concentration of nitrite produced by primary human dermal fibroblsts when treated with the mixture of 10 ng/mL TNF-α and 10 ng/mL IL-1β, DOX HCl solution (50 µM), IBU Na solution (400 µM), the mixture of DOX HCl solution (50 µM) and IBU Na solution (400 µM) or pre-treated with the drug solutions for 2 hours before the exposure to the cytokines. The values are means and standard deviations of triplicate samples (n = 3). * and ** define statistical significance at *p*-value < 0.05 and < 0.01, respectively.

Whilst, the pre-treatment with drug combination (50 µM DOX HCl and 400 µM IBU Na) led to the higher production of nitrite when compared to the pre-treatment with 400 µM IBU Na alone. This was because the presence of both drugs caused lower cell viability when compared to the presence of 400 µM IBU

Na alone. As discussed earlier, DOX HCl could interact with IBU Na. Hence, the inhibiting effect of IBU Na on the nitrite production decreased.

6.5.2.1.3 The expression of MMP-1 enzyme

As illustrated in Figure 6.12, the presence of 10 ng/mL TNF-α and 10 ng/mL IL-1β strongly induced the expression of MMP-1 enzyme in primary human dermal fibroblasts by approximately 14 fold when compared to the cell control (0.27 ± 0.06 pg·mL^{-1}·cell^{-1} *versus* 0.02 ± 0.001 pg·mL^{-1}·cell^{-1}). On the other hand, the expression of MMP-1 enzyme was not enhanced by neither of drug solutions.

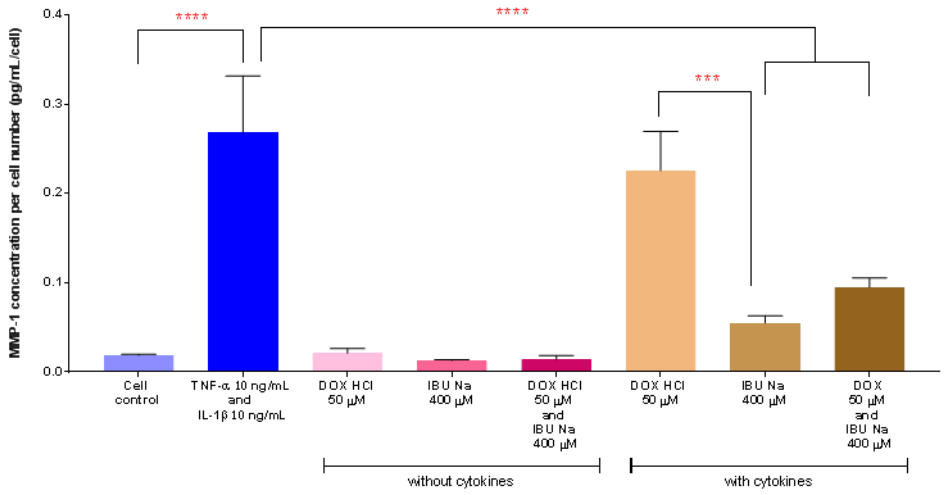


Figure 6.12. Normalised concentration of MMP-1 enzyme expressed by primary human dermal fibroblasts when treated with the mixture of 10 ng/mL TNF-α and 10 ng/mL IL-1β, DOX HCl solution (50 µM), IBU Na solution (400 µM), the mixture of DOX HCl solution (50 µM) and IBU Na solution (400 µM) or pre-treated with the drug solutions for 2 hours before the exposure to the cytokines. The values are means and standard deviations of triplicate samples (n = 3). *** and **** define statistical significance at *p*-value < 0.001 and < 0.0001, respectively.

It was observed that the cytokine-induced MMP-1 expression greatly decreased in cells that were pre-treated with 400 µM IBU Na alone (0.06 ± 0.01 $pg \cdot mL^{-1} \cdot cell^{-1}$) and cells that were pre-treated with the combination of 50 µM DOX HCl and 400 µM IBU Na (0.10 ± 0.01 $pg \cdot mL^{-1} \cdot cell^{-1}$).

The previous studies reported that the expression of MMP-1 enzyme was enhanced by TNF-α and IL-1β.[305,311–315,351] Although the pre-treatment of 50 µM DOX HCl did not significantly inhibit the cytokine-induced MMP-1 expression in this study, the lower MMP-1 level was noticed.

Interestingly, 400 µM IBU Na alone was capable of preventing the cytokine-induced MMP-1 expression in primary human dermal fibroblasts. This, however, contradicted to the literature that 100 µM ibuprofen induced the expression of MMP-1 enzyme in fibroblast-like synoviocytes.[351] It could be the fact that different cell types respond to the stimuli in a different fashion. The combination of DOX HCl and IBU Na also showed the reduction in the cytokine-induced MMP-1 expression, even though slightly weaker inhibiting effect was observed when compared to 400 µM IBU Na alone.

6.5.2.1.4 The production of PGE_2

The effects of 50 µM DOX HCl, 400 µM IBU Na and the drug combination on the production of PGE_2 were not observed in all cases (Figure 6.13). According to the results, it was observed that the pre-treatment with 400 µM IBU Na before the exposure to the cytokines seemed to reduce the production of PGE_2 when compared to other conditions. However, the difference was not statistically significant.

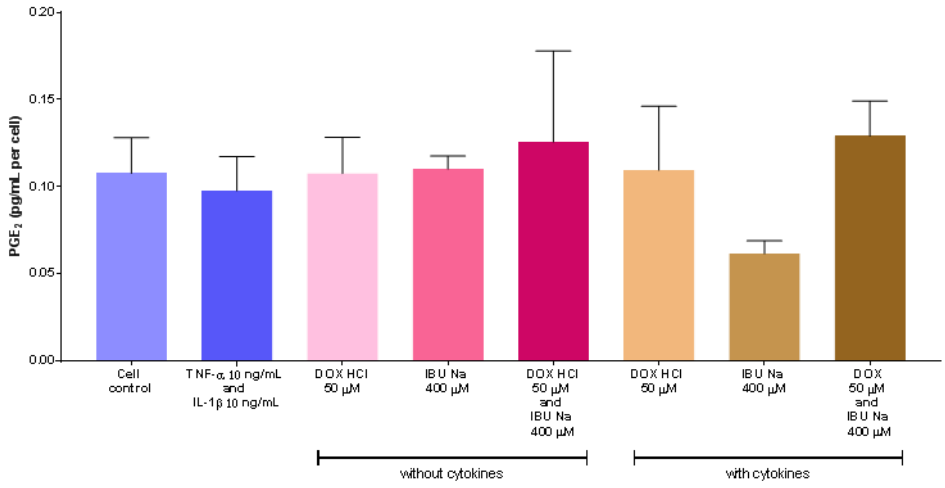


Figure 6.13. Normalised concentration of PGE_2 produced by primary human dermal fibroblasts when treated with the mixture of 10 ng/mL TNF-α and 10 ng/mL IL-1β, DOX HCl solution (50 µM), IBU Na solution (400 µM), the mixture of DOX HCl solution (50 µM) and IBU Na solution (400 µM) or pre-treated with the drug solutions for 2 hours before the exposure to the cytokines. The values are means and standard deviations of triplicate samples (n = 3).

The production of PGE_2 was not induced by TNF-α and IL-1β. As discussed previously, the proliferating cells produced PGE_2 in response to the cytokines less than the quiescent cells due to the secretion of cytoguardin.[342–345] Furthermore, the production of PGE_2 in the presence of 50 µM DOX HCl, 400 µM IBU Na and their combination was neither promoted nor inhibited when

compared to the cell control. The decrease in PGE_2 production in the presence of 400 μM IBU Na and the cytokines may link to the higher cell viability with respect to the cell control. The results implied that cell could proliferate quicker under such conditions. Hence, the amount of cytoguardin could get higher, resulting in lower PGE_2 production.[342,344] The production of PGE_2 did not decrease when both DOX HCl and IBU Na presented in cell culture media. It was perhaps because IBU Na-DOX HCl interaction interfered the effect of IBU Na and DOX HCl induced the production of PGE_2 production.[349]

It was reported that the co-delivery of ibuprofen and bFGF was able to reduce LPS-induced PGE_2 production in human gingival fibroblasts more effectively than ibuprofen alone.[352] This could be the case that the decrease in PGE_2 level was the result of the synergistic effect of 400 μM IBU Na and bFGF in cell culture media.

Table 6.4. Summary of cell viability, the expression of MMP-1 enzyme and the production of nitrite and PGE_2 by primary human dermal fibroblasts after being treated under the specific conditions.

Condition	Cell viability (%)	Nitrite ($pM \cdot cell^{-1}$)	MMP-1 ($pg \cdot mL^{-1} \cdot cell^{-1}$)	PGE_2 ($pg \cdot mL^{-1} \cdot cell^{-1}$)
Cell control	100.00 ± 6.53	63.70 ± 3.66	0.019 ± 0.001	0.11 ± 0.02
TNF-α and IL-1β (T+I)	129.20 ± 13.37	47.63 ± 3.55	0.268 ± 0.063	0.10 ± 0.02
50 µM DOX HCl	111.18 ± 28.26	58.57 ± 13.70	0.021 ± 0.005	0.11 ± 0.02
400 µM IBU Na	96.40 ± 5.79	72.14 ± 2.56	0.013 ± 0.001	0.11 ± 0.01
50 µM DOX HCl and 400 µM IBU Na	111.24 ± 38.66	69.37 ± 21.90	0.014 ± 0.004	0.13 ± 0.05
50 µM DOX HCl +T+I	111.95 ± 15.36	54.36 ± 7.05	0.226 ± 0.044	0.11 ± 0.04
400 µM IBU Na +T+I	185.82 ± 15.13	35.20 ± 1.51	0.055 ± 0.008	0.06 ± 0.01
50 µM DOX HCl and 400 µM IBU Na +T+I	90.45 ± 9.21	75.22 ± 6.87	0.095 ± 0.010	0.13 ± 0.02

6.5.2.2 Coaxial electrospun scaffolds

To evaluate the effect of drugs released from the coaxial electrospun scaffolds as well as the materials constructing the scaffolds on the production/expression of the inflammatory markers, coaxial PCL/PLGA, PCL-DOX HCl 1%/PLGA and PCL-DOX HCl 1%/PLGA-IBU Na 5% scaffolds fabricated in Chapter 5 were assessed in the same settings as PCL-DOX HCl scaffolds.

6.5.2.2.1 Cell viability

Figure 6.14 shows that there was no significant difference in the viability of primary human dermal fibroblasts when treated with PCL/PLGA, PCL-DOX HCl 1%/PLGA and PCL-DOX HCl 1%/PLGA-IBU Na 5% scaffolds both in the presence and the absence of the cytokines. This implied that these scaffolds did not exhibit the cytotoxic effect and showed good biocompatibility to cells.

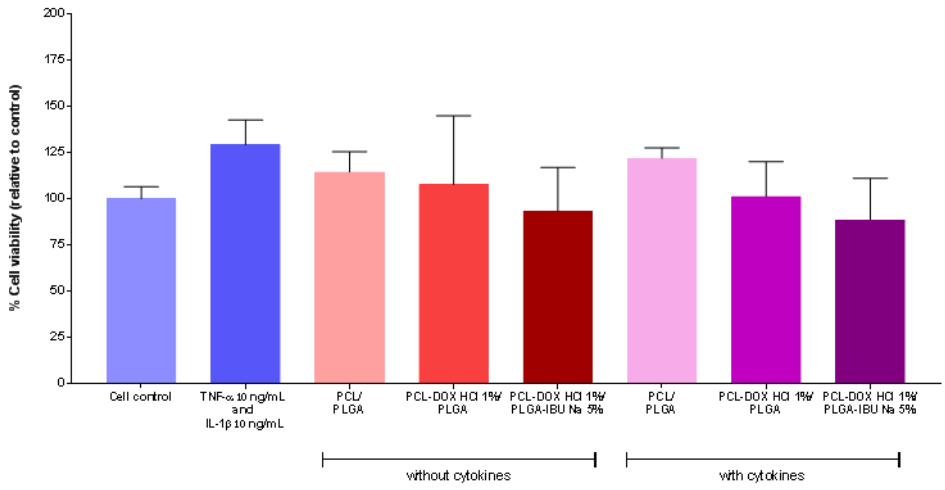


Figure 6.14. % Cell viability of primary human dermal fibroblasts when treated with the mixture of 10 ng/mL TNF-α and 10 ng/mL IL-1β, the coaxial scaffolds in cell culture media, or pre-treated with the coaxial scaffolds in cell culture media for 2 hours before the exposure to the cytokines. The values are means and standard deviations of triplicate samples (n = 3).

However, it is worth noting that drug-loaded scaffolds caused a small reduction in cell viability, which could impart to the cytotoxicity of DOX HCl. In Chapter 5, the higher release of DOX HCl from PCL-DOX HCl 1%/PLGA-IBU Na 5% scaffolds when compared to PCL-DOX HCl 1%/PLGA scaffolds was observed. As a result, the cell vitality was lower in the presence of PCL-DOX HCl 1%/PLGA-IBU Na 5% scaffolds.

6.5.2.2.2 Nitrite production

Despite a significant difference in nitrite level was not observed between the conditions, the results suggested that primary human dermal fibroblasts treated with PCL-DOX HCl 1%/PLGA and PCL-DOX HCl 1%/PLGA-IBU Na 5% scaffolds produced nitrite more than blank PCL/PLGA scaffolds both in the presence and the absence of TNF-α and IL-1β (Figure 6.15).

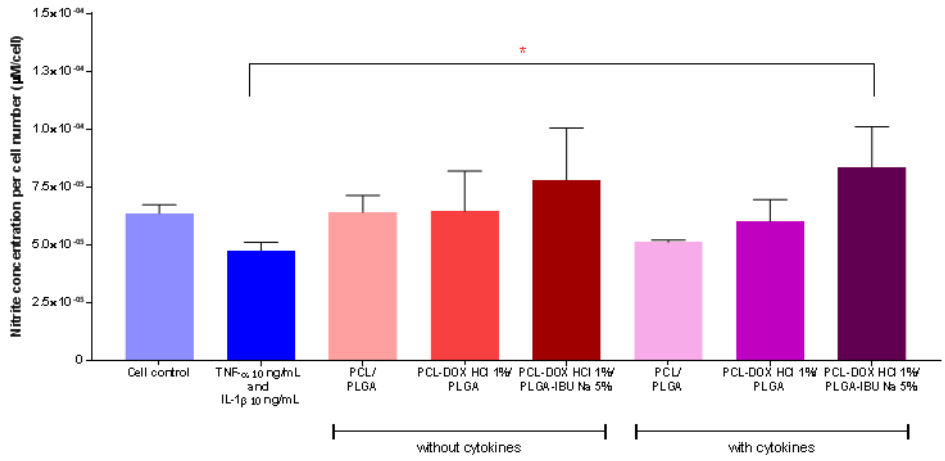


Figure 6.15. Normalised concentration of nitrite produced by primary human dermal fibroblasts when treated with the mixture of 10 ng/mL TNF-α and 10 ng/mL IL-1β, the coaxial scaffolds in cell culture media, or pre-treated with the coaxial scaffolds in cell culture media for 2 hours before the exposure to the cytokines. The values are means and standard deviations of triplicate samples (n = 3). * defined statistical significance at p-value < 0.05.

These results were similar to the results obtained from the study with drug solutions (Figure 6.11) that 50 µM DOX HCl alone could not reduce the production of nitrite. Whilst, drug combination (50 µM DOX HCl and 400 µM IBU Na) promoted nitrite production. It was perhaps a result of drug interaction that led to a lower cell viability and hence higher production of nitrite.

6.5.2.2.3 The expression of MMP-1 enzyme

Figure 6.16 reveals that all coaxial fibres themselves did not induce the expression of MMP-1 enzyme. The cytokine-induced MMP-1 expression was reduced in the presence of PCL-DOX HCl 1%/PLGA-IBU Na 5% scaffolds. Although the result was not significant, approximately half of MMP-1 enzyme was less expressed in the presence of the scaffolds. According to the results in Figure 6.12, IBU Na was likely to predominantly take part in the reduction of MMP-1 expression.

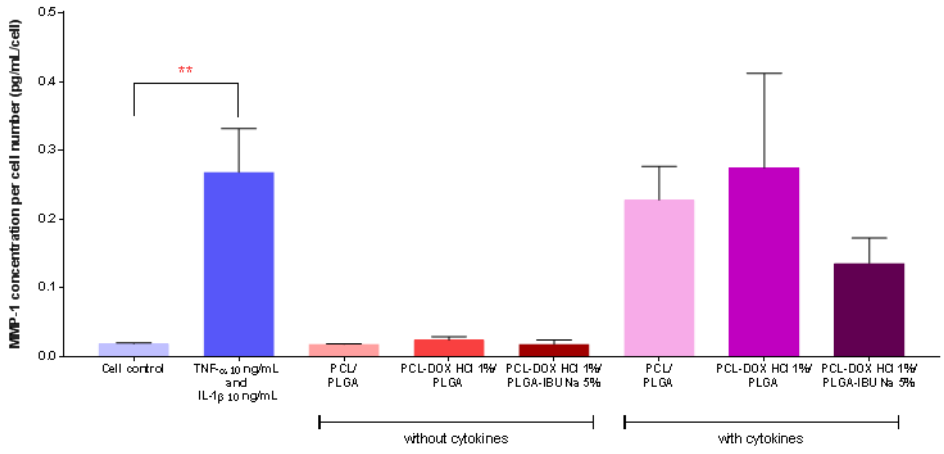


Figure 6.16. Normalised concentration of MMP-1 enzymes expressed by primary human dermal fibroblasts when treated with the mixture of 10 ng/mL TNF-α and 10 ng/mL IL-1β, the coaxial scaffolds in cell culture media, or pre-treated with the coaxial scaffolds in cell culture media for 2 hours before the exposure to the cytokines. The values are means and standard deviations of triplicate samples (n = 3). ** defined statistical significance at p-value < 0.01.

On the contrary, PCL-DOX HCl 1%/PLGA scaffolds could not prevent the expression of MMP-1 stimulated by the cytokines. This ought to be because of the incomplete release of DOX HCl from the scaffolds. Hence, the inhibitory effect on MMP-1 expression was lower than those of 50 µM DOX HCl solution (Figure 6.12). It should be noted again that more experiments needed to confirm the results. As the response of cells can be varied from experiment to experiment, the higher numbers of samples should be considered.

6.5.2.2.4 The production of PGE_2

Neither the cytokines nor the scaffolds significantly increased the production of PGE_2 in primary human dermal fibroblasts (Figure 6.17). However, it was observed that the production of PGE_2 was gradually induced when cells were pre-treated with PCL-DOX HCl 1%/PLGA and PCL-DOX HCl 1%/PLGA-IBU Na 5% scaffolds prior to the exposure to the cytokines when compared to blank PCL/PLGA scaffolds. This was a result of doxycycline-induced COX-2 expression and PGE_2 production.[348,349]

As observed in Chapter 5, the release of DOX HCl from PCL-DOX HCl 1%/PLGA-IBU Na 5% scaffolds was higher than those of PCL-DOX HCl 1%/PLGA scaffolds. This perhaps resulted in the higher production of PGE_2 as DOX HCl could stimulate PGE_2 production.[348,349]

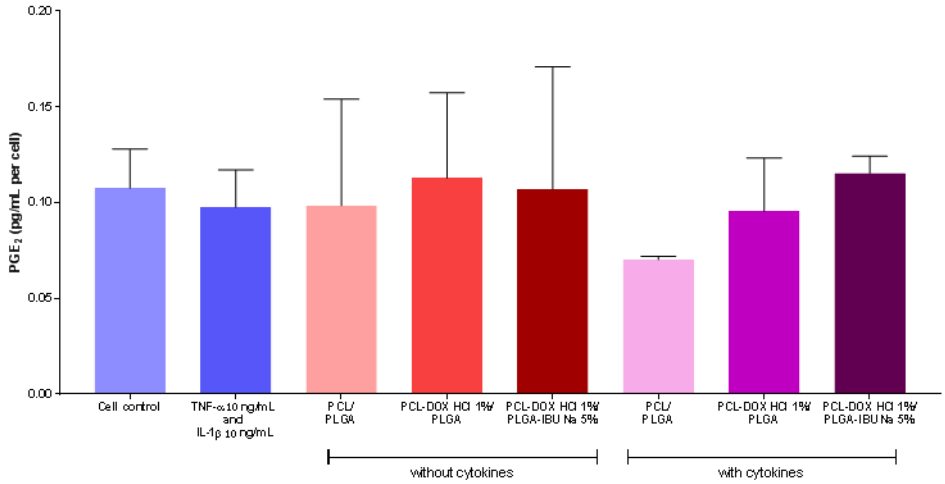


Figure 6.17. Normalised concentration of PGE_2 produced by primary human dermal fibroblasts when treated with the mixture of 10 ng/mL TNF-α and 10 ng/mL IL-1β, the coaxial scaffolds in cell culture media, or pre-treated with the coaxial scaffolds in cell culture media for 2 hours before treated with the cytokines. The values are means and standard deviations of triplicate samples (n = 3).

Table 6.5. Summary of cell viability, the expression of MMP-1 enzyme and the production of nitrite and PGE_2 by primary human dermal fibroblasts after being treated under the specific conditions.

Condition	Cell viability (%)	Nitrite ($pM \cdot cell^{-1}$)	MMP-1 ($pg \cdot mL^{-1} \cdot cell^{-1}$)	PGE_2 ($pg \cdot mL^{-1} \cdot cell^{-1}$)
Cell control	100.00 ± 6.53	63.70 ± 3.66	0.019 ± 0.001	0.108 ± 0.020
TNF-α and IL-1β (T+I)	129.20 ± 13.37	47.63 ± 3.55	0.268 ± 0.063	0.098 ± 0.020
PCL/ PLGA	114.48 ± 11.04	64.14 ± 7.24	0.018 ± 0.001	0.098 ± 0.056
PCL-DOX HCl 1%/ PLGA	107.74 ± 37.14	64.72 ± 17.25	0.024 ± 0.005	0.113 ± 0.045
PCL-DOX HCl 1%/ PLGA-IBU Na 5%	93.35 ± 23.55	78.16 ± 22.45	0.018 ± 0.006	0.107 ± 0.064
PCL/ PLGA +T+I	121.92 ± 5.63	51.32 ± 0.75	0.228 ± 0.049	0.070 ± 0.002
PCL-DOX HCl 1%/ PLGA +T+I	101.44 ± 18.62	60.12 ± 9.45	0.274 ± 0.138	0.095 ± 0.028
PCL-DOX HCl 1%/ PLGA-IBU Na 5% +T+I	88.73 ± 22.36	83.71 ± 17.39	0.136 ± 0.037	0.115 ± 0.009

6.6 Conclusion

The *in vitro* inflammation model was set up with a monolayer of primary human dermal fibroblasts in 24 well plates. The cytokines, 10 ng/mL TNF-α and 10 ng/mL IL-1β, did not affect the viability of cells and promoted the expression of MMP-1 enzyme, but not the production of nitrite and PGE_2 when compared to the cell control.

DOX HCl solutions at the concentrations of 50, 100 and 250 μM caused cytotoxicity and enhanced nitrite and PGE_2 production in a dose dependent manner. Whilst, the expression of MMP-1 was not stimulated with these DOX HCl solutions. The presence of DOX HCl and the cytokines in cell culture media led to higher cell viability when compared to the presence of DOX HCl alone in cell culture media at the same drug concentration. DOX HCl solutions could prevent the cytokine-induced MMP-1 expression in a dose-dependent manner. 250 μM DOX HCl concentrations resulted in a complete inhibition of cytokine-induced MMP-1 expression.

The scaffolds fabricated in Chapter 4 were tested with the same experimental set up as DOX HCl solutions. The decrease in cell viability was observed when PCL-DOX HCl 2% and PCL-DOX HCl 5% scaffolds were introduced to cells (indirect contact). This was because DOX HCl released from the scaffolds reached the concentrations that exhibited cytotoxicity. The proliferative effect of the cytokines attenuated the cytotoxic effect of DOX HCl released from the scaffolds as higher cell viability was observed in the presence of the cytokines.

The productions of nitrite and PGE_2 were significantly induced by PCL-DOX HCl 5% scaffolds, which were related to the cytotoxic effect of DOX HCl released. The cytokine-induced MMP-1 expression was significantly decreased by the pre-treatment of the PCL-DOX HCl scaffolds in a dose-dependent manner. Pre-treatment with PCL-DOX HCl 5% scaffolds led to a complete inhibition of cytokine-induced MMP-1 expression. Taking all into consideration, we can infer that PCL-DOX HCl 1%, PCL-DOX HCl 2% and PCL-DOX HCl 5% scaffolds were able to release DOX HCl to prevent the cytokine-stimulated MMP-1 expression. However, DOX HCl released from PCL-DOX HCl 5% scaffolds caused cytotoxicity, resulting in the higher productions of nitrite and PGE_2.

The assessment was further investigated with 400 µM IBU Na solution and the combination of 400 µM IBU Na and 50 µM DOX HCl solutions. The viability of primary human dermal fibroblasts was not affected by the addition of 400 µM IBU Na solution, and also the combination of 400 µM IBU Na and 50 µM DOX HCl solutions. TNF-α and IL-1β significantly promoted the proliferation of cells in conjunction with IBU Na pre-treatment. On the other hand, the cell proliferation was not promoted when cells were pre-treated with the drug combination as a result of IBU Na-DOX HCl interaction. The production of nitrite was slightly promoted by 400 µM IBU Na. Nevertheless, the cells that were exposed to the cytokines after IBU Na pre-treatment produced less nitrite, which corresponded to the higher cell viability. The cytokine-induced MMP-1 expression was significantly inhibited by 400 µM IBU Na and the combination of 400 µM IBU Na and 50 µM DOX HCl solutions. Although the decrease in

cytokine-induced PGE_2 production was not significantly observed, the pre-treatment of 400 μM IBU Na solution led to a lower level of PGE_2.

The efficacy of the coaxial electrospun scaffolds manufactured in Chapter 5 was assessed. The coaxial electrospun scaffolds did not exhibit cytotoxic effect on primary human dermal fibroblasts. However, gradual decrease in cell viability was observed when the number of drugs loaded in the scaffolds increased. The decrease in cell viability in the presence of the scaffolds resulted in the higher levels of nitrite and PGE_2. The scaffolds that contained drug(s) produced these two inflammatory mediators more than blank PCL/PLGA scaffolds. Lastly, the expression of MMP-1 stimulated by the cytokines was reduced with the pre-treatment of PCL-DOX HCl 1%/PLGA-IBU Na 5% scaffolds. It can be concluded that IBU Na could prevent the expression of MMP-1 enzyme. As the effect of PCL-DOX HCl 1%/PLGA scaffolds on cytokine-induced MMP-1 expression was not clearly observed. To summarise, PCL-DOX HCl 1%/PLGA-IBU Na 5% scaffolds could prevent the cytokine-induced MMP-1 expression in primary human dermal fibroblasts better than PCL-DOX HCl 1%/PLGA scaffolds, but such scaffolds promoted the higher cytokine-mediated productions of nitrite and PGE_2.

Chapter 7

Concluding Remarks and Future work

7.1 Conclusions

This thesis aimed to develop anti-inflammatory drug-loaded electrospun scaffolds to modulate the cytokine-induced inflammation as well as to support dermal fibroblast proliferation. Polymer-drug solutions with different drug loadings were used to generate fibrous scaffolds using monoaxial electrospinning. IBU Na was selected as a representative of NSAIDs which are known to modulate COX enzymes and the production of PGE_2.[109,110] Whilst, DOX HCl was chosen based on its inhibiting effect on the activities of MMP enzymes.[174–176] Furthermore, this work also investigated the feasibility of manufacturing coaxial electrospun scaffolds, containing both drugs. In the last Chapter, the efficacy testing using the *in vitro* cytokine-induced inflammation model was carried out to assess the effect of the fabricated scaffolds on the production/expression of the inflammatory mediators.

Although ibuprofen-loaded electrospun scaffolds have been prepared in several studies, the impact of the incorporated drug on the properties of electrospun scaffolds is not fully examined.[90,115,136,353] In Chapter 3, IBU Na-loaded electrospun PLGA scaffolds were fabricated with different drug loadings using monoaxial electrospinning. All scaffolds consisted of smooth and rounded microfibres. It turns out that incorporation of IBU Na into PLGA scaffolds resulted in an increase in porosity but decreases in mechanical strength and

Young's modulus when compared to blank PLGA scaffolds. The highest drug loading at 5% w/w caused brittleness in the scaffolds, which is potentially related to the hydrolysis in the PLGA backbone by acidic IBU Na. All scaffolds, except PLGA-IBU Na 5% scaffolds, possessed hydrophobic surfaces as their water contact angles were higher than 90°. The poor wettability of the scaffolds was likely to involve the surface roughness as the liquid-solid interaction was replaced by the air-liquid interaction. The release of IBU Na from PLGA-IBU Na scaffolds was a rapid burst release. This corresponded to the presence of IBU Na at the surfaces of fibres, which was confirmed by ToF-SIMS. Over 90 days in PBS, PCL-IBU Na 2% and PLGA-IBU Na 5% scaffolds completely lost the fibrous morphology. This again was linked to the faster hydrolysis of PLGA backbone accelerated by the higher amount of IBU Na. The scaffolds were seeded with mouse fibroblasts, and the metabolic activity of cells was investigated with PrestoBlue® assay to determine the ability of the scaffolds to support cell proliferation. Gradual increases in the cellular metabolic activity were observed over 14 day of cell culture. This implied that the scaffolds could support the proliferation of mouse fibroblasts. SEM images showed that the scaffolds were biocompatible as mouse fibroblasts could adhere and proliferate on the scaffolds.

In Chapter 4, the scaffolds were fabricated with biodegradable and biocompatible PCL polymer. DOX HCl was blended with PCL at the drug loadings of 1, 2 and 5% w/w. PCL and PCL-DOX HCl scaffolds were smooth rounded nanofibres. DOX HCl was found to affect the mechanical properties of PCL scaffolds regardless of the drug loadings—it increased the ultimate tensile

strength and Young's modulus but decreased strain at break of the scaffolds. The hydrophobic nature of PCL and rough surface of the scaffolds resulted in the poor wettability of the scaffolds. PCL scaffolds were able to carry high levels of DOX HCl—more than 89% of DOX HCl were encapsulated in the scaffolds after electrospinning. The deposition of DOX HCl at the surfaces of fibres led to a rapid burst drug release in PBS—more than 96% of drug were released in 30 minutes. The degradation study showed that the fibrous morphology of the scaffolds remained unchanged after immerged in PBS for 90 days. PrestoBlue® assay showed that the proliferation of primary human dermal fibroblasts on the scaffolds was rapid, and cells fully covered the surface of the scaffolds within 7 days. In addition, the morphology of cells was consistently in a spindle shape throughout the study.

The work in Chapter 5 aimed to develop the coaxial electrospun scaffolds containing IBU Na and DOX HCl. The scaffolds were fabricated to have the structure of PCL shell and PLGA core to ensure that the release of DOX HCl was not limited by PLGA. Blank PCL/PLGA scaffolds, PCL-DOX HCl 1%/PLGA scaffolds and PCL-DOX HCl 1%/PLGA-IBU Na 5% scaffolds were all prepared using coaxial electrospinning. The morphology of fibres in these scaffolds were rounded and smooth. Additionally, the fibre orientation was random, and no drug crystals were observed on the surfaces of fibres. The core-shell structures of the fibres in all scaffolds were confirmed by TEM. According to the water contact angle measurements, PCL-DOX HCl 1%/PLGA-IBU Na 5% scaffolds were completely wet. Whilst, PCL/PLGA and PCL-DOX HCl 1%/PLGA scaffolds showed hydrophobic property. Incorporation of drug(s)

into the scaffolds increased the ultimate tensile strength of the scaffolds. However, the presence of drug(s) also accelerated the degradation of the scaffolds as higher weight loss of drug-loaded scaffolds was observed when compared to blank PCL/PLGA scaffolds. ToF-SIMS analysis showed that both drug molecules deposited on the surfaces of the scaffolds, which correlated to a rapid burst drug release in PBS. All coaxial scaffolds fabricated in this Chapter were able to support the proliferation of primary human dermal fibroblasts as the increasing metabolic activity of cells in PrestoBlue® assay was observed. In addition, SEM images illustrated that cells could adhere and proliferate on the scaffolds throughout the study.

In Chapter 6, the efficacy testing was conducted to evaluate the ability of the scaffolds to modulate the cytokine-induced inflammation. The monolayer of primary human dermal fibroblasts was stimulated with pro-inflammatory cytokines, TNF-α and IL-1β. Albeit, it was found that the productions of PGE_2 and nitrite were not significantly enhanced. This was potentially due to the presence of bFGF in cell culture media. In contrast, the expression of MMP-1 enzyme was significantly induced by these cytokines.

PCL-DOX HCl scaffolds fabricated in Chapter 4 caused cytotoxicity when drug loadings were 2% and 5% w/w. Furthermore, PCL-DOX HCl 5% scaffolds resulted in the significant higher productions of nitrite and PGE_2 when compared to the cell control. The decrease in cytokine-induced MMP-1 expression was observed in a dose-dependent manner when cells were pre-treated with PCL-

DOX HCl scaffolds before the exposure to the cytokines. The pre-treatment with PCL-DOX HCl 5% scaffolds led to a complete inhibition of cytokine-induced MMP-1 expression in primary human dermal fibroblasts.

The efficacy of the coaxial electrospun scaffolds manufactured in Chapter 5 was evaluated in the same manner as what were done to PCL-DOX HCl scaffolds. The coaxial electrospun scaffolds were found to be biocompatible to cells. This was shown by the fact that the viability of primary human dermal fibroblasts was comparable to the cell control. However, the drug-loaded coaxial scaffolds induced the productions of nitrite and PGE_2. The cytokine-induced MMP-1 expression was significantly inhibited only when cells were pre-treated with PCL-DOX HCl 1%/PLGA-IBU Na 5% scaffolds before the exposure to the cytokines.

Taking every factor into account, it can be concluded that PCL-DOX HCl scaffolds and PCL-DOX HCl 1%/PLGA-IBU Na 5% were able to inhibit cytokine-induced MMP-1 expression. The synergistic inhibiting effect of IBU Na and DOX HCl toward the cytokine-induced MMP-1 expression was not observed, and further investigations are required.

7.2 Future work

As discussed in Chapters 3–5, it was clear that the drugs present in the scaffolds influence the mechanical properties. Therefore, the characterisation of the scaffolds using differential scanning calorimetry (DSC) and X-ray diffraction (XRD) can be carried out in order to confirm the effects of drugs on the crystallinity of the polymer constituting the scaffolds. In addition, gel permeation chromatography (GPC) can be performed to observe the change in polymer molecular weight, and the results from GPC can be used to confirm the scaffold degradation *via* hydrolysis. Drug release studies can also be conducted in cell culture media. This is because the composition of cell culture media could interfere with the release of drugs from the scaffolds. Determination of drug localisation in the fibres could be studied further by observing at several cross-sections of the fibres. This is to observe the distribution of drug in the matrix of polymer if the drug intensity is high at the surface of fibre as seen in lateral sections of the fibres. High lateral resolution mode must be used in ToF-SIMS analysis to ensure that each fibre could be seen clearly. To obtain more information on ECM secretion by cells seeded on the scaffolds, collagen staining should be carried out. In addition, the cytoskeleton of cells cultured on the scaffolds should be observed at higher magnifications to clearly show actin in an individual cell. Furthermore, all cell studies should be repeated to gather more information and determine the consistency of results. This includes the studies with different cell passages. Imaging cells cultured on the electrospun fibres in LIVE/DEAD® assay could be taken at higher magnifications to confirm the presence of cells and their morphology.

The modification of the scaffolds by blending polymers, using co-solvent system or changing drug isoforms can be considered to modulate the release of drugs from the scaffolds to be more sustained. Furthermore, the % drug loading in the coaxial electrospun scaffolds can be further studied with higher concentrations of DOX HCl in the PCL shell, and the lower concentrations of IBU Na in the PLGA core.

In addition, the protocols used in Chapter 6 can be improved. For example, the growth factor (bFGF) and serum in cell culture media can be removed to minimise or remove possible interference with the production of nitrite and PGE_2. It is very important to note that the removal of these two components can potentially cause a great change in cell viability and cell response towards the exposure to the cytokines and the scaffolds. Secondly, the duration of inducing the production/expression of the inflammatory mediators can be further optimised in order to determine the optimum incubation period to achieve the highest response from primary human dermal fibroblasts. Next, the scaffolds can be introduced to cells in different order of events (*e.g.* before and after the exposure to the cytokines). This is to observe whether consistent results can still be obtained. Lastly, fibroblasts can be cultured with other cell types (*e.g.* macrophages and keratinocytes) to increase the complexity of the model. Furthermore, the macrophage polarization—from M1 phenotype (inflammatory macrophages) to M2 phenotype (anti-inflammatory/healing macrophages)—can be used as a marker to assess scaffold capacity to modulate of cytokine-induced inflammation.

References

1. Yang, Y. *et al.* Promotion of skin regeneration in diabetic rats by electrospun core-sheath fibers loaded with basic fibroblast growth factor. *Biomaterials* (2011). doi:10.1016/j.biomaterials.2011.02.042

2. Jennemann, R. *et al.* Loss of ceramide synthase 3 causes lethal skin barrier disruption. *Hum. Mol. Genet.* (2012). doi:10.1093/hmg/ddr494

3. Xu, H., Timares, L. & Elmets, C. A. Host defenses in the skin. in *Clinical Immunology: Principles and Practice: Fourth Edition* (2012). doi:10.1016/B978-0-7234-3691-1.00039-8

4. Lopez-Ojeda, W. & Oakley, A. M. *Anatomy, Skin (Integument). StatPearls* (2018).

5. Hodge, B. D. & Brodell, R. T. *Anatomy, Skin, Sweat Glands*. *StatPearls* (2018).

6. Schoellhammer, C. M., Blankschtein, D. & Langer, R. Skin permeabilization for transdermal drug delivery: recent advances and future prospects. *Expert Opin. Drug Deliv.* (2014). doi:10.1517/17425247.2014.875528

7. Biga Lindsay M. , Dawson Sierra , Harwell Amy, Hopkins Robin, Kaufmann Joel, LeMaster Mike, Matern Philip, Q. K. M.-G. & Devon, R. J. *Anatomy & Physiology*. *Anatomy and physiology* (2014).

8. Murphrey, M. B. & Zito, P. M. *Histology, Stratum Corneum*. *StatPearls* (2018).

9. Chen, M., Przyborowski, M. & Berthiaume, F. Stem cells for skin tissue engineering and wound healing. *Crit. Rev. Biomed. Eng.* (2009).

10. Brown, T. M. & Krishnamurthy, K. *Histology*, *Dermis*. *StatPearls* (2019).

11. Zhao, R., Liang, H., Clarke, E., Jackson, C. & Xue, M. Inflammation in chronic wounds. *International Journal of Molecular Sciences* (2016). doi:10.3390/ijms17122085

12. Robson, M. C., Steed, D. L. & Franz, M. G. Wound healing: Biologic features and approaches to maximize healing trajectories. *Curr. Probl. Surg.* (2001). doi:10.1067/msg.2001.111167

13. Velnar, T., Bailey, T. & Smrkolj, V. The wound healing process: An overview of the cellular and molecular mechanisms. *Journal of International Medical Research* (2009). doi:10.1177/147323000903700531

14. Frykberg, R. G. & Banks, J. Challenges in the Treatment of Chronic Wounds. *Adv. wound care* (2015). doi:10.1089/wound.2015.0635

15. Gainza, G., Villullas, S., Pedraz, J. L., Hernandez, R. M. & Igartua, M. Advances in drug delivery systems (DDSs) to release growth factors for wound healing and skin regeneration. *Nanomedicine: Nanotechnology, Biology, and Medicine* (2015). doi:10.1016/j.nano.2015.03.002

16. Moura, L. I. F., Dias, A. M. A., Carvalho, E. & de Sousa, H. C. Recent advances on the development of wound dressings for diabetic foot ulcer treatment--a review. *Acta Biomater.* (2013).

doi:10.1016/j.actbio.2013.03.033

17. Gurtner, G. C., Werner, S., Barrandon, Y. & Longaker, M. T. 2008 Nature-Wound repair and regeneration. *Nature* (2008). doi:10.1038/nature07039

18. Boateng, J. & Catanzano, O. Advanced Therapeutic Dressings for Effective Wound Healing - A Review. *Journal of Pharmaceutical Sciences* (2015). doi:10.1002/jps.24610

19. Turner, N. J. & Badylak, S. F. The Use of Biologic Scaffolds in the Treatment of Chronic Nonhealing Wounds. *Adv. Wound Care* (2014). doi:10.1089/wound.2014.0604

20. Guo, S. & Dipietro, L. A. Factors affecting wound healing. *J. Dent. Res.* (2010). doi:10.1177/0022034509359125

21. Sen, C. K. *et al.* Human skin wounds: A major and snowballing threat to public health and the economy: PERSPECTIVE ARTICLE. *Wound Repair and Regeneration* (2009). doi:10.1111/j.1524-475X.2009.00543.x

22. Stechmiller, J., Cowan, L. & Schultz, G. The role of doxycycline as a matrix metalloproteinase inhibitor for the treatment of chronic wounds. *Biol. Res. Nurs.* (2010). doi:10.1177/1099800409346333

23. Bjarnsholt, T. *et al.* Why chronic wounds will not heal: A novel hypothesis. *Wound Repair and Regeneration* (2008). doi:10.1111/j.1524-475X.2007.00283.x

24. Lobmann, R., Zemlin, C., Motzkau, M., Reschke, K. & Lehnert, H.

Expression of matrix metalloproteinases and growth factors in diabetic foot wounds treated with a protease absorbent dressing. *J. Diabetes Complications* (2006). doi:10.1016/j.jdiacomp.2005.08.007

25. Liu, Y. *et al.* Increased matrix metalloproteinase-9 predicts poor wound healing in diabetic foot ulcers. *Diabetes Care* (2009). doi:10.2337/dc08-0763

26. WERNER, S. & GROSE, R. Regulation of Wound Healing by Growth Factors and Cytokines. *Physiol. Rev.* (2017). doi:10.1152/physrev.2003.83.3.835

27. Park, J. Y., Pillinger, M. H. & Abramson, S. B. Prostaglandin E2 synthesis and secretion: The role of PGE2 synthases. *Clinical Immunology* (2006). doi:10.1080/10407780600602374

28. Dinarello, C. A. Anti-inflammatory Agents: Present and Future. *Cell* (2010). doi:10.1016/j.cell.2010.02.043

29. Fitzpatrick, F. A. Cyclooxygenase enzymes: regulation and function. *Curr. Pharm. Des.* (2004).

30. Rouzer, C. A. & Marnett, L. J. Cyclooxygenases: structural and functional insights. *J. Lipid Res.* (2009). doi:10.1194/jlr.r800042-jlr200

31. Sandulache, V. C., Parekh, A., Li-Korotky, H., Dohar, J. E. & Hebda, P. A. Prostaglandin E2 inhibition of keloid fibroblast migration, contraction, and transforming growth factor (TGF)-β1-induced collagen synthesis. *Wound Repair Regen.* (2007). doi:10.1111/j.1524-475X.2006.00193.x

32. Ansari, K. M., Sung, Y. M., He, G. & Fischer, S. M. Prostaglandin

receptor EP2 is responsible for cyclooxygenase-2 induction by prostaglandin E2 in mouse skin. *Carcinogenesis* (2007). doi:10.1093/carcin/bgm011

33. Witte, M. B. & Barbul, A. Role of nitric oxide in wound repair. *Am. J. Surg.* (2002). doi:10.1016/S0002-9610(02)00815-2

34. Luo, J. D. & Chen, A. F. Nitric oxide: A newly discovered function on wound healing. *Acta Pharmacologica Sinica* (2005). doi:10.1111/j.1745-7254.2005.00058.x

35. Posnett, J. The burden of chronic wounds in The uK Venous leg ulcers. *Nt* **22**, (2008).

36. Powers, J. G., Higham, C., Broussard, K. & Phillips, T. J. Wound healing and treating wounds Chronic wound care and management. *Journal of the American Academy of Dermatology* (2016). doi:10.1016/j.jaad.2015.08.070

37. Davidson, J. R. Current Concepts in Wound Management and Wound Healing Products. *Veterinary Clinics of North America - Small Animal Practice* (2015). doi:10.1016/j.cvsm.2015.01.009

38. Leaper, D. J., Meaume, S., Apelqvist, J., Teot, L. & Gottrup, F. Debridement methods of non-viable tissue in wounds. in *Advanced Wound Repair Therapies* (2011). doi:10.1533/9780857093301.5.606

39. Dhivya, S., Padma, V. V. & Santhini, E. Wound dressings - A review. *BioMedicine (Netherlands)* (2015). doi:10.7603/s40681-015-0022-9

40. Cutting, K. F., White, R. J. & Mahoney, P. Wound infection, dressings

and pain, is there a relationship in the chronic wound? *Int. Wound J.* (2013). doi:10.1111/j.1742-481X.2012.00947.x

41. Serena, T., Yaakov, R., Aslam, S. & Aslam, R. Preventing, minimizing, and managing pain in patients with chronic wounds: challenges and solutions. *Chronic Wound Care Manag. Res.* (2016). doi:10.2147/cwcmr.s85463

42. Bechert, K. & Abraham, S. E. Pain Management and Wound Care. *Journal of the American College of Certified Wound Specialists* (2009). doi:10.1016/j.jcws.2008.12.001

43. Han, G. & Ceilley, R. Chronic Wound Healing: A Review of Current Management and Treatments. *Adv. Ther.* (2017). doi:10.1007/s12325-017-0478-y

44. Langer, R. & Vacanti, J. P. - ARTICLES Tissue Engineering. *Science (80-.).* (1993). doi:10.1126/science.8493529

45. Howard, D., Buttery, L. D., Shakesheff, K. M. & Roberts, S. J. Tissue engineering: Strategies, stem cells and scaffolds. *Journal of Anatomy* (2008). doi:10.1111/j.1469-7580.2008.00878.x

46. Caddeo, S., Boffito, M. & Sartori, S. Tissue engineering approaches in the design of healthy and pathological in vitro tissue models. *Frontiers in Bioengineering and Biotechnology* (2017). doi:10.3389/fbioe.2017.00040

47. Seo, S. & Na, K. Mesenchymal stem cell-based tissue engineering for chondrogenesis. *Journal of Biomedicine and Biotechnology* (2011).

doi:10.1155/2011/806891

48. Halim, A. S., Khoo, T. L. & Shah, S. J. Biologic and synthetic skin substitutes: An overview. *Indian Journal of Plastic Surgery* (2010). doi:10.4103/0970-0358.70712

49. Davison-Kotler, E., Sharma, V., Kang, N. V. & García-Gareta, E. A Universal Classification System of Skin Substitutes Inspired by Factorial Design. *Tissue Engineering - Part B: Reviews* (2018). doi:10.1089/ten.teb.2017.0477

50. Vyas, K. & Vasconez, H. Wound Healing: Biologics, Skin Substitutes, Biomembranes and Scaffolds. *Healthcare* (2014). doi:10.3390/healthcare2030356

51. Goodarzi, P. *et al.* Tissue engineered skin substitutes. in *Advances in Experimental Medicine and Biology* (2018). doi:10.1007/5584_2018_226

52. Jin, Y. & Bi, H. Current progress of skin tissue engineering: Seed cells, bioscaffolds, and construction strategies. *Burn. Trauma* **1**, 63 (2013).

53. Ikada, Y. Challenges in tissue engineering. *Journal of the Royal Society Interface* (2006). doi:10.1098/rsif.2006.0124

54. Nicholas, M. N., Jeschke, M. G. & Amini-Nik, S. Methodologies in creating skin substitutes. *Cellular and Molecular Life Sciences* (2016). doi:10.1007/s00018-016-2252-8

55. Savoji, H., Godau, B., Hassani, M. S. & Akbari, M. Skin Tissue Substitutes and Biomaterial Risk Assessment and Testing. *Front. Bioeng.*

Biotechnol. (2018). doi:10.3389/fbioe.2018.00086

56. Prunieras, M., Regnier, M. & Woodley, D. Methods for cultivation of keratinocytes with an air-liquid interface. *J. Invest. Dermatol.* (1983). doi:10.1111/1523-1747.ep12540324

57. Chaudhari, A. *et al.* Future Prospects for Scaffolding Methods and Biomaterials in Skin Tissue Engineering: A Review. *Int. J. Mol. Sci.* **17**, 1974 (2016).

58. Weigel, T., Schinkel, G. & Lendlein, A. Design and preparation of polymeric scaffolds for tissue engineering. *Expert Rev. Med. Devices* **3**, 835–851 (2006).

59. Lu, T., Li, Y. & Chen, T. Techniques for fabrication and construction of three-dimensional scaffolds for tissue engineering. *International Journal of Nanomedicine* (2013). doi:10.2147/IJN.S38635

60. Knight, E., Murray, B., Carnachan, R. & Przyborski, S. Alvetex®: polystyrene scaffold technology for routine three dimensional cell culture. *Methods Mol. Biol.* (2011).

61. Sill, T. J. & von Recum, H. A. Electrospinning: Applications in drug delivery and tissue engineering. *Biomaterials* (2008). doi:10.1016/j.biomaterials.2008.01.011

62. Li, W.-J., Laurencin, C. T., Caterson, E. J., Tuan, R. S. & Ko, F. K. Electrospun nanofibrous structure: a novel scaffold for tissue engineering. *J. Biomed. Mater. Res.* (2002).

63. Venugopal, J. & Ramakrishna, S. Applications of polymer nanofibers in

biomedicine and biotechnology. *Applied Biochemistry and Biotechnology - Part A Enzyme Engineering and Biotechnology* (2005). doi:10.1385/ABAB:125:3:147

64. Kumbar, S. G., Nair, L. S., Bhattacharyya, S. & Laurencin, C. T. Polymeric Nanofibers as Novel Carriers for the Delivery of Therapeutic Molecules. *J. Nanosci. Nanotechnol.* (2006). doi:10.1166/jnn.2006.462

65. Gunn, J. & Zhang, M. Polyblend nanofibers for biomedical applications: Perspectives and challenges. *Trends in Biotechnology* (2010). doi:10.1016/j.tibtech.2009.12.006

66. Beachley, V. & Wen, X. Polymer nanofibrous structures: Fabrication, biofunctionalization, and cell interactions. *Progress in Polymer Science (Oxford)* (2010). doi:10.1016/j.progpolymsci.2010.03.003

67. Chronakis, I. S. Novel nanocomposites and nanoceramics based on polymer nanofibers using electrospinning process - A review. *J. Mater. Process. Technol.* (2005). doi:10.1016/j.jmatprotec.2005.06.053

68. Abrigo, M., McArthur, S. L. & Kingshott, P. Electrospun nanofibers as dressings for chronic wound care: Advances, challenges, and future prospects. *Macromolecular Bioscience* (2014). doi:10.1002/mabi.201300561

69. Milleret, V., Simona, B., Neuenschwander, P. & Hall, H. Tuning electrospinning parameters for production of 3D-fiberfleeces with increased porosity for soft tissue engineering applications. *Eur. Cells Mater.* (2011). doi:10.22203/eCM.v021a22

70. Kim, S. J., Jang, D. H., Park, W. H. & Min, B. M. Fabrication and characterization of 3-dimensional PLGA nanofiber/microfiber composite scaffolds. *Polymer (Guildf).* (2010). doi:10.1016/j.polymer.2010.01.025

71. Trengove, N. J. *et al.* Analysis of the acute and chronic wound environments: The role of proteases and their inhibitors. *Wound Repair and Regeneration* (1999). doi:10.1046/j.1524-475X.1999.00442.x

72. Haider, A., Haider, S. & Kang, I. K. A comprehensive review summarizing the effect of electrospinning parameters and potential applications of nanofibers in biomedical and biotechnology. *Arabian Journal of Chemistry* (2018). doi:10.1016/j.arabjc.2015.11.015

73. Bhardwaj, N. & Kundu, S. C. Electrospinning: A fascinating fiber fabrication technique. *Biotechnology Advances* (2010). doi:10.1016/j.biotechadv.2010.01.004

74. Pelipenko, J., Kocbek, P. & Kristl, J. Critical attributes of nanofibers: Preparation, drug loading, and tissue regeneration. *International Journal of Pharmaceutics* (2015). doi:10.1016/j.ijpharm.2015.02.043

75. Son, W. K., Youk, J. H., Lee, T. S. & Park, W. H. The effects of solution properties and polyelectrolyte on electrospinning of ultrafine poly(ethylene oxide) fibers. *Polymer (Guildf).* (2004). doi:10.1016/j.polymer.2004.03.006

76. Raghavan, P. *et al.* Electrospun polymer nanofibers: The booming cutting edge technology. *React. Funct. Polym.* (2012). doi:10.1016/j.reactfunctpolym.2012.08.018

77. Luo, C. J., Stride, E. & Edirisinghe, M. Mapping the influence of solubility and dielectric constant on electrospinning polycaprolactone solutions. *Macromolecules* (2012). doi:10.1021/ma300656u

78. Pham, Q. P., Sharma, U. & Mikos, A. G. Electrospinning of polymeric nanofibers for tissue engineering applications: a review. *Tissue Eng.* (2006). doi:10.1089/ten.2006.12.1197

79. Cramariuc, B. *et al.* Fiber diameter in electrospinning process. *J. Electrostat.* (2013). doi:10.1016/j.elstat.2012.12.018

80. Su, Y. *et al.* Temperature effect on electrospinning of nanobelts: The case of hafnium oxide. *Nanotechnology* (2011). doi:10.1088/0957-4484/22/28/285609

81. Hu, X. *et al.* Electrospinning of polymeric nanofibers for drug delivery applications. *Journal of Controlled Release* (2014). doi:10.1016/j.jconrel.2014.04.018

82. Ding, Y. *et al.* Electrospun Fibrous Architectures for Drug Delivery, Tissue Engineering and Cancer Therapy. *Advanced Functional Materials* (2019). doi:10.1002/adfm.201802852

83. Wang, B., Wang, Y., Yin, T. & Yu, Q. Applications of electrospinning technique in drug delivery. *Chem. Eng. Commun.* (2010). doi:10.1080/00986441003625997

84. Yao, Y. *et al.* Effect of sustained heparin release from PCL/chitosan hybrid small-diameter vascular grafts on anti-thrombogenic property and endothelialization. *Acta Biomater*. (2014).

doi:10.1016/j.actbio.2014.02.042

85. Zhang, C., Feng, F. & Zhang, H. Emulsion electrospinning: Fundamentals, food applications and prospects. *Trends in Food Science and Technology* (2018). doi:10.1016/j.tifs.2018.08.005

86. Evrova, O. *et al.* Hybrid randomly electrospun poly(lactic-co-glycolic acid):poly(ethylene oxide) (PLGA:PEO) fibrous scaffolds enhancing myoblast differentiation and alignment. *ACS Appl. Mater. Interfaces* (2016). doi:10.1021/acsami.6b11291

87. Kostakova, E., Seps, M., Pokorny, P. & Lukas, D. Study of polycaprolactone wet electrospinning process. *Express Polym. Lett.* (2014). doi:10.3144/expresspolymlett.2014.59

88. Solowiej, K. & Upton, D. Painful dressing changes for chronic wounds: assessment and management. *Br. J. Nurs.* (2014). doi:10.12968/bjon.2012.21.sup14.s20

89. Woo K, S. R. Chronic Wound Pain : A Conceptual Model. *Adv. Skin Wound Care* (2008).

90. CantÃ³n, I. *et al.* Development of an Ibuprofen-releasing biodegradable PLA/PGA electrospun scaffold for tissue regeneration. *Biotechnol. Bioeng.* **105**, 396–408 (2010).

91. Shahverdi, S. *et al.* Fabrication and structure analysis of poly(lactide-co-glycolic acid)/silk fibroin hybrid scaffold for wound dressing applications. *Int. J. Pharm.* (2014). doi:10.1016/j.ijpharm.2014.07.021

92. Meng, Z. X. *et al.* Electrospinning of PLGA/gelatin randomly-oriented

and aligned nanofibers as potential scaffold in tissue engineering. *Mater. Sci. Eng. C* (2010). doi:10.1016/j.msec.2010.06.018

93. Zou, Q., Zhou, Q., Liu, L. & Dai, H. A highly hydrophilic and biodegradable novel poly(amide-imide) for biomedical applications. *Polymers (Basel).* (2016). doi:10.3390/polym8120441

94. Zhao, L. *et al.* Preparation and cytocompatibility of PLGA scaffolds with controllable fiber morphology and diameter using electrospinning method. *J. Biomed. Mater. Res. - Part B Appl. Biomater.* (2008). doi:10.1002/jbm.b.31060

95. Makadia, H. K. & Siegel, S. J. Poly Lactic-co-Glycolic Acid (PLGA) as Biodegradable Controlled Drug Delivery Carrier. *Polymers (Basel).* (2011). doi:10.3390/polym3031377

96. Lanao, R. P. F. *et al.* Physicochemical Properties and Applications of Poly(lactic-co-glycolic acid) for Use in Bone Regeneration. *Tissue Eng. Part B Rev.* (2013). doi:10.1089/ten.teb.2012.0443

97. Nair, L. S. & Laurencin, C. T. Biodegradable polymers as biomaterials. *Progress in Polymer Science (Oxford)* (2007). doi:10.1016/j.progpolymsci.2007.05.017

98. Woodard, L. N. & Grunlan, M. A. Hydrolytic Degradation and Erosion of Polyester Biomaterials. *ACS Macro Letters* (2018). doi:10.1021/acsmacrolett.8b00424

99. Mashiur. Degradation of Polyesters in Medical Applications. in *Polyester* (2012). doi:10.5772/47765

100. Xu, Y., Kim, C. S., Saylor, D. M. & Koo, D. Polymer degradation and drug delivery in PLGA-based drug–polymer applications: A review of experiments and theories. *Journal of Biomedical Materials Research - Part B Applied Biomaterials* (2017). doi:10.1002/jbm.b.33648

101. Virlan, M. J. R. *et al.* Current uses of poly(lactic-co-glycolic acid) in the dental field: A comprehensive review. *Journal of Chemistry* (2015). doi:10.1155/2015/525832

102. Cai, Q., Shi, G., Bei, J. & Wang, S. Enzymatic degradation behavior and mechanism of Poly(lactide-co-glycolide) foams by trypsin. *Biomaterials* (2003). doi:10.1016/S0142-9612(02)00377-0

103. Porporato, P. E. *et al.* Lactate stimulates angiogenesis and accelerates the healing of superficial and ischemic wounds in mice. *Angiogenesis* (2012). doi:10.1007/s10456-012-9282-0

104. Putnam, D. Drug delivery: The heart of the matter. *Nature Materials* (2008). doi:10.1038/nmat2309

105. Wang, C., Zhang, K., Wang, H., Xu, S. & Han, C. C. Evaluation of biodegradability of poly (DL-lactic-co-glycolic acid) scaffolds for post-surgical adhesion prevention: In vitro, in rats and in pigs. *Polymer (Guildf).* (2015). doi:10.1016/j.polymer.2015.02.001

106. Bookstaver, P. B., Miller, A. D., Rudisill, C. N. & Norris, L. B. Intravenous ibuprofen: the first injectable product for the treatment of pain and fever. *J. Pain Res.* (2010).

107. Vinklárková, L., Masteiková, R., Vetchý, D., Doležel, P. & Bernatoniene,

J. Formulation of novel layered sodium carboxymethylcellulose film wound dressings with ibuprofen for alleviating wound pain. *Biomed Res. Int.* (2015). doi:10.1155/2015/892671

108. Ho, K. Y. *et al.* Nonsteroidal anti-inflammatory drugs in chronic pain: Implications of new data for clinical practice. *Journal of Pain Research* (2018). doi:10.2147/JPR.S168188

109. Meek, I. L., van de Laar, M. A. F. J. & Vonkeman, H. E. Non-steroidal anti-inflammatory drugs: An overview of cardiovascular risks. *Pharmaceuticals* (2010). doi:10.3390/ph3072146

110. Ricciotti, E. & Fitzgerald, G. A. Prostaglandins and inflammation. *Arterioscler. Thromb. Vasc. Biol.* (2011). doi:10.1161/ATVBAHA.110.207449

111. Mazaleuskaya, L. L. *et al.* PharmGKB summary: Ibuprofen pathways. *Pharmacogenet. Genomics* (2015). doi:10.1097/FPC.0000000000000113

112. Manoukian, M. A. C., Migdal, C. W., Tembhekar, A. R., Harris, J. A. & DeMesa, C. Topical Administration of Ibuprofen for Injured Athletes: Considerations, Formulations, and Comparison to Oral Delivery. *Sports Medicine - Open* (2017). doi:10.1186/s40798-017-0103-2

113. Yuan, Z. *et al.* Ibuprofen-loaded electrospun fibrous scaffold doped with sodium bicarbonate for responsively inhibiting inflammation and promoting muscle wound healing in vivo. *Biomater. Sci.* (2014). doi:10.1039/c3bm60198f

114. Fogh, K. *et al.* Clinically relevant pain relief with an ibuprofen-releasing foam dressing: Results from a randomized, controlled, double-blind clinical trial in exuding, painful venous leg ulcers. *Wound Repair Regen.* (2012). doi:10.1111/j.1524-475X.2012.00844.x

115. Batool, F. *et al.* Synthesis of a Novel Electrospun Polycaprolactone Scaffold Functionalized with Ibuprofen for Periodontal Regeneration: An In Vitro andIn Vivo Study. *Materials (Basel).* **11**, 580 (2018).

116. Bancelin, S. *et al.* Determination of collagen fibril size via absolute measurements of second-harmonic generation signals. *Nat. Commun.* (2014). doi:10.1038/ncomms5920

117. Sasaki, S. *et al.* Principles and development of collagen-mediated tissue fusion induced by laser irradiation. *Sci. Rep.* (2019). doi:10.1038/s41598-019-45486-4

118. Ushiki, T. Collagen fibers, reticular fibers and elastic fibers. A comprehensive understanding from a morphological viewpoint. *Archives of Histology and Cytology* (2002). doi:10.1679/aohc.65.109

119. Frantz, C., Stewart, K. M. & Weaver, V. M. The extracellular matrix at a glance. *Journal of Cell Science* (2010). doi:10.1242/jcs.023820

120. Nunan, R., Harding, K. G. & Martin, P. Clinical challenges of chronic wounds: Searching for an optimal animal model to recapitulate their complexity. *DMM Dis. Model. Mech.* (2014). doi:10.1242/dmm.016782

121. Järbrink, K. *et al.* Prevalence and incidence of chronic wounds and related complications: A protocol for a systematic review. *Syst. Rev.* (2016).

doi:10.1186/s13643-016-0329-y

122. Sun, X. *et al.* A clinicoepidemiological profile of chronic wounds in wound healing Department in Shanghai. *Int. J. Low. Extrem. Wounds* (2017). doi:10.1177/1534734617696730

123. Ayyoob, M. & Kim, Y. J. Effect of chemical composition variant and oxygen plasma treatments on thewettability of PLGA thin films, synthesized by direct copolycondensation. *Polymers (Basel).* (2018). doi:10.3390/polym10101132

124. Meloun, M., Bordovská, S. & Galla, L. The thermodynamic dissociation constants of four non-steroidal anti-inflammatory drugs by the least-squares nonlinear regression of multiwavelength spectrophotometric pH-titration data. *J. Pharm. Biomed. Anal.* (2007). doi:10.1016/j.jpba.2007.07.029

125. Engineer, C., Parikh, J. & Raval, A. Review on hydrolytic degradation behavior of biodegradable polymers from controlled drug delivery system. *Trends in Biomaterials and Artificial Organs* (2011).

126. Apffel, A., Chakel, J. A., Fischer, S., Lichtenwalter, K. & Hancock, W. S. Analysis of oligonucleotides by HPLC-electrospray ionization mass spectrometry. *Anal. Chem.* (1997). doi:10.1021/ac960916h

127. You, Y., Lee, S. J., Min, B. M. & Park, W. H. Effect of solution properties on nanofibrous structure of electrospun poly(lactic-co-glycolic acid). *J. Appl. Polym. Sci.* (2006). doi:10.1002/app.22602

128. Khoo, W. & Koh, C. T. A review of electrospinning process and

microstructure morphology control. *ARPN Journal of Engineering and Applied Sciences* (2016).

129. Song, B., Cui, W. & Chang, J. Study on the effect of inorganic salts on the alignment of electrospun fiber. *J. Appl. Polym. Sci.* (2011). doi:10.1002/app.34197

130. Mi, H. Y. *et al.* Electrospinning of unidirectionally and orthogonally aligned thermoplastic polyurethane nanofibers: Fiber orientation and cell migration. *J. Biomed. Mater. Res. - Part A* (2015). doi:10.1002/jbm.a.35208

131. Vesely, I. Heart valve tissue engineering. *Circulation Research* (2005). doi:10.1161/01.RES.0000185326.04010.9f

132. Angammana, C. J. & Jayaram, S. H. Analysis of the effects of solution conductivity on electrospinning process and fiber morphology. *IEEE Trans. Ind. Appl.* (2011). doi:10.1109/TIA.2011.2127431

133. Tong, H. W. & Wang, M. Electrospinning of fibrous PHBV tissue engineering scaffolds: Fiber diameter control, fiber alignment and mechanical properties. in *5th Int. Conference on Information Technology and Applications in Biomedicine, ITAB 2008 in conjunction with 2nd Int. Symposium and Summer School on Biomedical and Health Engineering, IS3BHE 2008* (2008). doi:10.1109/ITAB.2008.4570640

134. Chen, S., Li, S., Liu, W. & Makse, H. A. Effect of long-range repulsive Coulomb interactions on packing structure of adhesive particles. *Soft Matter* (2016). doi:10.1039/c5sm02403j

135. Yousefzadeh, M., Latifi, M., Amani-Tehran, M., Teo, W.-E. & Ramakrishna, S. A Note on the 3D Structural Design of Electrospun Nanofibers. *J. Eng. Fiber. Fabr.* (2018). doi:10.1177/155892501200700204

136. Riggin, C. N. *et al.* Electrospun PLGA Nanofiber Scaffolds Release Ibuprofen Faster and Degrade Slower After In Vivo Implantation. *Ann. Biomed. Eng.* (2017). doi:10.1007/s10439-017-1876-7

137. Shirazi, R. N., Ronan, W., Rochev, Y. & McHugh, P. Modelling the degradation and elastic properties of poly(lactic-co-glycolic acid) films and regular open-cell tissue engineering scaffolds. *J. Mech. Behav. Biomed. Mater.* (2016). doi:10.1016/j.jmbbm.2015.08.030

138. Al-Nasassrah, M. A., Podczeck, F. & Newton, J. M. The effect of an increase in chain length on the mechanical properties of polyethylene glycols. *Eur. J. Pharm. Biopharm.* (1998). doi:10.1016/S0939-6411(97)00151-3

139. Yu, H., Matthew, H. W., Wooley, P. H. & Yang, S. Y. Effect of porosity and pore size on microstructures and mechanical properties of poly-ε-caprolactone-hydroxyapatite composites. *J. Biomed. Mater. Res. - Part B Appl. Biomater.* (2008). doi:10.1002/jbm.b.31054

140. Joodaki, H. & Panzer, M. B. Skin mechanical properties and modeling: A review. *Proceedings of the Institution of Mechanical Engineers, Part H: Journal of Engineering in Medicine* (2018). doi:10.1177/0954411918759801

141. Griffin, M. F., Leung, B. C., Premakumar, Y., Szarko, M. & Butler, P. E.

Comparison of the mechanical properties of different skin sites for auricular and nasal reconstruction. *J. Otolaryngol. - Head Neck Surg.* (2017). doi:10.1186/s40463-017-0210-6

142. Nuraje, N., Khan, W. S., Lei, Y., Ceylan, M. & Asmatulu, R. Superhydrophobic electrospun nanofibers. *J. Mater. Chem. A* (2013). doi:10.1039/c2ta00189f

143. Mohiti-Asli, M. *et al.* Ibuprofen loaded PLA nanofibrous scaffolds increase proliferation of human skin cells in vitro and promote healing of full thickness incision wounds in vivo. *J. Biomed. Mater. Res. - Part B Appl. Biomater.* (2017). doi:10.1002/jbm.b.33520

144. Kubiak, K. J., Wilson, M. C. T., Mathia, T. G. & Carval, P. Wettability versus roughness of engineering surfaces. *Wear* (2011). doi:10.1016/j.wear.2010.03.029

145. Park, J. Y., Ha, M. Y., Choi, H. J., Hong, S. Do & Yoon, H. S. A study on the contact angles of a water droplet on smooth and rough solid surfaces. *J. Mech. Sci. Technol.* (2011). doi:10.1007/s12206-010-1218-2

146. Yeh, K. Y., Chen, L. J. & Chang, J. Y. Contact angle hysteresis on regular pillar-like hydrophobic surfaces. *Langmuir* (2008). doi:10.1021/la7020337

147. Rapp, B. E. *Microfluidics: Modeling, mechanics and mathematics*. *Microfluidics: Modeling, Mechanics and Mathematics* (2016). doi:10.1016/c2012-0-02230-2

148. Yuan, T. T., DiGeorge Foushee, A. M., Johnson, M. C., Jockheck-Clark,

A. R. & Stahl, J. M. Development of Electrospun Chitosan-Polyethylene Oxide/Fibrinogen Biocomposite for Potential Wound Healing Applications. *Nanoscale Res. Lett.* (2018). doi:10.1186/s11671-018-2491-8

149. Hall Barrientos, I. J. *et al.* Fabrication and characterisation of drug-loaded electrospun polymeric nanofibers for controlled release in hernia repair. *Int. J. Pharm.* (2017). doi:10.1016/j.ijpharm.2016.12.022

150. Yu, C.-C. *et al.* Random and aligned electrospun PLGA nanofibers embedded in microfluidic chips for cancer cell isolation and integration with air foam technology for cell release. *J. Nanobiotechnology* (2019). doi:10.1186/s12951-019-0466-2

151. Ferrer, I. & Thurman, E. M. Measuring the mass of an electron by LC/TOF-MS: A study of 'twin ions'. *Anal. Chem.* (2005). doi:10.1021/ac0485942

152. Fu, Y. & Kao, W. J. Drug release kinetics and transport mechanisms of non-degradable and degradable polymeric delivery systems. *Expert Opin. Drug Deliv.* (2010). doi:10.1517/17425241003602259

153. Chou, S. F., Carson, D. & Woodrow, K. A. Current strategies for sustaining drug release from electrospun nanofibers. *Journal of Controlled Release* (2015). doi:10.1016/j.jconrel.2015.09.008

154. Kim, K. *et al.* Incorporation and controlled release of a hydrophilic antibiotic using poly(lactide-co-glycolide)-based electrospun nanofibrous scaffolds. *J. Control. Release* (2004). doi:10.1016/j.jconrel.2004.04.009

155. Gonzalez, G., Sagarzazu, A. & Zoltan, T. Infuence of Microstructure in Drug Release Behavior of Silica Nanocapsules. *J. Drug Deliv.* (2013). doi:10.1155/2013/803585

156. Rothstein, S. N. & Little, S. R. A 'tool box' for rational design of degradable controlled release formulations. *J. Mater. Chem.* (2011). doi:10.1039/c0jm01668c

157. Li, J., Jiang, G. & Ding, F. Effects of polymer degradation on drug release from PLGA-mPEG microparticles: A dynamic study of microparticle morphological and physicochemical properties. *J. Appl. Polym. Sci.* (2008). doi:10.1002/app.27823

158. Jenkins, T. L. & Little, D. Synthetic scaffolds for musculoskeletal tissue engineering: cellular responses to fiber parameters. *npj Regen. Med.* (2019). doi:10.1038/s41536-019-0076-5

159. Mattiasson, B., Kumar, A. & Galaev, I. Y. *Macroporous polymers: Production properties and biotechnological/biomedical applications*. *Macroporous Polymers: Production Properties and Biotechnological/Biomedical Applications* (2009).

160. Ushida, T., Furukawa, K., Toita, K. & Tateishi, T. Three-dimensional seeding of chondrocytes encapsulated in collagen gel into PLLA scaffolds. *Cell Transplant.* (2002). doi:10.3727/000000002783985611

161. Zhao, W. *et al.* Fabrication of functional PLGA-based electrospun scaffolds and their applications in biomedical engineering. *Materials Science and Engineering C* (2016). doi:10.1016/j.msec.2015.11.026

162. Asadian, M. *et al.* Effects of pre- and post-electrospinning plasma treatments on electrospun PCL nanofibers to improve cell interactions. in *Journal of Physics: Conference Series* (2017). doi:10.1088/1742-6596/841/1/012018

163. Liu, Y., Jiang, H., Li, Y. & Zhu, K. CONTROL OF DIMENSIONAL STABILITY AND DEGRADATION RATE IN ELECTROSPUN COMPOSITE SCAFFOLDS COMPOSED OF POLY(D,L-LACTIDE-co-GLYCOLIDE) AND POLY(ε-CAPROLACTONE). *Chinese J. Polym. Sci.* (2007). doi:10.1142/s0256767908002674

164. Ru, C. *et al.* Suspended, Shrinkage-Free, Electrospun PLGA Nanofibrous Scaffold for Skin Tissue Engineering. *ACS Appl. Mater. Interfaces* (2015). doi:10.1021/acsami.5b01953

165. Kähäri, V. M. & Saarialho-Kere, U. Matrix metalloproteinases in skin. *Experimental Dermatology* (1997). doi:10.1111/j.1600-0625.1997.tb00164.x

166. Nagase, H., Visse, R. & Murphy, G. Structure and function of matrix metalloproteinases and TIMPs. *Cardiovascular Research* (2006). doi:10.1016/j.cardiores.2005.12.002

167. Armstrong, D. G. & Jude, E. B. The Role of Matrix Metalloproteinases in Wound Healing. *J. Am. Podiatr. Med. Assoc.* (2014). doi:10.7547/87507315-92-1-12

168. Pittayapruek, P., Meephansan, J., Prapapan, O., Komine, M. & Ohtsuki, M. Role of matrix metalloproteinases in Photoaging and photocarcinogenesis. *International Journal of Molecular Sciences*

(2016). doi:10.3390/ijms17060868

169. Freitas-Rodríguez, S., Folgueras, A. R. & López-Otín, C. The role of matrix metalloproteinases in aging: Tissue remodeling and beyond. *Biochimica et Biophysica Acta - Molecular Cell Research* (2017). doi:10.1016/j.bbamcr.2017.05.007

170. Jabłońska-Trypuć, A., Matejczyk, M. & Rosochacki, S. Matrix metalloproteinases (MMPs), the main extracellular matrix (ECM) enzymes in collagen degradation, as a target for anticancer drugs. *Journal of Enzyme Inhibition and Medicinal Chemistry* (2016). doi:10.3109/14756366.2016.1161620

171. Lobmann, R. *et al.* Expression of matrix-metalloproteinases and their inhibitors in the wounds of diabetic and non-diabetic patients. *Diabetologia* (2002). doi:10.1007/s00125-002-0868-8

172. Muller, M. *et al.* Matrix metalloproteinases and diabetic foot ulcers: The ratio of MMP-1 to TIMP-1 is a predictor of wound healing. *Diabet. Med.* (2008). doi:10.1111/j.1464-5491.2008.02414.x

173. Rayment, E. A. & Upton, Z. Review: Finding the culprit: A review of the influences of proteases on the chronic wound environment. *International Journal of Lower Extremity Wounds* (2009). doi:10.1177/1534734609331596

174. Skidmore, R. *et al.* Effects of subantimicrobial-dose doxycycline in the treatment of moderate acne. *Arch. Dermatol.* (2003). doi:10.1001/archderm.139.4.459

175. Payne, J. B. *et al.* The effect of subantimicrobial-dosedoxycycline periodontal therapy on serum biomarkers of systemic inflammation: A randomized, double-masked, placebo-controlled clinical trial. *J. Am. Dent. Assoc.* (2011). doi:10.14219/jada.archive.2011.0165

176. Di Caprio, R., Lembo, S., Di Costanzo, L., Balato, A. & Monfrecola, G. Anti-inflammatory properties of low and high doxycycline doses: An in vitro study. *Mediators Inflamm.* (2015). doi:10.1155/2015/329418

177. Sapadin, A. N. & Fleischmajer, R. Tetracyclines: Nonantibiotic properties and their clinical implications. *J. Am. Acad. Dermatol.* (2006). doi:10.1016/j.jaad.2005.10.004

178. Valentín, S., Morales, A., Sánchez, J. L. & Rivera, A. Safety and efficacy of doxycycline in the treatment of rosacea. *Clinical, Cosmetic and Investigational Dermatology* (2009).

179. Smith, G. N., Mickler, E. A., Hasty, K. A. & Brandt, K. D. Specificity of inhibition of matrix metalloproteinase activity by doxycycline: Relationship to structure of the enzyme. *Arthritis Rheum.* (1999). doi:10.1002/1529-0131(199906)42:6<1140::AID-ANR10>3.0.CO;2-7

180. Acharya, M. R., Venitz, J., Figg, W. D. & Sparreboom, A. Chemically modified tetracyclines as inhibitors of matrix metalloproteinases. *Drug Resist. Updat.* (2004). doi:10.1016/j.drup.2004.04.002

181. Henehan, M., Montuno, M. & De Benedetto, A. Doxycycline as an anti-inflammatory agent: updates in dermatology. *Journal of the European Academy of Dermatology and Venereology* (2017). doi:10.1111/jdv.14345

182. Del Rosso, J. Q. Oral doxycycline in the management of acne vulgaris: Current perspectives on clinical use and recent findings with a new double-scored small tablet formulation. *Journal of Clinical and Aesthetic Dermatology* (2015).

183. Rivero, A. L. & Whitfeld, M. An update on the treatment of rosacea. *Aust. Prescr.* (2018). doi:10.18773/austprescr.2018.004

184. Caton, J. G. *et al.* Treatment With Subantimicrobial Dose Doxycycline Improves the Efficacy of Scaling and Root Planing in Patients With Adult Periodontitis. *J. Periodontol.* (2005). doi:10.1902/jop.2000.71.4.521

185. Gabriele, S. *et al.* Stability, Activity, and Application of Topical Doxycycline Formulations in a Diabetic Wound Case Study. *Wounds* (2019).

186. Serra, R. *et al.* Doxycycline speeds up healing of chronic venous ulcers. *Int. Wound J.* (2015). doi:10.1111/iwj.12077

187. Chaturvedi, T. P., Srivastava, R., Srivastava, A. K., Gupta, V. & Verma, P. K. Doxycycline poly e-caprolactone nanofibers in patients with chronic periodontitis - A clinical evaluation. *J. Clin. Diagnostic Res.* (2013). doi:10.7860/JCDR/2013/5858.3519

188. Jia, L. N. *et al.* Development of a Doxycycline Hydrochloride-Loaded Electrospun Nanofibrous Membrane for GTR/GBR Applications. *J. Nanomater.* (2016). doi:10.1155/2016/6507459

189. Yamawaki-Ogata, A. *et al.* A doxycycline loaded, controlled-release, biodegradable fiber for the treatment of aortic aneurysms. *Biomaterials*

(2010). doi:10.1016/j.biomaterials.2010.08.069

190. Cui, J. Z. *et al.* In vivo characterization of doxycycline-mediated protection of aortic function and structure in a mouse model of Marfan syndrome-associated aortic aneurysm. *Sci. Rep.* (2019). doi:10.1038/s41598-018-38235-6

191. Mondal, D., Griffith, M. & Venkatraman, S. S. Polycaprolactone-based biomaterials for tissue engineering and drug delivery: Current scenario and challenges. *International Journal of Polymeric Materials and Polymeric Biomaterials* (2016). doi:10.1080/00914037.2015.1103241

192. Woodruff, M. A. & Hutmacher, D. W. The return of a forgotten polymer - Polycaprolactone in the 21st century. *Progress in Polymer Science (Oxford)* (2010). doi:10.1016/j.progpolymsci.2010.04.002

193. Gad, H. A., El-Nabarawi, M. A. & Abd El-Hady, S. S. Formulation and Evaluation of PLA and PLGA In Situ Implants Containing Secnidazole and/or Doxycycline for Treatment of Periodontitis. *AAPS PharmSciTech* (2008). doi:10.1208/s12249-008-9126-9

194. Cui, F. *et al.* Preparation and characterization of melittin-loaded poly (DL-lactic acid) or poly (DL-lactic-co-glycolic acid) microspheres made by the double emulsion method. *J. Control. Release* (2005). doi:10.1016/j.jconrel.2005.07.001

195. Feng, K. *et al.* Novel antibacterial nanofibrous PLLA scaffolds. *J. Control. Release* (2010). doi:10.1016/j.jconrel.2010.05.035

196. Bolobajev, J., Trapido, M. & Goi, A. Effect of iron ion on doxycycline

photocatalytic and Fenton-based autocatatalytic decomposition. *Chemosphere* (2016). doi:10.1016/j.chemosphere.2016.03.042

197. Hassani, M., Lázaro, R., Pérez, C., Condón, S. & Pagán, R. Thermostability of oxytetracycline, tetracycline, and doxycycline at ultrahigh temperatures. *J. Agric. Food Chem.* (2008). doi:10.1021/jf800008p

198. Jutglar, M., Foradada, M., Caballero, F., Hoogmartens, J. & Adams, E. Influence of the solvent system on the stability of doxycycline solutions. *J. Pharm. Biomed. Anal.* (2018). doi:10.1016/j.jpba.2018.06.054

199. Skúlason, S., Ingólfsson, E. & Kristmundsdóttir, T. Development of a simple HPLC method for separation of doxycycline and its degradation products. *J. Pharm. Biomed. Anal.* (2003). doi:10.1016/S0731-7085(03)00316-9

200. Redelsperger, I. M. *et al.* Stability of doxycycline in feed and water and minimal effective doses in tetracycline-inducible systems. *J. Am. Assoc. Lab. Anim. Sci.* (2016).

201. Eskitoros-Togay, M. *et al.* Fabrication of doxycycline-loaded electrospun PCL/PEO membranes for a potential drug delivery system. *Int. J. Pharm.* (2019). doi:10.1016/j.ijpharm.2019.04.073

202. Pillay, V. *et al.* A review of the effect of processing variables on the fabrication of electrospun nanofibers for drug delivery applications. *Journal of Nanomaterials* (2013). doi:10.1155/2013/789289

203. Amariei, N., Manea, L. R., Bertea, A. P., Bertea, A. & Popa, A. The

Influence of Polymer Solution on the Properties of Electrospun 3D Nanostructures. in *IOP Conference Series: Materials Science and Engineering* (2017). doi:10.1088/1757-899X/209/1/012092

204. Sun, B. *et al.* Advances in three-dimensional nanofibrous macrostructures via electrospinning. *Progress in Polymer Science* (2014). doi:10.1016/j.progpolymsci.2013.06.002

205. Soliman, S. *et al.* Controlling the porosity of fibrous scaffolds by modulating the fiber diameter and packing density. *J. Biomed. Mater. Res. - Part A* (2011). doi:10.1002/jbm.a.33010

206. Kancheva, M., Toncheva, A., Manolova, N. & Rashkov, I. Enhancing the mechanical properties of electrospun polyester mats by heat treatment. *Express Polym. Lett.* (2015). doi:10.3144/expresspolymlett.2015.6

207. Bosworth, L. A. & Downes, S. Physicochemical characterisation of degrading polycaprolactone scaffolds. *Polym. Degrad. Stab.* (2010). doi:10.1016/j.polymdegradstab.2010.09.007

208. Lee, H. *et al.* Enhancement of mechanical properties of polymeric nanofibers by controlling crystallization behavior using a simple freezing/thawing process. *RSC Adv.* (2017). doi:10.1039/c7ra06545k

209. Pitt, C. G., Chasalow, F. I., Hibionada, Y. M., Klimas, D. M. & Schindler, A. Aliphatic polyesters. I. The degradation of poly(ϵ-caprolactone) in vivo. *J. Appl. Polym. Sci.* (1981). doi:10.1002/app.1981.070261124

210. Heimowska, A., Morawska, M. & Bocho-Janiszewska, A. Biodegradation of poly(ϵ-caprolactone) in natural water environments.

Polish J. Chem. Technol. (2017). doi:10.1515/pjct-2017-0017

211. Al-Qadhi, M. *et al.* Preparation of superhydrophobic and self-cleaning polysulfone non-wovens by electrospinning: influence of process parameters on morphology and hydrophobicity. *J. Polym. Res.* (2015). doi:10.1007/s10965-015-0844-x

212. Karuppuswamy, P., Reddy Venugopal, J., Navaneethan, B., Luwang Laiva, A. & Ramakrishna, S. Polycaprolactone nanofibers for the controlled release of tetracycline hydrochloride. *Mater. Lett.* (2015). doi:10.1016/j.matlet.2014.11.044

213. Xue, S. W. Synthesis, characterization, biodegradation, and drug delivery application of biodegradable lactic/glycolic acid polymers: Part III. Drug delivery application. *Artif. Cells. Blood Substit. Immobil. Biotechnol.* (2004). doi:10.1081/BIO-200039635

214. Van Royen, P., Schacht, E., Ruys, L. & Van Vaeck, L. Static secondary ion mass spectrometry for nanoscale analysis: Surface characterisation of electrospun nanofibres. *Rapid Commun. Mass Spectrom.* (2006). doi:10.1002/rcm.2311

215. Bouslimani, A., Sanchez, L. M., Garg, N. & Dorrestein, P. C. Mass spectrometry of natural products: Current, emerging and future technologies. *Natural Product Reports* (2014). doi:10.1039/c4np00044g

216. Mundargi, R. C. *et al.* Development and evaluation of novel biodegradable microspheres based on poly(d,l-lactide-co-glycolide) and poly(ε-caprolactone) for controlled delivery of doxycycline in the treatment of human periodontal pocket: In vitro and in vivo studies. *J.*

Control. Release (2007). doi:10.1016/j.jconrel.2007.01.008

217. Raval, J. P., Naik, D. R., Amin, K. A. & Patel, P. S. Controlled-release and antibacterial studies of doxycycline-loaded poly(ε-caprolactone) microspheres. *J. Saudi Chem. Soc.* (2014). doi:10.1016/j.jscs.2011.11.004

218. Yuan, Y., Choi, K., Choi, S. O. & Kim, J. Early stage release control of an anticancer drug by drug-polymer miscibility in a hydrophobic fiber-based drug delivery system. *RSC Adv.* (2018). doi:10.1039/c8ra01467a

219. Carson, D., Jiang, Y. & Woodrow, K. A. Tunable Release of Multiclass Anti-HIV Drugs that are Water-Soluble and Loaded at High Drug Content in Polyester Blended Electrospun Fibers. *Pharm. Res.* (2016). doi:10.1007/s11095-015-1769-0

220. Casy, A. F. & Yasin, A. Stereochemical studies of tetracycline antibiotics and their common impurities by 400 MHz 1H NMR spectroscopy. *Magn. Reson. Chem.* (1985). doi:10.1002/mrc.1260230917

221. Casy, A. F. & Yasin, A. The identification and stereochemical study of tetracycline antibiotics by 1H nuclear magnetic resonance spectroscopy. *J. Pharm. Biomed. Anal.* (1983). doi:10.1016/0731-7085(83)80040-5

222. Karplus, M. Vicinal Proton Coupling in Nuclear Magnetic Resonance. *Journal of the American Chemical Society* (1963). doi:10.1021/ja00901a059

223. Ha, J. H. *et al.* Albumin release from bioerodible hydrogels based on semi- interpenetrating polymer networks composed of poly(ε-

caprolactone) and poly(ethylene glycol) macromer. *J. Control. Release* (1997). doi:10.1016/S0168-3659(97)00096-5

224. Abedalwafa, M., Wang, F., Wang, L. & Li, C. Biodegradable poly-epsilon-caprolactone (PCL) for tissue engineering applications: A review. *Rev. Adv. Mater. Sci.* (2013).

225. Díaz, E., Sandonis, I. & Valle, M. B. In vitro degradation of poly(caprolactone)/nHA composites. *J. Nanomater.* (2014). doi:10.1155/2014/802435

226. Chiellini, E. & Solaro, R. Biodegradable polymeric materials. *Adv. Mater.* (1996). doi:10.1002/adma.19960080406

227. França, D. C., Bezerra, E. B., De Souza Morais, D. D., Araújo, E. M. & Wellen, R. M. R. Hydrolytic and thermal degradation of PCL and PCL/bentonite compounds. *Mater. Res.* (2016). doi:10.1590/1980-5373-MR-2015-0797

228. Augustine, R., Thomas, S. & Kalarikkal, N. In Vitro Degradation of Electrospun Polycaprolactone Membranes in Simulated Body Fluid. *Int. J. Inst. Mater. Malaysia* (2014).

229. Detillieux, K. A., Sheikh, F., Kardami, E. & Cattini, P. A. Biological activities of fibroblast growth factor-2 in the adult myocardium. *Cardiovascular Research* (2003). doi:10.1016/S0008-6363(02)00708-3

230. Rubert, M. *et al.* Electrospun PCL/PEO coaxial fibers for basic fibroblast growth factor delivery. *J. Mater. Chem. B* (2014). doi:10.1039/c4tb01258e

231. Yun, Y. R. *et al.* Fibroblast growth factors: Biology, function, and application for tissue regeneration. *Journal of Tissue Engineering* (2010). doi:10.4061/2010/218142

232. Kumorek, M. *et al.* Cellular responses modulated by FGF-2 adsorbed on albumin/heparin layer-by-layer assemblies. *PLoS One* (2015). doi:10.1371/journal.pone.0125484

233. Franks, P. J. & Moffatt, C. J. Do clinical and social factors predict quality of life in leg ulceration? *Int. J. Low. Extrem. Wounds* (2006). doi:10.1177/1534734606293786

234. Brown, A. Strategies to reduce or eliminate wound pain. *Nurs. Times* (2014).

235. Muldoon, J. Pain, inflammation and wound healing. *Nurse Prescr.* **15**, 14–18 (2018).

236. Stein, C. & Küchler, S. Targeting inflammation and wound healing by opioids. *Trends in Pharmacological Sciences* (2013). doi:10.1016/j.tips.2013.03.006

237. Wilcox, J. R., Covington, D. S. & Paez, N. Doxycycline as a Modulator of Inflammation in Chronic Wounds. *Wounds* **24**, 339–349 (2012).

238. Golub, L. M. *et al.* Tetracyclines Inhibit Connective Tissue Breakdown by Multiple Non-Antimicrobial Mechanisms. *Adv. Dent. Res.* (1998). doi:10.1177/08959374980120010501

239. Eady, E. A., Ingham, E., Walters, C. E., Cove, J. H. & Cunliffe, W. J. Modulation of comedonal levels of interleukin-1 in acne patients treated

with tetracyclines. *J. Invest. Dermatol.* (1993). doi:10.1111/1523-1747.ep12360123

240. LAUHIO, A. *et al.* In vivo inhibition of human neutrophil collagenase (MMP-8) activity during long-term combination therapy of doxycycline and non-steroidal anti-inflammatory drugs (NSAID) in acute reactive arthritis. *Clin. Exp. Immunol.* (2008). doi:10.1111/j.1365-2249.1994.tb06601.x

241. Greenwald, R. A., Moak, S. A., Ramamurthy, N. S. & Golub, L. N. Tetracyclines suppress matrix metalloproteinase activity in adjuvant arthritis and in combination with flurbiprofen, ameliorate bone damage. *J. Rheumatol.* (1992).

242. Lee, H.-M. *et al.* Subantimicrobial Dose Doxycycline Efficacy as a Matrix Metalloproteinase Inhibitor in Chronic Periodontitis Patients Is Enhanced When Combined With a Non-Steroidal Anti-Inflammatory Drug. *J. Periodontol.* (2005). doi:10.1902/jop.2004.75.3.453

243. Lu, Y. *et al.* Coaxial electrospun fibers: applications in drug delivery and tissue engineering. *Wiley Interdisciplinary Reviews: Nanomedicine and Nanobiotechnology* (2016). doi:10.1002/wnan.1391

244. Torres-Martinez, E. J., Cornejo Bravo, J. M., Serrano Medina, A., Pérez González, G. L. & Villarreal Gómez, L. J. A Summary of Electrospun Nanofibers as Drug Delivery System: Drugs Loaded and Biopolymers Used as Matrices. *Curr. Drug Deliv.* (2018). doi:10.2174/1567201815666180723114326

245. Díaz, E., Fernández-Nieves, A., Barrero, A., Márquez, M. & Loscertales,

G. Fabrication of structured micro and nanofibers by coaxial electrospinning. *J. Phys. Conf. Ser.* (2008). doi:10.1088/1742-6596/127/1/012008

246. Qu, H., Wei, S. & Guo, Z. Coaxial electrospun nanostructures and their applications. *J. Mater. Chem. A* (2013). doi:10.1039/c3ta12390a

247. Elahi, M. F. & Lu, W. Core-shell Fibers for Biomedical Applications-A Review. *J. Bioeng. Biomed. Sci.* (2013). doi:10.4172/2155-9538.1000121

248. Wang, J. & Windbergs, M. Controlled dual drug release by coaxial electrospun fibers – Impact of the core fluid on drug encapsulation and release. *Int. J. Pharm.* (2019). doi:10.1016/j.ijpharm.2018.12.026

249. Maleki, M., Latifi, M., Amani-Tehran, M. & Mathur, S. Electrospun core-shell nanofibers for drug encapsulation and sustained release. *Polym. Eng. Sci.* (2013). doi:10.1002/pen.23426

250. Yu, D. G. *et al.* Dual drug release nanocomposites prepared using a combination of electrospraying and electrospinning. *RSC Adv.* (2013). doi:10.1039/c3ra40334c

251. Han, D. & Steckl, A. J. Triaxial electrospun nanofiber membranes for controlled dual release of functional molecules. *ACS Appl. Mater. Interfaces* (2013). doi:10.1021/am402376c

252. Manoukian, O. S. *et al.* Bioactive nanofiber dressings for wound healing. in *Wound Healing Biomaterials* (2016). doi:10.1016/B978-1-78242-456-7.00022-2

253. Li, C., Wang, Z. H., Yu, D. G. & Williams, G. R. Tunable biphasic drug

release from ethyl cellulose nanofibers fabricated using a modified coaxial electrospinning process. *Nanoscale Res. Lett.* (2014). doi:10.1186/1556-276X-9-258

254. Pant, B., Park, M. & Park, S.-J. Drug Delivery Applications of Core-Sheath Nanofibers Prepared by Coaxial Electrospinning: A Review. *Pharmaceutics* **11**, 305 (2019).

255. Yoon, J., Yang, H. S., Lee, B. S. & Yu, W. R. Recent Progress in Coaxial Electrospinning: New Parameters, Various Structures, and Wide Applications. *Advanced Materials* (2018). doi:10.1002/adma.201704765

256. Kurban, Z. *et al.* A solution selection model for coaxial electrospinning and its application to nanostructured hydrogen storage materials. *J. Phys. Chem. C* (2010). doi:10.1021/jp107871v

257. Zhu, J. *et al.* Aqueous-based coaxial electrospinning of genetically engineered silk elastin core-shell nanofibers. *Materials (Basel).* (2016). doi:10.3390/ma9040221

258. Tort, S., Acartürk, F. & Beşikci, A. Evaluation of three-layered doxycycline-collagen loaded nanofiber wound dressing. *Int. J. Pharm.* (2017). doi:10.1016/j.ijpharm.2017.07.027

259. Yan, X. *et al.* Slit-surface electrospinning: A novel process developed for high-throughput fabrication of core-sheath fibers. *PLoS One* (2015). doi:10.1371/journal.pone.0125407

260. Qin, X. Coaxial electrospinning of nanofibers. in *Electrospun Nanofibers* (2016). doi:10.1016/B978-0-08-100907-9.00003-9

261. Wang, L. *et al.* Effect of the electrical conductivity of core solutions on the morphology and structure of core-shell CA-PCL/CS nanofibers. *New J. Chem.* (2017). doi:10.1039/c7nj02805a

262. Melo, L. P. De, Salmoria, G. V., Fancello, E. A. & Roesler, C. R. D. M. Effect of Injection Molding Melt Temperatures on PLGA Craniofacial Plate Properties during in Vitro Degradation. *Int. J. Biomater.* (2017). doi:10.1155/2017/1256537

263. Baji, A., Mai, Y. W., Wong, S. C., Abtahi, M. & Chen, P. Electrospinning of polymer nanofibers: Effects on oriented morphology, structures and tensile properties. *Composites Science and Technology* (2010). doi:10.1016/j.compscitech.2010.01.010

264. Wong, S. C., Baji, A. & Leng, S. Effect of fiber diameter on tensile properties of electrospun poly(ε-caprolactone). *Polymer (Guildf).* (2008). doi:10.1016/j.polymer.2008.08.022

265. Morel, A. *et al.* Correlating diameter, mechanical and structural properties of poly(L-lactide) fibres from needleless electrospinning. *Acta Biomater.* (2018). doi:10.1016/j.actbio.2018.09.055

266. Tan, E. P. S. & Lim, C. T. Physical properties of a single polymeric nanofiber. *Appl. Phys. Lett.* (2004). doi:10.1063/1.1651643

267. Lim, C. T., Tan, E. P. S. & Ng, S. Y. Effects of crystalline morphology on the tensile properties of electrospun polymer nanofibers. *Appl. Phys. Lett.* (2008). doi:10.1063/1.2857478

268. Chew, S. Y., Hufnagel, T. C., Lim, C. T. & Leong, K. W. Mechanical

properties of single electrospun drug-encapsulated nanofibres. *Nanotechnology* (2006). doi:10.1088/0957-4484/17/15/045

269. Yuan, Y. & Lee, T. R. Contact angle and wetting properties. *Springer Ser. Surf. Sci.* (2013). doi:10.1007/978-3-642-34243-1_1

270. Mikaeili, F. & Gouma, P. I. Super Water-Repellent Cellulose Acetate Mats. *Sci. Rep.* (2018). doi:10.1038/s41598-018-30693-2

271. Areias, A. C. *et al.* Influence of crystallinity and fiber orientation on hydrophobicity and biological response of poly(l-lactide) electrospun mats. *Soft Matter* (2012). doi:10.1039/c2sm25557j

272. Sun, H. *et al.* The π-π stacked geometries and association thermodynamics of quinacridone derivatives studied by 1 H NMR. *J. Phys. Chem. A* (2006). doi:10.1021/jp057232a

273. Gholipour, A., Abolhassanzadeh Parizi, M. & Sadat Neyband, R. The effect of Π-Π stacking interaction on hydrogen bonding in a molecular seesaw balance: A NMR study. *Chem. Phys. Lett.* (2018). doi:10.1016/j.cplett.2018.08.018

274. Tyo, K. *et al.* Relating Advanced Electrospun Fiber Architectures to the Temporal Release of Active Agents to Meet the Needs of Next-Generation Intravaginal Delivery Applications. *Pharmaceutics* (2019). doi:10.3390/pharmaceutics11040160

275. Repanas, A. & Wolkers, W. F. Coaxial Electrospinning as a Process to Engineer Biodegradable Polymeric Scaffolds as Drug Delivery Systems for Anti-Inflammatory and Anti- Thrombotic Pharmaceutical Agents.

Clin. Exp. Pharmacol. (2015). doi:10.4172/2161-1459.1000192

276. Topuz, F. & Uyar, T. Electrospinning of cyclodextrin functional nanofibers for drug delivery applications. *Pharmaceutics* (2019). doi:10.3390/pharmaceutics11010006

277. He, C. L. *et al.* Coaxial electrospun poly(L-lactic acid) ultrafine fibers for sustained drug delivery. in *Journal of Macromolecular Science, Part B: Physics* (2006). doi:10.1080/00222340600769832

278. Zhang, Y. Z. *et al.* Coaxial electrospinning of (fluorescein isothiocyanate-conjugated bovine serum albumin)-encapsulated poly(ε-caprolactone) nanofibers for sustained release. *Biomacromolecules* (2006). doi:10.1021/bm050743i

279. Huang, W. *et al.* Drug-Loaded Zein Nanofibers Prepared Using a Modified Coaxial Electrospinning Process. *AAPS PharmSciTech* (2013). doi:10.1208/s12249-013-9953-1

280. Xu, Y. *et al.* Influence of the drug distribution in electrospun gliadin fibers on drug-release behavior. *Eur. J. Pharm. Sci.* (2017). doi:10.1016/j.ejps.2017.06.017

281. Abdullah, M. F., Nuge, T., Andriyana, A., Ang, B. C. & Muhamad, F. Core-Shell fibers: Design, roles, and controllable release strategies in tissue engineering and drug delivery. *Polymers* (2019). doi:10.3390/polym11122008

282. Wan, F. *et al.* One-Step Production of Protein-Loaded PLGA Microparticles via Spray Drying Using 3-Fluid Nozzle. *Pharm. Res.*

(2014). doi:10.1007/s11095-014-1299-1

283. Kai, D., Jiang, S., Low, Z. W. & Loh, X. J. Engineering highly stretchable lignin-based electrospun nanofibers for potential biomedical applications. *J. Mater. Chem. B* (2015). doi:10.1039/c5tb00765h

284. Singal, A. G., Higgins, P. D. R. & Waljee, A. K. A primer on effectiveness and efficacy trials. *Clin. Transl. Gastroenterol.* (2014). doi:10.1038/ctg.2013.13

285. Phanse, M. A., Patil, M. J., Abbulu, K., Chaudhari, P. D. & Patel, B. In-vivo and in-vitro screening of medicinal plants for their anti-inflammatory activity: An overview. *J. Appl. Pharm. Sci.* (2012). doi:10.7324/JAPS.2012.2704

286. Ullah, H. M. A. *et al.* Evaluation of antinociceptive, in-vivo & in-vitro anti-inflammatory activity of ethanolic extract of Curcuma zedoaria rhizome. *BMC Complement. Altern. Med.* (2014). doi:10.1186/1472-6882-14-346

287. Jensen, G. S. *et al.* In vitro and in vivo antioxidant and anti-inflammatory capacities of an antioxidant-rich fruit and berry juice blend. Results of a pilot and randomized, double-blinded, placebo-controlled, crossover study. *J. Agric. Food Chem.* (2008). doi:10.1021/jf8016157

288. Deldar, Y. *et al.* An in vitro examination of the antioxidant, cytoprotective and anti-inflammatory properties of chrysin-loaded nanofibrous mats for potential wound healing applications. *Artif. Cells, Nanomedicine Biotechnol.* (2018). doi:10.1080/21691401.2017.1337022

289. Biglari, S. *et al.* Simulating Inflammation in a Wound Microenvironment Using a Dermal Wound-on-a-Chip Model. *Adv. Healthc. Mater.* (2019). doi:10.1002/adhm.201801307

290. Mitra, M., Ho, L. D. & Coller, H. A. An in vitro model of cellular quiescence in primary human dermal fibroblasts. in *Methods in Molecular Biology* (2018). doi:10.1007/978-1-4939-7371-2_2

291. Nickien, M., Heuijerjans, A., Ito, K. & van Donkelaar, C. C. Comparison between in vitro and in vivo cartilage overloading studies based on a systematic literature review. *Journal of Orthopaedic Research* (2018). doi:10.1002/jor.23910

292. Wufuer, M. *et al.* Skin-on-a-chip model simulating inflammation, edema and drug-based treatment. *Sci. Rep.* (2016). doi:10.1038/srep37471

293. Niehues, H. & van den Bogaard, E. H. Past, present and future of in vitro 3D reconstructed inflammatory skin models to study psoriasis. *Experimental Dermatology* (2018). doi:10.1111/exd.13525

294. Wang, X., Coradin, T. & Hélary, C. Modulating inflammation in a cutaneous chronic wound model by IL-10 released from collagen-silica nanocomposites: Via gene delivery. *Biomater. Sci.* (2018). doi:10.1039/c7bm01024a

295. Chung, E., Choi, H., Lim, J. E. & Son, Y. Development of skin inflammation test model by co-culture of reconstituted 3D skin and RAW264.7 cells. *Tissue Eng. Regen. Med.* (2014). doi:10.1007/s13770-013-1113-x

296. Neagu, M. *et al.* Inflammation: A key process in skin tumorigenesis (Review). *Oncol. Lett.* (2019). doi:10.3892/ol.2018.9735

297. Bashir, M. M., Sharma, M. R. & Werth, V. P. UVB and proinflammatory cytokines synergistically activate TNF-α production in keratinocytes through enhanced gene transcription. *J. Invest. Dermatol.* (2009). doi:10.1038/jid.2008.332

298. Zhu, X. *et al.* Activation of Sirt1 by Resveratrol Inhibits TNF-α Induced Inflammation in Fibroblasts. *PLoS One* **6**, e27081 (2011).

299. Kim, E. C. *et al.* Cytokine-mediated PGE2 expression in human colonic fibroblasts. *Am. J. Physiol. - Cell Physiol.* (1998).

300. Tsai, M. H. *et al.* Eupafolin inhibits PGE2 production and COX2 expression in LPS-stimulated human dermal fibroblasts by blocking JNK/AP-1 and Nox2/p47phox pathway. *Toxicol. Appl. Pharmacol.* (2014). doi:10.1016/j.taap.2014.06.012

301. Noguchi, K. *et al.* Prostaglandin production via induction of cyclooxygenase-2 by human gingival fibroblasts stimulated with lipopolysaccharides. *Inflammation* **20**, 555–568 (1996).

302. Arasa, J. *et al.* Defective Induction of COX-2 Expression by Psoriatic Fibroblasts Promotes Pro-inflammatory Activation of Macrophages. *Front. Immunol.* **10**, (2019).

303. Daghigh, F., Borghaei, R. C., Thornton, R. D. & Bee, J. H. Human Gingival Fibroblasts Produce Nitric Oxide in Response to Proinflammatory Cytokines. *J. Periodontol.* **73**, 392–400 (2002).

304. Au, R. Y., Al-Talib, T. K., Au, A. Y., Phan, P. V. & Frondoza, C. G. Avocado soybean unsaponifiables (ASU) suppress TNF-α, IL-1β, COX-2, iNOS gene expression, and prostaglandin E2 and nitric oxide production in articular chondrocytes and monocyte/macrophages. *Osteoarthr. Cartil.* **15**, 1249–1255 (2007).

305. Bae, S., Jung, Y., Choi, Y. M. & Li, S. Effects of Er-Miao-San extracts on TNF-alpha-induced MMP-1 expression in human dermal fibroblasts. *Biol. Res.* (2015). doi:10.1186/0717-6287-48-8

306. Sasaki, M. *et al.* Differential regulation of metalloproteinase production, proliferation and chemotaxis of human lung fibroblasts by PDGF, Interleukin-1β and TNF-α. *Mediators Inflamm.* **9**, 155–160 (2000).

307. Nakao, S. *et al.* Tumor necrosis factor α (TNF-α)-induced prostaglandin E2 release is mediated by the activation of cyclooxygenase-2 (COX-2) transcription via NFκB in human gingival fibroblasts. *Mol. Cell. Biochem.* (2002). doi:10.1023/A:1019927616000

308. Wang, R., Ghahary, A., Shen, Y. J., Scott, P. G. & Tredget, E. E. Human Dermal Fibroblasts Produce Nitric Oxide and Express Both Constitutive and Inducible Nitric Oxide Synthase Isoforms. *J. Invest. Dermatol.* **106**, 419–427 (1996).

309. P. Kwesiga, M. *et al.* Investigative Study on Nitric Oxide Production in Human Dermal Fibroblast Cells under Normal and High Glucose Conditions. *Med. Sci.* **6**, 99 (2018).

310. Sonoki, A., Okano, Y. & Yoshitake, Y. Dermal fibroblasts can activate matrix metalloproteinase-1 independent of keratinocytes via plasmin in a

3D collagen model. *Exp. Dermatol.* **27**, 520–525 (2018).

311. Lindner, D. *et al.* Differential expression of matrix metalloproteases in human fibroblasts with different origins. *Biochem. Res. Int.* (2012). doi:10.1155/2012/875742

312. Mia, M. M., Boersema, M. & Bank, R. A. Interleukin-1β attenuates myofibroblast formation and extracellular matrix production in dermal and lung fibroblasts exposed to transforming growth factor-β1. *PLoS One* (2014). doi:10.1371/journal.pone.0091559

313. Reunanen, N. *et al.* Enhancement of fibroblast collagenase (matrix metalloproteinase-1) gene expression by ceramide is mediated by extracellular signal-regulated and stress-activated protein kinase pathways. *J. Biol. Chem.* (1998). doi:10.1074/jbc.273.9.5137

314. Wong, W., Kossodo, S. & Kochevar, I. E. I NFLUENCE OF C YTOKINES ON M ATRIX M ETALLOPROTEINASES P RODUCED BY F IBROBLASTS R esults. **100**, 377–382 (2001).

315. Dasu, M. R. K., Barrow, R. E., Spies, M. & Herndon, D. N. Matrix metalloproteinase expression in cytokine stimulated human dermal fibroblasts. *Burns* (2003). doi:10.1016/S0305-4179(03)00154-2

316. Wallace, H. J. & Stacey, M. C. Levels of tumor necrosis factor-α (TNF-α) and soluble TNF receptors in chronic venous leg ulcers - Correlations to healing status. *J. Invest. Dermatol.* (1998). doi:10.1046/j.1523-1747.1998.00113.x

317. Tarnuzzer, R. W. & Schultz, G. S. Biochemical analysis of acute and

chronic wound environments. *Wound Repair Regen.* (1996). doi:10.1046/j.1524-475X.1996.40307.x

318. Trengove, N. J., Bielefeldt-Ohmann, H. & Stacey, M. C. Mitogenic activity and cytokine levels in non-healing and healing chronic leg ulcers. *Wound Repair Regen.* (2000). doi:10.1046/j.1524-475X.2000.00013.x

319. Xu, F., Zhang, C. & Graves, D. T. Abnormal cell responses and role of TNF- α in impaired diabetic wound healing. *BioMed Research International* (2013). doi:10.1155/2013/754802

320. Gohel, M. S., Windhaber, R. A. J., Tarlton, J. F., Whyman, M. R. & Poskitt, K. R. The relationship between cytokine concentrations and wound healing in chronic venous ulceration. *J. Vasc. Surg.* (2008). doi:10.1016/j.jvs.2008.06.042

321. Kitanaka, T. *et al.* JNK activation is essential for activation of MEK/ERK signaling in IL-1β-induced COX-2 expression in synovial fibroblasts. *Sci. Rep.* (2017). doi:10.1038/srep39914

322. Han, Y. P., Tuan, T. L., Wu, H., Hughes, M. & Garner, W. L. TNF-α stimulates activation of pro-MMP2 in human skin through NF-κB mediated induction of MT1-MMP. *J. Cell Sci.* (2001).

323. Solomon, A., Li, D. Q., Lee, S. B. & Tseng, S. C. G. Regulation of collagenase, stromelysin, and urokinase-type plasminogen activator in primary pterygium body fibroblasts by inflammatory cytokines. *Investig. Ophthalmol. Vis. Sci.* (2000).

324. E J Battegay, E W Raines, T. C. and R. R. TNF-α stimulation of fibroblast

proliferation: Dependence on platelet- derived growth factor (PDGF) secretion and alteration of PDGF receptor expression. *J. Immunol.* **154**, 6040–6047 (1995).

325. Mavrogonatou, E., Konstantinou, A. & Kletsas, D. Long-term exposure to TNF-α leads human skin fibroblasts to a p38 MAPK- and ROS-mediated premature senescence. *Biogerontology* (2018). doi:10.1007/s10522-018-9753-9

326. Lertchirakarn, V. Effects of interleukin-1β on human pulpal fibroblast proliferation and collagen synthesis. *J. Endod.* **24**, (1998).

327. Gitter, B. D., Labus, J. M., Lees, S. L. & Scheetz, M. E. Characteristics of human synovial fibroblast activation by IL-1 beta and TNF alpha. *Immunology* **66**, 196–200 (1989).

328. Protasoni, M., Kroon, A. M. & Taanman, J.-W. Mitochondria as oncotarget: a comparison between the tetracycline analogs doxycycline and COL-3. *Oncotarget* (2018). doi:10.18632/oncotarget.26107

329. Neuvians, T. P., Schams, D., Berisha, B. & Pfaffl, M. W. Involvement of Pro-Inflammatory Cytokines, Mediators of Inflammation, and Basic Fibroblast Growth Factor in Prostaglandin F2α-Induced Luteolysis in Bovine Corpus Luteum1. *Biol. Reprod.* **70**, 473–480 (2004).

330. Taube, C. *et al.* Factor B of the alternative complement pathway regulates development of airway hyperresponsiveness and inflammation. *Proc. Natl. Acad. Sci.* **103**, 8084–8089 (2006).

331. Circoloso, A., Piercetl, G. F., Katzsii, Y. & Strunksllss, R. C.

Antiinflammatory Effects of Polypeptide Growth Factors GROWTH FACTOR INHIBIT THE CYTOKINE-INDUCED EXPRESSION OF. *J. Biol. Chem.* **265**, 5066–5071 (1990).

332. Iwai-Kanai, E. *et al.* Basic fibroblast growth factor protects cardiac myocytes from iNOS-mediated apoptosis. *J. Cell. Physiol.* (2002). doi:10.1002/jcp.10036

333. Fernando, D. M., Wijesundera, R. L. C., Soysa, P., de Silva, D. & Nanayakkara, C. M. Antioxidant potential, in vitro cytotoxicity and apoptotic effect induced by crude organic extract of Anthracophyllum lateritium against RD sarcoma cells. *BMC Complement. Altern. Med.* (2015). doi:10.1186/s12906-015-0924-9

334. Lee, Y. H., Seo, E. K. & Lee, S. T. Skullcapflavone II Inhibits Degradation of Type I Collagen by Suppressing MMP-1 Transcription in Human Skin Fibroblasts. *Int. J. Mol. Sci.* (2019). doi:10.3390/ijms20112734

335. Fuchs, S., Skwara, A., Bloch, M. & Dankbar, B. Differential induction and regulation of matrix metalloproteinases in osteoarthritic tissue and fluid synovial fibroblasts. *Osteoarthr. Cartil.* (2004). doi:10.1016/j.joca.2004.02.005

336. Kanangat, S. *et al.* Induction of multiple matrix metalloproteinases in human dermal and synovial fibroblasts by Staphylococcus aureus: Implications in the pathogenesis of septic arthritis and other soft tissue infections. *Arthritis Res. Ther.* (2006). doi:10.1186/ar2086

337. Eto, H. *et al.* Therapeutic potential of fibroblast growth factor-2 for

hypertrophic scars: Upregulation of MMP-1 and HGF expression. *Lab. Investig.* (2012). doi:10.1038/labinvest.2011.127

338. Palasuk, J. *et al.* Doxycycline-loaded nanotube-modified adhesives inhibit MMP in a dose-dependent fashion. *Clin. Oral Investig.* **22**, 1243–1252 (2018).

339. Ghasemi, S., Sardari, K., Mirshokraei, P. & Hassanpour, H. In vitro study of matrix metalloproteinases 1, 2, 9, 13 and serum amyloid a mRNAs expression in equine fibroblast-like synoviocytes treated with doxycycline. *Can. J. Vet. Res.* (2018).

340. Ferrer, R. A. *et al.* Dermal Fibroblasts Promote Alternative Macrophage Activation Improving Impaired Wound Healing. *J. Invest. Dermatol.* **137**, 941–950 (2017).

341. Gilroy, D. W., Saunders, M. A. & Wu, K. K. COX-2 expression and cell cycle progression in human fibroblasts. *Am. J. Physiol. Physiol.* (2017). doi:10.1152/ajpcell.2001.281.1.c188

342. Cheng, H.-H. *et al.* Quiescent and Proliferative Fibroblasts Exhibit Differential p300 HAT Activation through Control of 5-Methoxytryptophan Production. *PLoS One* **9**, e88507 (2014).

343. Wu, K. K. Differential cyclooxygenase-2 transcriptional control in proliferating versus quiescent fibroblasts. *Prostaglandins Other Lipid Mediat.* **83**, 175–181 (2007).

344. Chen, B.-R. *et al.* Quiescent Fibroblasts Are More Active in Mounting Robust Inflammatory Responses Than Proliferative Fibroblasts. *PLoS*

One **7**, e49232 (2012).

345. Deng, W. G. *et al.* Purification and characterization of a cyclooxygenase-2 and angiogenesis suppressing factor produced by human fibroblasts. *FASEB J.* (2002).

346. Chu, L.-Y., Wang, Y.-F., Cheng, H.-H., Kuo, C.-C. & Wu, K. K. Endothelium-Derived 5-Methoxytryptophan Protects Endothelial Barrier Function by Blocking p38 MAPK Activation. *PLoS One* **11**, e0152166 (2016).

347. Hangai, S. *et al.* PGE2 induced in and released by dying cells functions as an inhibitory DAMP. *Proc. Natl. Acad. Sci.* **113**, 3844–3849 (2016).

348. Huang, J. *et al.* Doxycycline Attenuates Endotoxin-Induced Uveitis by Prostaglandin E2-EP4 Signaling. *Investig. Opthalmology Vis. Sci.* **56**, 6686 (2015).

349. Attur, M. G., Patel, R. N., Patel, P. D., Abramson, S. B. & Amin, A. R. Tetracycline up-regulates COX-2 expression and prostaglandin E2 production independent of its effect on nitric oxide. *J. Immunol.* (1999).

350. Kämpfer, A. A. M. *et al.* Development of an in vitro co-culture model to mimic the human intestine in healthy and diseased state. *Toxicol. Vitr.* (2017). doi:10.1016/j.tiv.2017.08.011

351. Pillinger, M. H. *et al.* Cyclooxygenase-2-Derived E Prostaglandins Down-Regulate Matrix Metalloproteinase-1 Expression in Fibroblast-Like Synoviocytes via Inhibition of Extracellular Signal-Regulated Kinase Activation. *J. Immunol.* (2003).

doi:10.4049/jimmunol.171.11.6080

352. Chen, W. *et al.* Sustained co-delivery of ibuprofen and basic fibroblast growth factor by thermosensitive nanoparticle hydrogel as early local treatment of peri-implantitis. *Int. J. Nanomedicine* **Volume 14**, 1347–1358 (2019).

353. Yu, D.-G., Zhang, X.-F., Shen, X.-X., Brandford-White, C. & Zhu, L.-M. Ultrafine ibuprofen-loaded polyvinylpyrrolidone fiber mats using electrospinning. *Polym. Int.* **58**, 1010–1013 (2009).

Chapter 8

Appendix

8.1 Supplementary data for Chapter 3

8.1.1 Effect of PLGA8515 concentrations on the morphology of the scaffolds

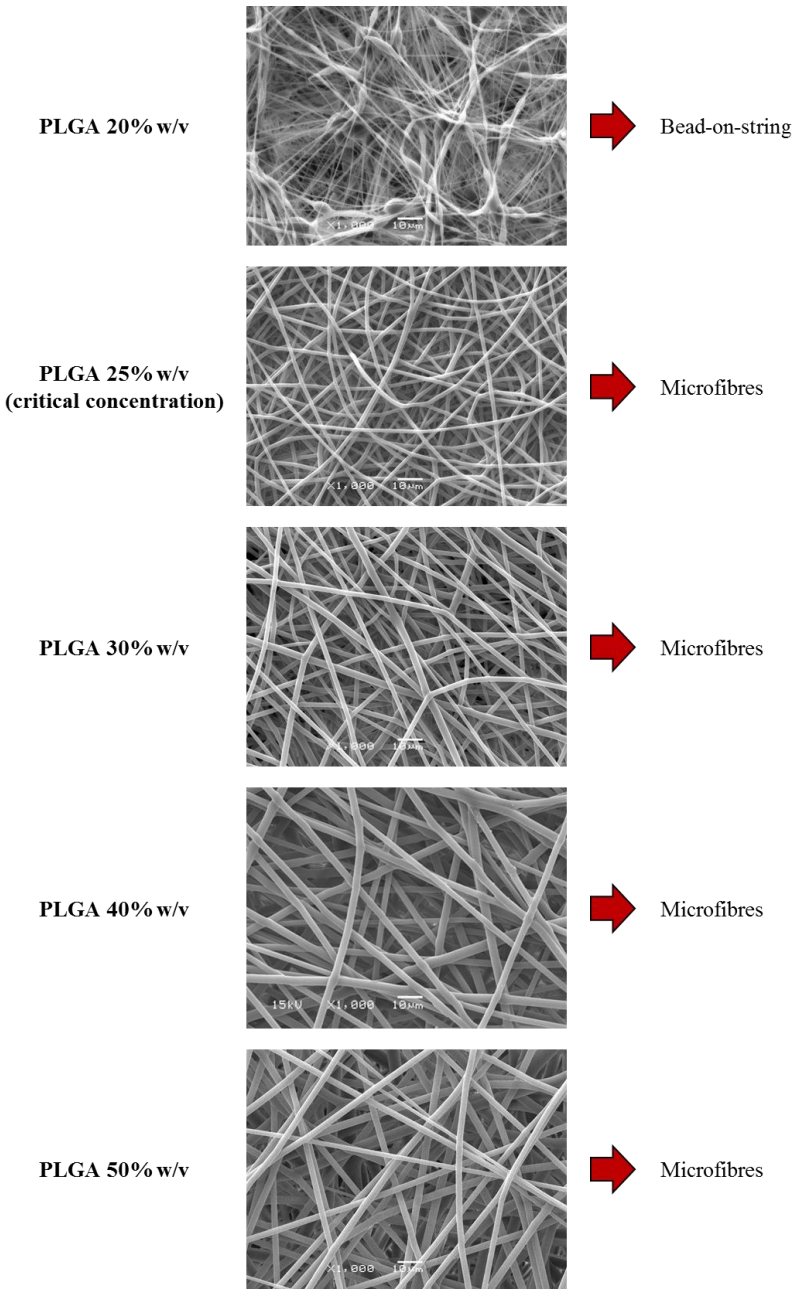


Figure 8.1. Representative SEM images of the scaffolds that were fabricated with different concentrations of PLGA8515 polymer in HFIP solutions. The magnification of all images is 1,000X with the scale bar of 10 µm.

8.1.2 Standard curve for determining drug encapsulation efficiency

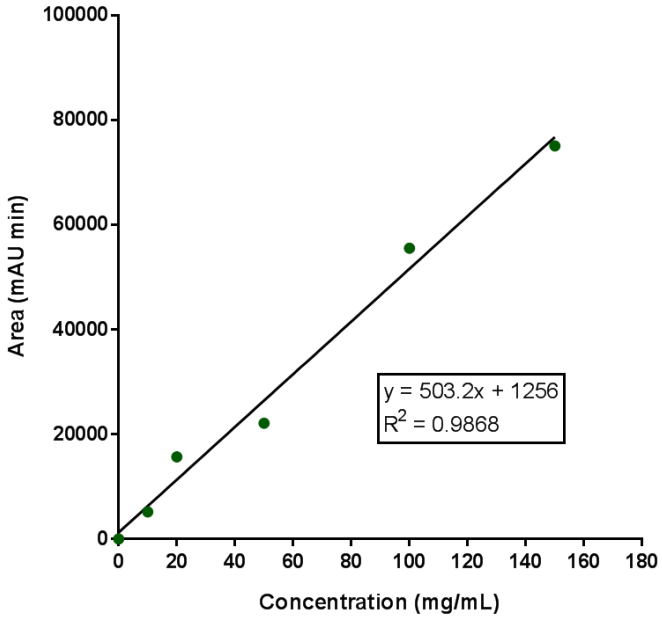


Figure 8.2. Standard curve for ibuprofen sodium (IBU Na) determined by HPLC.

8.1.3 Standard curve for drug release study

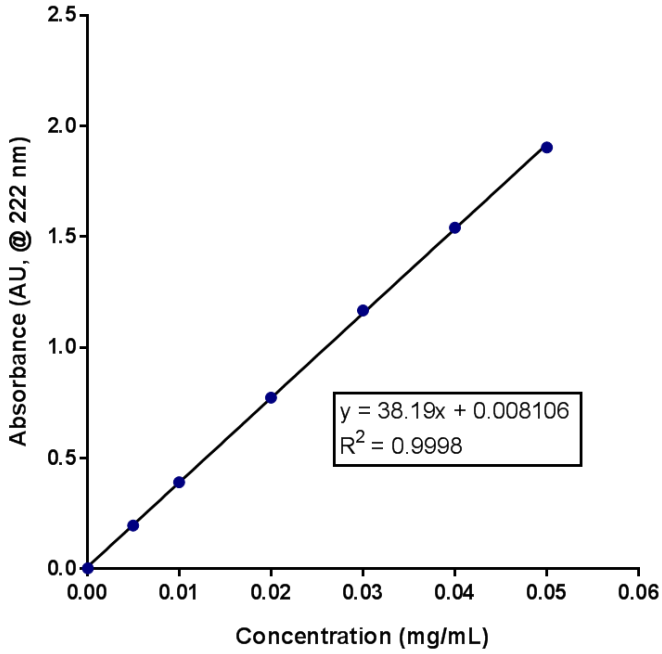


Figure 8.3. Standard curve for ibuprofen sodium (IBU Na) obtained from UV-Vis spectrophotometry.

8.1.4 Determination of cellular metabolic activity using PrestoBlue® assay

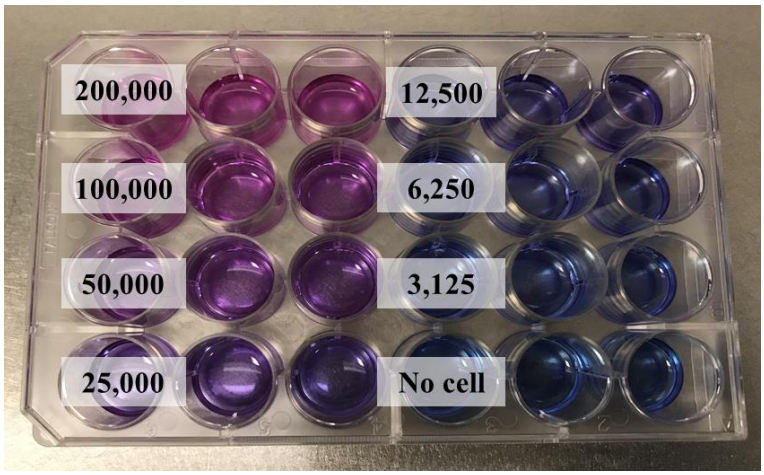


Figure 8.4. The colour changes of PrestoBlue® reagent from resazurin (blue) to resorufin (red) by different numbers of cells.

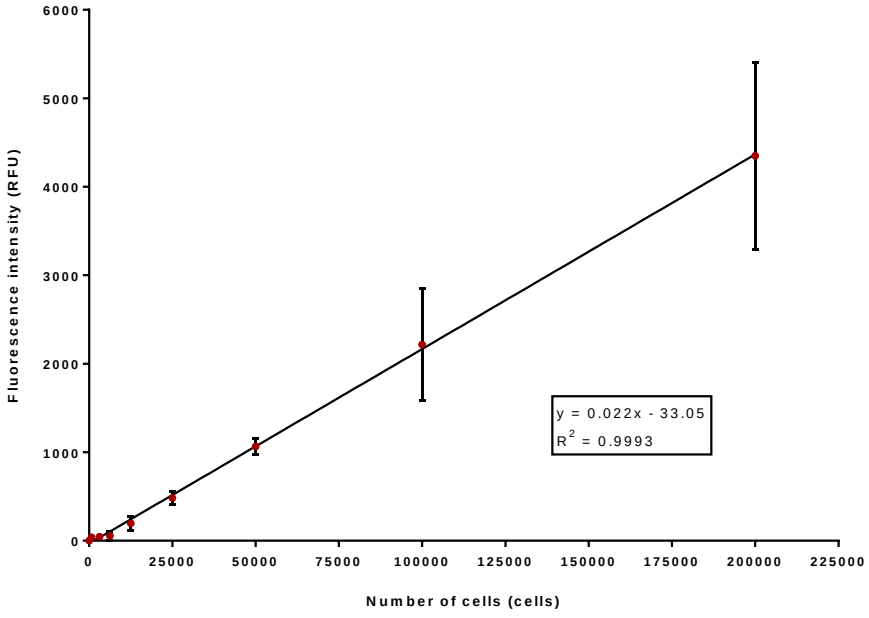


Figure 8.5. Reduction of PrestoBlue® reagent from resazurin (non-fluorescent) to resorufin (highly fluorescent) by different numbers of living mouse fibroblasts (3T3 cells).

8.2 Supplementary data for Chapter 4

8.2.1 The morphology of doxycycline hydrochloride (DOX HCl)-loaded electrospun scaffolds

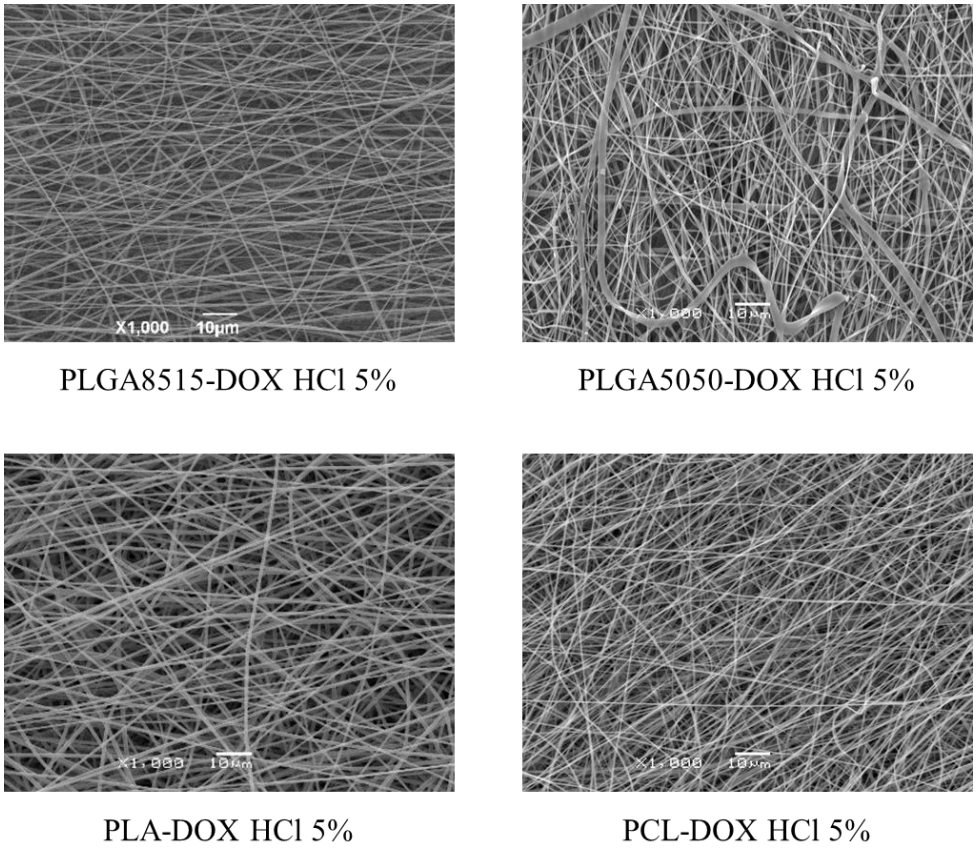


Figure 8.6. Representative SEM images of DOX HCl-loaded electrospun scaffolds fabricated with PLGA8515, PLGA5050, PLA and PCL polymers.

8.2.2 Drug release profiles

8.2.2.1 PLGA8515-DOX HCl scaffolds

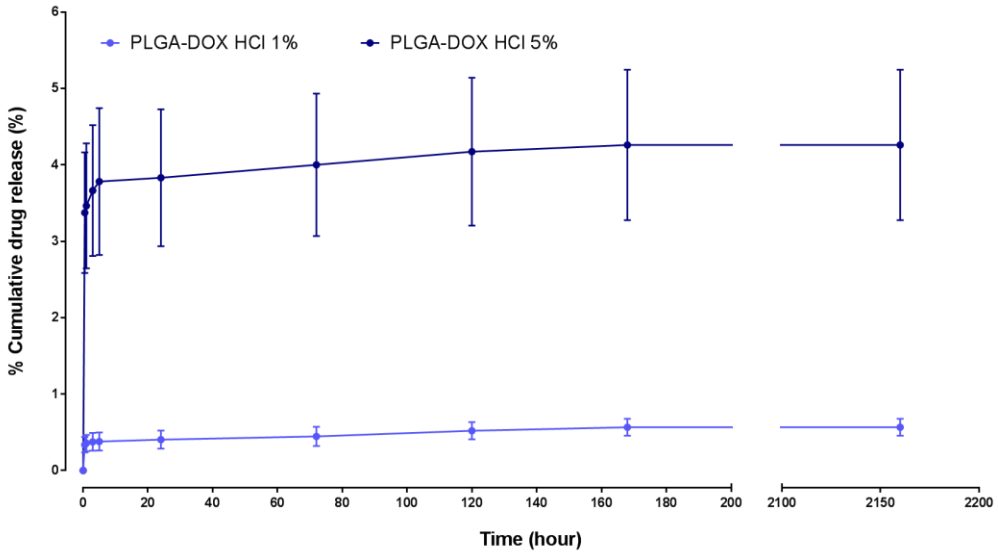


Figure 8.7. Cumulative drug release of DOX HCl from PLGA8515-DOX HCl 1% and PLGA8515-DOX HCl 5% scaffolds in PBS over 90 days (2,160 h). The values represent means and standard deviations of triplicate samples.

8.2.2.2 PLGA5050-DOX HCl and PLA-DOX HCl scaffolds

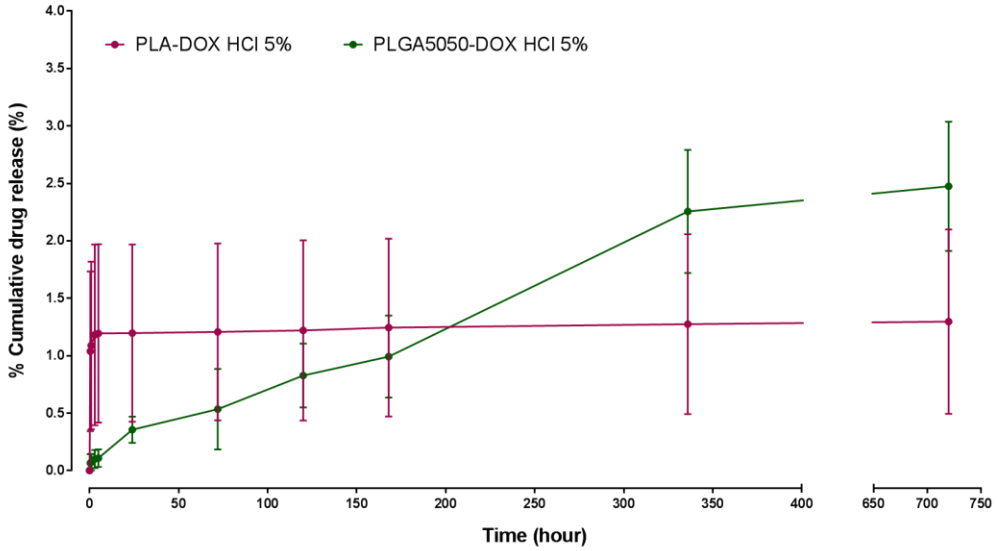


Figure 8.8. Cumulative drug release of DOX HCl from PLGA5050-DOX HCl 5% and PLA-DOX HCl 5% scaffolds in PBS over 30 days (720 h). The values represent means and standard deviations of triplicate samples.

8.2.3. Drug degradation in the scaffolds

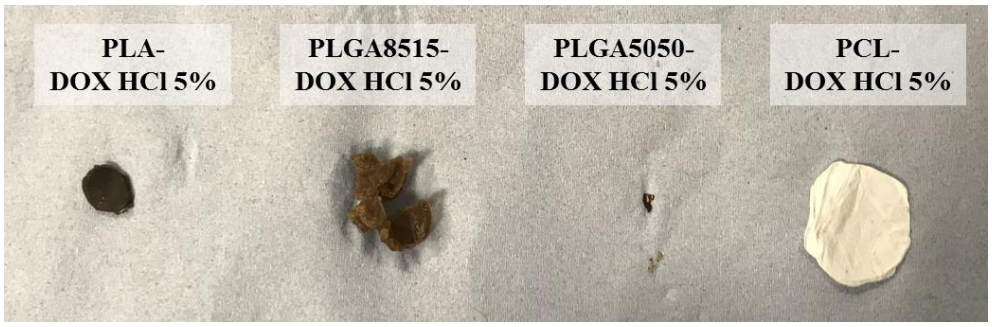


Figure 8.9. The electrospun scaffolds after incubating in PBS at 37 °C for 90 days. The degradation of DOX HCl encapsulated in the scaffolds was shown as brown/back colour.

8.2.4 Standard curve for determining drug encapsulation efficiency

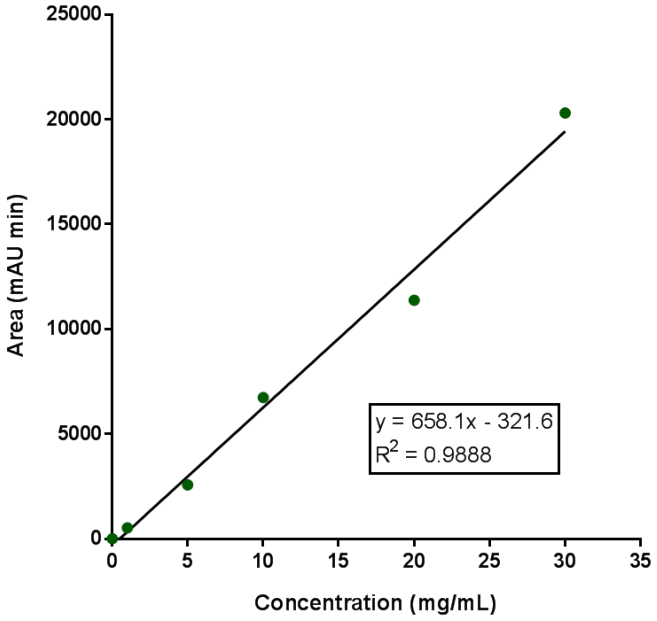


Figure 8.10. Standard curve for doxycycline hydrochloride (DOX HCl) determined by HPLC.

8.2.5 Standard curve for drug release study

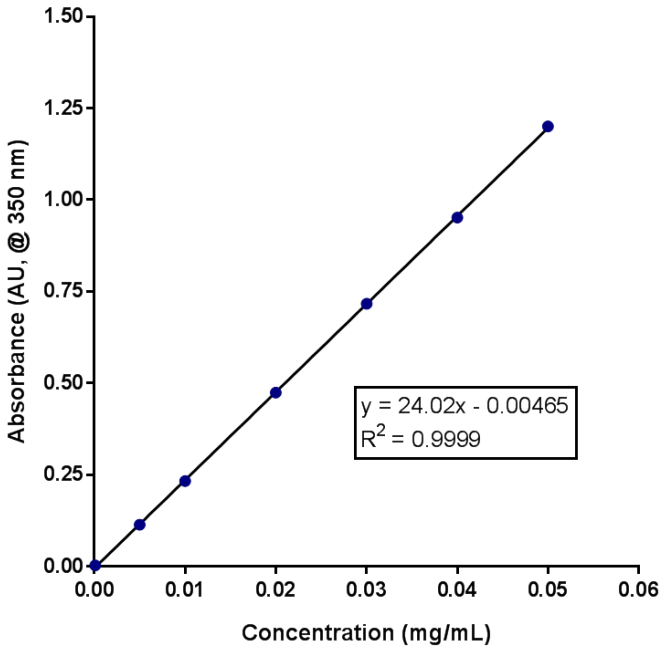


Figure 8.11. Standard curve for doxycycline hydrochloride (DOX HCl) obtained from UV-Vis spectrophotometry.

8.2.6 Determination of cellular metabolic activity using PrestoBlue® assay

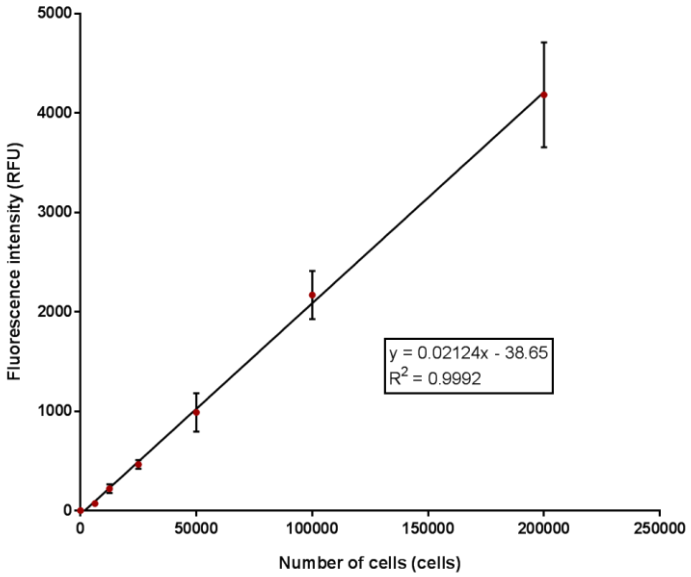


Figure 8.12. Reduction of PrestoBlue® reagent from resazurin (non-fluorescent) to resorufin (highly fluorescent) by different numbers of living mouse fibroblasts (3T3 cells).

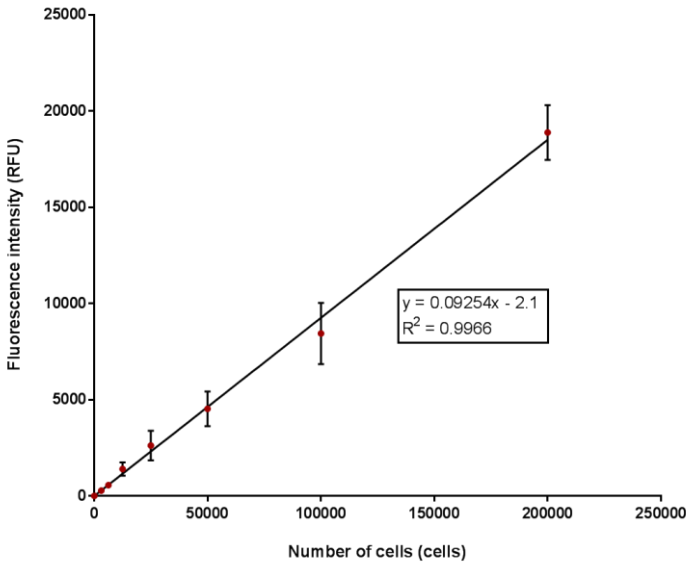


Figure 8.13. Reduction of PrestoBlue® reagent from resazurin (non-fluorescent) to resorufin (highly fluorescent) by different numbers of living primary human dermal fibroblasts.

8.2.7 The release of doxycycline hydrochloride (DOX HCl) from PCL scaffolds in cell culture media

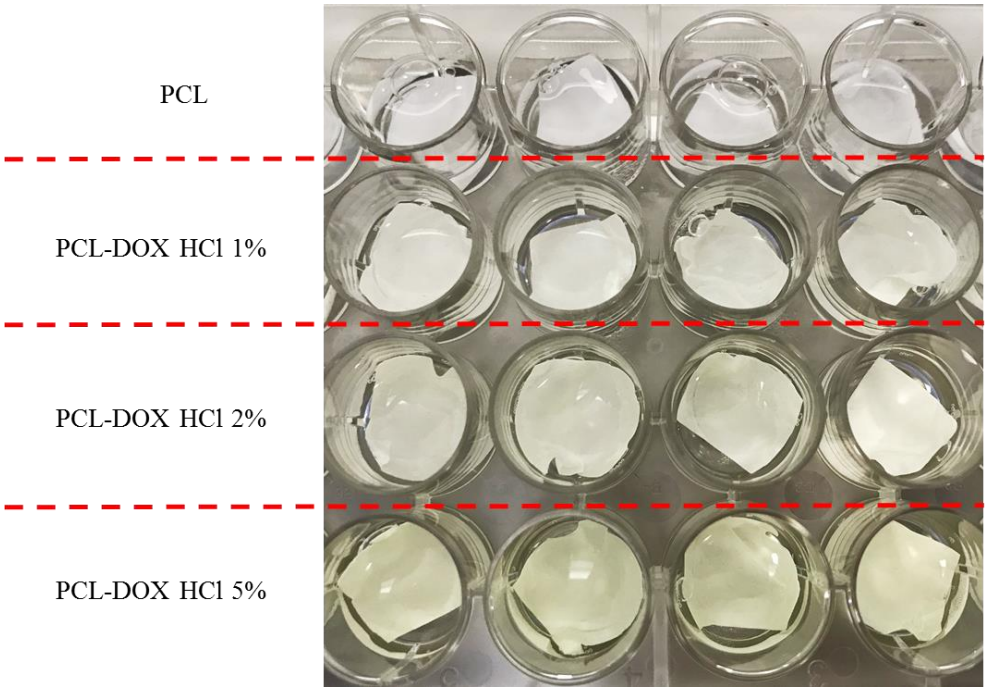


Figure 8.14. The release of doxycycline hydrochloride (DOX HCl) from PCL scaffolds in cell culture media. The intensity of yellow colour in cell culture media increases with the higher drug loadings.

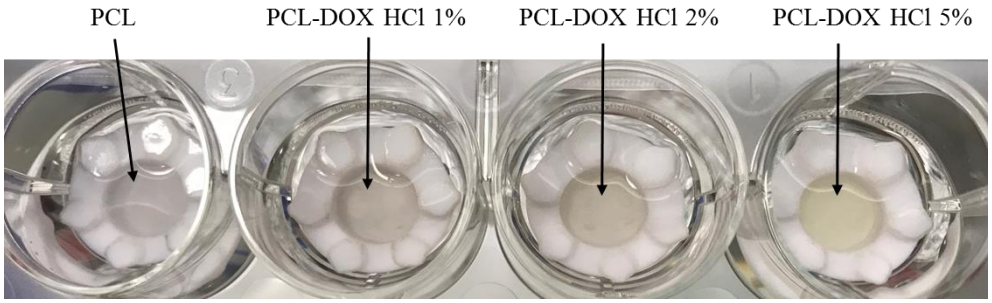


Figure 8.15. Representative images of the scaffolds after incubating in cell culture media for 24 hours. The remaining doxycycline hydrochloride (DOX HCl) in PCL scaffolds is present as yellow colour.

8.3 Supplementary data for Chapter 5

8.3.1 The morphology of the scaffold and core-shell structure of fibres

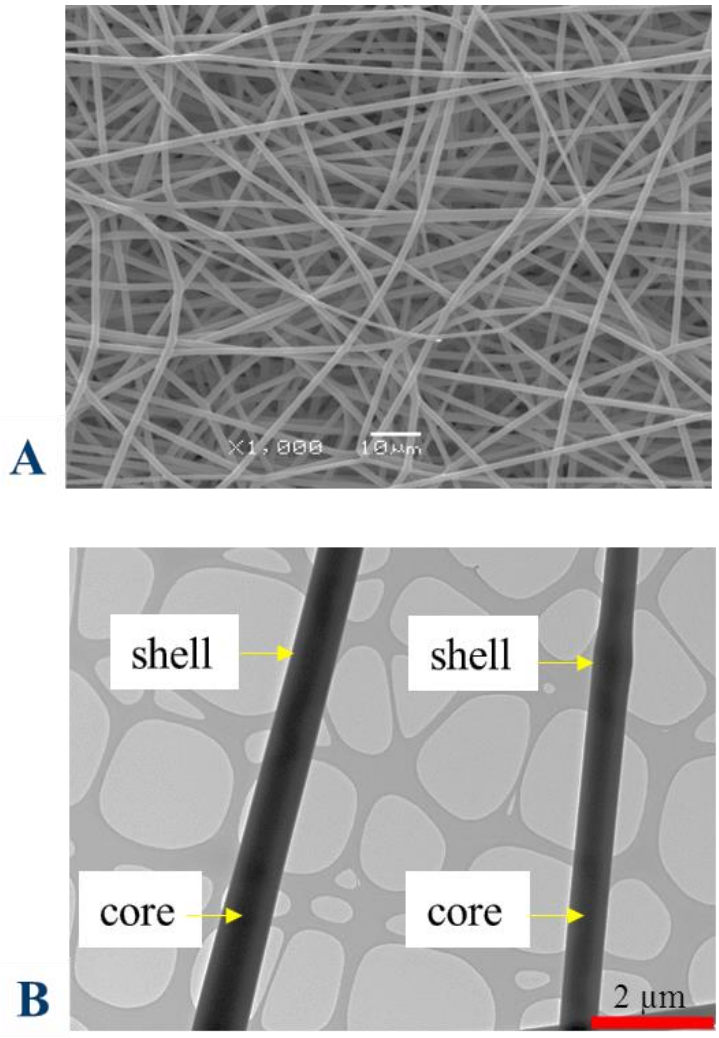


Figure 8.16. Representative (A) SEM and (B) TEM images of coaxial PLGA-IBU Na 1% (shell)/PCL-DOX HCl 5% (core) scaffolds at the magnification of 1,000X (scale bar: 10 μm) and 8,200X (scale bar: 2 μm), respectively.

8.3.2 Standard curve for drug release study

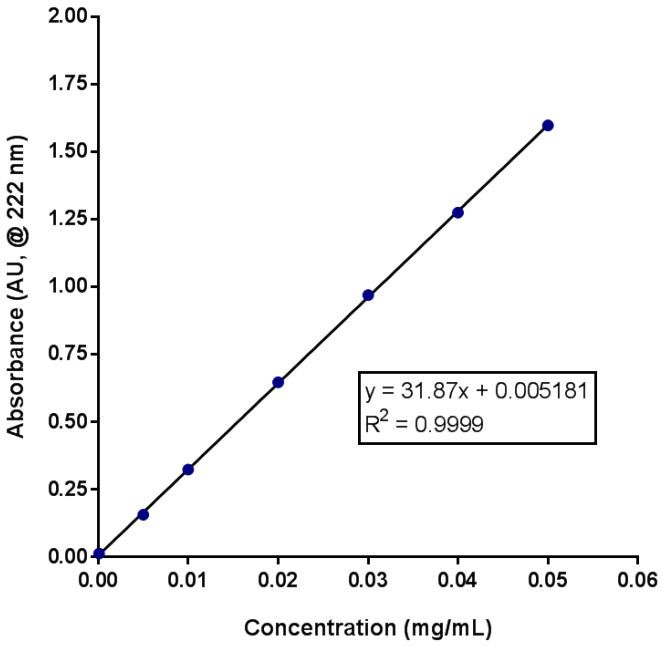


Figure 8.17. Standard curve for ibuprofen sodium (IBU Na) in the mixture of ibuprofen sodium and doxycycline hydrochloride determined by UV-Vis spectrometry at the wavelength of 222 nm.

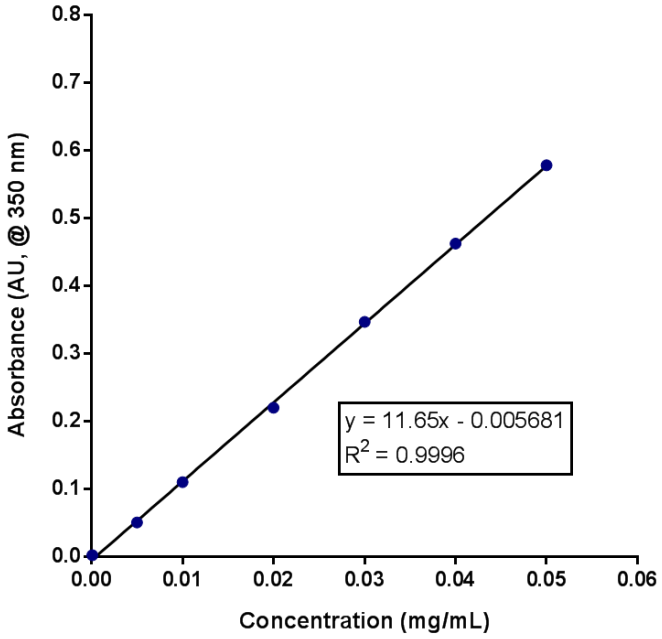


Figure 8.18. Standard curve for doxycycline hydrochloride (DOX HCl) in the mixture of ibuprofen sodium and doxycycline hydrochloride determined by UV-Vis spectrometry at the wavelength of 350 nm.

8.3.3 Drug release profile of coaxial PLGA-IBU Na 1% (shell)/PCL-DOX HCl 5% (core) electrospun scaffolds

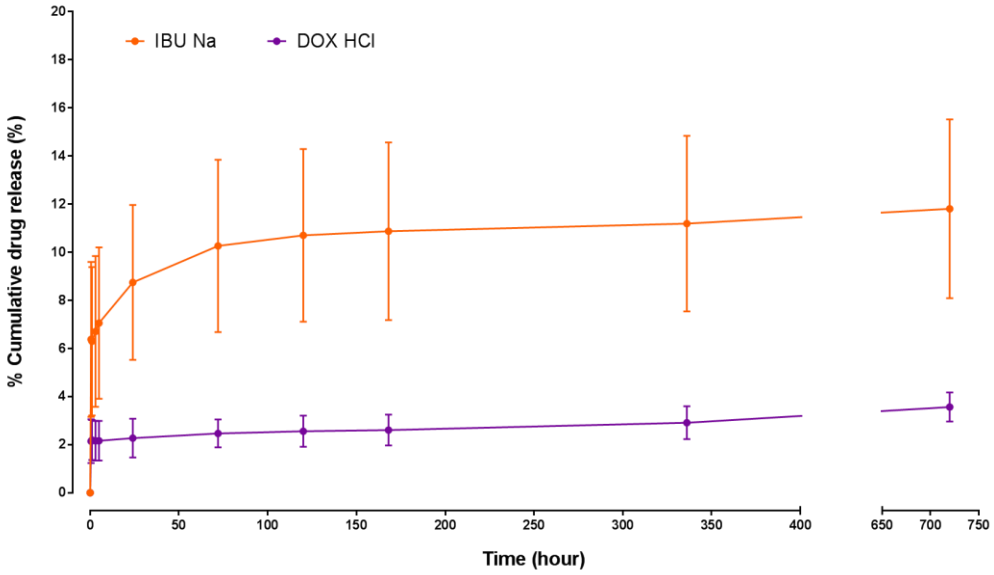


Figure 8.19. Cumulative drug release of IBU Na and DOX HCl from coaxial PLGA-IBU Na 1% (shell)/PCL-DOX HCl 5% (core) electrospun scaffolds in PBS over 30 days (720 h). The values represent means and standard deviations of triplicate samples.

8.3.4 Determination of cellular metabolic activity using PrestoBlue® assay

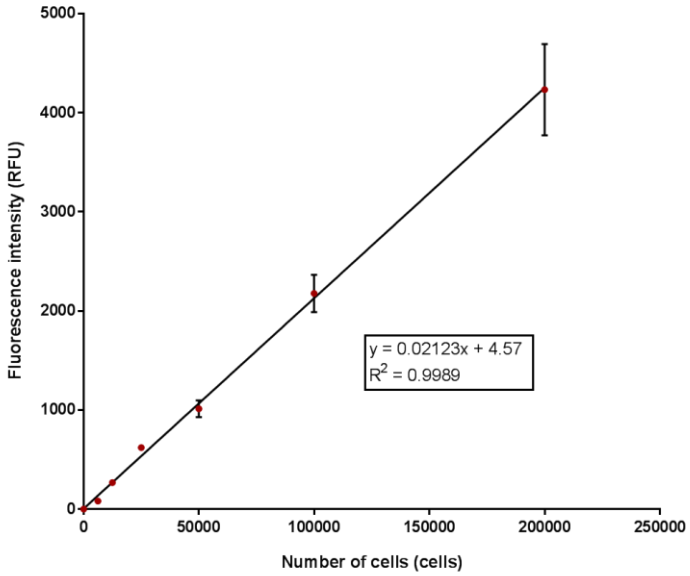


Figure 8.20. Reduction of PrestoBlue® reagent from resazurin (non-fluorescent) to resorufin (highly fluorescent) by different numbers of living mouse fibroblasts (3T3 cells).

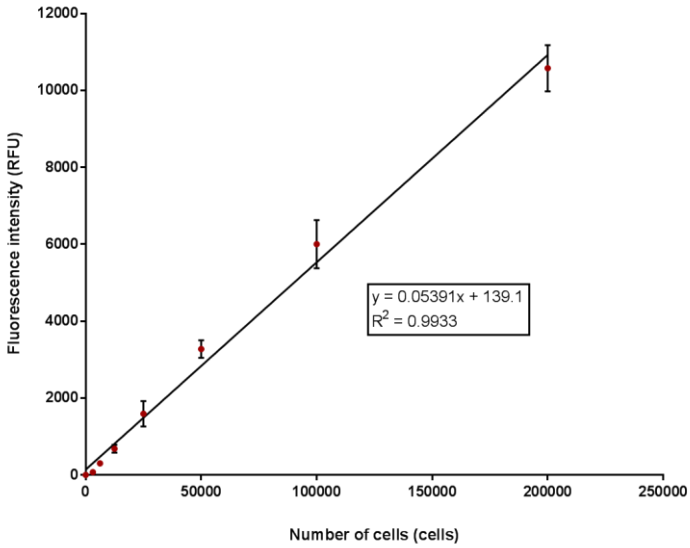


Figure 8.21. Reduction of PrestoBlue® reagent from resazurin (non-fluorescent) to resorufin (highly fluorescent) by different numbers of living primary human dermal fibroblasts.

8.4 Supplementary data for Chapter 6

8.4.1 PCL-DOX HCl scaffolds

8.4.1.1 Determination of cellular metabolic activity using PrestoBlue® assay

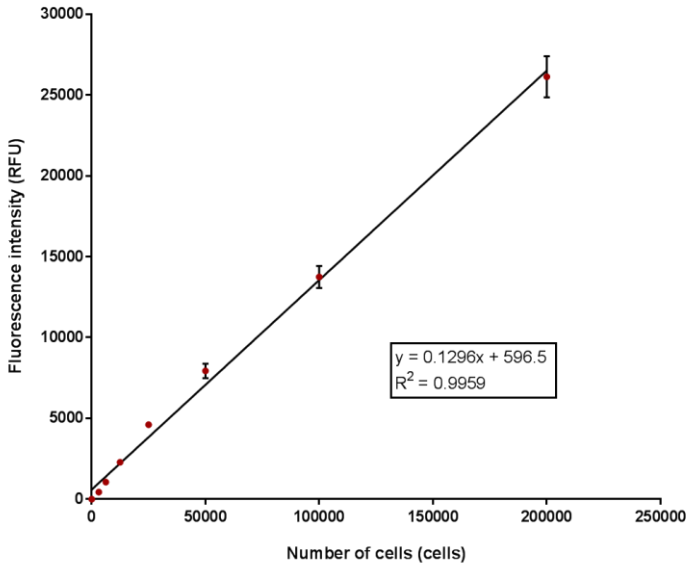


Figure 8.22. Reduction of PrestoBlue® reagent from resazurin (non-fluorescent) to resorufin (highly fluorescent) by living primary human dermal fibroblasts.

8.4.1.2 Determination of nitrite concentration using Griess assay

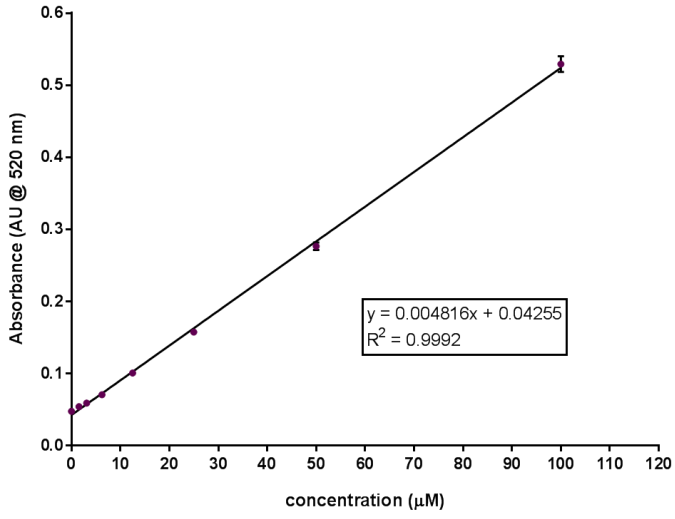


Figure 8.23. Standard curve for nitrite quantification

8.4.2 Coaxial electrospun scaffolds

8.4.2.1 Determination of cellular metabolic activity using PrestoBlue® assay

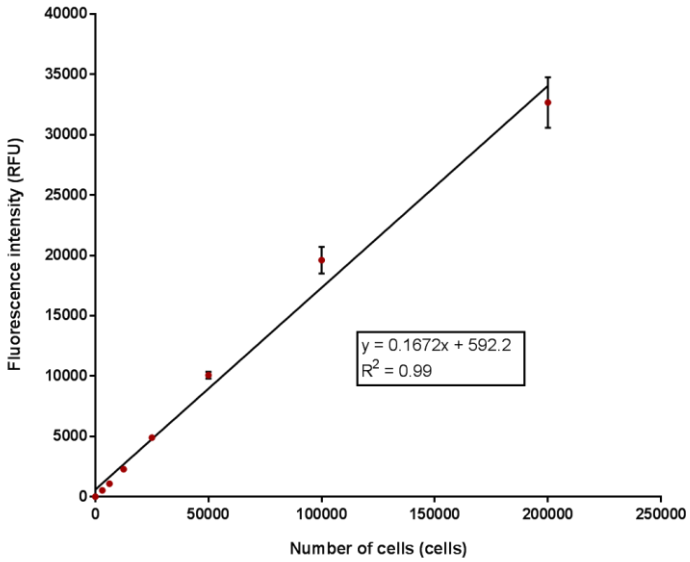


Figure 8.24. Reduction of PrestoBlue® reagent from resazurin (non-fluorescent) to resorufin (highly fluorescent) by living primary human dermal fibroblasts.

8.4.2.2 Determination of nitrite concentration using Griess assay

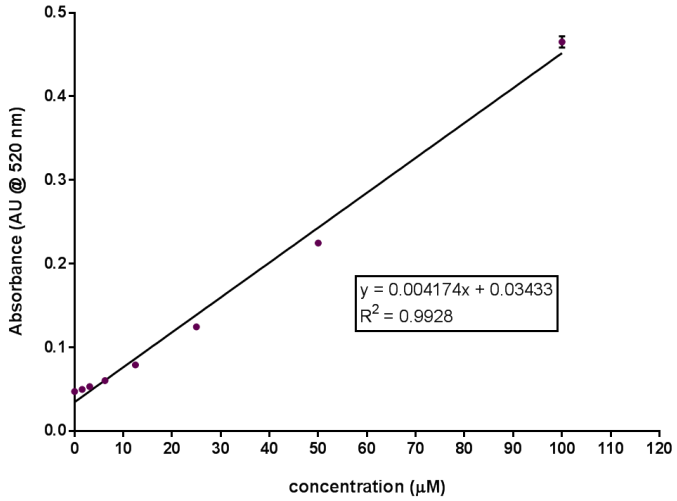


Figure 8.25. Standard curve for nitrite quantification